



THE HONG KONG
POLYTECHNIC UNIVERSITY

香港理工大學

Pao Yue-kong Library

包玉剛圖書館

Copyright Undertaking

This thesis is protected by copyright, with all rights reserved.

By reading and using the thesis, the reader understands and agrees to the following terms:

1. The reader will abide by the rules and legal ordinances governing copyright regarding the use of the thesis.
2. The reader will use the thesis for the purpose of research or private study only and not for distribution or further reproduction or any other purpose.
3. The reader agrees to indemnify and hold the University harmless from and against any loss, damage, cost, liability or expenses arising from copyright infringement or unauthorized usage.

IMPORTANT

If you have reasons to believe that any materials in this thesis are deemed not suitable to be distributed in this form, or a copyright owner having difficulty with the material being included in our database, please contact lbsys@polyu.edu.hk providing details. The Library will look into your claim and consider taking remedial action upon receipt of the written requests.

Pao Yue-kong Library, The Hong Kong Polytechnic University, Hung Hom, Kowloon, Hong Kong

<http://www.lib.polyu.edu.hk>

**AN EXPERIMENTAL STUDY OF CRACK GROWTH AND
ITS EFFECT ON THE MECHANICAL AND SEISMIC
PROPERTIES OF ROCKS USING 3D PRINTING,
MICRO-CT AND ACOUSTIC EMISSION**

ZHOU TAO

PhD

The Hong Kong Polytechnic University

2019

The Hong Kong Polytechnic University
Department of Civil and Environmental Engineering

An Experimental Study of Crack Growth and Its Effect on the
Mechanical and Seismic Properties of Rocks using 3D Printing,
Micro-CT and Acoustic Emission

ZHOU Tao

A thesis submitted in partial fulfillment of the requirements for the
degree of doctor of philosophy

October 2018

CERTIFICATE OF ORIGINALITY

I hereby declare that this thesis is my own work and that, to the best of my knowledge and belief, it reproduces no material previously published or written, nor material that has been accepted for the award of any other degree or diploma, except where due acknowledgement has been made in the text.

_____ (Signed)

_____ ZHOU Tao _____ (Name of student)

ABSTRACT

Rock is heterogeneous and contains numerous discontinuities, e.g., cracks, voids, and joints. The presence of these discontinuities not only governs the mechanical behaviors of rock masses but also significantly affects the rocks' seismic responses. In the past, great efforts have been devoted to studying the effects of discontinuities on the mechanical and seismic behaviors of rocks. Nevertheless, some scientific problems remain. For instance, few studies have been conducted to investigate three-dimensional (3D) internal crack growth and its effects on the mechanical and fracture behaviors of rocks. Thus far, no studies have been reported considering the combined effects of joint geometry (e.g., joint matching coefficient (JMC)) and infilling materials (e.g., infilling types and water content) on wave propagation across joints.

Focusing on the remaining problems, experimental research of cracks, especially 3D internal micro and macrocracks, crack growth and the effects on the mechanical and seismic properties of rocks are investigated in this thesis.

To replicate naturally brittle and hard rocks, 3D printing (3DP) is introduced to the study of rock mechanics. The translucent resin produced via stereolithography (SLA) is identified as the most suitable 3DP material for replicating brittle and hard rocks based on currently available 3DP techniques. Three methods, including freezing, incorporation of internal macrocracks and the addition of microdefects are adopted to enhance the brittleness of the 3DP resin. To some extent, 3DP application to rock mechanics can solve the problem of preparing artificial rock-like samples with internal structures identical to the prototype rocks.

The 3DP technique is adopted to fabricate resin-based artificial rocks containing single and double, pre-existing, penny-shaped 3D internal flaws. Static and dynamic compression tests are performed on these samples to investigate the influence of flaw geometry and loading types on the mechanical and fracturing behaviors of 3DP artificial rocks. For the first time, high-speed cameras are applied to the study of 3D crack growth inside the transparent 3DP resin samples in real-time. Distinctions between the volumetric fracturing of resin-based artificial rocks under static and dynamic loading conditions are compared, and the physical mechanisms behind these types of fractures are proposed.

In this research, 3DP is adopted to replicate internal defects and study the mechanical and fracture behaviors of rock in combination with microcomputed tomography (micro-CT). The validity and efficiency of this method is confirmed by comparing the results with the physical tests conducted on the natural prototype volcanic rocks. The advantages and disadvantages as well as potential improvements of the method are compared and discussed. The proposed method provide a promising means to quantify, replicate and visualize the pre-existing defects and microstructures and to understand their influences on the mechanical and fracture behavior of rock under different loading conditions.

In addition to mechanical and fracture properties, the damage evolution effects on low-amplitude ultrasonic wave propagation in rock samples are also studied. Acoustic emission activities are employed to quantify damage evolution during uniaxial compression loading. In addition, micro-CT detection is applied to quantitatively determine damage inside the rock sample after the loading and unloading processes. Then, the relationship between damage evolution and ultrasonic wave propagation is quantitatively analyzed.

Based on the split Hopkinson rock bar system, stress wave propagation is conducted to study the coupling effects of JMC, loading rate and water contents of the infilling mixture on the mechanical and seismic properties of a single, rough joint. JMC is found to play a dominant role in affecting the mechanical and seismic properties of the joint compared with the infilling mixture and loading rate.

PUBLICATIONS

PUBLICATIONS ARISING FROM THE THESIS

1. Zhou T, Zhu JB. Identification of a suitable 3D printing material for mimicking brittle and hard rocks and its brittleness enhancements. *Rock Mechanics and Rock Engineering*. 2018; 51(3): 765-777.
2. Zhu JB, Zhou T, Liao ZY, Sun L, Li XB, Chen R. Replication of internal defects and investigation of mechanical and fracture behaviour of rock using 3D printing and 3D numerical methods in combination with X-ray computerized tomography. *International Journal of Rock Mechanics and Mining Sciences*. 2018; 106: 198-212.
3. Zhou T, Zhu JB, Ju Y, Xie HP. Volumetric fracturing behavior of 3D printed artificial rocks containing single and double 3D internal flaws under static uniaxial compression. *Engineering Fracture Mechanics*. 2019; 205: 190-204.
4. Zhou T, Zhu JB, Xie HP. An experimental study of volumetric fracturing and mechanical properties of resin-based artificial rock under dynamic compression. (submitted to *Rock Mechanics and Rock Engineering*, revised).

CONFERENCE PAPERS

1. Zhou T, Zhu JB. Application of 3D printing and micro-CT scan to rock dynamics. In *Proceedings of the 2nd international conference on rock dynamics and applications*. Suzhou; 2016; 18-20 May. 2016. p. 247-252.
2. Zhou T, Zhu JB. Experimental study of propagation of 3D flaws under static and dynamic loading conditions with the application of 3D printing. *The 9th Asian Rock Mechanics Symposium, Bali, Indonesia; 2016*.
3. Zhu JB, Zhou T. Replicating brittle and hard rocks using 3D printing with applications to rock dynamics and crack propagation. *The International Geotechnics Symposium cum International Meeting of CSRME 14th Biennial National Congress, Hong Kong; 2016 (Theme Lecture)*.
4. Zhou T, Zhu JB. An experimental investigation of tensile fracturing behavior of natural and artificial rocks in static and dynamic Brazilian disc tests. *The 2017 ISRM European Rock Mechanics Symposium, Ostrava, Czech; 2017; Procedia Engineering*.

191:992-998.

5. Zhou T, Zhu JB. Damage evolution of granite under uniaxial compression with acoustic emissions and its effect on ultrasonic P-wave propagation. 3rd International Conference on Rock Dynamics and Applications, Trondheim, Norway; 2018.

ACKNOWLEDGEMENTS

First and foremost, I wish to express my warmest and deepest thanks to my chief supervisor, Associate Professor Cheng Yungming, and co-supervisor, Professor Xia Yong, for their endless tolerance, support and encouragement during my final year. I also deeply indebted to my ex-chief supervisor, Professor Zhu Jianbo at Tianjin University (TJU), who is responsible for bringing me to PolyU and guiding me during my normal period study. I thank him for his invaluable guidance and numerous suggestions as well as endless support to my research. I also thank him for his understanding and support when I experienced great difficulties.

I am grateful to the other co-supervisor, Professor Li Xibing at Central South University (CSU), who was my chief supervisor when I was a five-year PhD student at CSU. His enthusiasm and rigorous attitude toward research gave me deep impression, which shaped my understanding and attitude toward scientific research in my early research career.

Mr. Leung Kwokman (Raymond) is gratefully acknowledged for his practical advice, full support and willingness to help whenever needed during performing my experiments in Rock Mechanics Lab. His warm tips, kindness care and friendliness are also appreciated and acknowledged. I also thank Professor Chau Kamtim, who was the examiner of my Certification Presentation. He gave me many constructive comments which benefited to improve the quality of my research. I also thank Dr. Wong Hoi Chu (Robina) for her valuable suggestions to my research. Dr. Leung Yatfai (Andy) is also gratefully thanked for his financial support during my final year. I wish to thank Mr. Lin Hoiyung for helping me doing thin section tests to characterize mineral components of rock samples.

I would like to especially thank Dr. Zou Yang, who introduced me to Professor Zhu Jianbo when he was an academic staff at PolyU. Without his help, I would not have the chance to write this thesis. Drs. Zou Yang, Wang Shiming, Zhou Jian, Du Kun and Tao Ming are also acknowledged for their help and guidance when I was a green man in rock dynamics at CSU. I also thank Professor Li Diyuan and Dr. Wang Zewei at CSU and Dr. Liao Zhiyi at Dalian University of Technology. It is my pleasure to collaborate with all of you on carrying out researches.

I sincerely thank those who helped me to successfully conduct experiments at CSU, TJU and National University of Defense Technology (NUDT). They are Dr. Yu Changyi, Mr. Wang Shuai, Mr. Bao Weiyue and Mr. Li Rui at TJU, and Dr. Chen Rong and Mr. Li Kang at NUDT. I also thank Mr. Wong Wingfat (Sidney) from Industrial Centre of PolyU for his great support in 3DP sample preparation.

I wish to thank the geotechnical group for their discussions, useful suggestions and friendship. They are Dr. Liao Zhiyi, Miss Yang Hui, Mr. Han Dongya, Dr. Liu Leilei, Mr. Li Kaihui, Mr. Li Hua, Dr. Zheng Fei and Mr. Li Jian. I will miss the happy time we spent on cooking and playing werewolf games.

I lovingly thank my family for their love, tolerance, encouragement and endless support throughout my study period. I would like to especially thank my two elder sisters, for their taking care of our parents at home so that I could concentrate on pursuing my PhD degree outside.

Finally and most importantly, I lovingly express my sincere thanks to my wife, Wei Chunyu. Since meeting eight years ago, Chunyu has been a continuous source of love, pleasure, support and encouragement.

This thesis is dedicated to my parents and wife!

TABLE OF CONTENTS

ABSTRACT	I
PUBLICATIONS	III
ACKNOWLEDGEMENTS	V
TABLE OF CONTENTS	VII
LIST OF FIGURES.....	XI
LIST OF TABLES.....	XX
CHAPTER 1 INTRODUCTION	1
1.1 Background	1
1.2 Research objectives.....	3
1.3 Organization of the thesis.....	4
CHAPTER 2 LITERATURE REVIEW.....	6
2.1 Review of crack growth	6
2.1.1 2D crack growth.....	6
2.1.2 3D crack growth.....	12
2.1.2.1 3D surface crack growth	12
2.1.2.2 3D internal crack growth.....	14
2.1.3 Review of damage characterization	17
2.1.4 Effect of damage on wave propagation in rocks	20
2.1.5 Review of mechanical and seismic behaviors of rock joints	22
2.2 Review of the main apparatus and techniques	24
2.2.1 SHPB.....	24
2.2.2 Micro-CT	27
2.2.3 AE	29
2.2.4 The 3DP technique	31
CHAPTER 3 IDENTIFICATION OF A SUITABLE 3D PRINTING MATERIAL FOR MIMICKING BRITTLE AND HARD ROCKS AND ITS BRITTLENESS ENHANCEMENTS	34
3.1 Introduction	34
3.2 3DP principle.....	35
3.3 Experimental setup.....	36
3.3.1 Specimen preparation.....	36
3.3.2 Testing apparatuses	38

3.4	Results and analysis	39
3.4.1	Identification of the most suitable 3DP material.....	40
3.4.2	Brittleness enhancement for 3DP resin material.....	43
3.4.2.1	Freezing.....	43
3.4.2.2	Incorporation of a macro-crack.....	46
3.4.2.3	Addition of micro-defects	47
3.5	Discussion	50
3.6	Conclusions.....	53
CHAPTER 4 FABRICATION OF 3D INTERNAL FLAWS WITH 3DP AND INVESTIGATION OF THEIR FRACTURING AND MECHANICAL BEHAVIORS UNDER STATIC AND DYNAMIC COMPRESSION		55
4.1	Introduction.....	55
4.2	Experimental setup.....	56
4.2.1	Sample preparation	56
4.2.2	Testing apparatus.....	59
4.3	Results.....	60
4.3.1	Static uniaxial compression tests	60
4.3.1.1	Static strength and deformation	60
4.3.1.2	Three-dimensional crack growth behaviors.....	62
4.3.2	Dynamic compression tests.....	70
4.3.2.1	Dynamic strength and deformation.....	70
4.3.2.2	The initiation stress of the first crack.....	71
4.3.2.3	Three-dimensional crack growth in specimens with single 3D internal flaw	72
4.3.2.4	Three-dimensional crack growth in specimens with double 3D internal flaws	74
4.3.2.5	Crack propagation velocity	76
4.4	Discussion	77
4.5	Conclusions.....	85
CHAPTER 5 REPLICATION OF INTERNAL DEFECTS AND INVESTIGATION OF MECHANICAL AND FRACTURE BEHAVIOR OF ROCK USING 3DP AND MICRO-CT		87
5.1	Introduction.....	87
5.2	Experimental setup.....	88

5.2.1	Rock sample preparation.....	88
5.2.2	X-ray micro-CT scanning of rock samples	89
5.2.3	Reproduction of natural rocks using 3DP	90
5.2.4	Testing apparatus.....	92
5.3	Results.....	93
5.3.1	Static uniaxial compression tests	93
5.3.2	Static Brazilian disc tests	95
5.3.3	Dynamic uniaxial compression tests.....	96
5.3.3.1	Dynamic Brazilian disc tests.....	98
5.4	Discussion	100
5.5	Conclusions.....	103
CHAPTER 6 DAMAGE EVOLUTION IN GRANITE UNDER UNIAXIAL COMPRESSION AND ITS EFFECT ON ULTRASONIC P-WAVE PROPAGATION		104
6.1	Introduction.....	104
6.2	Experimental setup.....	105
6.2.1	Sample preparation.....	105
6.2.2	Testing system.....	107
6.3	Results.....	109
6.3.1	P-wave propagation during loading process	109
6.3.1.1	P-waveforms	109
6.3.1.2	P-wave spectra	110
6.3.1.3	P-wave velocity.....	111
6.3.1.4	P-wave amplitude.....	112
6.3.2	AE	113
6.4	Analysis.....	114
6.4.1	Damage evolution during loading process.....	114
6.4.2	Effect of damage evolution on P-wave propagation	119
6.4.2.1	Relationship between D and V_P	119
6.4.2.2	Relationship between D and A_P	121
6.4.3	Damage induced after uniaxial compression	122
6.4.3.1	P-wave propagation in granite sample after loading and unloading process 122	
6.4.3.2	Characterization of stress-induced damage using micro-CT	124

6.4.3.3 Relationship between D_N and V_P and A_P	129
6.5 Discussion	130
6.6 Conclusions.....	133
CHAPTER 7 INFLUENCE OF JMC, WATER CONTENT AND LOADING RATE ON THE MECHANICAL AND SEISMIC PROPERTIES OF A SINGLE ROUGH JOINT IN SHRB TESTS	135
7.1 Introduction.....	135
7.2 Experiment setup.....	137
7.2.1 Rock bar preparation.....	137
7.2.2 Split Hopkinson rock bar	138
7.2.3 Rock joint.....	139
7.2.4 Spring clamping device.....	141
7.2.5 Data processing	141
7.3 Results.....	142
7.3.1 Determination of the critical incident stress	142
7.3.2 Verification of the SHRB test.....	144
7.3.3 SHRB wave propagation with single rough joint	145
7.3.3.1 Stress-strain behaviors	148
7.3.3.2 Deformation behaviors.....	149
7.3.3.3 Joint specific stiffness	152
7.3.3.4 Transmission and reflection coefficients.....	155
7.3.3.5 Energy dissipation.....	158
7.4 Discussions.....	160
7.5 Conclusions.....	162
CHAPTER 8 CONCLUSIONS AND SUGGESTIONS FOR FUTURE RESEARCH	164
8.1 Conclusions.....	164
8.2 Recommendations for future works	167
REFERENCES.....	169

LIST OF FIGURES

Figure 1.1 Organization of the main contents of this thesis.....	5
Figure 2.1 Formation of macro shear crack or fault due to the interactive crack growth at smaller flaws under biaxial compression (Nemat-Nasser and Horii 1982)	8
Figure 2.2 Comparison of 2D flaw growth under uniaxial and biaxial compressions (Bobet and Einstein 1998).....	9
Figure 2.3 Seven typical crack types initiated from the pre-existing flaws identified by Wong and Einstein (2009a). T= tensile cracking opening, S= shearing displacement.....	10
Figure 2.4 Relation between axial stress, AE counts and loading time of sandstone sample containing longer flaw. a and b: flaw angle of 45°, flaw length of 20mm and 25mm, respectively (Yang and Jing 2011)	11
Figure 2.5 Crack growths from a 3D internal flaw in PMMA (Adams and Sines 1978)	15
Figure 2.6 Experimental results from high-temperature fracture of rhyolitic obsidian. (a) Axial stress, normalized cumulative AE energy, and AE <i>b</i> -values against time for uniaxial deformation of rhyolitic obsidian at 645°C and 10 ^{-4.3} s ⁻¹ . (b) Waveform (top) and power spectrum (bottom) of a typical acoustic-emission event, showing the sharp onset and high frequency content (predominantly 100-300 kHz) that are characteristic of brittle failure (Tuffen et al. 2008).....	19
Figure 2.7 Schematic of a conventional SHPB (Dai 2010a). ϵ_i , ϵ_r and ϵ_t refer to incident, reflected and transmitted strain signals obtained through the strain gauges pasted on the incident and transmitted bars, respectively. v_1 and v_2 refer to particle vibration velocities at the end of the incident and transmitted bars, respectively. P_1 and P_2 indicate the input force and output force at the end of the incident and transmitted bars, respectively.	26
Figure 2.8(a) 3D micro-CT image; (b) and (c) 3D images of microcracks in the rock sample viewed from two angles. Grey dots represent cracks and the black arrow is the view direction. (Huang et al. 2013a)	28
Figure 2.9 Evolution of cracks in volume under elevated impacts (Huang et al. 2013a)	29
Figure 3.1 3DP samples before testing. Nominal sample size: 50 mm in diameter and	

100 mm in length	38
Figure 3.2 Testing equipment. (a) VJ Tech tester with a loading capacity of 100 kN; (b) Matest with a loading capacity of 3,000 kN.....	39
Figure 3.3 Stress-strain curves and the failure patterns of the 3DP samples in uniaxial compression tests. (a) Stress-strain curves of the powder-based 3DP samples; (b) Stress-strain curves of samples fabricated using SLA (resin) and FDM techniques (SR20); (c) Failure patterns of the 3DP samples.....	41
Figure 3.4 The status of the 3DP ceramic sample during firing. The numbers below the pictures indicate temperature and duration for the firing treatment.....	42
Figure 3.5 Stress-strain curves of the resin samples with and without pre-existing micro-defects in uniaxial compression tests	48
Figure 3.6 Failure patterns of resin sample with pre-existing micro-defects after uniaxial compression test. (a) Fracturing status before the final failure of the specimen; (b) Fragments in uniaxial compression test	49
Figure 4.1 Preparation of artificial rock using 3DP. (a) 3D model in STL format; (b) Digitally sliced 3D model with arranged printing information; (c) 3DP using the SLA-based Viper si ² printer; (d) Original 3DP artificial rock sample; (e) 3DP artificial rock sample with a single pre-existing internal 3D flaw after transparentizing treatment. The structure in pink color in (b) is a cushion used to support the 3DP sample.	57
Figure 4.2 Geometry of the pre-existing flaws in artificial rock samples. (a) A sample with a single 3D internal flaw; (b) A sample with double 3D internal flaws. α is flaw inclination angle, β is ligament angle, $2a$ is flaw length, and b is ligament length. The arrows represent the loading direction during compression.	57
Figure 4.3 Schematic of the SHPB system	59
Figure 4.4 Axial stress-strain curves of the 3DP resin samples with and without internal penny-shaped flaws under static compression.....	61
Figure 4.5 Stress-strain curve and crack propagation of S-30 sample under static uniaxial compression. (a) Progressive fracturing stages under different loading levels recorded by HSCs; (b) Stress-strain curve and fracturing stages; (c) Failed fragments. The Roman characters I-IV in (a) and (b) indicate the fracturing sequential. <i>FS</i> and <i>SS</i> represent images shot from the front surface and side surface of the resin sample, respectively. The time in (a) is the relative	

- time recorded upon the initiation of the secondary crack. The sketches in (a) are corresponding wing and anti-wing cracks. The arrows show the propagated direction of the secondary cracks and the dashed rectangle shows the initiation place of the secondary crack. WC and AWC indicate wing crack and anti-wing crack, respectively. 63
- Figure 4.6 Anti-wing crack propagation processes in static test. The arrows represent the growing anti-wing cracks. The number in the rightest image refers to the length of the cracks with regard to the radius of the pre-existing flaw. The time below the images represent the absolute time recorded upon the initiation of the anti-wing crack. 64
- Figure 4.7 Crack coalescence patterns in double-flawed 3DP resin samples. The high-speed images illustrate fracturing states before the final failure of the sample. The sketches are corresponding crack patterns of the double-flawed samples. PC and CC refer to petal crack and coplanar crack, respectively. Other abbreviations have the same meaning as those in Fig. 4.5. 65
- Figure 4.8 High-speed images, stress-strain curve and sample after failures of D-105 sample under uniaxial compression. (a) 3D crack propagation and coalescence process recorded by HSCs; (b) Stress-strain curve and fracturing stages; (c) Top and front views of the chaotic cracks in the failed sample. The time in (a) is the relative time recorded upon the initiation of cracks at each stage. PC refers to petal crack. Other abbreviations, the arrows and the dashed rectangle have the same meaning as those in Fig. 4.5. 66
- Figure 4.9 Initiation stress of new crack, peak stress (strength) and the ratio of initiation stress to peak stress versus flaw angle and ligament angle. (a) Specimens with single flaw; (b) Specimens with double flaws. The bars with cyan, red and blue colors represent initiation stress of new crack, peak stress and the ratio of initiation stress to peak stress, respectively. 67
- Figure 4.10 Crack propagation velocity. (a) Wing crack propagation velocity; (b) Upper wing crack propagation process in specimen with α of 30° ; (c) Secondary crack propagation velocity; (d) Upper secondary crack propagation process in specimen with β of 45° . The time in (a) - (d) represents the absolute time recorded upon the initiation of the cracks. The red arrows in (b) and (d) point to the crack tips. 68
- Figure 4.11 Stress-strain curves of the 3DP samples with single and double flaws in

dynamic and static compression tests	71
Figure 4.12 The initiation stress of the first crack	72
Figure 4.13 Fracturing of sample with single 3D flaw under dynamic and static compression. (a) and (b) Progressive fracturing in dynamic and static tests; (c) Axial stress-strain curves; (d) Failure fragments after compression tests. The capital letters A and A'-D' in (a)-(c) indicate fracturing activities at different loading stages. Other abbreviations have the same meaning as those in Fig. 4.5.	73
Figure 4.14 3D crack growth of specimen with double 3D flaws under dynamic and static compression. (a) and (b) Progressive fracturing in dynamic and static tests; (c) Axial stress strain curves; (d) Failure fragments after compression tests. The capital letters in (a)-(c) and other abbreviations as well as time marks have the same meaning as those in Fig. 4.13.	75
Figure 4.15 Comparison of crack propagation velocities in dynamic and static compression tests. (a) and (b) Specimens containing single and double pre-existing 3D internal flaws, respectively	76
Figure 4.16 Patterns of wing cracks generated at the tips of the pre-existing flaw. (a) Present findings from 3DP resin; (b) Findings from regular resin (Dyskin et al. 2003); (c) Findings from PMMA (Germanovich et al. 1994). In (b) and (c) the flaws were produced by embedding aluminum foil disk and high energy laser pulse, respectively.	78
Figure 4.17 Wing cracks in samples with 2D and 3D flaws under static compression. (a) and (b) 2D wing cracks initiated in specimen produced by Columbia resin CR39 (Horii and Nemat-Nasser 1985) and sandstone (Yang and Jing 2011) with single pre-existing 2D flaw; (c) and (d) 3D wing cracks generated in 3DP resin sample with single and double pre-existing 3D internal flaws	79
Figure 4.18 Crack patterns in samples with 2D and 3D flaws under dynamic loading. (a) Marble specimen with a single pre-existing 2D flaw (Zou and Wong 2014); (b) 3DP resin sample with a single pre-existing 3D internal flaw	80
Figure 4.19 Fragments of the specimens after static compression tests	81
Figure 4.20 Comparison of oblique cracks generated at the tips of 3D and 2D flaws. (a) Oblique cracks generated in 3DP resin specimen with a 3D internal flaw; (b) Shear cracks generated at the tips of the PMMA plate with a 2D throughout flaw (Petit and Barquins 1988); (c) Stress concentration shown by distribution	

of isochromes (lines of equal value of maximum shearing stress) from photograph taken after branch fracture generation in (b). bf and sz refer to branch fracture and shear zone, respectively.....	82
Figure 4.21 Failure patterns of single-flawed specimens with $\alpha =$ (a) 0° and (b) 90°	84
Figure 4.22 The minimum principal stresses at flaw tips in 3D FEM modeling. (a) Sketch of a FEM model with single internal flaw and two key points at the flaw tips where wing cracks initiate in physical test; (b) and (c) The minimum principal stress at point 1 (upper right corner of the flaw) and point 2 (lower left corner of the flaw) of the flawed-samples with α equal to 0° , 30° , 60° and 90° under different applied stresses. Note that in FEM modeling compressive stress is positive and tensile stress is negative.	84
Figure 5.1 Micrograph of the volcanic rock using optical microscope.....	89
Figure 5.2 (a) Principle of X-ray micro-CT scanning; (b) 2D micro-CT image of a volcanic rock sample with a spatial resolution of $50\ \mu\text{m}$, where the black color within the circle represents cracks and voids, while the white and grey colors represent mineral grains.	90
Figure 5.3 Workflow of replicating natural volcanic rock sample. (a) Natural volcanic rock sample. (b) 2D micro-CT images with resolution of $50\ \mu\text{m}$. (c) 3D reconstructed micro-CT image. (d) STL formatted 3DP model generated using MM 16.0 software program. (e) Reproducing volcanic rocks using the Viper si2 system. (f) Post-processing of the replicated rocks	91
Figure 5.4 Stress-strain curves and failure patterns in static uniaxial compression tests. (a) Stress-strain curves of the natural volcanic rock and resin-based 3DP rock. (b-c) Failure patterns of volcanic rock and resin-based 3DP rock after compression tests	94
Figure 5.5 Progressive fracturing process of resin-based 3DP rock in static compression test. (a) Axial stress-strain curve. (b) Fragments after compression test. (c) Progressive fracturing images. The numbers on the stress-strain curve and below the sample images represent the observed fracturing sequences at different loading levels.....	94
Figure 5.6 Tensile stress-strain curves of volcanic rock and resin-based 3DP rock from static Brazilian disc tests	96
Figure 5.7 Fracturing process in static Brazilian disc tests. (a-b) Fracturing process	

of natural volcanic rock and resin-based 3DP rock sample, respectively. The time below the high-speed images indicates the relative time recorded since the onset of new cracks	96
Figure 5.8 Stress equilibrium in dynamic compression and Brazilian disc tests. (a-b) Volcanic rock sample and 3DP rock sample in dynamic compression tests. (c-d) Volcanic rock sample and 3DP rock sample in dynamic Brazilian disc tests .	97
Figure 5.9 Dynamic compression tests on volcanic rock and resin-based 3DP rock samples. (a) Compressive stress-time curves. (b) Dynamic fracturing processes. The upper and lower rows of high-speed photography pictures show the fracturing process of volcanic rock and 3DP rock, respectively. The time below the high-speed images indicates the absolute time recorded since the beginning of the dynamic loading.....	98
Figure 5.10 Dynamic Brazilian disc tests on volcanic rock and resin-based 3DP rock. (a) Tensile stress-time curves. (b) Dynamic fracturing processes. The upper and lower rows of high-speed photography pictures show the fracturing process of volcanic rock and 3DP rock, respectively. The time below the high-speed images indicates the absolute time recorded since the beginning of the dynamic loading.....	99
Figure 6.1 Thin section of the tested granite.....	106
Figure 6.2 Prepared granite samples	106
Figure 6.3 Experimental setup for P-wave propagation measurement and AE detection under uniaxial compression.....	107
Figure 6.4 P-wave velocity measurement method. (a) P-wave propagation through the anvils; (b) P-wave propagation through the anvils and the granite sample.	108
Figure 6.5 P-waveforms under different loading stresses. The arrows indicate the arriving time of the first transmitted waveform with respect to the starting point at 0 μ s	109
Figure 6.6 Examples of the initial pulse, a half-cosine taper and the tapered pulse. (a) and (b) Initial pulses obtained under the axial stresses of 0 MPa and 60 MPa, respectively.....	111
Figure 6.7 Spectra of the first-arriving waveform as shown in Fig. 6.5	111
Figure 6.8 Variation of P-wave velocity with respect to axial loading percentages	112

Figure 6.9 Variation of normalized P-wave amplitude with respect to axial loading percentages.....	113
Figure 6.10 Axial stresses and AE activities of the granite samples subjected to different loading levels. (a)-(h) indicate the samples that were loaded to 20%, 40%, 60%, 78%, 87%, 92%, 97% and 100% of UCS, respectively.	115
Figure 6.11 AE activity and damage evolution of a typical specimen (G-23) under uniaxial compression.....	117
Figure 6.12 Relationship between damage degree and loading percentage.....	118
Figure 6.13 Comparison of damage coefficient determined by fitting function and AE counts in experiment of sample G-23	119
Figure 6.14 Principle of using D determined by AE to analyze V_P	120
Figure 6.15 Relationship between V_P and D	120
Figure 6.16 Principle of using D determined by AE to analyze A_P	121
Figure 6.17 Relationship between A_P and D	122
Figure 6.18 Measurement of P-wave propagation in granite sample before and after loading process.....	124
Figure 6.19 (a) NanoVoxel 2000 micro-CT scanner; (b) 2D micro-CT image of a failed granite sample (G-23)	125
Figure 6.20 2D micro-CT images and the corresponding cracks of the granite samples subjected to different axial stresses. The loading percentage of the samples from (a) to (f) are 100%, 97%, 87%, 80%, 60% and 40% of UCS, respectively. The red and blue colors in the images beside the micro-CT images indicate solid materials and cracks, respectively.....	126
Figure 6.21 Determination of cracks from two characterized rock elements extracted from the failed granite sample G-23. (a) Exhibition of the locations of the two characterized rock elements; (b) and (d) The characterized rock elements that are parallel and perpendicular to the loading directions, respectively. (c) and (e) Cracks (marked by red colour) within the characterized rock elements shown in (b) and (d), respectively.....	127
Figure 6.22 Variation of normalized damage of the granite samples after loading to different UCS%.....	128
Figure 6.23 Relationship between V_P and D_N	129
Figure 6.24 Relationship between A_P and D_N	130
Figure 6.25 Comparison of normalized damages between after loading and	

unloading process and during loading process	132
Figure 6.26 Comparison of normalized damages characterized in this chapter with the previous studies (Kim et al. 2015)	132
Figure 7.1 Rock bar drilling site	137
Figure 7.2 (a) Split Hopkinson rock bar system with spring clamping device; (b) Schematic view of the rock bars section.....	139
Figure 7.3 Schematic view of distribution of the joint with different JMC. The shaded part indicates the asperities on joint surface.	140
Figure 7.4 Illustration of sand-clay mixture with different water content	140
Figure 7.5 (a) P-wave velocity of the rock bar after each impact; (b) The peak-to-peak amplitude of the first arriving ultrasonic waveform after each impact; (c) Nine typical waveforms of the first arriving ultrasonic wave after the corresponding impact.....	144
Figure 7.6 (a) Strain signals recorded on the incident and transmitted rock bars; (b) Stress equilibrium between incident and transmitted rock bars.....	145
Figure 7.7 Loading rate calculation from incident stress-time curve	148
Figure 7.8(a) Typical stress-strain curves of the unfilled joints under different loading rate impacts; (b) Typical stress-strain curves of the joint (JMC=19%) filled with sand-clay mixture with different water contents	149
Figure 7.9 Joint closure vs JMC of the non-filled and filled joints	149
Figure 7.10 (a) Joint closure vs loading rate of the non-filled joint; (b) Joint closure vs loading rate of the joint filled with sand-clay mixture	150
Figure 7.11 Joint closure vs water content and loading rate of the joint with infilling material. (a)-(d): Joints with JMC equal to 8%, 19%, 30% and 0%, respectively	151
Figure 7.12 Joint specific stiffness calculation from transmitted stress-closure curve	152
Figure 7.13 Variation of joint specific stiffness with JMC of the filled and non-filled joints under different loading rate impacts. k is the slope of the fitting curve.	153
Figure 7.14 Joint specific stiffness vs loading rate of the non-filled and filled joints. (a) Non-filled joint; (b) Joint filled with sand-clay mixture. k is the slope of the fitting curve.....	153
Figure 7.15 Joint specific stiffness vs water content and loading rate of the joint	

filled with sand-clay mixture. (a)-(d): Joints with JMC equal to 8%, 19%, 30% and 0%.....	154
Figure 7.16 (a) Transmission and reflection coefficients vs JMC of the joint with and without infilling with error bars. (a) Transmission coefficient; (b) Reflection coefficient. Note that the effects of water content and loading rate are not considered.	155
Figure 7.17 Transmission and reflection coefficients vs loading rate of the joint with and without filling materials. (a) and (c) Joint without sand-clay mixture; (b) and (d) Joint filled with sand-clay mixture	157
Figure 7.18 Transmission and reflection coefficients vs water content and loading rate of the joint filled with sand-clay mixture. (a)-(d): Joints with JMC equal to 8%, 19%, 30% and 0%, respectively	158
Figure 7.19 Energy dissipation rate vs JMC and loading rate of the non-filled and filled joints; (b) Energy dissipation rate vs water content of the joints filled with sand-clay mixture with error bars	159
Figure 7.20 (a) Energy dissipation rate vs loading rate of the joint with JMC=0%; (b) Energy dissipation rate vs water content of the joint (JMC=0%) filled with sand-clay mixture with error bars	160

LIST OF TABLES

Table 3.1 The printing details of the 3DP samples.....	37
Table 3.2 Mechanical properties of the 3DP samples	41
Table 3.3 Mechanical properties of the 3DP resin samples	45
Table 4.1 Geometries and experimental results of the flawed samples	58
Table 5.1 Mechanical properties of the volcanic rock and resin-based 3DP rock in static compression tests.....	93
Table 6.1 Physical and mechanical properties of the granite	106
Table 6.2 AE counts and damage coefficient of the granite samples compressed to different loading levels.....	116
Table 6.3 Variation of V_P and A_P after uniaxial compression process.....	123
Table 6.4 Crack areas and damage coefficient of the damaged rocks	128
Table 7.1 Summary of some major results in average values	146

CHAPTER 1 INTRODUCTION

1.1 Background

Rock is a heterogeneous material containing numerous, pre-existing discontinuities, e.g., voids, cracks and joints, and the scales of these discontinuities generally range from grain boundaries to regional faults (Sagong and Bobet 2002). The presence of discontinuities in rock masses has two major effects. On the one hand, discontinuities undermine the mechanical properties, e.g., strength and elastic modulus, of the rock matrix, thereby making the rock mass more susceptible to failure and stability loss (Sagong and Bobet 2002; Sinha and Singh 2000). On the other hand, discontinuities act as dampers that attenuate wave amplitude, filter high-frequency components and delay the group velocity when a stress wave propagates through the discontinuities (Pyrak-Nolt et al. 1990a; Zhu and Zhao 2013). Therefore, a comprehensive understanding of flaw (henceforth referring to the pre-existing discontinuities) growth and its effects on the mechanical and seismic behaviors of rocks is of great concern for rock engineers and seismologists to evaluate the safety and stability of underground structures built on or in rock subjected to static and dynamic loads.

The evolution of flaws and their influence on the mechanical and fracture behaviors of rocks has been extensively studied over the past decades. Due to the heterogeneity of rock material, it is difficult to predict and analyze crack initiation, propagation and coalescence in rocks using theoretical methods (Fang and Harrison 2002; Liang et al. 2012; Liu et al. 2004). In contrast, as a fundamental and effective method, laboratory experiments enable scholars to directly monitor and study flaw growth in rocks under various circumstances (Liu et al. 2004). Therefore, experimental studies of flaw evolution have always been significant. Currently, there are two main research branches for investigating flaw evolution problems, i.e., throughout two-dimensional (2D) flaw growth, 3D surface and 3D internal flaw growth.

Regarding 2D flaw growth, a large number of experimental investigations have been performed in rock and rock-like materials under static or dynamic compression conditions (Bobet and Einstein 1998; Feng et al. 2009; Lajtai 1974; Lee and Jeon 2011; Li et al. 2005a, 2017a; Shen et al. 1995; Wong et al. 2001; Wong and Einstein 2009a; Yang et

al. 2009, 2017; Zou and Wong 2014). The academic community has reached a consensus on the evolutionary mechanism of 2D flaws, which is attributed to these basic and solid studies. In short, new cracks generated from pre-existing 2D flaws can be characterized into three main types, i.e., tensile cracks, shear cracks and mixed tensile-shear cracks, and the failure of rock samples is a mixture of these three major crack types and some other far-field cracks (Wong and Chau 1998; Wong and Einstein 2009a). Under compression, the tensile cracks first generate at or around the flaw(s) tips under relatively low stress; then, tensile cracks continually propagate, accompanied by the initiation and propagation of secondary shear cracks and mixed tensile-shear cracks; finally, the initial tensile cracks and secondary cracks coalesce with each other, ultimately leading to the failure of the specimen (Lee and Jeon 2011; Sagong and Bobet 2002; Wong and Chau 1998; Wong and Einstein 2009b; Yang 2011).

For 3D flaw cases, these flaws appear either as 3D internal flaws (i.e., fully embedded in rocks) or as 3D surface flaws (i.e., part of the flaw intersecting the surface of the rocks) (Yin et al. 2014). Since 3D surface flaws can be conveniently manufactured on rock surfaces by saw cut, much effort have been devoted to studying the evolution of 3D surface flaws (Cannon et al. 1990; Liu et al. 2008; Lu et al. 2015; Wong et al. 2004a, b; Yin et al. 2014). By investigating crack growth in rocks and rock-like materials containing 3D surface flaws, Wong et al. (2004a, b) and Yin et al. (2014) concluded that the growth of 3D surface flaws is more complicated than the growth of 2D flaws, the crack propagation length depends on the penetration and inclination angle of the pre-existing flaws, and the coalescence mechanism of 3D surface flaws involves both the linkage by surface fracturing and the linkage inside the specimen.

In terms of the 3D internal flaws, due to the difficulty of accurately fabricating 3D internal flaws inside rock specimens, few experimental studies have been reported so far. To date, some researchers have used rock-like samples produced by transparent, rock-like materials, such as glass (Germanovich et al. 1994; Schmitt and Zoback 1993), polymethyl methacrylate (PMMA) (Adams and Sines 1978; Zhou et al. 2018a) and epoxy resin (Dyskin et al. 2003; Fu et al. 2016, 2017) to investigate the mechanical and internal fracture behaviors of rocks. Nevertheless, in these studies, only some regular flaws, e.g., penny-shaped, elliptical and borehole cracks, are considered, which are distinct from the flaws inside natural rocks. The primary reason is that it is impossible to produce rock-like

samples with internal flaws identical to those in natural rocks using traditional manufacturing methods. Therefore, there is a demand for more effective techniques or methods that can be applied to conveniently prepare rock specimens with internal flaws identical to those of natural rocks and to study real-time damage and fracture evolution within rocks subjected to static or dynamic loads.

In addition to flaw growth, the mechanical and seismic properties of discontinuities with a joint range scale have also been widely investigated. The Bandis-Barton model (Bandis et al. 1983) has been widely used to predict joint deformation and stiffness variation under static loads. Based on the split Hopkinson pressure bar (SHPB) device, many tests were conducted to study the dynamic response of the artificial joints under compressive impacts (Chen et al. 2015; Li and Ma 2009; Li et al. 2010, 2017b; Wu et al. 2012, 2014). The dynamic normal stiffness and wave transmission coefficient of joints increased with JMC and loading rates but decreased with joint thickness (Li et al. 2017b; Li and Ma 2009; Wu et al. 2012, 2014).

However, natural joints are neither always open nor solely filled with sand and clay mixtures. Instead, the joint surfaces are often partially contacted or even bonded via asperities, while the remaining part is filled or partially filled with various mixtures of sand, clay, water and air (Barton 1974; Sinha and Singh 2000; Zhao 1997a). Studies considering the effects of joint geometry and infilling materials on stress wave propagation have not been reported thus far. Therefore, investigations focusing on the above mentioned issue are needed.

1.2 Research objectives

The overall objective of this thesis is to experimentally study crack growth and its influences on the mechanical and seismic properties of rocks. A series of experiments are performed using 3DP, micro-CT and acoustic emissions (AE) as well as high-speed cameras (HSCs) and SHPB techniques. The detailed scope of the study is as follows:

- 1) Identification of a superior 3DP material for replicating hard and brittle rocks with reproducible defects and mechanical properties.
- 2) Preparation of artificial rock samples with pre-existing 3D internal flaws using the

identified 3DP material and to study 3D flaw growth using these 3D printed rocks, which are subjected to static and dynamic loading compressions.

- 3) Replication of internal defects and investigation of the mechanical and fracture behavior of rocks using 3DP method in combination with micro-CT.
- 4) Quantification of damage evolution and its effects on low-amplitude ultrasonic P-wave propagation in rock samples using AE and micro-CT.
- 5) Study the coupling effects of JMC, loading rate and water content of the infilling mixture on the mechanical and seismic properties of a single rough joint with stress wave propagation in rock bars.

1.3 Organization of the thesis

This thesis is composed of 8 chapters. Chapter 1 provides an overview of the evolution of pre-existing flaws and their effects on the mechanical and seismic behaviors of rocks, and the objectives of the thesis are presented. In Chapter 2, a literature review of previous studies is conducted. The previous experimental studies with respect to the growth of 2D and 3D surface and internal flaws are reviewed in detail. Previous theoretical and experimental studies focusing on low-amplitude ultrasonic P-wave and high-amplitude stress wave propagation in damaged and jointed rocks are summarized. In addition, the developments and applications of the testing system, i.e., the SHPB, micro-CT, 3DP, AE and numerical modeling, are also reviewed. In Chapter 3, a superior 3DP material is identified for replicating rocks with reproducible defects and mechanical properties and the materials' brittleness enhancements are presented. The preparation of artificial, resin-based 3DP rocks with 3D internal flaws and an investigation of 3D flaw growth and its effect on the mechanical and fracture behaviors of 3DP rocks subjected to static and dynamic compression are demonstrated in Chapter 4. In Chapter 5, 3DP method is first proposed to replicate the internal defects of natural rocks in combination with micro-CT. Then, the validity and accuracy of this method are verified by comparing the experimental results of the 3DP samples with the physical tests conducted on the natural prototype rocks. Subsequently, damage evolution characterization in granite rock samples during static uniaxial compression and an investigation of the influence of damage evolution on low-amplitude ultrasonic P-wave propagation in rocks are shown

in Chapter 6. In Chapter 7, stress wave propagation in split Hopkinson rock bars (SHRB) with a single rough joint is performed. The effects of JMC, loading rate and water content of the infilling sand-clay mixture on the mechanical and seismic properties of the single rough joint are analyzed in detail. Finally, the conclusions of the entire study and some suggestions for future research are presented in Chapter 8.

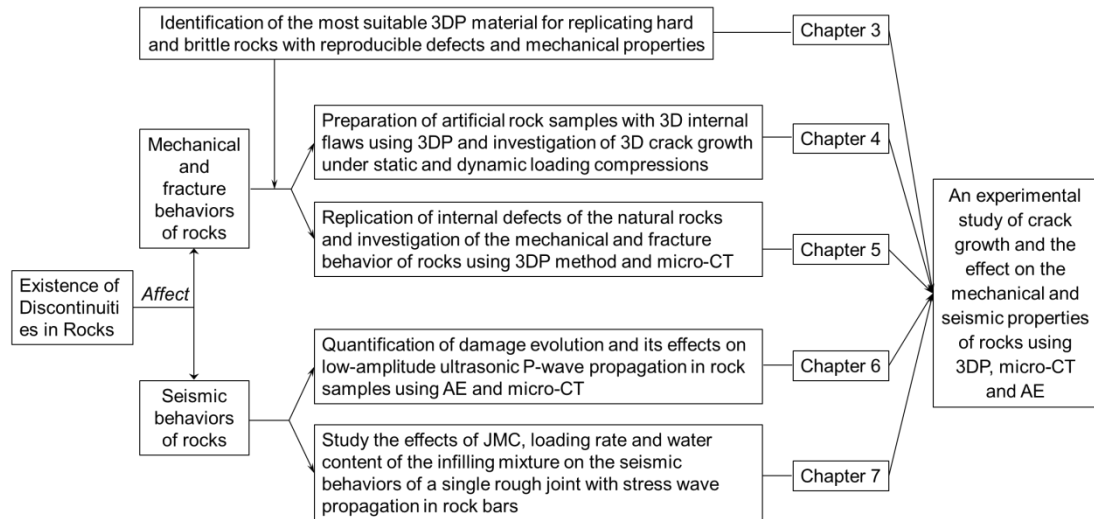


Figure 1.1 Organization of the main contents of this thesis

CHAPTER 2 LITERATURE REVIEW

A literature review of previous research is presented in this chapter. First, the experimental studies on the growth of 2D and 3D flaws and their effects on the mechanical and fracture behaviors of rocks are reviewed in detail. Then, a brief review of the numerical modeling of crack growth is also conducted. Subsequently, investigations of damage evolution in rocks and its effects on ultrasonic wave propagation in both intact and damaged rocks are performed. Then, research work with respect to the mechanical and seismic behaviors of rock joints under static and dynamic loading conditions is reviewed. Finally, a brief review of the major apparatus, i.e., SHPB, and techniques, i.e., micro-CT, 3DP and AE, is also performed.

2.1 Review of crack growth

2.1.1 2D crack growth

It is known that studies of crack evolution began with 2D crack growth and then gradually extended to 3D surface and internal crack propagation and coalescence problems. Therefore, studies of 2D crack growth are first reviewed. It is believed that investigation of 2D crack development could provide a reference for the investigation of 3D crack growth.

The studies on 2D crack growth have lasted for more than half a century and mainly underwent three main stages. In general, the study of 2D crack growth was mainly conducted on transparent, brittle rock-like materials, e.g., PMMA, resin and glass, between the 1960s and 1980s. At this stage, only some intermittent studies were performed on single flaw propagation and multiple flaw coalescence behaviors (Brace and Bombolakis 1963; Hoek and Bieniawski 1965; Horii and Nemat-Nasser 1985, 1986; Nemat-Nasser and Horii 1982). Then, over the next three decades, comprehensive studies were conducted to systematically reveal the evolutionary laws of 2D flaws using artificial, rock-like materials such as gypsum and sandstone-like material (Bobet 2000; Bobet and Einstein 1998; Park and Bobet 2009; Reyes and Einstein 1991; Shen 1995; Shen et al. 1995; Sagong and Bobet 2002; Wong and Chau 1998; Wong et al. 2001). Thereafter, studies of 2D crack propagation and coalescence properties were directly performed on real rock samples with the aid of advanced techniques, such as high-speed

cameras, scanning electron microscopy (SEM) and AEs (Brooks et al. 2013; Lee and Jeon 2011; Li et al. 2005a, 2017a; Wong and Einstein 2009a, 2009b; Yang et al. 2009, 2015, 2017; Yang and Jing 2011).

In the first stage, Bombolakis (1963), Brace (1964) and Brace and Bombolakis (1963) were likely the first to experimentally study 2D crack growth using photoelastic material and glass. Based on their results, these researchers found that under uniaxial tension conditions, a single 2D flaw grew in the direction of its long axis and could continuously extend to the free boundary of the sample, whereas under uniaxial compression, the crack growth that developed at the flaw tips stopped when the cracks curved into the loading direction. Further growth of these branch cracks required an increase in the loading pressure (Brace and Bombolakis 1963). Another important finding reported by Bombolakis (1963) and Brace and Bombolakis (1963) is that the formation of shear fractures or faults in nature would likely be due to the interaction and coalescence between adjacent pairs of parallel flaws. Further research conducted by Hoek and Bieniawski (1965) showed that a single 2D flaw cannot result in the final failure of a specimen under biaxial compression conditions, and the required stress to further drive the crack growth that developed at the flaw tips would be as much as approximately ten times greater than the initiation stress. Later, Nemat-Nasser and Horii (1982) and Horii and Nemat-Nasser (1985) performed experiments on thin plates of Columbia Resin CR 39 to investigate the failure mechanism of brittle solids with single and multiple, appropriately arranged flaws. These researchers concluded that the relative frictional sliding of the pre-existing flaw faces may result in the formation of tension cracks at the flaw tips, and these tension cracks initiated at an angle close to 70° from the long axis of the pre-existing flaw. Moreover, they deduced that the basic mechanism of axial splitting could be the existence of some lateral tension accompanying the axial compression that resulted in the unstable propagation of the tensile cracks developed at the flaw tips. In addition, these researchers also found that under biaxial compression, the sample would not be split by the propagation of the isolated, long pre-existing 2D flaws; instead, the sample would fail by the shear macrocrack that formed by the interaction and coalescence of the tensile cracks generated at the tips of the suitably oriented short 2D flaws, as shown in Fig. 2.1.

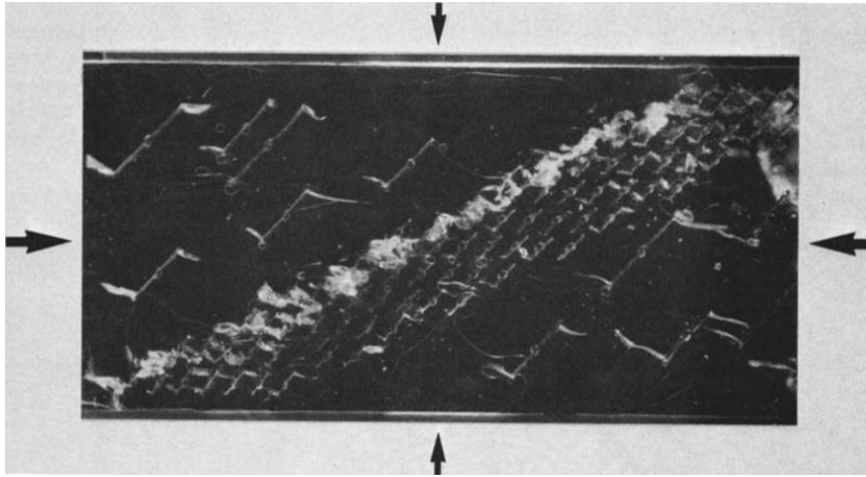


Figure 2.1 Formation of macro shear crack or fault due to the interactive crack growth at smaller flaws under biaxial compression (Nemat-Nasser and Horii 1982)

During the second stage, Einstein and his colleagues (Bobet 2000; Bobet and Einstein 1998; Reyes and Einstein 1991; Shen et al. 1995; Sagong and Bobet 2002) conducted extensive experiments to investigate the evolution of 2D flaws in rock-like gypsum specimens with single, double and multiple open and closed 2D flaws under uniaxial compression. Reyes and Einstein (1991) found that the bridge angle affected the coalescence type between two pre-existing flaws. When the bridge angle was larger than 90° , the two flaws would be coalesced by tensile cracks, while with a bridge angle smaller than 90° , the coalescence between the two flaws became more complicated and could be linked by either tensile cracks, mixed tensile-shear cracks or shear cracks. By performing experiments on gypsum samples with open and closed flaws, Shen et al. (1995) demonstrated that two major differences in flaw growth were found between the open and closed 2D flaws. On the one hand, the tensile wing cracks generated at the closed flaw tips were straighter than those developed from the open flaws. On the other hand, the coalescence stress of the closed flaws was higher than that of the open flaws by approximately 35%. Further investigations conducted by Bobet and Einstein (1998) revealed that the confining stresses made the growth of 2D flaws more complicated than that in uniaxial compression tests, as shown in Fig. 2.2.

	Uniaxial	Biaxial
Crack pattern	Combination of wing (tensile) and secondary (shear) cracks	
Wing cracks	Stable They align with the most compressive stress direction Internal and external wing cracks initiate at the same stress Stress initiation increases with the flaw angle, ligament length and confining stress Closed flaws have higher initiation stresses than open flaws	Initiate from the middle of the flaw for confining stress (σ_h) < 5 MPa No wing cracks for σ_h > 5 MPa Small wing cracks
Secondary cracks	Initially stable. Later on they may be unstable Initiate from the tips of the flaw and initially grow in the plane of the flaw Internal and external secondary cracks initiate at the same stress. Initiation stress increases with the flaw angle, ligament length and confining stress. Closed flaws have higher initiation stresses than open flaws	Initiate before the wing cracks
Coalescence	Coalescence stress increases with the flaw angle, ligament length and confining stress Closed flaws have higher coalescence stresses than open flaws Types I, II, III*	Types I, II*
Failure	Coincides with coalescence	After coalescence

* Specific description of these coalescence types can be found in Table 3, 4 in Bobet and Einstein (1998)

Figure 2.2 Comparison of 2D flaw growth under uniaxial and biaxial compressions (Bobet and Einstein 1998)

During nearly the same period, Wong and Chau (1997, 1998) and Wong et al. (2001) also conducted a series of experimental studies on 2D flaw growth, particularly the pattern of flaw coalescence between double and triple 2D flaws using sandstone-like materials. These researchers found that the coalescence pattern of the closed flaws with different surface frictions could be characterized into three main modes: shear mode, mixed shear/tensile mode and wing tensile mode, and the strength of the flawed samples increased with an increasing frictional coefficient on the pre-existing flaw surfaces (Wong and Chau 1998). Subsequently, these researchers further revealed that the mixed and wing tensile modes of coalescence were the dominant modes when the coalescence stress between the two flaws was very close (within 5%), and the strength of the flawed specimens was determined by the actual number of cracks that took part in the coalescence rather than the initial flaw density (Wong and Chau 1997; Wong et al. 2001).

In the past decade, researchers began to conduct experiments on real rock samples

containing well-fabricated, pre-existing 2D flaws. With the aid of a highly pressurized water-jet system, 2D flaws could be cut throughout rock samples with thicknesses between 20 and 50 mm (Lee and Jeon 2011; Li et al. 2017a; Wong 2008; Wong and Einstein 2009a, 2009b; Yang et al. 2009; Yang and Jing 2011). Wong (2008) examined the quality of the flaws with SEM and confirmed that the damage induced by the pressurized water around the flaw surfaces was negligible. With the aid of a high-speed video system and SEM, Wong (2008) and Wong and Einstein (2009a, 2009b) performed a series of experiments on Carrara marble samples with various geometric parameters, e.g., flaw angle, length, number and bridge angle and length. These researchers reported that the cracks generated from the tips of the pre-existing 2D flaw under uniaxial compression can be mainly characterized into seven typical crack types, as shown in Fig. 2.3, in which three types were tensile cracks, three types were shear cracks and the remaining crack was a mixed tensile-shear crack (Wong 2008; Wong and Einstein 2009a). The ultimate failure mode of the flawed samples under uniaxial compression was a mixture of several typical cracks, as demonstrated in Fig. 2.3.

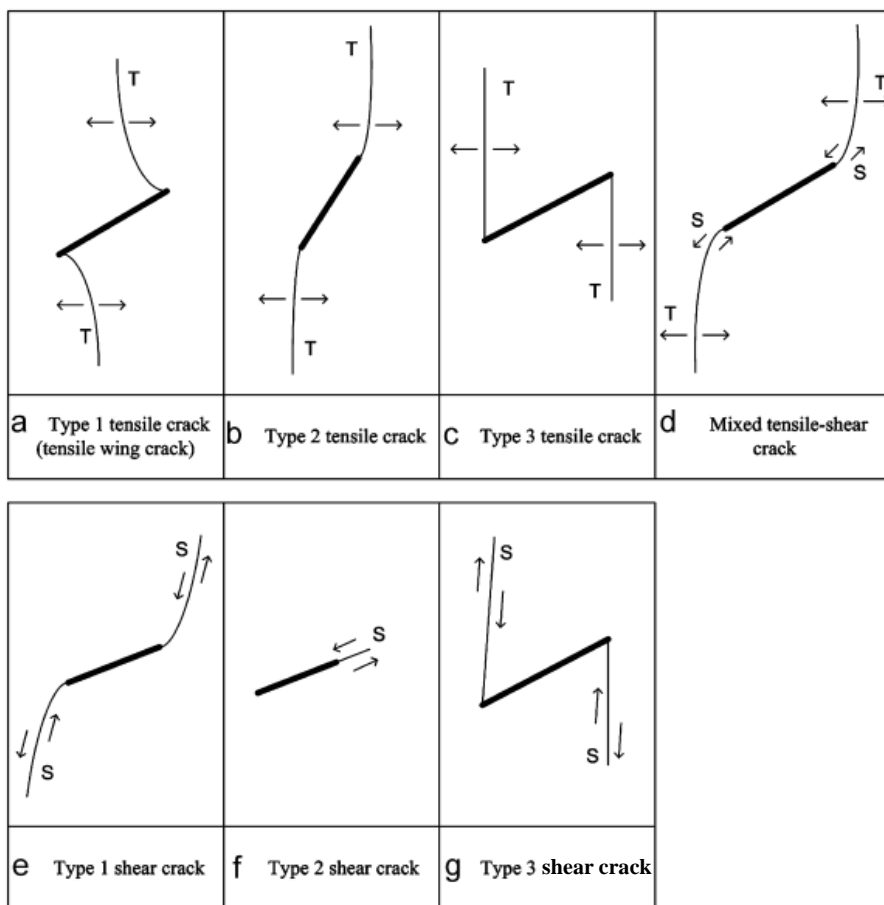


Figure 2.3 Seven typical crack types initiated from the pre-existing flaws identified by

Wong and Einstein (2009a). T= tensile cracking opening, S= shearing displacement

With photographic monitoring and AE detection techniques, Yang and his colleagues performed extensive research on the growth of 2D flaws and their effect on the mechanical and fracture behaviors of sandstone and marble specimens (Yang 2011; Yang et al. 2009, 2017; Yang and Jing 2011). Similar to Wong and Einstein (2009a), Yang and Jing (2011) also identified nine typical crack types to describe the crack growth from pre-existing 2D flaws under uniaxial compression. However, to some extent, the characterized cracks determined by these researchers were similar to those identified by Wong and Einstein (2009a), except for two types of far-field tensile and shear cracks. In addition, the results also showed that the presence of the pre-existing 2D flaws greatly weakened the strength and elastic modulus of the rock samples. Specifically, the longer the flaw length, the lower the strength and elastic modulus of the rocks (Yang 2011; Yang and Jing 2011). One interesting point demonstrated by Yang and his colleagues was that the AE activities during compression agreed well with the progressive fracturing of the flawed samples, as shown in Fig. 2.4 (Yang and Jing 2011; Yang et al. 2009, 2017). This indicates that we may adopt AE to monitor the growth of the discontinuities inside the rock structures, e.g., rock slopes and underground mining pillars, and then, we can assess and even produce warnings regarding the stability of these rock structures.

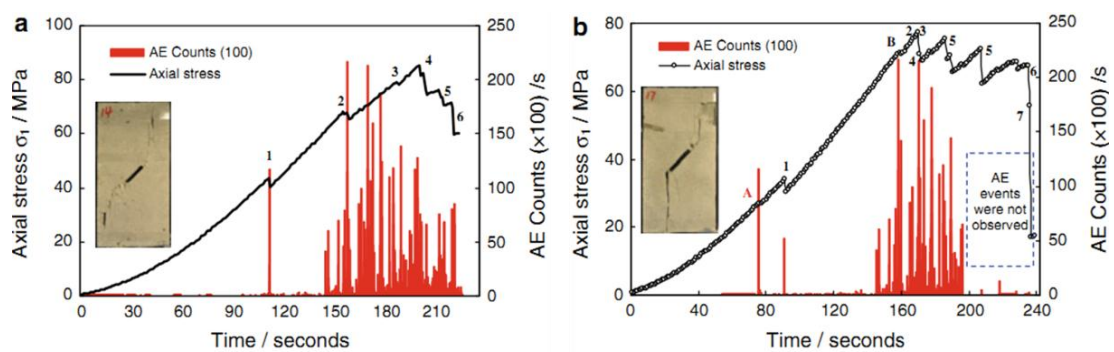


Figure 2.4 Relation between axial stress, AE counts and loading time of sandstone sample containing longer flaw. a and b: flaw angle of 45° , flaw length of 20mm and 25mm, respectively (Yang and Jing 2011)

In addition to static loading conditions, studies on 2D crack growth in rock and gypsum specimens under dynamic loading were also investigated during this time (Li et al. 2017a; Li and Wong 2012; Zou and Wong 2014). Zou and Wong (2014) extended the

research of cracking processes in rock specimens with pre-existing 2D flaws from quasistatic compression conditions to dynamic loading conditions. Li et al. (2017a) performed experiments on prismatic marble samples containing a single, pre-existing 2D flaw using the SHPB device. In these studies, shear cracks were found to always appear earlier than tensile cracks under dynamic loading, and tensile cracks were often suppressed by the dominant propagated shear cracks. Additionally, Li et al. (2017a) and Zou and Wong (2014) reported that the presence of a pre-existing flaw may change the failure mode of marble from splitting-dominated to shear-dominated under dynamic loading.

2.1.2 3D crack growth

In addition to 2D flaws, in nature, pre-existing discontinuities are often 3D, i.e., either as 3D surface flaws or as 3D internal flaws, which may result in more complicated fracturing behaviors in the flawed rocks. Considering this, numerous efforts have been devoted to investigating the growth of 3D flaws in the past several decades. Because the preparation of 3D surface flaws in rock or rock-like samples is much easier than fabricating 3D internal flaws inside the rock samples, most of the studies with respect to 3D crack growth are an aspect of 3D surface flaws thus far. Therefore, the study of 3D surface flaws is first reviewed in this section, which is followed by a review of 3D internal flaws.

2.1.2.1 3D surface crack growth

To study the problem of earthquake gestation, for the first time, Teng et al. (1987) proposed using pre-existing 3D surface flaws to simulate fault rupture in the laboratory. These researchers believed that the 3D surface flaw was closer to the natural faults than the 2D surface flaw through thickness flaws. They conducted uniaxial compression tests on glass, PMMA, marble and gemstone samples containing a single, pre-existing 3D surface flaw. The effects of the flaw angle with respect to the loading direction and the friction coefficient of the flaw surfaces were considered. The results of their study indicated that the crack propagation of the 3D surface flaw was more complicated and essentially different from that of the penetrating 2D flaws. In the 3D surface flaw, a series of petal cracks, approximately helix-shaped, were found to first generate at the front of the flaw, but the cracks only extended a limited length. When the loading stress

was increased to a higher level, wing cracks generated at the tips of the 3D surface flaw. Nevertheless, the wing cracks wrapped around the flaw and could extend to the boundary of the sample in both the axial and lateral directions. In addition, the friction of the flaw surface had a significant effect on crack formation and propagation. Due to the self-locking of frictional stress on the flaw surfaces, the petal crack and wing crack generation positions were shifted and generated into the self-locking zones, and the crack propagation became unstable. The crack growth in marble and gemstone samples was similar to the glass samples but slightly different from the crack growth in PMMA. The research conducted by Teng et al. (1987) was a breakthrough in the investigation of flaw growth under compression, despite the fact that only a single flaw was considered.

Cannon et al. (1990) performed static uniaxial compression experiments on PMMA samples containing a half penny shaped 3D surface flaw. These researchers also found that crack propagation from pre-existing 3D surface flaws was different from that in 2D flaws. Wing cracks were observed to sprout from the pre-existing semicircular flaw, and then, the cracks wrapped around the edge of the inclined flaw both through the thickness and along the loading direction, eventually converging to approximately the same vertical plane (Cannon et al. 1990). The findings presented by Cannon et al. (1990) were similar to those reported by Teng et al. (1987).

Recently, after systematically investigating the crack growth mechanism in rock and rock-like materials containing single and double, saw cut 3D surface flaws, Wong and her colleagues (Wong et al. 2003, 2004a, 2004b, 2006, 2007) concluded that the length of crack propagation depended on the penetration and inclination angle of the flaw, and the coalescence of the 3D surface flaws was significantly affected by the penetration of flaws and the bridge angle between two pre-existing flaws. For instance, when the cutting depth of the flaw is greater than 0.3 times the thickness of the PMMA sample, wing cracks at flaw tips can propagate to the boundary and split the sample, while wing cracks can only extend by approximately 0.5-1.5 times the length of the 3D surface flaw for shallower flaws (Wong et al. 2004b). Yin et al. (2014) studied the coalescence mechanism between two parallel, pre-existing 3D surface flaws in granite specimens under uniaxial compression using the AE and digital speckle correlation method (DSCM), also known as digital image correlation. Based on the concept of critical strain during crack initiation, Yin et al. (2014) applied the DSCM for the first time to

distinguish whether the initiated crack was a tensile crack, shear crack or mixed tensile-shear crack. They found that wing cracks were “tensile-dominant mixed mode” or a mixed mode with tensile dominance, while anti-wing cracks could be considered as a mixed mode with tensile dominance and a tensile-dominant mixed mode plus shear slippage modes. In addition, these researchers reported that the coalescence mechanism of pre-existing 3D surface flaws involves both linkage by cracking on the specimen surface and linkage between petal cracks inside the specimen.

2.1.2.2 3D internal crack growth

In addition to the 2D throughout flaws and 3D surface flaws, flaws are always fully embedded inside rocks in 3D. In the laboratory, rock samples often fail due to the evolution of internal flaws (Eberhardt et al. 1999; Yin et al. 2014). Therefore, it is of great significance to investigate the growth of 3D internal flaws in rocks.

To study the 3D crack growth mechanism under compression, the foremost task is to prepare rock samples with suitable internal 3D flaws, and the second task is to visualize 3D crack growth inside rocks. Since rock is opaque, it is very difficult to clearly observe and analyze 3D crack growth in rock samples in real-time. Therefore, as a compromise, scientists turned to utilizing transparent rock-like materials, e.g., glass (Germanovich et al. 1994; Schmitt and Zoback 1993), PMMA (Adams and Sines 1978; Zhou et al. 2018a) and epoxy resin (Dyskin et al. 1994, 2003; Sahouryeh et al. 2002), to fabricate artificial rock specimens with 3D internal flaws. To date, there have been three main methods used to produce 3D internal flaws in transparent rock-like materials. The first method is cutting a half penny-shaped 3D surface flaw in two identical PMMA blocks and then gluing them together to form an imbedded penny-shaped flaw (Adams and Sines 1978; Zhou et al. 2018a). The second method uses a high energy laser pulse focused inside a glass sample to generate 3D internal flaws (Germanovich et al 1994; Stewart et al. 2012). The third approach is using cotton threads with hanging aluminum foil disk(s) within the model when curing resin specimens (Dyskin et al. 2003; Fu et al. 2016).

Based on the samples prepared by those three manufacturing methods, some investigations have been conducted to analyze the growth behavior of 3D internal flaws. Adams and Sines (1978) first explored the mechanisms of cracks generated from 3D internal flaws in PMMA. They also claimed that the crack extension from either a 3D

surface or 3D internal flaws was more complicated than the crack mode predicted by the 2D theory. In their experiments, both the pre-existing 3D flaw type and the loading types would exert significant effects on the crack initiation stress and the crack formations. The wing crack initiation stress from a 3D internal flaw was much lower than that from a 3D surface flaw, and the initiation stress under uniaxial compression was also lower than that under biaxial compression. In addition, three typical cracks were observed in samples with a single 3D internal flaw, which was different from the previous results obtained from studies regarding 2D flaws (Hoek and Bieniawski 1965; Nemat-Nasser and Horii 1982; Wong and Einstein 2009a; Yang and Jing 2011) and 3D surface flaws (Cannon et al. 1990; Teng et al. 1987; Wong et al. 2004a, 2004b). Figure 2.5 presents the typical cracks found by Adams and Sines (1978), in which the primary tensile wing cracks were initiated at the flaw tips and curved around the perimeter of the pre-existing flaw. Nevertheless, wing cracks could only extend a limited distance along the loading direction. Petal cracks, similar to those found by Wong et al. (2004a, b), were generated on the flaw perimeter adjacent to the primary wing cracks, which was speculated to be induced by the concentrated shear on the crack plane. Fish fin cracks formed near the center of the flat surface of the pre-existing 3D internal flaw were believed to be generated by tensile stress normal to the fish fin crack plane. However, notably, fish fin cracks were not found in other similar studies (Scholz 1990).

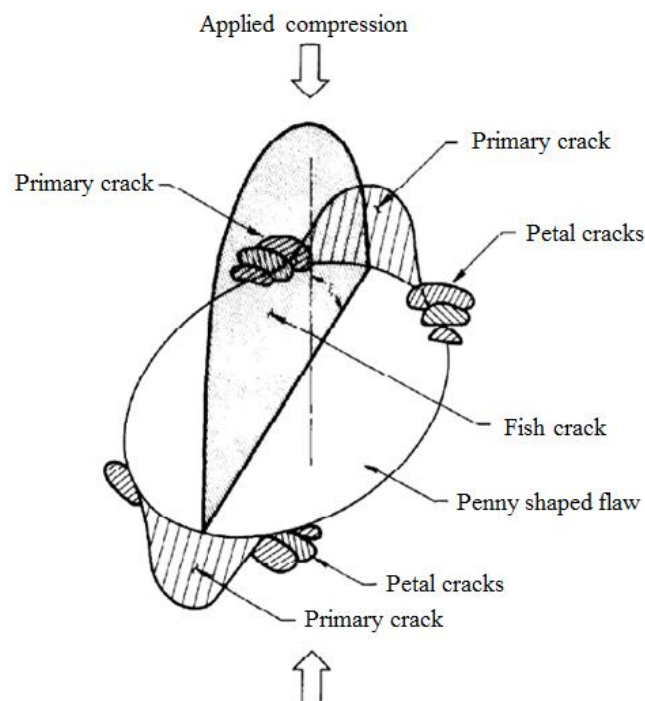


Figure 2.5 Crack growths from a 3D internal flaw in PMMA (Adams and Sines 1978)

After conducting many static compression tests on glass and resin specimens containing a single 3D internal flaw, Dyskin et al. (1994, 2003) reported that unlike 2D cracking, the emerging wing cracks around the pre-existing 3D internal flaw could only propagate approximately 1-1.5 times the length of the initial flaws without reaching the sample ends. Dyskin et al. (2003) revealed that the intrinsic reason that impeded the propagation of the tensile wing cracks was due to the wrapping or curving of the wing cracks around the perimeter of the 3D flaw, which is possibly attributed to the inability of the initial crack to extend itself in a lateral direction. In addition to a single 3D flaw, Dyskin et al. (2003) also investigated the crack growth and interaction between double and multiple 3D flaws. These researchers found that the spatial distribution or arrangement would significantly affect the growth of multiple 3D flaws under compression. For instance, the crack interaction between two parallel, horizontally aligned, inclined flaws hampered the extension or opening of each crack, thereby restricting tensile wing crack propagation. However, when the flaws were vertically aligned or obliquely aligned within a short distance, i.e., less than the diameter of the flaw, the crack interaction would amplify the growth of wings to form a large tensile crack (Dyskin et al. 2003). Based on this interaction mechanism, it could therefore be speculated that the macro failure of rocks could result from the interaction between many initial flaws inside the heterogeneous rocks.

Recently, Zhou et al. (2018a) studied the crack initiation and coalescence of two sets of 3D cross-embedded flaws in PMMA specimens under uniaxial compression. They found that both the crack initiation stress and the peak stress of the flawed samples were dependent on the flaw inclination angle and the nonoverlapping length of the flaws. The fracturing behaviors would be greatly influenced by the interaction between two sets of 3D cross-embedded flaws if the nonoverlapping length was small, whereas the bridge zone would not be coalesced for a large nonoverlapping length of pre-existing flaws. In addition, these researchers revealed that the mechanism of the initiation of wing cracks, oblique secondary cracks and anti-wing cracks was that the concentrated tensile stress on the sides of the flaws surpassed the tensile strength of the PMMA material, thereby causing tensile splitting (Zhou et al. 2018a).

Although those studies facilitate understanding of 3D internal crack growth behaviors under uniaxial compression, the 3D internal crack evolution mechanism affected by the

confining pressure, geometry of the 3D flaws and loading types is not fully understood. In addition, there are also some drawbacks in the above mentioned methods in the preparation of samples with 3D internal flaws, e.g., the existence of an unavoidable glued interface for the first method, the requirement of sophisticated skills for the second method, and the difficulties in fabricating 3D internal flaws in the intended position in the sample and the remainder of aluminum foil disks for the third method. Moreover, in previous studies, only some regular cracks, e.g., penny-shaped, elliptical and borehole cracks are considered, which are distinct from the defects inside the natural rocks. It is believed that those drawbacks may influence the 3D internal flaw growth. Furthermore, 3D crack growth under dynamic loading conditions has never been reported, even though rock masses are often subjected to dynamic loads such as earthquakes and blast waves. Hence, further studies focusing on developing new techniques or methods are needed, which can be used to easily fabricate rock or rock-like samples with internal microstructures similar to those of natural rocks and to investigate the progressive failure mechanism of rocks subjected to static and dynamic loads.

2.1.3 Review of damage characterization

To analyze the damage evolution and characterize the damage degree of rocks, a suitable damage variable must be chosen and a suitable method must be used to quantify this damage variable. To date, many damage variables, e.g., void space area, elastic modulus, ultrasonic velocity, AE, and CT value, have been proposed to quantitatively assess the damage evolution of brittle materials such rock and concrete.

The study on damage mechanics was pioneered by the work of Kachanov (1958) and Rabotnov (1963). They introduced a damage factor $\omega = 1 - \psi$ to represent the relative reduction of the load-bearing area due to damage. The field variable ψ is continuity, which is defined as the ratio of the net or effective load-bearing area over the total or nominal cross-section area of the specimen. However, this model is mainly for the damage of a material under uniaxial tension. In addition, the failure cross-section of the material is difficult to predict, and its surface is not always flat. Recently, Yang and Liu (2007) and Ma et al. (2016) introduced using sliced CT images to count the void space of the damaged material. This is because the number of pixels with a gray value of 1 can be

regarded as the void space area and matrix.

As a straightforward extension of Kachanov-Rabotnov's damage concept, Lemaitre and Chaboche (1994) defined an isotropic damage model by $\omega = 1 - \tilde{E}/E$. The parameter E is the Young's modulus of the undamaged material, and \tilde{E} is the Young's modulus after damage. This method of damage definition has been widely used to evaluate damage in brittle materials such as concrete, ceramic and rock (Horii and Nemat-Nasser 1985; Ortiz 1985; Peng et al. 2012). However, the Young's modulus of the undamaged material is difficult to obtain due to the pre-existing damage of the rock and rock-like materials. In addition, cyclic loading is needed to compute the damaged Young's modulus from the unloading curves.

Since the ultrasonic wave velocity is closely related to rock elastic constants, density and internal microcracks, it is therefore possible to define rock damage using ultrasonic velocity (Ahrens and Rubin 1993; Zhao and Xu 2000) by the following formula:

$$D = 1 - (V'/V)^2 \quad (2.1)$$

where V and V' are the velocity of the ultrasonic wave in rock material with and without damage.

Using the ultrasonic method, Goodfellow et al. (2015) studied the evolution of attenuation properties in a sample of Fontainebleau sandstone during a true-triaxial test. Their results demonstrated that during the initial compaction phase, the energy attenuation decreases and velocity increases as a result of closer stress-induced cracks. During the dilation phase, the P-wave velocity decreased, and the energy attenuation increased mainly along the minimum principle stress direction. In the final phase, severe high-frequency attenuation was detected due to the generation of remarkably large vertical macrofractures. However, Chow et al. (1995) noted that wave slowness exhibited anisotropic features in uniaxial compression tests, which indicates it is difficult to characterize the spatial distribution of damage in rock materials with the ultrasonic velocity method.

AE is the phenomenon in which energy is released in the form of elastic waves within a material that is subjected to some form of external stress. AE in rock is mostly produced by microcrack growth, frictional slip, and pore collapse (Eberhardt et al. 1999). The AE

signals detected during rock fracturing can thus be applied to analyze damage evolution during loading. An example is shown in Fig. 2.6, which demonstrates the progressive damage characterized by AE detection during deformation experiments (Tuffen et al. 2008). The b -value is defined as the ‘log-linear slope of the frequency-magnitude distribution’ of AE. This value represents the ‘scaling of magnitude distribution’ of the AE. A high b -value arises due to a large number of small AE hits (or events) representing new crack formation and slow crack growth, whereas a low b -value indicates faster or unstable crack growth accompanied by relatively high-amplitude AE in large numbers (Rao and Lakshmi 2005).

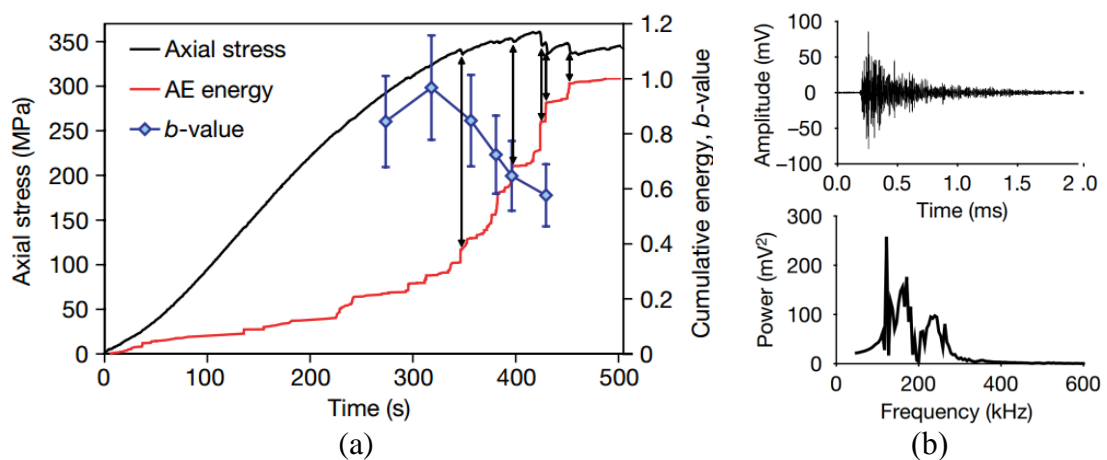


Figure 2.6 Experimental results from high-temperature fracture of rhyolitic obsidian. (a) Axial stress, normalized cumulative AE energy, and AE b -values against time for uniaxial deformation of rhyolitic obsidian at 645°C and $10^{-4.3}\text{ s}^{-1}$. (b) Waveform (top) and power spectrum (bottom) of a typical acoustic-emission event, showing the sharp onset and high frequency content (predominantly 100-300 kHz) that are characteristic of brittle failure (Tuffen et al. 2008).

Recently, some scholars proposed using AE information to quantitatively characterize damage evolution in concrete (Abdelrahman et al. 2014, 2015; Iturrioz et al. 2013; Mangual et al. 2013; Abouhussien and Hassan 2016) and rocks (Liu et al. 2009; Zhang et al. 2015) during compression tests. For instance, AE intensity analysis was proposed to classify damage to concrete (Golaski et al. 2002). The cumulative AE counts and energy during the loading process were also utilized to quantify damage evolution in rock samples (Kim et al. 2015; Zhang et al. 2015).

In addition, the flourishing development of X-ray computed tomography (CT) provides a

unique nondestructive method to visualize a sample at high-resolution in 3D (Renard et al. 2009). This technique has been widely adopted to investigate the hydraulic and physical properties and failure mechanisms of geomaterials. The application of CT has two major advantages: first, though real-time scanning of the rock sample or scanning of the recovered damaged sample, the 3D crack network can be extracted from the 3D-reconstructed CT images. The 3D crack network facilitates a better understanding of the spatial evolution of the micro and macrocracks (Raynaud 1989; Kawakata et al. 1999; Otani 2004; Renard et al. 2009; Huang et al. 2013). Second, the information conveyed by the CT images, e.g., CT value and gray value, can be adopted to quantitatively characterize the damage evolution of rocks during loading or unloading (Yang et al. 1998; Ge et al. 1999; Feng et al. 2004; Yang and Liu 2007; Huang and Xia 2015; Ma et al. 2016). Feng et al. (2004) proposed a novel method to calculate the damage variable of sandstone. They reported that the CT value could be used as an index to describe the damage evolution during the test.

$$D = \frac{(H - H_0)(\rho_0 - \rho_w)}{m_0^2(H_0 - H_w)\rho_0} \quad (2.2)$$

where H is the CT value, ρ_0 is the initial density of rock, ρ_w is the pore water density, H_0 is the initial CT value of the rock before testing, H_w is the CT value of pore water, and m_0 is the spatial resolution of the CT machine.

This model considers the pore water influence upon the rock damage evolution. Combining the two abovementioned advantages, an X-ray CT scan can be used to qualitatively and quantitatively analyze the damage evolution of rocks during tests.

Among the methods, AE and micro-CT appear to be the most promising methods that can be used to nondestructively quantify damage evolution both during and after loading processes.

2.1.4 Effect of damage on wave propagation in rocks

In addition to damage characterization in rocks, wave propagation and attenuation in predamaged or microdefected rock has also received considerable attention in the past several decades because of its practical importance in reservoir exploration engineering and seismic engineering. For instance, Gupta (1973) measured P and S-wave velocities

along three orthogonal directions as a function of the axial load on Indiana limestone specimens for the first time. He reported that prior to rupture, both P and S velocities decrease in all three directions but by quite different amounts. Toksöz et al. (1979) measured the attenuation of compressional P and shear S-waves in sandstone and limestone and found that in the frequency range of approximately 0.1-1.0 MHz, the attenuation coefficient was linearly proportional to the frequency both for P and S-waves, and the attenuation decreased substantially with increasing differential pressure for both P and S-waves. Pyrak-Nolte et al. (1990a) studied seismic waves transmitted across rock samples with a single fracture and revealed that adding normal stress and wetting the joint with liquid could both increase the transmission coefficient and reduce frequency attenuation. Through ultrasonic P-wave attenuation in low and high porosity rocks, Shatilo et al. (1998) and Xi et al. (1997) concluded that seismic attenuation grows with increasing porosity. Ahrens and Rubin (1993) studied the damage generated by planar impact using the ultrasonic wave velocity method. These researchers found that ultrasonic P-wave velocity decreased up to 50-60% in the vicinity of the crater, and the damage defined by the P-wave velocity variation decreased by $\sim r^{-1.5}$ from the crater, indicating a dependence on the magnitude and duration of the tensile pulse. Ai and Ahrens (2007) investigated the effects of shock-induced damage on ultrasonic velocity and attenuation in granite. The experimental results demonstrated that the P-wave velocity and normalized distance from the impact point followed an exponential decay relation, while the P-wave attenuation coefficient followed a power law decay with respect to distance. Recently, Figueiredo et al. (2013) experimentally studied the influence of source frequency on S-wave propagation in anisotropic media containing aligned penny-shaped cracks. The results show that the magnitude of S-wave birefringence in cracked media directly depends on the source frequency as well as crack size and density. Martínez-Martínez et al. (2016) investigated the effects of progressive fracture damage in rocks on ultrasonic P-wave attenuation. Their results demonstrated that the ultrasonic response in the time domain is less sensitive to fracture damage than the frequency domain. The P-wave velocity increases during the loading test until the beginning of the unstable crack propagation and decreases only when rock damage is very high. Barnhoorn et al. (2018) measured P and S-wave velocities and attenuation during an increase in stress and fracture formation until complete failure of the shale, limestone, and sandstone samples. They found that wave attenuation is more sensitive to

crack breakage than wave velocity. These researchers proposed that the minimum ultrasonic attenuation (corresponding to the maximum wave amplitude) could be used to identify the transition from recoverable elastic to permanent inelastic deformation of rocks. In summary, ultrasonic wave attenuation in rocks with predamage is source frequency- and damage degree-dependent, i.e., higher source frequency and damage degree results in higher wave attenuation.

Based on the above review, the investigation of damage evolution and ultrasonic wave propagation in rocks has been separately studied in the past. Few experiments have been conducted to quantitatively analyze these two scientific problems at the same time. Since damage evolution in rocks under external loading is a dynamic process, the influence of damage on ultrasonic propagation will also be a dynamic process. Therefore, further studies should be performed to quantify damage evolution in rocks and its effect on ultrasonic wave propagation and attenuation.

2.1.5 Review of mechanical and seismic behaviors of rock joints

To date, extensive studies have been performed to investigate the mechanical and seismic behaviors of joints. In terms of the mechanical properties of joints, the Bandis-Barton model (Bandis et al. 1983) is widely used to predict joint deformation and stiffness variation under static loads. In this model, the normal stiffness of joints is determined by the effective contact area, joint roughness coefficient (JRC), compressive strength of the joint asperity/wall, and thickness and properties of the filling material (Bandis et al. 1983). In addition, Zhao (1997a) noted that the joint matching coefficient (JMC), which is defined as the percentage of joint surface area in contact relative to the total joint surface area, has an important and crucial impact on the aperture, normal closure, stiffness and hydraulic conductivity of the joints. Thus, JMC was proposed to be coupled with JRC to estimate and predict the mechanical behavior of joints (Zhao 1997a, b).

In addition to static loads, rock masses frequently endure dynamic loads such as earthquakes and blast waves. Under dynamic loading, the normal stiffness of natural joints was found to be higher than that under static loading (Pyrak-Nolte et al. 1990a; Pyrak-Nolte and Nolte 1992). Based on the SHPB device, Li and her coauthors (Chen et al. 2015; Li and Ma 2009; Li et al. 2010; Li et al. 2017b) conducted a series of

experiments to investigate the mechanical response of the artificial open and filled joints subjected to dynamic compressive loads. They reported that the dynamic normal stiffness of joints increases with JMC but decreases with joint thickness (Chen et al. 2015; Li et al. 2017b), and the deformation of the quartz sand filled joint increases with increasing water content and filling thickness as well as the loading rate/amplitude (Li and Ma 2009; Li et al. 2010). With SHRB, Wu et al. (2012, 2014) further studied the dynamic behaviors of filled joints. They noted that the deformation of the filled joints was nonlinear and much larger than that of the nonfilled joints (Wu et al. 2012), and the addition of a 30% kaolin clay weight fraction into the quartz sand granular could enhance the stiffness but reduce the filling joint deformation (Wu et al. 2014).

In addition to the study of joint mechanical properties, numerous efforts have been devoted to theoretically and experimentally investigating the seismic behaviors of joints. To theoretically analyze wave propagation across joints, the boundary condition of the joint must be characterized. The displacement discontinuity method (DDM) developed by Mindlin (1960) and Schoenberg (1980) has been validated to accurately predict transmission and reflection coefficients for a given incident wave propagation through linear or nonlinear joints with or without filling materials (Cai and Zhao 2000; Fan and Wong 2013; Li et al. 2010; Pyrak-Nolte et al. 1990a, b; Zhao et al. 2006; Zhu et al. 2011a). In this model, a joint is considered to be a nonwelded plane boundary of zero thickness, and the stress across the joint is assumed to be continuous, while displacement is discontinuous and equals the joint closure. According to the theoretical solution of Eq. (21) in Pyrak-Nolte et al. (1990a), longitudinal wave (P-wave) propagation across joints will be affected by the following three parameters: the stiffness of the joint, the seismic impedance of the rock matrix and the frequency of the incident P-wave. Nevertheless, if a joint is filled with viscous material, e.g., unsaturated sand-clay mixture, and the density and thickness of the filler cannot be neglected, the DDM model is no longer applicable (Zhu et al. 2012). To address this problem, Zhu et al. (2011b) extended the DDM to a displacement and stress discontinuity model (DSDM), which treated the boundary condition of the viscous, filled joint as both discontinuous displacement and stress. In accordance with the DSDM method, the joint viscosity and acoustic impedance of the filled material also affect the magnitude of reflection and transmission coefficients.

Regarding the experimental investigation of wave propagation across joints, there are two

major techniques: the ultrasonic wave testing system and SHPB system. The former is used to generate low-amplitude ultrasonic waves in the high-frequency range, e.g., 0.1 MHz and 1.0 MHz, and the latter is applied to produce high-amplitude stress waves in the low-frequency range (usually below 10 kHz). With ultrasonic transducers, Pyrak-Nolte et al. (1990a) studied wave propagation through a dry and wet natural nonwelded joint. They found that adding normal stress and wetting the joint with liquid could both increase the transmission coefficient and reduce frequency attenuation. Through performing ultrasonic P-wave propagation across fluid-filled rock joints, Yang et al. (unpublished manuscript) concluded that an increase in joint thickness could cause more wave attenuation, while an increase in water content could result in less wave attenuation. Recently, based on the SHPB and SHRB systems, a great number of experiments were conducted to study stress wave propagation through filled and nonfilled joints (Chen et al. 2015; Fan and Wong 2013; Huang et al. 2018; Ju et al. 2007; Li and Ma 2009; Li et al. 2010, 2017b; Wu et al. 2012, 2014). For instance, Chen et al. (2015) and Li et al. (2017b) showed that the wave transmission coefficient grew significantly with the JMC of the artificial joint with rectangular asperities. Ju et al. (2007) claimed that the rougher the joint surface, the more the stress wave attenuated. After conducting a series of SHRB tests on the quartz sand filled joints, Li and Ma (2009) and Wu et al. (2012, 2013, 2014) revealed that wave transmission increased with loading rate but declined with joint filling thickness and water content within the granular sands.

2.2 Review of the main apparatus and techniques

2.2.1 SHPB

Among the various experimental methods, the SHPB, also known as the Kolsky bar system, has been widely used to investigate the dynamic behaviors of different materials with strain rates between 10^1 and 10^3 s⁻¹. When it was originally developed by Kolsky (1949), the SHPB was mainly used to test the dynamic compression stress-strain behavior of metal materials. In 1968, Kumar (1968) first introduced the SHPB to rock dynamics and obtained the dynamic stress-strain behaviors of rock samples using this apparatus for the first time. Afterwards, more researchers started using the SHPB to perform rock dynamics tests (Chong et al. 1980; Goldsmith et al. 1976; Lindholm et al. 1974; Melosh et al. 1992; Perkins et al. 1970). After entering the 21st century, studies on the dynamic responses of rock-like materials using SHPB equipment have expanded

(Dai et al., 2010a; Doan and Gary 2009; Frew et al. 2001, 2002; Li et al. 2000, 2005, 2017; Lok et al. 2002; Song and Chen 2004a, b; Xia et al., 2008; Yuan et al. 2011; Zhang and Wong 2013; Zhang and Zhao et al. 2013, 2014a, b; Zhou et al. 2010, 2018; Zou and Wong 2014). In addition to obtaining the dynamic compressive stress-strain behaviors of rocks, the SHPB device has also been modified to determine the dynamic tensile strength of rocks via dynamic Brazilian disc tests (Dai et al., 2010a; Saksala et al. 2013; Zhou et al. 2014; Zhu et al. 2015), to test the dynamic fracture toughness of rocks through dynamic three-point bending tests (Chen et al. 2009; Dai et al. 2010b; Xu et al. 2016; Yin et al. 2018) and to characterize the dynamic shear strength of rocks by dynamic punch shear tests (Huang et al. 2011; Lukić and Forquin 2016; Yao et al. 2017). Due to more than half a century of continuous SHPB improvement, the SHPB has recently been recommended by the International Society of Rock Mechanics (Zhou et al. 2012) as a standard experimental technique for testing the dynamic properties of rock materials.

The SHPB compressive tests are based on two fundamental assumptions: (1) 1D elastic wave propagation in the bars and (2) homogeneous deformation of the sample (Kolsky 1953). The assumption of 1D stress wave propagation is ensured by using long bars, and the elasticity of the bar deformation is guaranteed throughout the test by limiting the impacting velocity of the striker. The homogeneous deformation of the sample is mainly affected by two factors: inertial effects (i.e., the axial inertial effect and the radial inertial effect) and the interfacial friction effect (Dai et al. 2010a). To minimize the inertial effects and facilitate dynamic stress equilibrium between the sample ends, a slowly rising incident pulse is needed (Frantz et al. 1984). Considering this, Frew et al. (2001, 2002) proposed placing a small and thin disc material, e.g., copper and rub, on the front end of the incident bar, and then, the striker impacts the shaper before directly contacting the front end of the incident bar. In this manner, the shaper aids in shaping the traditional rectangular wave into a triangular wave or half-sine wave with a slowly rising wave front. Li et al. (2000, 2005) found that changing the conventional cylindrical striker into a cone-shaped striker could well shape the rectangular wave into a half-sine wave, thereby minimizing the effects of dispersion and inertia and realizing stress equilibrium between the ends of the rock sample.

In general, the SHPB consists of a striker bar, an incident bar, a transmitted bar and an

absorption bar, with a specimen sandwiched between the incident and transmitted bars, as shown in Fig. 2.7. When the striker bar impacts the incident bar, a compressive pulse (incident stress wave) is generated and propagates toward the specimen. Upon reaching the interface between the incident bar and the specimen, a portion of the stress pulse travels through the specimen and then spreads into the transmitted bar as a transmitted stress wave, while the remaining portion is reflected back into the incident bar as a tension pulse (reflected stress wave). Strain gauges are usually mounted at midpoints along the length of the incident and transmitted bars to record all three stress waves.

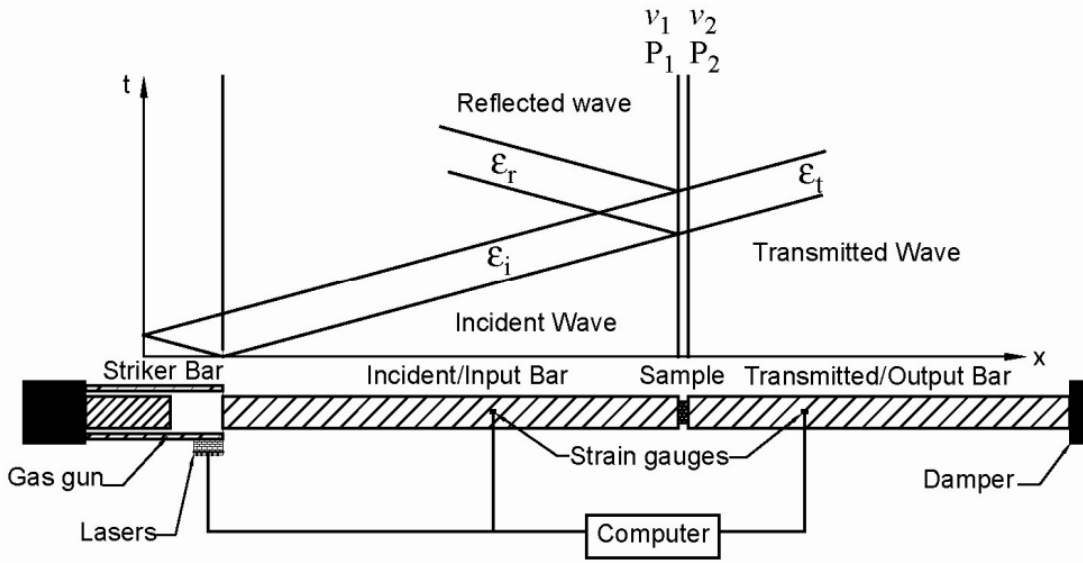


Figure 2.7 Schematic of a conventional SHPB (Dai 2010a). ε_i , ε_r and ε_t refer to incident, reflected and transmitted strain signals obtained through the strain gauges pasted on the incident and transmitted bars, respectively. v_1 and v_2 refer to particle vibration velocities at the end of the incident and transmitted bars, respectively. P_1 and P_2 indicate the input force and output force at the end of the incident and transmitted bars, respectively.

Once the dynamic stress equilibrium of the sample is verified, based on the one-dimensional stress wave propagation, the axial stress $\sigma(t)$, strain $\varepsilon(t)$ and strain rate $\dot{\varepsilon}(t)$ of the specimen can be determined as follows (Zhou et al. 2012):

$$\sigma(t) = \frac{A_e E_e}{2A_s} [\varepsilon_i(t) + \varepsilon_r(t) + \varepsilon_t(t)] \quad (2.3)$$

$$\varepsilon(t) = \frac{C_e}{L_s} \int_0^t [\varepsilon_i(t) - \varepsilon_r(t) - \varepsilon_t(t)] dt \quad (2.4)$$

$$\dot{\varepsilon}(t) = \frac{C_e}{L_s} [\varepsilon_I(t) - \varepsilon_R(t) - \varepsilon_T(t)] \quad (2.5)$$

where $\varepsilon_I(t)$, $\varepsilon_R(t)$ and $\varepsilon_T(t)$ are incident strain waves, reflected strain waves and transmitted strain waves, respectively; A_e , C_e , and E_e are the cross-sectional areas, P -wave velocity, and Young's modulus of elastic bars, respectively; and A_s and L_s are the cross-sectional area and length of the specimen.

2.2.2 Micro-CT

Industrial micro-CT scanning is a computer-aided tomographic process that commonly uses X-rays to produce 3D representations of the scanned object both externally and internally. Industrial micro-CT scanning has been used in many areas of industry for internal inspection of components (Flisch et al. 1999).

Unlike the traditional destructive microscopic observation technique that involves sample cutting and polishing (Curran et al. 1987), micro-CT scanning is a nondestructive method that allows for a series of 2D cross-sectional images to be obtained from the damaged sample (Ho and Hutmacher 2006). In combination with the 3D reconstruction technique, the damage information, i.e., mainly referring to micro and macrocracks inside the sample, can be reconstructed and presented in 3D. With the reconstructed 3D micro-CT image, researchers can conveniently observe and quantitatively analyze the spatial distribution of the developed micro and macrocracks that are externally invisible without the aid of micro-CT (Kawakata et al. 1999). Due to these advantages, micro-CT scanning has been widely applied to investigate the damage evolution and failure mechanics of geomaterials (Huang et al. 2013a; Kawakata et al. 1997; Nasser et al. 2011; Otani and Obara 2004; Raynaud et al. 1989; Renard et al. 2009). In 1989, Raynaud et al. (1989) introduced X-ray CT to scan cracks inside rock samples that were statically deformed and fractured in a triaxial cell. Kawakata et al. (1997) observed the faulting process under triaxial conditions by X-ray CT scanning. Feng et al. (2004) applied micro-CT scans to detect damage evolution during triaxial compression with chemical corrosion on sandstones. Since the CT value (unit is Hounsfield) is proportional to the material density, the distribution of the CT values reflects the spatial distribution of rock damage. Considering this, Feng et al. (2004) proposed using the CT value of the scanned image to quantitatively determine the damage variable of the rock sample under static

compression loading.

However, despite the effective and successful application of micro-CT scan in studying brittle solids damage evolution in static or quasistatic loading tests, it is difficult to effectively use this technique to detect dynamic damage evolution during dynamic tests (Huang et al. 2013a). This is because the current high-resolution micro-CT scanners cannot be used to scan the tested samples in real-time (Zhu et al. 2018). A common way to overcome these limitations is to recover the sample at different deformation levels and conduct a postmortem examination (Curran et al. 1987).

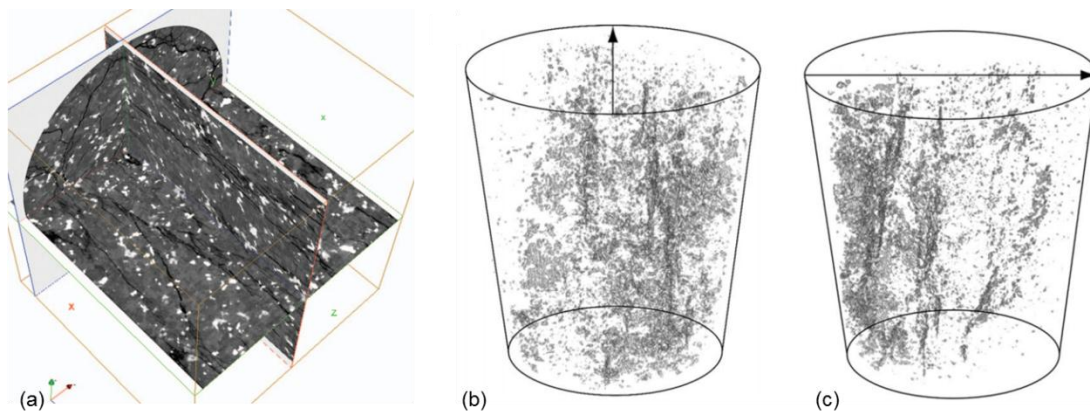


Figure 2.8(a) 3D micro-CT image; (b) and (c) 3D images of microcracks in the rock sample viewed from two angles. Grey dots represent cracks and the black arrow is the view direction. (Huang et al. 2013a)

Recently, Huang et al. (2013a) proposed a methodology to observe dynamic damage accumulation in brittle rocks and verified this by studying the dynamic compressive damage evolution of a granitic rock loaded with a modified SHPB system. Through controlling the axial deformation of the specimen using a steel ring that was slightly shorter than the tested specimen, the researchers recovered the damaged rock samples and then successfully extracted the spatially distributed microcrack network using the micro-CT scanning technique. Figure 2.8 shows the 3D micro-CT image and 3D images of microcracks inside the damaged rock sample. Then, they applied the open source software Fiji to automatically calculate the crack volume inside the damaged sample. Their results showed that the crack volume increased with increasing total dynamic strain of the sample, as shown in Fig. 2.9.

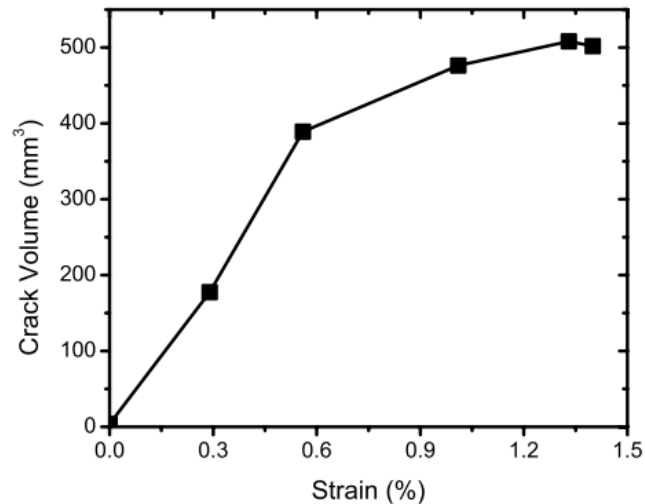


Figure 2.9 Evolution of cracks in volume under elevated impacts (Huang et al. 2013a)

Based on the above review, the micro-CT provides an ideal way for us to nondestructively analyze damage evolution inside opaque rock samples. In addition, although it is impossible to directly scan damage evolution inside relatively large rock samples (e.g., 38 mm in diameter and length) during the dynamic loading process due to the scanning power and speed limitations, this method still offers us a valuable tool to postanalyze dynamic damage development and spatial distribution of micro and macrocracks inside rock samples, as shown in Figs. 2.8 and 2.9. Moreover, by combining micro-CT with 3D reconstruction techniques, researchers can obtain digital rock cores with internal structures that are nearly identical to prototype natural rock samples (Ishutov et al. 2015; Ju et al. 2014; Zhu et al. 2018). Then, digital rock cores can be further combined with the 3DP technique to replicate artificial rock samples with mechanical and fracture properties similar to the corresponding natural rock samples. An investigation of using micro-CT, 3D reconstruction and 3DP techniques to replicate natural rocks is presented in detail in Chapter 5.

2.2.3 AE

AE is the phenomenon in which energy is released in the form of elastic waves within a material that is subjected to some form of external stress. AE sources originate in the change of the stress field inside the material, which is related to the deformation processes, crack growth, dislocation movement, inclusion cracks, etc. AE is usually transitory in nature, occurring during discrete events. Detected events, known as hits, are analyzed in

their waveform, studying parameters such as energy, duration, rise time, amplitude, etc. (Filipussi et al. 2015).

AE in the rock is mostly produced by microcrack nucleation and is a local phenomenon associated with fragile cracking, which provides a great deal of information on the development of rock damage (Cai et al. 2007; Heap and Faulkner 2008). When the loading stress on the rock sample reaches a certain critical value, AE is generated at different spatial and temporal scales (Lockner 1993). If the AE monitoring system was used during the loading process, the AE signals could be captured and recorded by the AE piezoelectric sensors. Then, using an appropriate back-analysis method, the AE signals could provide useful information for characterizing rock sample or rock mass behavior at all deformation stages. Therefore, the AE can be used as a supplementary tool for rock damage assessments (Cai et al. 2007).

In view of this, the AE technique has been widely applied to investigate the damage and fracture behavior within rock materials (Eberhardt et al. 1999; Ghaffari and Young 2013; Lei et al. 2000; Lei et al. 2004; Lockner 1993; Lockner et al. 1991; Steen et al. 2005; Wassermann et al. 2009). Eberhardt et al. (1999) analyzed the influence of grain size on the initiation and propagation thresholds of stress-induced brittle fractures through AE monitoring. Ganne and Vervoort (2007) studied the effects of the stress path on prepeak damage in rock material induced by the macrocompressive and tensile stress fields. The results show that previously induced (by compressive stresses) intragranular cracks influence the occurrence and growth of intergranular cracks resulting from tensile stresses, while previously induced (by tensile stresses) intergranular cracks influence the occurrence and growth of intragranular cracks resulting from compressive stresses.

Recently, some researchers proposed using AE information to quantify damage evolution in concrete (Abdelrahman et al. 2014, 2015; Iturrioz et al. 2013; Abouhussien and Hassan 2016) and rocks (Liu et al. 2009; Zhang et al. 2015) during compression tests. For example, Golaski et al (2002) quantitatively analyzed damaged development in concrete using AE intensity. Kim et al. (2015) and Zhang et al. (2015) quantified damage evolution in granite rock samples and salt rock specimens utilizing cumulative AE counts and energy during the compressive loading process.

Based on the above review, AE could be a useful tool for qualitatively and

quantitatively characterizing damage evolution in rocks during loading process. In view of this, in Chapter 6, the AE technique will be applied to quantify damage evolution in granite samples during uniaxial compressive loading, and then the damage coefficient determined by cumulative AE counts will be further used to analyze the effect of damage evolution on low-amplitude ultrasonic P-wave propagation and attenuation in granite rocks during compression.

2.2.4 The 3DP technique

The 3DP technique, which is also termed additive manufacturing or rapid prototyping, is defined as the process of joining a material one layer at a time to produce an object from a virtual 3D model (Yan and Gu 1996). Since Charles Hull created the first working 3D printer in 1983, the 3DP technique has undergone rapid development. Various new 3DP techniques, such as fused deposition manufacturing (FDM), powder-based 3DP, stereolithography (SLA) and selective laser sintering (SLS), have been developed.

Because 3DP is a computer-aided design and manufacturing process, the 3DP technique has many advantages over traditional manufacturing methods, such as machining and stamping, which fabricate products by removing materials from a larger stock or sheet metal. The 3DP technique creates the final shape by adding materials, which can make efficient use of raw materials and produce minimal waste while reaching satisfactory geometric accuracy. In addition, 3DP is flexible, repeatedly and accurately fabricating objects with complex geometry and internal structures (Huang et al. 2013). Due to these benefits, 3DP has recently been widely applied in various aspects, such as biomedicine (Wu et al. 2011), aerospace (Rochus et al. 2007), construction (Buswell et al. 2007) and soil science (Otten et al. 2012).

Among these aspects, the investigation and application of 3DP has resulted in breakthroughs in the aerospace field. Based on the EOS EOSINT P730 nylon laser sintering machine, engineers have manufactured and flown the world's first 'printed' aircraft - SULSA (Southampton University Laser Sintered Aircraft) (Marks 2011). In September 2014, the first zero-gravity 3D printer in space was delivered to the International Space Station by a SpaceX resupply mission (Anthony 2014). Approximately three months later, this 3D printer completed the first phase of a National Aeronautics and Space Administration (NASA) technology demonstration by printing a

ratchet wrench with a design file transmitted from the ground to the printer in space (NASA 2014). The 3DP technique is predicted to potentially change the way scientific research is conducted on the Space Station. For instance, the 3DP technique may be able to prepare objects that could not be sent to space (NASA 2014).

The 3DP technique has also been increasingly utilized in the field of biological medicine. Although 3DP was initially used as presurgical visualization models and tooling molds, it has gradually evolved to create one-of-a-kind devices, implants, scaffolds for tissue engineering, and drug delivery systems (Chia and Wu 2015). For example, 3DP functional materials such as hydroxyapatite scaffolds (Michna et al. 2005), bioactive glass (Wu et al. 2011) and calcium silicate ceramics (Wu et al. 2012) with a controllable pore structure for bone tissue engineering have been increasingly applied in bone regeneration due to their excellent in vitro apatite-mineralization, bioactivity, degradation and drug delivery ability.

The 3DP technique has recently been preliminarily applied in geoscience. By combining X-ray computed tomography (CT) with 3DP technology, Otten et al. (2012) and Dal Ferro and Morari (2015) fabricated a complicated pore network that exhibited the physical heterogeneity of undisturbed soils to study soil-water dynamics and fungal growth, respectively. These researchers anticipated that the application of 3DP would enhance studies of soil biology and biogeochemistry. Similarly, Ishutov et al. (2015) incorporated X-ray CT, digital pore network modeling and 3DP techniques to transfer the digital rock model of the Idaho Gray sandstone with an estimated porosity of 29% and permeability of 2,200 mD into tangible porosity samples. Although the resolutions of CT images and 3D printers were insufficient to replicate the microporosity of the sandstone at the original scale, researchers found that these 3DP samples helped to better understand the contributions of pore system characteristics and fluid flow at various scales to petrophysical properties in oil and gas reservoirs. Huang et al. (2016) produced two physical models with and without penny-shaped inclusions using the 3DP technique. They reported that the measured P and S- wave velocities from the 3D printed models agreed well with the theoretical predictions (within 5%).

Although 3DP technology has been available for a number of years and has been increasingly applied in the foregoing fields, the study and application of 3DP in rock

mechanics are still in its infancy. Ju et al. (2014, 2017) reported the application of 3DP in rock mechanics, where physical models were produced to duplicate the prototype coal and glutenite rock with complicated fractures by combining the CT scan, 3D reconstruction and 3DP technique. Attributed to the satisfactory photoelastic property demonstrated by the 3DP physical model, 3D frozen stress and photoelastic techniques were further used to characterize and visualize the stress distribution within the fractured rocks under uniaxial compression. Jiang and Zhao (2015) prepared 3DP samples with polylactic acid (PLA) using the FDM technique. However, they concluded that it is unsuitable for PLA to simulate rock due to its ductile property (Jiang and Zhao 2015). Fereshkenejad and Song (2016) enhanced the compressive strength of 3DP gypsum specimens by increasing binder saturation and heating samples at 150°C for approximately one hour. Nevertheless, the 3DP samples failed/yielded with low compressive strength, i.e., between 1 MPa and 30 MPa and exhibited ductile behavior. In addition, microscopic observation revealed that a layered orthotropic microstructure existed within the 3DP gypsum specimens, resulting in apparent orthotropic mechanical behavior (Feng et al. 2015).

Although the application of 3DP to rock mechanics has attracted some attention, and some encouraging findings have been achieved, the application of 3DP to rock mechanics is still in the preliminary stages. Because 3DP has advantages in preparing complicated structures, it may help to solve the difficulty in repeatedly fabricating brittle artificial rock samples with internal, pre-existing defects that are identical to those of natural rocks. With these 3DP artificial rocks, systematic experiments could be designed that may facilitate understanding of the structure and stress distribution inside rocks (Ju et al. 2014, 2017), the mechanical properties of natural rock joints (Jiang et al. 2016), the fracture behaviors of rocks, particularly layered/bedded rocks (Hart and Wetzel 2017), and the petrophysical and permeability properties of reservoir rocks (Ishutov et al. 2015). Therefore, further studies on the identification or development of a more suitable 3DP technique and its corresponding, supporting material to mimic brittle and hard rocks are needed. Considering this, the application of 3DP to rock mechanics is the research premise of this thesis, and the specific contents are presented in Chapters 3-5.

CHAPTER 3 IDENTIFICATION OF A SUITABLE 3D PRINTING MATERIAL FOR MIMICKING BRITTLE AND HARD ROCKS AND ITS BRITTLENESS ENHANCEMENTS

This chapter focuses on identifying the most suitable 3DP material from five targeted, available 3DP materials, i.e., ceramics, gypsum, PMMA, SR20 (acrylic copolymer) and resin (Accura® 60), to simulate brittle and hard rocks. The 3DP principle is introduced in the first part. Then, the preparation of 3D printed rock-like samples is presented in detail. Subsequently, uniaxial compression tests are performed on the 3D printed sample, with the aim to identify the most suitable 3DP material for mimicking brittle and hard rocks based on the currently available 3DP techniques and materials. The results indicate that the resin produced via SLA is the most suitable 3DP material for mimicking brittle and hard rocks. Thereafter, three methods including freezing, incorporation of internal macrocracks and the addition of microdefects are adopted to enhance the brittleness of the 3DP resin. Finally, some prospective improvements that can be used to facilitate the application of 3DP techniques to rock mechanics are discussed. The research content of this chapter is the foundation of Chapters 4 and 5.

3.1 Introduction

Rock fracturing and faulting have traditionally been studied in the laboratory using natural rocks. However, it is difficult to characterize the spatial evolution of cracks during rock failure because natural rocks are heterogeneous, unrepeatable and opaque. To solve this problem, many advanced techniques, such as SEM (Baud et al. 2004; Brooks et al. 2013; Hirth and Tullis 1994), AE detection (Goebel et al. 2013; Lockner et al. 1991; Townend et al. 2008) and X-ray CT (Benson et al. 2007; Huang et al. 2013b; Kawakata et al. 1999) have been used to investigate the spatial evolution of cracks in rocks. These studies show that the growth of dispersed cracks leads to rock failure. However, currently, the experimental study of rocks is encumbered by three problems: first, rocks are inhomogeneous, making it difficult to ensure the repeatability of the experimental results (Kumano and Goldsmith 1982); second, rock cores from deep underground are difficult and expensive to obtain (Teagle and Ildefonse 2011), and comprehensive material testing requires many samples (Barton and Choubey 1977); and

third, artificial rock samples with internal fractures or pores are difficult to produce (Germanovich et al. 1994). To address these issues, the aim of this chapter is to investigate 3DP as a cost-effective method of producing artificial brittle and hard rocks with reproducible microstructures and mechanical properties. The other objective is to study 3D fracture problems using 3DP artificial rocks with pre-existing internal cracks.

3.2 3DP principle

In this Chapter, laboratory tests on 3DP samples fabricated with three mainstream-printing techniques, i.e., the FDM, SLA and powder-based 3DP methods, are carried out to identify the most suitable 3DP technique and its supporting material for mimicking brittle and hard rocks and replicating their mechanical behavior. Although each 3DP method has its unique features, all of them share a common principle, i.e., sequential-layer material joining throughout a 3D work envelope under automated control (Mitchell 2016). The general printing process includes the following steps: 1) to prepare a 3D printable model with a computer aided design package (e.g., Auto CAD); 2) to transform the 3D printable model into an STL format file which can be read by the 3D printers; 3) to assign the model with the printing instructions (e.g., layer thickness and printing path) tailored to a targeted 3D printer; 4) to print the object layer upon layer; 5) to post-process the 3DP specimens, e.g., to recycle the unused powder, to remove the trapped and unbound powder on the specimens, to clean and remove the wet resin remained on the 3DP resin sample, and to further cure the 3DP resin sample in a ultraviolet (UV) oven.

During printing with the FDM (Jiang and Zhao 2015), the thermoplastic material is extruded into a molten plastic filament by a heated extrusion nozzle, which is then deposited on the printing layer by a computer-controlled extrusion head in accordance with the printing instructions. The deposited filaments form layers as the molten plastic hardens immediately after extrusion from the nozzle. When a layer is completed, the platform descends a layer thickness, and subsequently, a new layer is deposited again. These steps are repeated till all layers are produced one atop another to complete the whole model (Jiang and Zhao 2015)

Powder-based 3DP method consists of two steps, i.e., to spread gypsum powder and to spray binder to consolidate the gypsum powder (Feng et al. 2015; Jiang et al. 2016). At

the beginning of the 3DP process, a roller spreads gypsum powders to form a foundation layer with a sufficient thickness at the base of the print chamber. Then, a layer of printing thickness is spread and smoothed by the roller over the foundation layer. Subsequently, the printing nozzle sprays the binder solution to specific locations to consolidate the gypsum powder. The powder chamber is then raised by a layer thickness, whilst the print chamber lowers by the same height to allow the next layer to be spread. This cycle repeats until the whole object is completed (Feng et al. 2015; Jiang et al. 2016).

During printing with the SLA, a concentrated light beam such as UV laser, whose motion is controlled by the computer, traces the cross-section onto a bath of liquid photopolymer resin which solidifies the cross-section. Then the platform descends a layer thickness into the bath filled with liquid resin, and a new layer of liquid resin is spread onto the surface of the solidified object, followed by the next round of laser irradiation. This process is repeated until the object is ready. Thereafter, the platform will be lifted out of the bath, and the excess resin will be drained. The printed object is finally collected from the platform, cleaned in a solvent solution to remove wet resin remaining on the object, and placed in a UV oven for a final curing (Chen et al. 2017).

3.3 Experimental setup

3.3.1 Specimen preparation

3DP specimens were prepared in the Industrial Centre of the Hong Kong Polytechnic University. It started to carry out 3DP relevant research in 1994 and currently owns over twenty 3D printers based on various techniques such as the FDM, SLA, SLS and powder-based method.

After trying a number of 3DP materials, five targeted available 3DP materials, specifically ceramics, gypsum and PMMA (polymethyl methacrylate), which are traditionally regarded as brittle (Seweryn et al. 1997), SR20 (acrylic copolymer) and resin (accura® 60), which are of high strength, were chosen to produce 3DP samples using the current prevalent 3DP techniques, i.e., powder-based 3DP, FDM and SLA. The components for preparing ceramic sample consisted of Xtra-White slip powder (62.50 % in weight), powder additives (6.25 % of PolyVinyl Alcohol and 31.25 % of extra-fine sugar in weight) and alcohol-water binder (Ganter et al. 2009). The particle size

of the ceramic powder is 200 mesh (74 μm). The materials used for manufacturing gypsum sample were calcium sulfate hemihydrate $\text{CaSO}_4 \cdot \frac{1}{2}\text{H}_2\text{O}$ powder, with a diameter of 70 μm , and water-based binder (Zb63) supplied by Z Corporation. The PMMA particles (55 μm in diameter) were consolidated by the PolyPor B* binder. The SR20 consisted of 2-propenoic acid, 2-methyl-, polymer with methyl 2-methyl-2-propenoate (weight per cent > 90 for those three), triphenyl phosphate (weight per cent < 3.6) and phosphate, bis (tert-butylphenyl) phenyl (weight per cent < 1.6). The material of resin is a liquid photosensitive accura® 60 whose specific component was not available from the manufacturer, i.e., 3D Systems. Table 3.1 shows the printing details, and Fig. 3.1 presents the 3DP specimens before testing. Each specimen has a nominal size of 50 mm in diameter and 100 mm in length. Note that as one of the advantages of 3DP is high repeatability (Hiller and Lipson 2009; Jiang and Zhao 2015; Wang et al. 2017), only one sample was fabricated for each material.

Table 3.1 The printing details of the 3DP samples

Material	Transparency	Printer	Layer thickness	Density (g/cm^3)	Printing method	Price (HKD)
Ceramics	Opaque	ZPrinter 301	0.10 mm	1.37	3DP	2900
Gypsum	Opaque	ProJet 860	0.10 mm	1.27	3DP	2000
PMMA	Opaque	VX200	0.15 mm	0.66	3DP	1300
SR20	Opaque	Fortus 380	0.25 mm	1.11	FDM	1500
Resin	Translucent	Viper si ²	0.05 mm	1.21	SLA	2300

FDM-fused deposition manufacturing; 3DP-powder-based 3DP; SLA-stereolithography

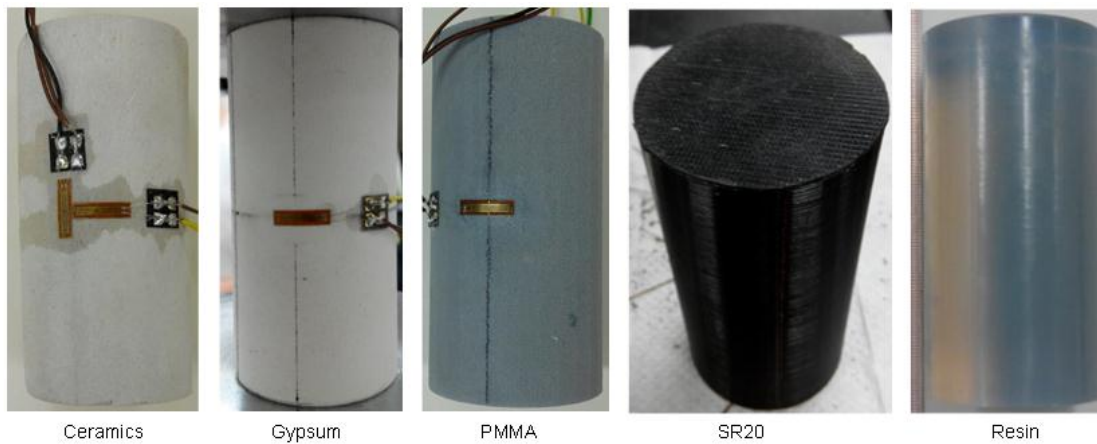


Figure 3.1 3DP samples before testing. Nominal sample size: 50 mm in diameter and 100 mm in length

3.3.2 Testing apparatuses

Uniaxial compression tests were carried out to obtain the basic mechanical properties of the 3DP samples. To ensure accuracy, a VJ Tech machine with a low loading capacity of 100 kN (Fig. 3.2a) was used to test the powder-based 3DP samples, i.e., ceramic sample, gypsum and PMMA. This is because we found that the uniaxial compressive strength of powder-based 3DP specimens was very low, although those materials are conventionally considered as brittle and of high strength (Munz and Fett 1999; Wong 2008). The other two samples, i.e., SR20 and resin, were tested with a Matest loading machine whose maximum loading capacity is as high as 3,000 kN as illustrated in Fig. 3.2b. All of the samples were tested at a loading rate of 2 mm/min at room temperature (approximately 20 °C). Two pairs of BX120-10AA strain gauges with a measuring grid size of 10 × 2 mm (length × width) were attached on the central part of the sample, among which one pair is for axial strain measurement and the other for lateral strain measurement. As the glue stuck on the surface of sample may penetrate into the powder-based 3DP specimens and form a thin crust, the strength and homogeneity of samples will be affected. Hence, selecting an appropriate glue is essential. In this work, the CN adhesive with low permeability was used to attach strain gauges so as to minimize the disturbance.



Figure 3.2 Testing equipment. (a) VJ Tech tester with a loading capacity of 100 kN; (b) Matest with a loading capacity of 3,000 kN

3.4 Results and analysis

To well simulate natural rock materials, selecting an appropriate model material is a key issue. According to the similitude law, the physical parameters (e.g., geometric size, unit weight, the Young's modulus and Poisson ratio), the mechanical responses (e.g., strength and strain properties) and the ultimate failure mode of the model material must be the same as or similar to the corresponding prototype rock material (Karaca and Egger 1993; Liu et al. 2014). However, different from the traditional analogue material, which is usually a mixture of several components mixed in a certain proportion, 3DP material is usually a single material (for example, in the present study). Therefore, it is difficult to select an appropriate simulation material in strict accordance with the similitude law of physical parameters. In view of this, in this chapter, the similitude law for identifying the most suitable 3DP material to simulate hard and brittle rock is mainly focused on the mechanical properties and the failure mode. That is to say, if there is a similarity between the sample produced by 3DP material and natural rock specimen in mechanical responses and macro failure mode under the same condition, the 3DP material will be considered as the superior one for mimicking hard and brittle rocks.

3.4.1 Identification of the most suitable 3DP material

The mechanical properties of the 3DP samples determined from uniaxial compression tests are shown in Table 3.2, where σ_c is the peak stress, ε_A and ε_L refer to the axial and lateral strains corresponding to the peak stress, respectively, and E and ν are the Young's modulus and the Poisson's ratio, respectively. Figure 3.3 displays stress-strain curves and the 3DP samples after tests. It can be seen from Table 3.2 that the samples can be divided into two types based on the failure/yielding strength. The samples fabricated via powder-based 3DP method, i.e., ceramic sample, gypsum and PMMA, failed at very low loading (approximately 3 MPa) and relatively small deformation, while the FDM- and SLA-produced specimens, i.e., SR20 and resin, respectively, yielded with high stress (approximately 100 MPa).

In powder-based 3DP samples, i.e., ceramic, gypsum and PMMA specimens, particles were consolidated by sprayed binder without being compacted by the roller during printing. Therefore, the strength and the Young's modulus of the powder-based 3DP samples are much lower than those of the common natural rocks, which are hard and brittle. Though the strain at the peak stress of the gypsum sample is comparable to that of some brittle rocks such as porous sandstone (Wong et al. 1997), it did not fail with significant stress drop after the peak stress. Instead, the gypsum sample failed with swelling during the final loading stage, exhibiting high ductile property as shown in Fig. 3.3c. Therefore, in accordance with the similitude law described above, it is believed that the powder-based 3DP samples are unsuitable to mimic rocks, particularly brittle and hard rocks such as marble and granite. Note that the strain at peak stress of the PMMA sample is significantly larger than that of the other two powder-based 3DP samples, i.e., ceramics and gypsum. This is mainly because the glue sprayed on the PMMA sample strengthened the surface layer of the sample. The sample thus can withstand large deformation until the stiff layer was peeled off (see PMMA sample in Fig. 3.3c).

As the conventional clay-based ceramics have higher yield strength and brittleness after firing compared with 3DP ceramic sample, firing treatment to the 3DP ceramic sample thus was performed in the present work, aiming to enhance the compressive strength and brittleness. Nevertheless, experimental results show that it is difficult to improve its strength and brittleness, because they swelled and eventually crushed due to the generated

cracks when they were heated. Figure 3.4 demonstrates the statuses of a 3DP ceramic sample during firing.

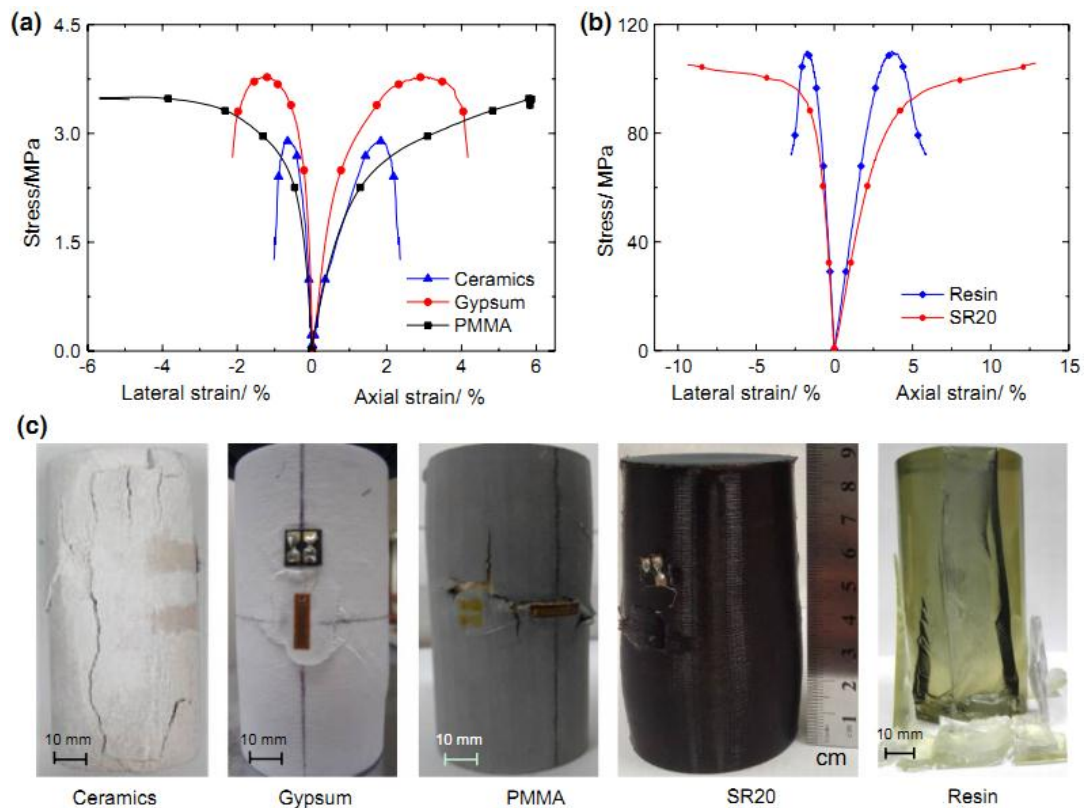


Figure 3.3 Stress-strain curves and the failure patterns of the 3DP samples in uniaxial compression tests. (a) Stress-strain curves of the powder-based 3DP samples; (b) Stress-strain curves of samples fabricated using SLA (resin) and FDM techniques (SR20); (c) Failure patterns of the 3DP samples

Table 3.2 Mechanical properties of the 3DP samples

Sample	σ_c (MPa)	ε_A (%)	ε_L (%)	E (GPa)	ν
Ceramics	2.9	1.83	-0.64	0.17	0.20
Gypsum	3.8	3.07	-1.28	0.43	0.29
PMMA	3.5	5.87	-4.36	0.21	0.33
SR20	105.6	12.23	-10.05	2.74	0.36
Resin	110.3	3.60	-1.75	3.81	0.40

σ_c is the peak stress, ε_A and ε_L refer to the axial and lateral strains corresponding to the peak stress, respectively, and E and ν are the Young's modulus and the Poisson's ratio

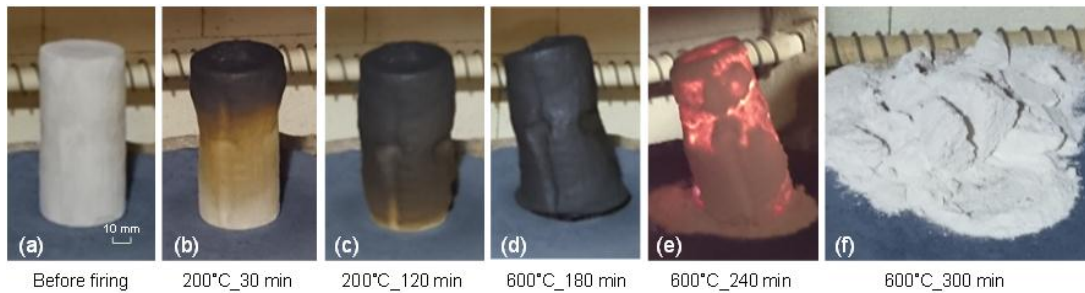


Figure 3.4 The status of the 3DP ceramic sample during firing. The numbers below the pictures indicate temperature and duration for the firing treatment

For the SR20 sample, though its yield stress (105.56 MPa) is comparable to the strength of some hard rocks, e.g., marble (Fredrich et al. 1990) and siltstone (Alber et al. 2009), it showed typical elastoplastic behavior. As shown in Fig. 3.3b, SR20 exhibited perfect elasticity in the elastic region, followed by plastic behavior in the post-yield stress region. Additionally, the SR20 sample swelled by approximately 7.5% when the compressive pressure exceeded the yield stress (Fig. 3.3c), whereas the natural brittle rock specimens usually fail with negligible plastic deformation in uniaxial compression tests. Consequently, the SR20 material fabricated via FDM method is also considered inappropriate for mimicking brittle rocks.

With regard to the SLA-fabricated resin sample, its uniaxial compressive strength (110 MPa) and stress evolution process agree well with those of some hard rocks, e.g., fine-grained sandstone (Alber et al. 2009) and Tennessee marble (Wawersik and Fairhurst 1970), in spite of the relatively large deformation, which is 3.60% and -1.75% for axial and lateral strain at peak stress, respectively. Unlike SR20 specimen, the 3DP resin deformed without significant barreling or swelling in the post-peak stress region, and a layer of resin was peeled off at the final loading stage. In addition, because of the transparent feature of 3DP resin, it is possible to directly observe and analyze the spatial evolution of cracks during the fracturing and failure, which could facilitate understanding rock failure mechanism.

Hence, after comprehensive consideration of all aforementioned factors, it is believed that among the five targeted 3DP materials based on current 3DP techniques, the translucent resin fabricated by SLA is the most suitable 3DP material for mimicking brittle and hard intact rocks where no defect is included at all, although its brittleness, defined as breaking without significant plastic deformation, needs improvement.

3.4.2 Brittleness enhancement for 3DP resin material

In nature, brittle and hard rocks always fail in a brittle manner with small deformation when they are subjected to uniaxial compression (Tang and Kaiser 1998). In order to effectively replicate natural rocks with the SLA-fabricated resin material, three measures, i.e., freezing, incorporation of a macro-crack, and addition of micro-defects, are applied to enhance its brittleness.

3.4.2.1 Freezing

Resin is a temperature dependent material, whose mechanical properties, e.g., strength, the Young's modulus and fracture toughness vary significantly with the testing temperature (Wu et al. 2005). To enhance the brittleness of the 3DP resin samples, they were frozen in a cooler with dry ice (-77°C) for a period of 24 hours prior to the test. During uniaxial compression tests, the 3DP resin sample was surrounded by dry ice to prevent temperature rising. Figure 3.6 shows the dry ice treatment device during tests. A T-type thermocouple was placed on the surface of the resin sample to measure its temperature during tests. It is found that the temperature almost kept constant during tests as shown on the thermometer in Fig. 3.5. Note that as the dry ice temperature (-77°C) is beyond the service temperature of the strain gauge used in this study, strain gauges were not employed for strain measurement, and only the axial deformation was recorded by the built-in sensors of the loading machine.

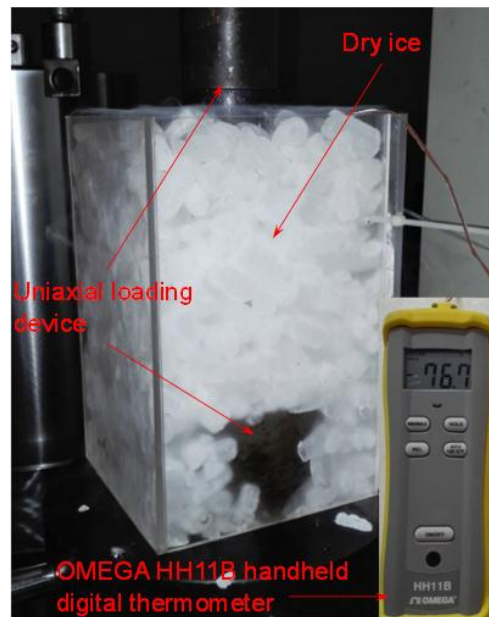


Figure 3.5 Freezing treatment device for the test at low temperature

Figure 3.6 shows the axial stress-strain curves of 3DP resin samples in uniaxial compression tests at room temperature and after dry ice treatment. The mechanical properties of those two samples are shown in Table 3.3. It can be found that the uniaxial compressive strength and the Young's modulus of the frozen 3DP resin sample were higher than those at room temperature. Although the uniaxial compressive strength of the frozen resin sample increased by 70%, the axial strain only increased by approximately 10%. Meanwhile, as shown in Fig. 3.6, the axial stress dropped rapidly after the peak stress. In addition, the frozen resin sample failed in an explosive manner with fragments ejected outward. Figure 3.7 presents the fragments of the frozen 3DP resin sample after failure. The existence of strip fragments indicates splitting failure. These evidences demonstrate that the brittleness of the 3DP resin could be greatly enhanced via low temperature treatment.

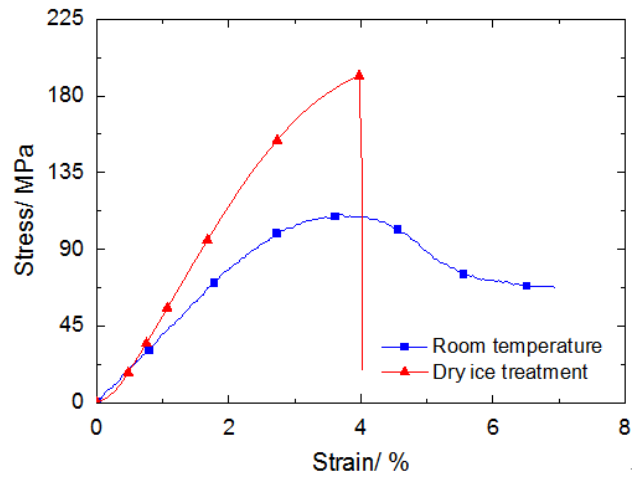


Figure 3.6 Axial stress-strain curves of 3DP resin samples determined from uniaxial compression tests at room and low temperatures

Table 3.3 Mechanical properties of the 3DP resin samples

Sample	σ_c (MPa)	ε_A (%)	ε_L (%)	E (GPa)	ν
Intact resin at room temperature	110.3	3.60	-1.75	3.81	0.40
Frozen intact resin	191.8	3.97	-	6.36	-
Resin with a macro-crack	51.3	1.37	-0.41	4.23	0.37
Resin with micro-defects	82.1	2.62	-1.33	3.52	0.35



Figure 3.7 Fragments of resin sample after low temperature testing

3.4.2.2 Incorporation of a macro-crack

The presence of cracks within elastic solid result in stress concentration that could increase its brittleness (Roylance 2001). When a crack reaches a certain critical length, it can propagate catastrophically through the solid, even though the gross stress is much lower than yield or failure strength of the elastic solid. In view of this, a single pre-existing internal macro-crack was fabricated in the 3DP resin sample, aiming to enhance the brittleness of the 3DP resin. The side length, opening and inclination (with respect to the horizontal direction) of the pre-existing square defect are 20 mm, 1 mm and 45°, respectively. Since the macro-crack was produced by non-laser irradiation treatment, the crack zone was thus filled with unsolidified liquid resin. The fabrication of the resin sample with a single pre-existing internal macro-crack is the same as that described for SLA in Section 3.2, except that a macro-crack was included in the 3D printable model in the first step.

The stress-strain curves of 3DP resin samples with and without a pre-existing internal macro-crack from uniaxial compression tests are shown in Fig. 3.8. The mechanical properties of those two samples are shown in Table 3.3. The results indicate that the existence of the macro-crack exerted significant influence on the compressive strength and strain at peak stress of the 3DP resin sample. After incorporating a macro-crack, the uniaxial compressive strength of the resin sample was almost halved, and the strains at peak stress were decreased to one third. However, the Young's modulus and the Poisson's ratio did not change a lot. The stress-strain curve of the sample with a single macro-crack is almost linear before the sharp stress drop at the peak stress (Fig. 3.8). Figure 3.9 shows the failure patterns and newly generated cracks at the upper tip of the pre-existing macro-crack after uniaxial compression test. It can be seen that the resin sample splits, attributed to the generation and propagation of the 3D wing cracks and anti-wing cracks. It needs to be noted that the generation of the wing or anti-wing cracks was accompanied by a clear snap. These evidences support that the pre-existing internal macro-crack could significantly enhance the brittleness of the 3DP resin.

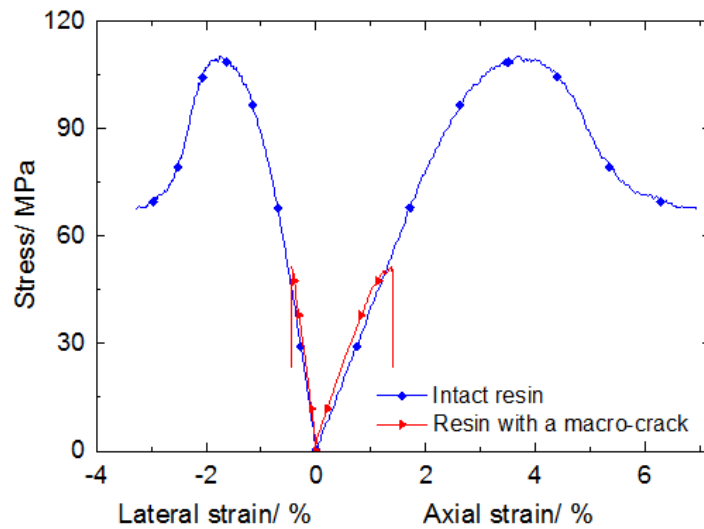


Figure 3.8 Stress-strain curves of the resin samples with and without a macro-crack from uniaxial compression tests

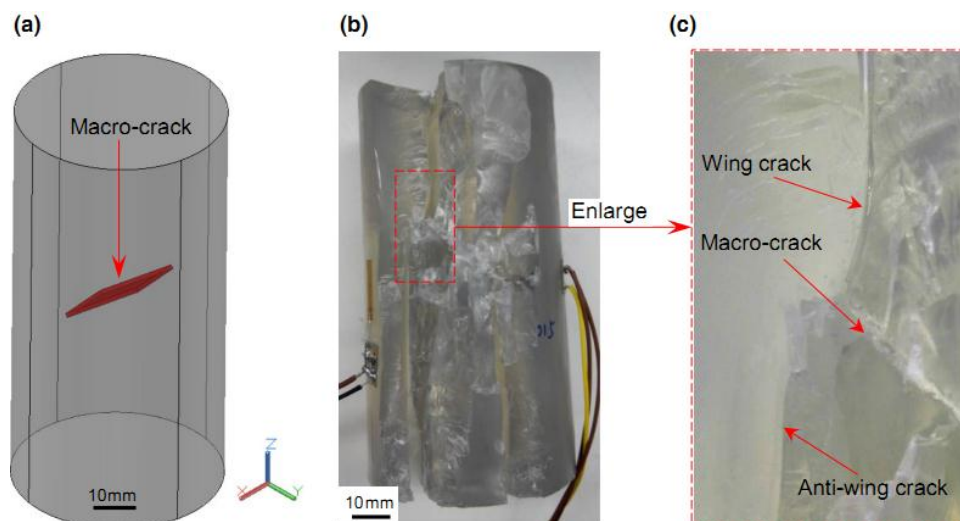


Figure 3.9 Failure patterns of resin sample with an internal macro-crack after uniaxial compression test. (a) Schematic diagram of the 3D printed model containing an internal square macro-crack; (b) Failure pattern; (c) Cracks generated from the macro-crack

3.4.2.3 Addition of micro-defects

In nature, rock contains numerous pre-existing micro-defects such as fissures, voids and notches. When the stress reaches a certain critical value, the pre-existing micro-defects will be activated. The propagation and coalescence of these micro-defects lead to the brittle failure of rocks. Therefore, to effectively replicate brittle rocks, the pre-existing

micro-defects should be included in the 3DP resin samples. To fulfill this requirement, three techniques, i.e., micro-CT scanning, 3D reconstruction and SLA 3DP, were adopted to replicate natural rocks with identical micro-structures. Hainan volcanic rock was chosen as the natural rock. Its porosity is 7.2% with numerous micro-defects. The specific information of this rock will be described in Chapter 5 in detail.

The fabrication of a 3D printed sample with micro-defects contains four steps. First, to obtain a set of consecutive 2D micro-CT images of the natural volcanic rock sample through scanning it with an X-ray micro-CT XRM 500 scanner. Second, to reconstruct a 3D digital data of the volcanic rock from the 2D micro-CT images using the Mimics 16.0 software. Third, to convert the 3D digital data into a STL formatted file. Fourth, to fabricate the 3D printed sample with its micro-defects identical to the prototype volcanic rock sample using the Viper si² printer. More details of the manufacturing process will be described in Chapter 5 in detail.

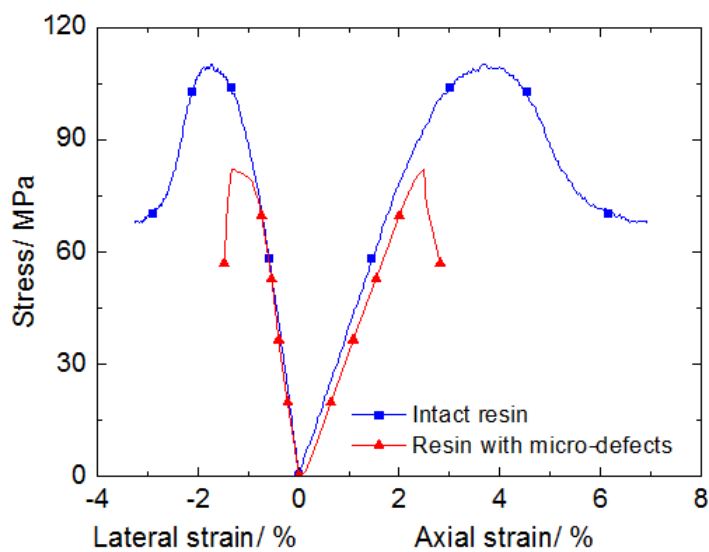


Figure 3.5 Stress-strain curves of the resin samples with and without pre-existing micro-defects in uniaxial compression tests

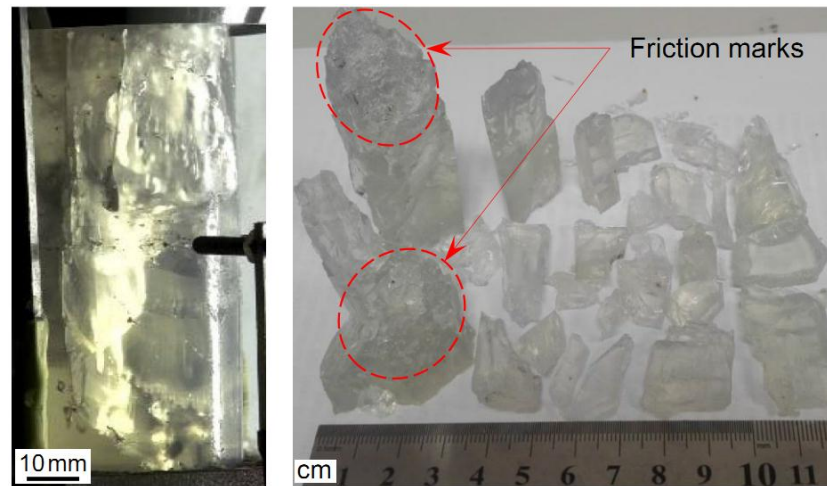


Figure 3.6 Failure patterns of resin sample with pre-existing micro-defects after uniaxial compression test. (a) Fracturing status before the final failure of the specimen; (b) Fragments in uniaxial compression test

Figure 3.10 presents the stress-strain curves of 3DP resin samples with and without pre-existing micro-defects in uniaxial compression tests. The mechanical properties of these two samples are shown in Table 3.3. After adding micro-defects, both of the uniaxial compressive strength and strains at peak stress decreased, while the Young's modulus and the Poisson's ratio did not change much. The general effect of adding micro-defects is similar to that of incorporating a macro-crack, although the affecting extent is different. The existence of a macro-crack affects more the mechanical properties of 3DP resin, compared with micro-defects. Figure 3.11 shows the internal fracturing pattern and the fragments after failure of the 3DP resin sample with pre-existing micro-defects. Figure 3.11(a) was taken before the final burst-like failure. It is found that the failure plane initiated at the pre-existing micro-defects, propagated in the axial direction, and finally led to the burst-like failure of the sample. Through analyzing the fragments after compression, it is found that the failure mode was a tensile-shear mixed one, as some fragment surfaces presented friction marks. Based on the observed stress evolution characteristics, i.e., a linear stress-strain relationship prior to the rapid stress drop after the peak stress, and failure mode, it can be claimed that pre-existing micro-defects could significantly enhance the brittleness of the 3DP resin. In addition, the transparency of the identified 3DP resin enables researchers to directly observe and analyze the spatial evolution of internal micro- and macro-cracks.

3.5 Discussion

In this Chapter, the SLA-fabricated resin is identified as the most suitable material among five targeted 3DP materials, i.e., ceramic, gypsum, PMMA, resin and SR20, for simulating brittle and hard rocks. Although the brittleness of the 3DP resin is not exactly the same as natural highly brittle rocks, it is much higher than that of the FDM-fabricated SR20 and the PLA material previously studied (Jiang and Zhao 2015). The high compressive strength (110 MPa) enables the SLA-fabricated resin to simulate moderate/high strength rocks such as sandstone (Alber et al. 2009) and marble (Wawersik and Fairhurst 1970). In addition, the transparency of 3DP resin enables researchers to directly observe the fracturing process within the sample using the high-speed cameras, which is an advantage over opaque 3DP materials and natural rocks. The transparent nature prevails over other traditional means such as acoustic emission detection (Lockner et al. 1991; Eberhardt et al. 1999) and X-ray CT scanning (Huang et al. 2013b; Kawakata et al. 1999) where clearly and accurately monitoring the internal crack growth in real-time is difficult.

Moreover, as 3DP almost has no restriction in geometrical shape during fabrication (Huang et al. 2013a; Kokkinis et al. 2015), more complex 3D flaws within the 3DP resin samples could be produced using the SLA 3DP. For instance, resin-based 3D fault models could be flexibly and repeatedly produced, providing 3D tomographic data of a natural fault are available. Therefore, rather than using the simplified 2D fault model (Griffith et al. 2009; Sammis et al. 2009), 3D laboratory earthquakes could be achieved with the resin-based artificial 3D fault model.

As the brittleness of the SLA-fabricated resin is lower than that of highly brittle rocks, three methods including freezing, incorporation of a macro-crack and addition of micro-defects were applied to enhance its brittleness. After frozen by dry ice, both the uniaxial compressive strength and brittleness of the 3DP resin significantly increased. This is mainly because the 3DP resin is an amorphous polymer, whose macromolecular chains are entangled together. When the environment temperature is far below the glass transition temperature, the interaction between macromolecular chains increases and the movement of the chains such as rotation and stretching is strongly constrained to resist the force applied (Richeton et al. 2006). The glass transition temperature is a temperature

range where a polymer changes from a “glassy”, rigid or hard state to a more compliant, pliable or “rubbery” state (Saba et al. 2016). The glass transition temperature of the 3DP resin is 58°C (Capel et al. 2013). Therefore, the frozen resin failed at a high stress without significant deformation, indicating high brittleness. When micro- or macro-defects were included in the 3DP resin, it deformed without barreling or swelling and exhibited almost linear stress-strain relationship prior to the splitting failure. It is because the 3DP resin samples changes from isotropic to anisotropic ones after replication of internal micro- and macro-defects and microstructures from the natural rocks. Under external loading, the existence of defects results in stress concentration around the tips of defects, and the pre-existing defects will grow if the stress exceeds the critical value. Therefore, as the compression increased, cracks propagated, interacted and coalesced, ultimately leading to the brittle failure.

Although findings in this chapter indicate that the FDM- fabricated samples and the powder-based 3DP samples are inappropriate for simulating brittle and hard rocks, it does not mean that the FDM and powder-based 3DP techniques cannot be applied to rock mechanics. Further improvement and development of these two techniques might improve their applicability in simulating rocks.

The typical elastoplastic behavior of the FDM-based specimen makes the FDM technique unsuitable for simulating brittle and hard rocks. To facilitate the application of FDM in mimicking rocks, appropriate improvement measures are recommended, e.g., development of innovative substitutions with more rigid and brittle properties to mimic rocks, development of additives that can be used to improve the stiffness and brittleness of the existing FDM-supported 3DP materials, development of techniques to fill the voids in the printed parts with compositions to enhance the overall strength and stiffness (Belter and Dollar 2015), and improvement of the printing resolutions and printing structures (Jiang and Zhao 2015). In addition, as a compromising approach, the FDM technique may be used to print samples that could simulate some specific physical property of natural rocks. For example, it has been applied in duplicating the micro- and macro-pore network of the coarse-grained Idaho Gray Sandstone with an estimated porosity of 29% (Ishutov et al. 2015).

In terms of the powder-based 3DP materials, the low strength, high ductility and

inhomogeneity of the fabricated samples constrained their application to mimic brittle and hard rocks. During printing, powder particles are consolidated by sprayed binder. However, the roller to spread the particle layers cannot apply sufficiently high pressure to fully consolidate the particles between layers. Therefore, the bond strength between particles is mainly provided by the adhesive strength of binder. Consequently, the powder-based 3DP samples exhibited the features mentioned, i.e., low strength, high ductility and inhomogeneity. To overcome these drawbacks, three means are suggested. First, new printers which could apply sufficiently high pressure by the roller to compact and consolidate particles are needed. This is because high compaction may enhance the bond strength between particles. Second, new 3DP binders which not solely have high adhesive strength but also show brittle characteristics when solidified need to be included in 3D printers. Lastly, some appropriate post-processing methods are suggested to further enhance the strength and brittleness of the powder-based 3DP samples. For example, high temperature (150°C) heating was proved to be an effective way to enhance the strength of the powder-based 3DP samples, although the strength was still not high enough (Fereshtenejad and Song 2016). In particular, the powder-based 3DP ceramics has the potential to be an ideal material to study micro-cracks evolution of brittle rocks, provided that the 3DP ceramics could be effectively fired without shrinking and cracking. Similarly, freezing may also be effective to enhance the brittleness of the powder-based 3DP samples since the binder becomes brittle in low temperature (Vaitkus et al. 2014).

Although the merits of 3DP in mimicking intact and defected rocks and investigating their mechanical and fracture behaviors are promising as discussed in the aforementioned part, there exist limitations of the present 3DP technique, which may impede its application in rock mechanics. For instance, the Young's modulus of the present 3D printed specimens is much lower than that of the natural rocks. Lower Young's modulus could result in larger deformation of the 3DP rock sample than natural rock specimen under the same external load (Jiang and Zhao 2015; Ju et al. 2017). In addition, it is impossible to reflect the heterogeneity of natural rocks through utilizing a single 3DP material to prepare 3DP rocks (Feng et al. 2015; Fereshtenejad and Song 2016; Jiang and Zhao 2015; Zhu et al. 2018). Besides, it is difficult to replicate strongly cemented grain boundaries of the natural rocks using the currently available 3DP techniques. These demerits of 3DP in mimicking brittle and hard rocks need to be addressed in the future with the development of 3DP techniques.

3.6 Conclusions

This Chapter reports the identification of the most suitable 3DP material to mimic brittle and hard rocks from ceramics, gypsum, PMMA, SR20 and resin in terms of currently prevalent 3DP techniques, i.e., powder-based 3DP, FDM and SLA. Main conclusions are as follows:

- (1) The powder-based 3DP specimens, i.e., ceramics, gypsum and PMMA, failed at very low compressive stress and exhibited highly ductile behavior, which renders them unsuitable for mimicking common brittle and hard rocks. The FDM-fabricated SR20 sample showed typical elastoplastic behavior, which is different from most natural rocks. Despite the relatively large deformation, the strength and stress evolution process of the 3DP resin sample produced by SLA method are comparable to those of many rocks, e.g., marble and sandstone. Meanwhile, the 3DP resin sample deformed with little barreling or swelling during the whole loading period. Therefore, resin is the most suitable 3DP material for replicating brittle and hard rocks, although its brittleness needs to be improved.
- (2) Three methods including freezing, incorporation of a macro-crack and addition of micro-defects can effectively enhance the brittleness of the 3DP resin. With freezing treatment, the compressive strength of the 3DP resin increases by approximately 70% without changing its maximum axial deformation. The frozen sample failed in an explosive manner. After incorporating a macro-crack or adding micro-defects, both the uniaxial compressive strength and the strains at peak stress significantly decreased. And the existence of a macro-crack affects more the strength and strains of 3DP resins, compared with micro-defects. In addition, after adding cracks, the stress-strain curves were almost linear before the sharp stress drop at the peak stress.
- (3) The transparent 3DP resin could be adopted to directly observe and analyze internal crack evolution during rock fracturing, which may help better understand the failure mechanisms.

In this chapter, the Accura® 60 resin is identified as the most suitable 3DP material for replicating brittle and hard rocks. Based on this finding, the Accura® 60 resin and the SLA based 3DP technique will be used to solve the problem of preparing transparent rock-like samples with 3D internal flaws, and studies on 3D crack growth behaviors

will be conducted with these artificial rock samples in Chapter 4; Replication of internal defects and investigation of the mechanical and fracture behavior of rocks using 3DP and 3D numerical methods in combination with micro-CT will be performed in Chapter 5.

CHAPTER 4 FABRICATION OF 3D INTERNAL FLAWS WITH 3DP AND INVESTIGATION OF THEIR FRACTURING AND MECHANICAL BEHAVIORS UNDER STATIC AND DYNAMIC COMPRESSION

Based on the Accura 60 resin material identified in Chapter 3, 3DP is adopted to solve the difficulty of preparing artificial rock samples with single and double pre-existing 3D internal flaws. Static and dynamic uniaxial compression tests are subsequently conducted on these samples to investigate the influence of flaw number, flaw angle (α) and ligament angle (β) as well as loading types on the mechanical and fracturing behaviors of 3DP artificial rocks. The dynamic tests are performed with the SHPB device. The real-time 3D internal crack growth subject to static and dynamic compression are monitored and analyzed from two orthogonal directions with two high-speed cameras. Distinctions between the mechanical and fracturing behaviors of rock-like samples under dynamic and static loading conditions are compared, and the physical mechanisms underlying these processes are discussed. The results verify that the SLA 3DP can rapidly, repeatedly and precisely produce resin-based artificial rock specimens with 3D internal flaws.

4.1 Introduction

Rock is an inhomogeneous media that contains many pre-existing defects, such as fissures, joints and weak surfaces. The existence of these defects greatly threatens the stability and safety of rock engineering. When rocks are subjected to static or dynamic loads, cracks are often initiated and propagate along these pre-existing flaws, ultimately leading to the catastrophic failure of rock masses. Therefore, a comprehensive study of crack growth behaviors in rock under static and dynamic loading conditions is essential for rock engineering excavation and maintenance.

As reviewed in Chapter 2, extensive investigations have been performed to study crack growth in brittle rock and rock-like materials. However, the overwhelming majority of the studies focused on 2D crack propagation and coalescence problems (Bobet and Einstein 2002; Li et al. 2005a, 2017a; Nemat-Nasser and Horii 1982; Shen et al. 1995;

Wong et al. 2001; Wong and Chau 1998; Wong and Einstein 2009a, 2009b; Yang et al. 2017; Zhang and Wong 2012). In nature, most of the pre-existing defects are in 3D. Nevertheless, studies concerning 3D cracks, especially for 3D internal cracks, have received insufficient attention. To study the mechanism of 3D crack growth under compression, Adams and Sines (1978), Germanovich et al. (1994) and Dyskin et al. (2003) developed three methods to generate 3D internal flaws in transparent PMMA, resin and silica glass samples. As stated in Chapter 2, all three methods have their own drawbacks, e.g., unavoidable glued interface, difficulties in guaranteeing the precise position of pre-existing cracks and requiring sophisticated skills to operate the high energy laser pulse generator, which may affect the 3D internal flaw growth. Therefore, a new method for preparing samples with pre-existing internal 3D flaws has appeal. Additional studies on 3D flaw growth are also needed.

In this chapter, SLA 3DP is applied to prepare samples containing single or double 3D internal flaws using the resin material identified in Chapter 3. Static and dynamic compressive tests are performed on these 3DP samples to study 3D crack growth behaviors using two HSCs. The effects of flaw geometry, i.e., flaw angle, flaw number and bridge angle, and loading types on mechanical and fracturing behaviors of the 3DP artificial resin rock samples with internal 3D flaws are analyzed. Distinctions among fracturing under dynamic and static loading conditions are compared, and the underlying physical mechanisms are analyzed.

4.2 Experimental setup

4.2.1 Sample preparation

The SLA-based 3D printer Viper si² and the corresponding supporting material accura® 60 identified in Chapter 3 are applied to produce resin-based artificial rock samples containing single and double pre-existing 3D internal penny-shaped flaws. The reason for preparing penny-shaped flaws is that it is the simplest flaw in brittle materials that incorporates appropriate flaw variables (Evans 1978). In addition, penny-shaped flaw has commonly been used to study 3D crack growth behaviors (Adams and Sines 1978; Dyskin et al. 2003; Germanovich et al. 1994).

Figure 4.1 shows the workflow of fabricating artificial rock sample using 3DP method.

It mainly consists of the following four steps: (1) to prepare a 3D model of the sample using a computer-aided design and drafting software such as Auto CAD and save it as an STL format file (a general file format for 3DP); (2) to digitally slice the model in STL file into a series of cross-sectional layers and assign them with printing information, e.g., layer thickness and printing path, using 3D light year software; (3) to print the artificial rock sample layer by layer using the SLA-based Viper si²; (4) to post-process the 3DP rock samples such as transparentizing the sample via grinding and polishing treatments. Note that other parts of the sample are solidified by ultraviolet irradiation except the flaws.

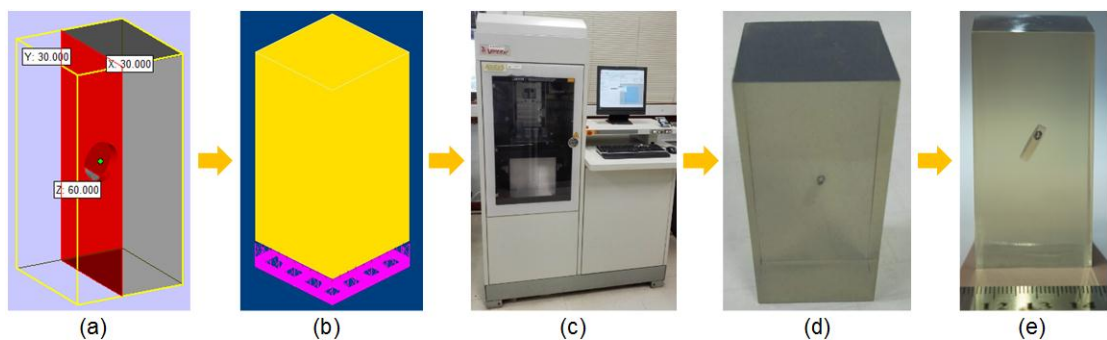


Figure 4.1 Preparation of artificial rock using 3DP. (a) 3D model in STL format; (b) Digitally sliced 3D model with arranged printing information; (c) 3DP using the SLA-based Viper si² printer; (d) Original 3DP artificial rock sample; (e) 3DP artificial rock sample with a single pre-existing internal 3D flaw after transparentizing treatment.

The structure in pink color in (b) is a cushion used to support the 3DP sample.

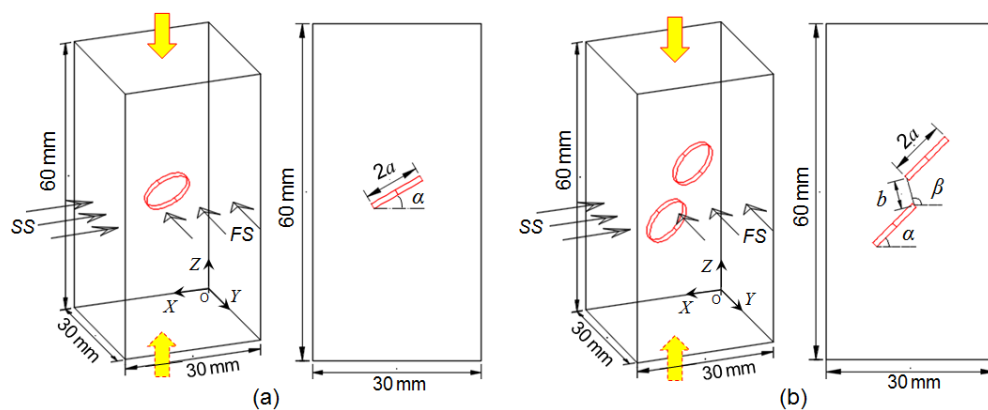


Figure 4.2 Geometry of the pre-existing flaws in artificial rock samples. (a) A sample with a single 3D internal flaw; (b) A sample with double 3D internal flaws. α is flaw inclination angle, β is ligament angle, $2a$ is flaw length, and b is ligament length. The arrows represent the loading direction during compression.

Table 4.1 Geometries and experimental results of the flawed samples

Sample*	Flaw center	α (°)	β (°)	σ_c (MPa)	ε_a (%)	σ_1 (MPa)	σ_1/σ_c (%)
Intact	-	-	-	113.8	3.81	-	-
S-0	(15,15,30)	0	-	109.3	3.14	-	-
S-30	(15,15,30)	30	-	107.3	2.72	59.9	55.8
S-60	(15,15,30)	60	-	99.9	2.38	52.9	53.0
S-90	(15,15,30)	90	-	110.5	3.16	-	-
D-45	(9.7,15,35.3) (20.3,15,24.7)	45	45	79.3	1.92	41.9	52.8
D-65	(10.2,15,35.7) (19.8,15,24.3)	45	65	87.8	2.18	37.8	43.1
D-85	(11.25,15,36) (18.75,15,24)	45	85	80.9	1.98	45.4	56.1
D-105	(12.1,15,35.95) (17.9,15,24.05)	45	105	85.7	2.09	49.2	57.4
D-S-30	(15,15,30)	30	-	113.7	1.66	103.8	91.3
D-D-105	(12.1,15,35.95) (17.9,15,24.05)	45	105	95.9	1.58	84.9	88.6

*S-Single flaw, D-Double flaws; D-S: Dynamic test on single flawed sample, D-D: Dynamic test on double flawed sample. The upper and lower rows of parentheses represent the center coordinates of the upper and lower pre-existing flaws, respectively. The origin of the coordinates is shown in Fig. 4.2.

To clearly and accurately detect 3D crack growth from different angles, specimens were designed in a prismatic shape rather than a conventional cylindrical one. The length to width ratio of the specimen is 2:1, and all samples with different flaw arrangements have a nominal size of $60 \times 30 \times 30$ mm. To investigate the effect of flaw geometry on the mechanical and fracture behaviors of the artificial rock under uniaxial compression, three flaw parameters, i.e., flaw number, flaw inclination angle and ligament angle, are considered in this chapter. The geometry of a single flaw is described by two geometrical parameters: flaw length $2a$ (“ a ” is the radius of the penny-shaped flaw) and flaw inclination angle α (the angle of the flaw with respect to the horizontal direction) as shown in Fig. 4.2a. The geometry of double flaws is defined by four geometrical parameters: flaw length $2a$, ligament length b (5 mm), flaw inclination angle α and ligament angle β as shown in Fig. 4.2b. For specimens with a single flaw, α varies from 0°

to 90° at an interval of 30° . For specimens with double flaws, β varies from 45° to 105° with an interval of 20° , where α remains constant and equal to 45° . After conducting some trial tests, it is found that the aperture of flaw of 2 mm is conducive to the generation of new cracks at the tips of the pre-existing flaw. Thus, the penny-shaped flaw is a circular disc with 5 mm in radius and a constant thickness of 2 mm. Geometries of artificial rock samples used in this chapter are listed in Table 4.1, in which the sample number S-30 indicates an artificial rock sample with a single pre-existing 3D internal flaw of inclination angle 30° , while D-65 represents an artificial rock sample with double pre-existing 3D internal flaws of ligament angle 65° . The sample D-S-30 refers to a dynamic compressive test conducted on a single flawed sample with its inclination angle of 30° .

4.2.2 Testing apparatus

The static uniaxial compression tests were carried out on a servo controlled testing system (TAW-2000), at School of Science of the National University of Defense Technology, with the maximum loading capacity of 2000 KN. The static tests were performed at a loading rate of 2 mm/min under room temperature (about 20°C). To clearly monitor the 3D crack growth behaviors, no strain gauges were mounted on the surfaces of the samples.

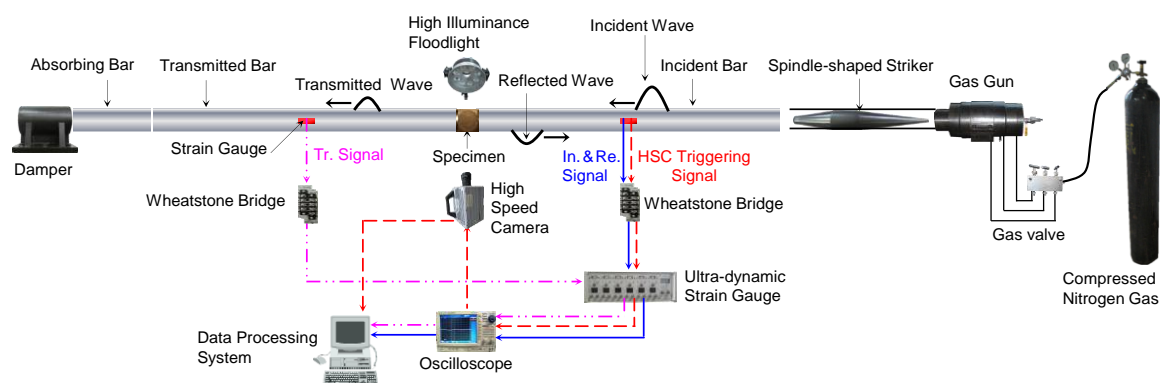


Figure 4.3 Schematic of the SHPB system

Dynamic compression tests were performed using a modified SHPB with a spindle-shaped striker (Li et al. 2005b) at the Central South University. Figure 4.3 illustrates the schematic of the SHPB system, which mainly consists of two parts, i.e., three bars (an incident bar with length of 2m, a transmitted bar with length of 1.5m and

an absorbing bar with length of 0.5m) and a data acquisition subsystem. The bars are made of the hardened 40 Cr, with diameter, Young's modulus and P-wave velocity of 50 mm, 240 GPa and 5400 m/s, respectively. Using the spindle-shaped striker, incident pulse wave with a long and ramped wavefront can be repeatedly generated that can not only reduce wave oscillation and minimize dispersion effects, but also facilitate achieving stress equilibrium at the ends of the specimen (Zhang and Zhao 2014a). The principle of the SHPB system was reviewed in Chapter 2. Once the dynamic stress equilibrium in the sample is achieved, based on the 1D stress wave theory, the dynamic compressive stress $\sigma(t)$ and axial strain $\varepsilon(t)$ of the specimen can be determined by Eqs. (2.1) and (2.2) respectively.

During testing, two FASTCAM SA1.1 HSCs were adopted to record 3D crack growth in real-time from two orthogonal directions. Under static loading, the HSCs were manually triggered upon the initiation of new cracks at the tip of the pre-existing flaw under the pre-trigger mode. The HSCs were set at a frame rate of 100,000 frames per second (fps) with a resolution of 128×256 pixels to observe crack growth of specimens with a single pre-existing flaw. For specimens with double 3D flaws, to accurately capture the crack initiation and coalescence between the inner tips of the two pre-existing flaws, the HSC frame rate was 150,000 fps with a resolution of 128×160 pixels in the early stage, and once the coalescence process completed, the frame rate was set to 100,000 fps to monitor the full field of crack propagation within the specimen. In SHPB tests, the HSCs were automatically triggered by a transistor-transistor logic (TTL) pulse generated by the oscilloscope synchronously with the incident signal, where the frame rate and resolutions were 125,000 fps and 256×128 pixels, respectively.

4.3 Results

4.3.1 Static uniaxial compression tests

4.3.1.1 Static strength and deformation

The mechanical properties of the resin-based 3DP samples are summarized in Table 4.1, in which σ_c , ε_a and σ_1 represent the uniaxial compressive strength, axial deformation at peak stress and the initiation stress of the first wing crack. Figure 4.4 shows the axial stress-strain curves of 3DP resin samples with and without pre-existing flaws. It is evident

that α , β and the flaw number have considerable effects on σ_c and ε_a . In terms of the single flawed samples, the sample whose α is 60° has the lowest σ_c (99.9 MPa) and ε_a (2.38%), which are decreased by approximately 12.2% and 37.5% compared with those of the intact sample. Although the σ_c of the other single flawed specimens only slightly decreased, their ε_a decreased by more than 17% compared with that of the intact sample. Considering the specimens with double pre-existing flaws, the sample with β equal to 45° has the lowest σ_c (79.3 MPa) and ε_a (1.92%), which are 30.3% and 49.6% lower, respectively than those of the intact sample. σ_c and ε_a slightly increase by approximately 10% with β changing from 45° to 105° . When the number of flaws increases from one to two, the average σ_c and ε_a decrease by 21.8% and 28.3%, respectively. This indicates that the flaw number affects the mechanical properties of the artificial samples more, compared with α and β . From Fig. 4.4, the stress-strain curves of the specimens nearly overlap with each other prior to the peak stress, which indicates that the flaw geometry has almost no influence on the Young's modulus of the 3DP resin samples. Notably, single flawed 3DP resin samples with α of 0° and 90° did not generate macrocracks and failed to break in a burst-like manner after the peak stress, which is different from other flawed samples.

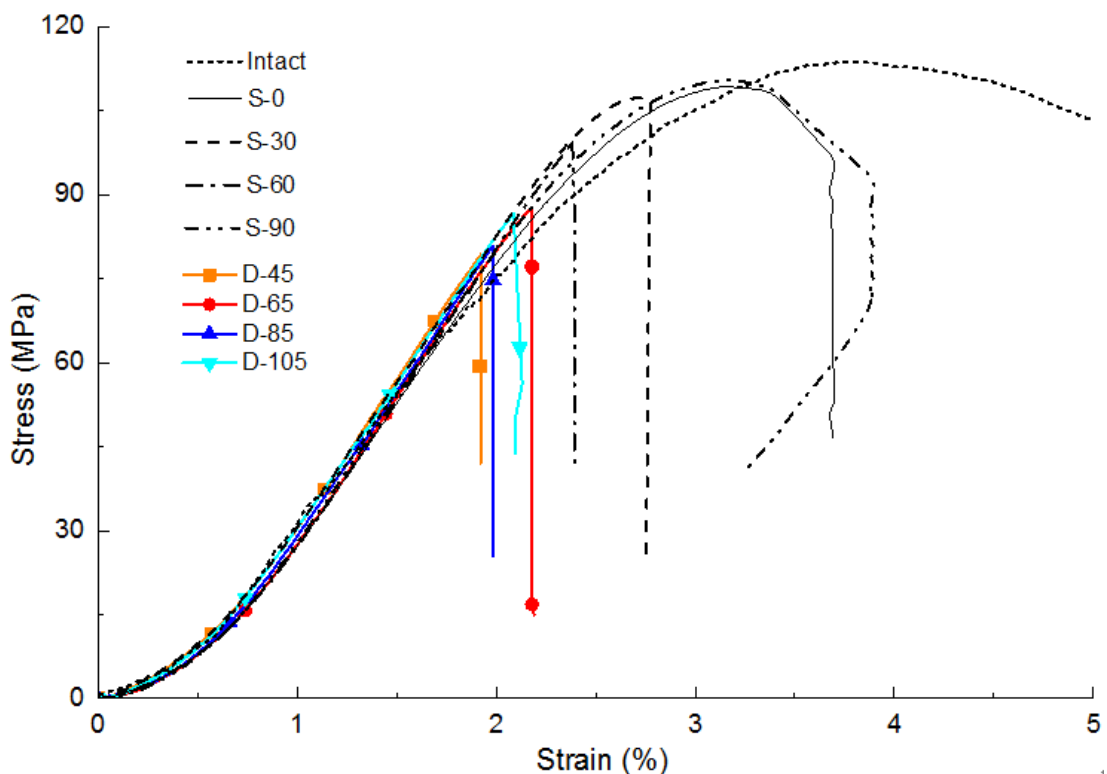


Figure 4.4 Axial stress-strain curves of the 3DP resin samples with and without internal

penny-shaped flaws under static compression

4.3.1.2 Three-dimensional crack growth behaviors

To study 3D fracturing behaviors, especially the fracturing process, two high-speed cameras (HSCs) were adopted to capture and record the transient crack propagation process from two orthogonal directions. Because there were no external signals to automatically trigger the HSCs to monitor and record the 3D crack growth within the flawed samples under static compression loading, the HSCs were manually triggered upon the initiation of new cracks at the tips of the pre-existing flaws. However, due to the limited storage space (8 GB) of the HSC, its recording time is limited to approximately 0.7 seconds under the frame rate of 100,000 fps. Therefore, the camera operator is required to respond sufficiently quickly upon observing the occurrence of new cracks; otherwise, it is impossible to capture and record the crack propagation process. In the present study, the final 3D crack growth behaviors in the single flawed sample with an α of 60° failed to be recorded.

In addition, because the entire loading time for one sample under static loading lasts for approximately 2 minutes, it is impossible to monitor and record all the progressive fracturing behaviors during the entire static loading process at one time. Therefore, in order to capture all the fracturing process, the compression machine was paused nearly at the same time that the HSC was triggered, so as to win sufficient time (i.e., approximately 20 seconds) to save the video of the crack propagation process, to restore the storage space of the HSC, and to prepare for the next record cycle. During pausing, the displacement of the platen remained stable and the axial load was kept relatively constant. When the HSC was ready for the next record, the sample was reloaded. The above processes were repeated until the final failure of the specimen.

Three-dimensional crack propagation in single flawed samples

Figure 4.5 illustrates crack growth behaviors and the axial stress-strain curve of the sample with α of 30° under static compression. Notably, the black speckles in the high-speed photography images indicate newly generated cracks. In general, the single flawed resin sample failed in a progressive manner. Under compression, when the compressive stress was loaded to approximately 56% (60 MPa) of its σ_c (107.3 MPa),

tensile wing cracks were first generated at the lower tip of the flaw, as shown in Fig. 4.5aI. The crack propagation was terminated roughly at the length of the pre-existing flaw, despite increasing axial stress. As the load increased to approximately 68% and 73% of σ_c , wing and anti-wing cracks initiated at the upper tip of the flaw (Figs. 4.5aII and III).

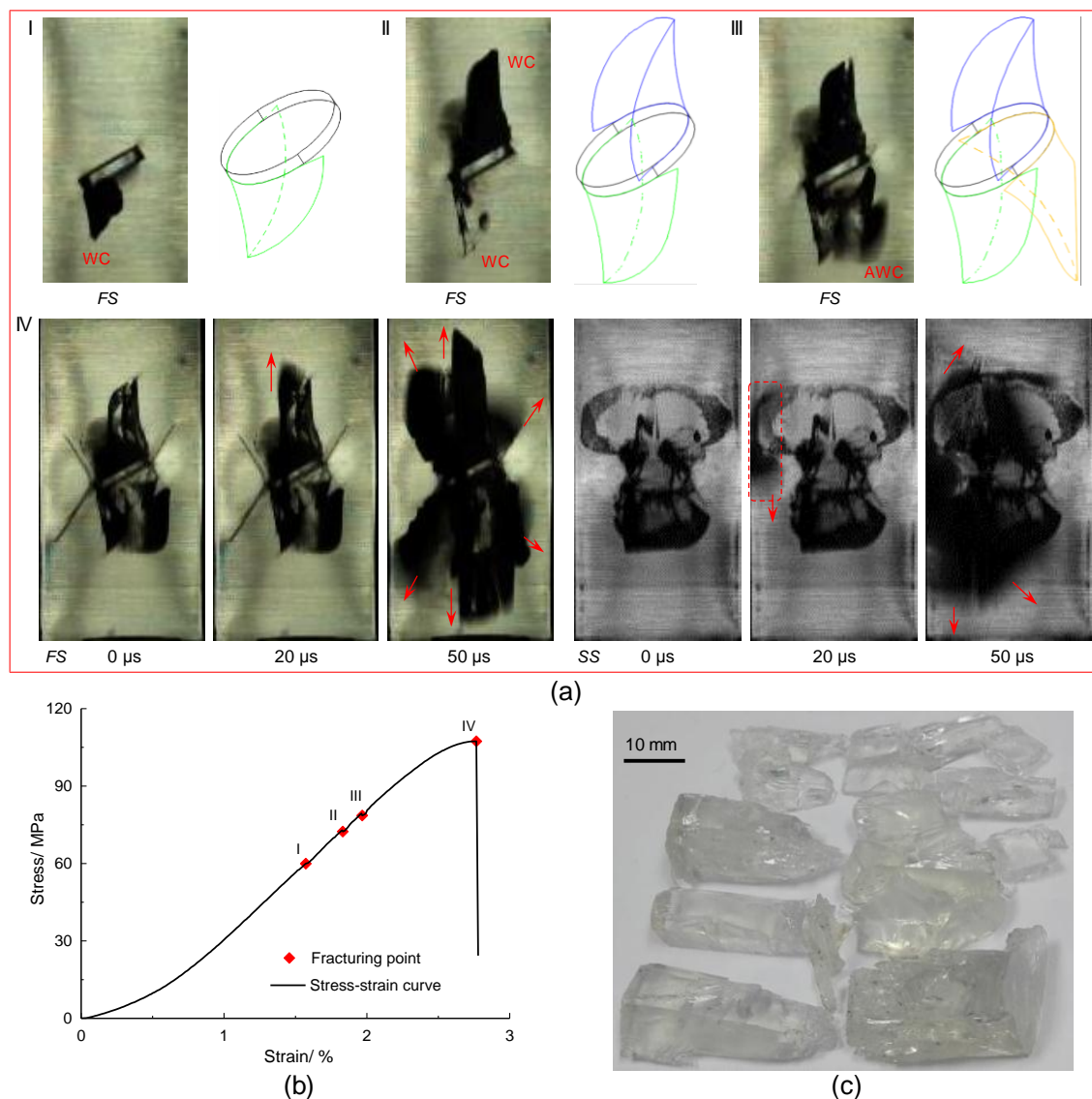


Figure 4.5 Stress-strain curve and crack propagation of S-30 sample under static uniaxial compression. (a) Progressive fracturing stages under different loading levels recorded by HSCs; (b) Stress-strain curve and fracturing stages; (c) Failed fragments. The Roman characters I-IV in (a) and (b) indicate the fracturing sequential. *FS* and *SS* represent images shot from the front surface and side surface of the resin sample, respectively. The time in (a) is the relative time recorded upon the initiation of the secondary crack. The sketches in (a) are corresponding wing and anti-wing cracks. The arrows show the propagated direction of the secondary cracks and the dashed rectangle

shows the initiation place of the secondary crack. WC and AWC indicate wing crack and anti-wing crack, respectively.

Figure 4.6 shows the anti-wing crack propagation process captured by the HSC from the front side of the sample. A tensile crack is generated along the opposite direction of the wing crack, which has rarely been reported in previous studies on 3D crack growth (Fu et al. 2016). Similar to wing cracks, an anti-wing crack was arrested after propagating approximately 1.5 times the length of the initial flaw within approximately 60 μs , as shown in Fig. 4.6. When the compressive load reached the peak stress, secondary cracks were generated along the left edge of the upper wing crack and then propagated in the axial and lateral directions, ultimately leading to burst-like failure of the sample, as shown in Fig. 4.5a. Notably, secondary cracks refer to those generated later than wing and anti-wing cracks.

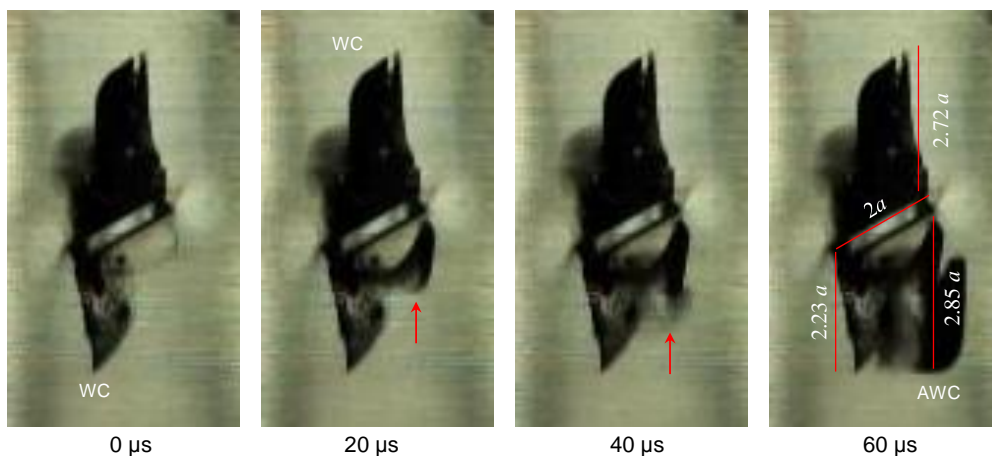


Figure 4.6 Anti-wing crack propagation processes in static test. The arrows represent the growing anti-wing cracks. The number in the rightest image refers to the length of the cracks with regard to the radius of the pre-existing flaw. The time below the images represent the absolute time recorded upon the initiation of the anti-wing crack.

Three-dimensional crack propagation in double flawed samples

For specimens containing multiple pre-existing flaws, crack coalescence between the pre-existing flaws usually occurs prior to the final failure of the samples (Fu et al. 2017; Sagong and Bobet 2002; Wong and Chau 1998; Yin et al. 2014). In the present study, a similar phenomenon was observed in the 3DP resin samples containing double pre-existing 3D internal flaws. Figure 4.7 illustrates the fracturing states before the final

catastrophic failure of the double flawed samples. The results indicate that crack coalescence patterns depend on ligament angles. When β is less than or equal to 85° , wing cracks generated at the inner tips of the pre-existing flaws cannot coalesce with each other. When β equals 105° , wing cracks initiated at the inner tip of the upper flaw grew until the cracks coalesced with the lower flaw tip. For specimens whose β equals 45° and 65° , coplanar cracks generated at the inner tips of the pre-existing flaws. Although the coplanar cracks gradually propagated in the prolongation of the pre-existing flaw, they did not coalesce with each other. The formation of coplanar cracks may be more or less associated with plastic deformation resulting from quasistatic stress concentrations at the flaw tips when the two pre-existing flaws are coplanar or quasi-coplanar (Petit and Barquins 1988). In addition, petal cracks were produced in specimens with β values of 45° and 105° . The petal crack observed in this chapter is similar to that found by Wong et al. (2004b) in PMMA specimens with 3D surface flaws.

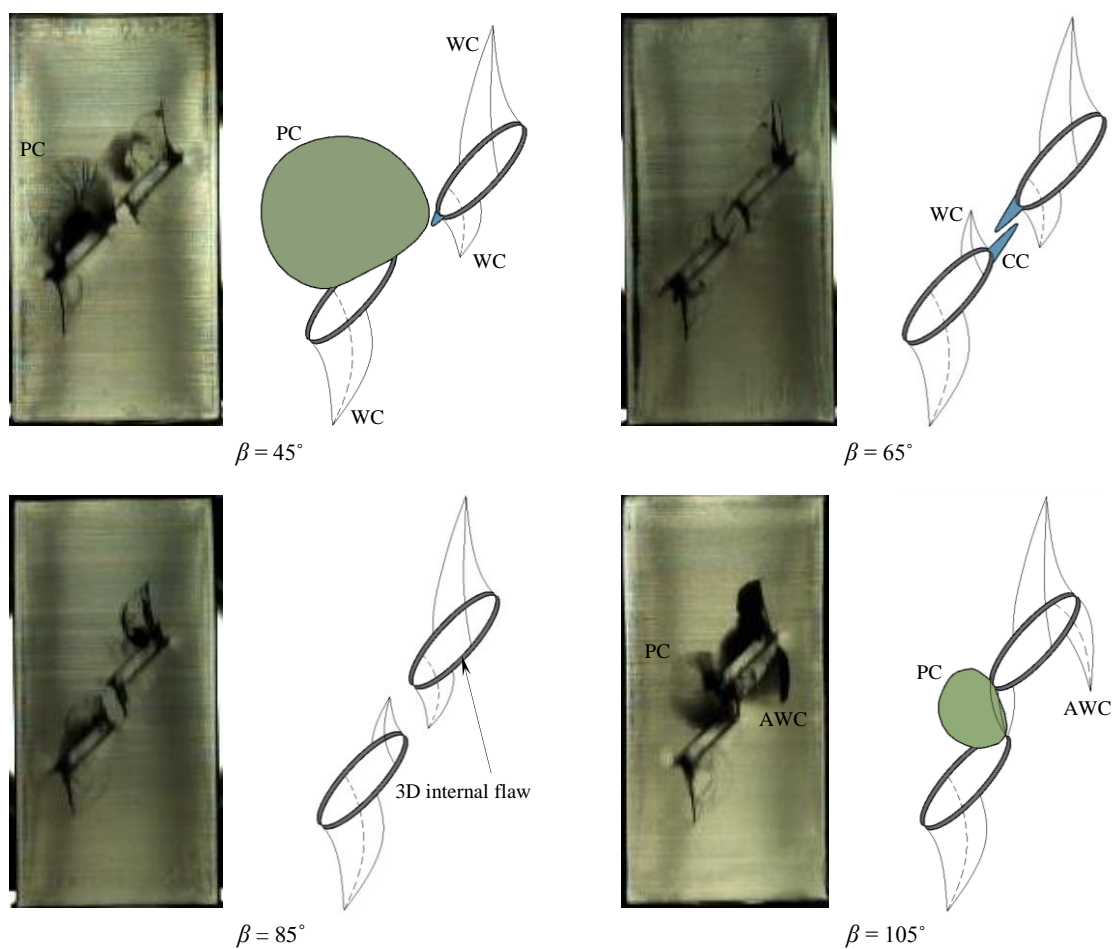


Figure 4.7 Crack coalescence patterns in double-flawed 3DP resin samples. The high-speed images illustrate fracturing states before the final failure of the sample. The

sketches are corresponding crack patterns of the double-flawed samples. PC and CC refer to petal crack and coplanar crack, respectively. Other abbreviations have the same meaning as those in Fig. 4.5.

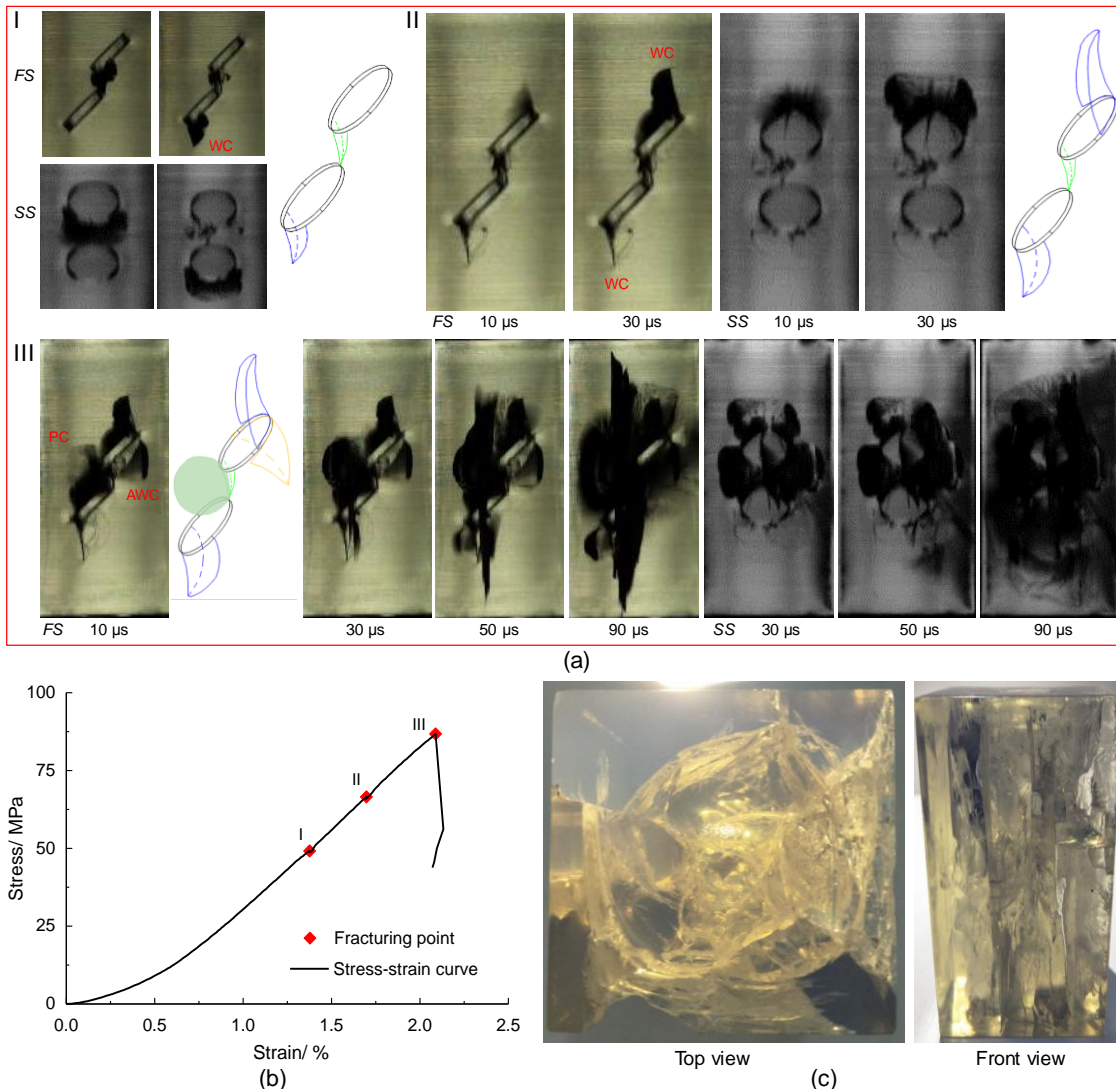


Figure 4.8 High-speed images, stress-strain curve and sample after failures of D-105 sample under uniaxial compression. (a) 3D crack propagation and coalescence process recorded by HSCs; (b) Stress-strain curve and fracturing stages; (c) Top and front views of the chaotic cracks in the failed sample. The time in (a) is the relative time recorded upon the initiation of cracks at each stage. PC refers to petal crack. Other abbreviations, the arrows and the dashed rectangle have the same meaning as those in Fig. 4.5.

Although the ligament angle has effects on crack coalescence in double flawed samples, the 3D crack growth behaviors of specimens with different β values are generally similar. Figure 4.8 shows the typical 3D crack propagation and coalescence in a double flawed

sample whose β is 105° . When the compressive stress was loaded to approximately 57% of the peak stress (86.7 MPa), wing cracks were generated at the inner tip of the upper pre-existing flaw, then propagated and eventually coalesced with the inner tip of the lower pre-existing flaw (Fig. 4.8aI). Nearly simultaneously, another wing crack sprouted from the outer tip of the lower flaw, as shown in Fig. 4.8aI. As the load increased to approximately 75% of the peak stress, a new wing crack was generated at the outer tip of the upper flaw. Similarly, these two wing cracks cannot extend to the boundary of the sample; the cracks grew by roughly the length of the initial flaw before termination. Nevertheless, the coalescent wing crack terminated despite the continuous increase in the compressive load. When the stress approached the peak, a petal crack and an anti-wing crack (Fig. 4.8aIII) were successively generated at the inner and outer tips of the upper flaw, respectively. The petal crack propagated perpendicular to the flaw surface and coalesced with the lower flaw. After the peak stress, secondary cracks were generated in the coalescent region and rapidly propagated in the axial and lateral directions, ultimately leading to the explosion-like failure of the sample (Fig. 4.8aIII). The complicated, chaotic (disorderly) cracks in the failed sample (Fig. 4.7c) indicated that there was violent fracturing during the final failure process.

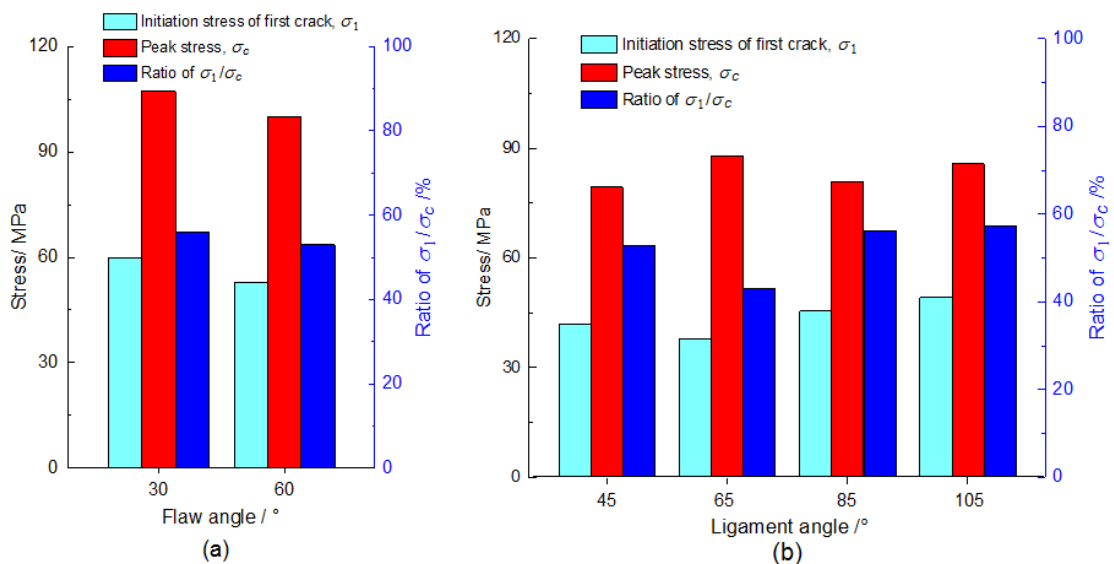


Figure 4.9 Initiation stress of new crack, peak stress (strength) and the ratio of initiation stress to peak stress versus flaw angle and ligament angle. (a) Specimens with single flaw; (b) Specimens with double flaws. The bars with cyan, red and blue colors represent initiation stress of new crack, peak stress and the ratio of initiation stress to peak stress, respectively.

Initiation stress of the first crack

Figure 4.9 illustrates plots of σ_1 , σ_c and the ratio of σ_1/σ_c versus flaw angles α and β in the artificial rock samples with single flaw and double pre-existing 3D internal flaws. In general, σ_1 is affected by both α and β . σ_1 of the specimen with α equal to 60° (52.9 MPa) is lower by approximately 12% than that of the sample with α equal to 30° (59.9 MPa). For double flawed samples, the sample with β of 65° has the lowest σ_1 (37.8 MPa), which is approximately 23% lower than that of the sample with β of 105° (49.2 MPa). However, the ratios of σ_1/σ_c of the flawed 3DP resin samples are approximately 55%, which appears to be unaffected by the flaw geometry, i.e., α , β and flaw number, except for the sample with β of 65° . Note that the resin samples with α equal to 0° and 90° are not included here because these two samples do not generate macrocracks prior to the peak stress.

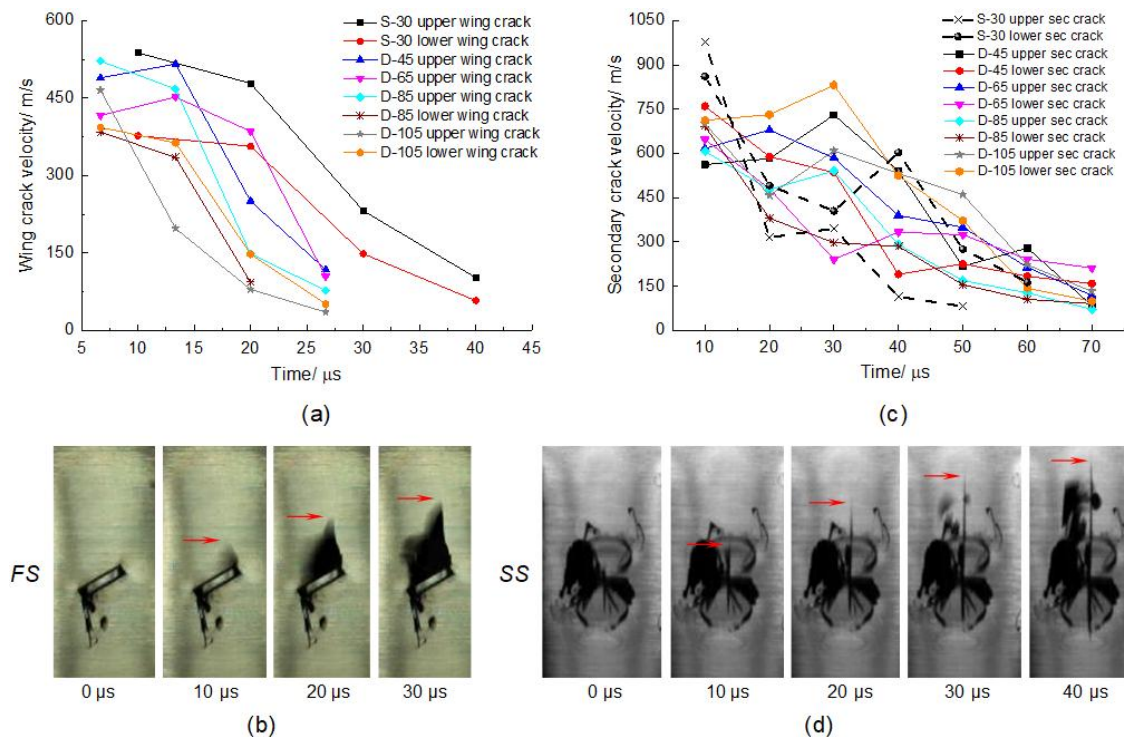


Figure 4.10 Crack propagation velocity. (a) Wing crack propagation velocity; (b) Upper wing crack propagation process in specimen with α of 30° ; (c) Secondary crack propagation velocity; (d) Upper secondary crack propagation process in specimen with β of 45° . The time in (a) - (d) represents the absolute time recorded upon the initiation of the cracks. The red arrows in (b) and (d) point to the crack tips.

Three-dimensional crack propagation velocity

With high-speed photography, 3D wing and secondary crack propagation trajectories can be detected, and thus, the crack growth length can be obtained utilizing an image-measuring technique. Therefore, the 3D wing and secondary crack growth velocities can be calculated, as the shooting interval is fixed at 6.67 or 10 μ s. Notably, the calculation error is within 20% when the crack propagation velocity is greater than 400 m/s. Figure 4.10 demonstrates the 3D wing and secondary crack propagation velocity histories and the corresponding crack growth images detected by HSCs in resin specimens containing single flaws and double 3D internal flaws. Regarding the 3D wing cracks, they suddenly emerged in an unstable/jump-like manner (dynamically), attaining a finite length, and their propagation velocities quickly slowed down with increasing propagation time or distance. This phenomenon differs from the stable propagation of wing cracks initiated at the pre-existing 2D flaw tips under uniaxial compression, where a stable or quasi-stable wing crack grows gradually as load increases (Germanovich et al. 1994; Hoek and Bieniawski 1965; Nemat-Nasser and Horii 1982; Park and Bobet 2010) [52,53]. In terms of the secondary cracks, their unstable growth after the peak stress (the ultimate strength) was immediately followed by the dynamic failure of the entire sample. This is similar to the final splitting or explosive-like failure of the specimens that were caused by the unstable growth of 2D wing cracks or 3D secondary tensile cracks after the peak stress under similar loading conditions (Dyskin et al. 2003; Germanovich et al. 1994; Horii and Nemat-Nasser 1985; Nemat-Nasser and Horii 1982). Similarly, the secondary crack propagation velocity sharply dropped as the crack extended to the boundary of the sample. However, the 3D wing cracks could only propagate a certain distance, which was much shorter than that of the secondary cracks. The mean values of the maximum 3D wing crack propagation velocities are approximately 60% of that of the 3D secondary cracks. Although the flaw geometry shows no remarkable influence on the wing and secondary crack propagation velocities, the flaw number affects the maximum propagation velocity of secondary cracks. For instance, the maximum secondary crack propagation velocity in double flawed samples (831 m/s) is 15% lower than that in single flawed samples (977 m/s). Two factors may explain this feature. On the one hand, the parallel-arranged double cracks may reduce each other's stress intensity factor (SIF), making the SIF at the secondary crack initiation position lower than the SIF in the single flawed sample (Dyskin et al. 1999). On the other hand, a larger σ_c of the single flawed sample might generate a higher SIF than that in the double flawed samples with

lower σ_c during the initiation of secondary cracks. While the crack propagation velocity is found experimentally to be related to the stress intensity according to Charles' law, i.e., $V = A \cdot K^n$, where A is a constant, K is SIF and n is known as the stress corrosion index, ranging from 20 to 60 for earth materials (Atkinson and Meredith 1987a,b; Main et al. 1989). It therefore results in a slower crack propagation velocity for specimens with smaller SIF (Guo et al. 2001).

4.3.2 Dynamic compression tests

Apart from static loads, rock masses often endure dynamic loads, such as earthquakes and blast waves. As reviewed in Chapter 2, 2D crack growth under dynamic compression differs from that under static uniaxial compression. Therefore, it is reasonable to speculate that 3D crack growth subject to dynamic compression may also differ from that under static compression. Considering this, the investigation of 3D crack growth is extended from static loading to dynamic loading for the first time in this chapter. To highlight the difference between dynamic loading and static loading, the mechanical and fracturing behaviors of 3D crack growth under dynamic compression are compared with those under static compression within the corresponding samples.

4.3.2.1 Dynamic strength and deformation

The stress-strain curves of the 3DP samples with single and double pre-existing 3D internal flaws subjected to dynamic compression are shown in Fig. 4.11, where curves under static compression are also included. Under dynamic compression, the uniaxial compressive strength is 113.7 MPa and 95.9 MPa, respectively, for specimens with single and double pre-existing flaws. The tangent modulus, which is defined as the slope of a line drawn tangent to the half peak stress point on the stress-strain curve, decreases by 11.8%, when the number of flaws changes from one to two. The maximum axial strain at failure of the sample changes little (4.8%) with number of flaws.

The mechanical behavior of the flawed specimens is strongly affected by the type of loading. From static compression to dynamic compression, the maximum axial strain at failure decreases by 40.1% and 24.4% for 3DP resin specimens with single and double pre-existing 3D internal flaws, respectively. The uniaxial compressive strength changes little, i.e., approximately 8%, with loading types. The tangent modulus increases by 52%

and 38% for 3DP resin specimens with single and double pre-existing 3D internal flaws, respectively, when the loading type changes from static compression to dynamic compression. This indicates that the deformational behavior of the 3DP resin is rate-dependent and that the brittleness of the resin could be enhanced at a high strain rate (Gilat et al. 2007).

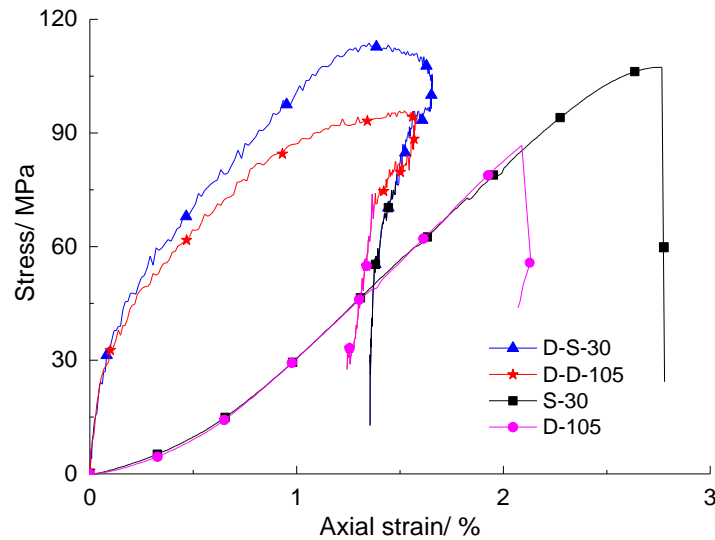


Figure 4.11 Stress-strain curves of the 3DP samples with single and double flaws in dynamic and static compression tests

4.3.2.2 The initiation stress of the first crack

Figure 4.12 illustrates σ_i in 3DP resin specimens with single and double pre-existing 3D internal flaws under dynamic loading as well as static compression. Under dynamic compression, the impact of the flaw number on σ_i is consistent with that on the peak stress (σ_c), i.e., with an increasing number of pre-existing flaws, σ_i decreases. However, the ratio of σ_i/σ_c , which is approximately 90% for the flawed specimens in dynamic tests, appears to be unaffected by the flaw number. For static compression tests, σ_i/σ_c also seems to be unaffected by the flaw number, despite the fact that σ_i in specimens with double pre-existing flaws is lower than that in specimens with a single flaw.

Although the high strain rate (approximately 150 s^{-1}) shows very few effects on σ_c for the flawed 3DP specimens, as shown in Fig. 4.11, strong strain rate effect exists on σ_i . σ_i in dynamic tests increased by approximately 73% and 80% for specimens with single and double flaws, respectively, compared with static tests. This phenomenon is consistent

with the results found in experimental and numerical studies with a single 2D flaw, despite the difference in the amount of increase (Zhang and Wong 2013).

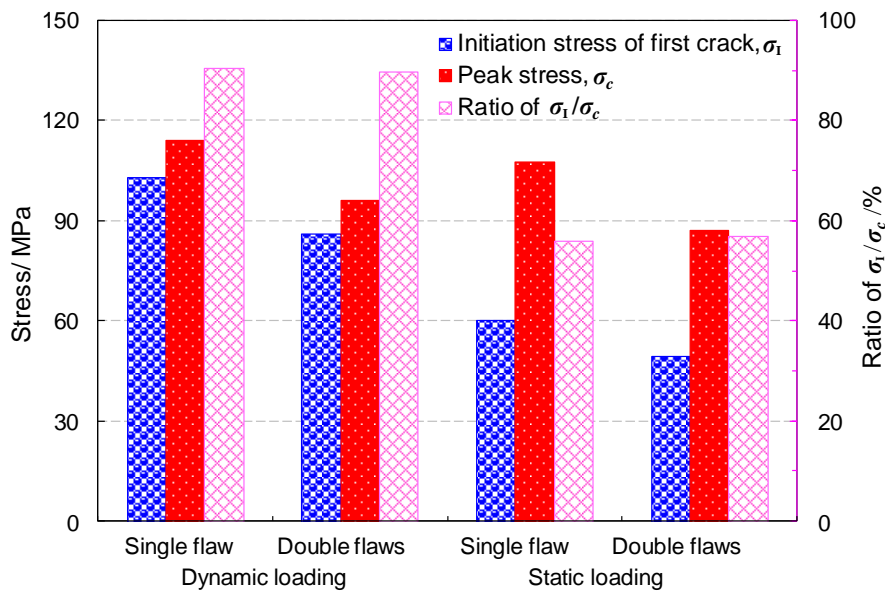


Figure 4.12 The initiation stress of the first crack

4.3.2.3 Three-dimensional crack growth in specimens with single 3D internal flaw

The 3D crack growth of single-flawed specimens subjected to dynamic compression and its comparison with that under static compression are shown in Fig. 4.13. When the dynamic load increased to approximately 91% of the peak stress, symmetrical wing cracks almost simultaneously initiated at the upper and lower tips of the pre-existing flaw at the loading time of about 112 μ s (Fig. 4.13a). With increasing load, wing cracks slightly wrapped around the boundary of the pre-existing flaw and synchronously propagated in a relatively steady rate toward the sample ends, eventually splitting the 3DP resin sample into strips, as shown in Fig. 4.13d.

Under static loading, wing cracks intermittently generate at the tips of the pre-existing flaw with increasing loading, but they could only propagate a distance of approximately 1-1.5 times the length of the pre-existing flaw (Fig. 4.13b-A'~C'). Further loading resulted in a burst-like failure of the sample by the secondary cracks initiated around the flaw edge as shown in Fig. 4.13b-D'. Secondary cracks refer to those generated later than wing and anti-wing cracks.

The major differences between 3D crack growth in dynamic and static compressions are

the propagation features of wing cracks and the sample failure mode. Under dynamic compression, wing cracks sharply propagated in an unstable manner which continuously

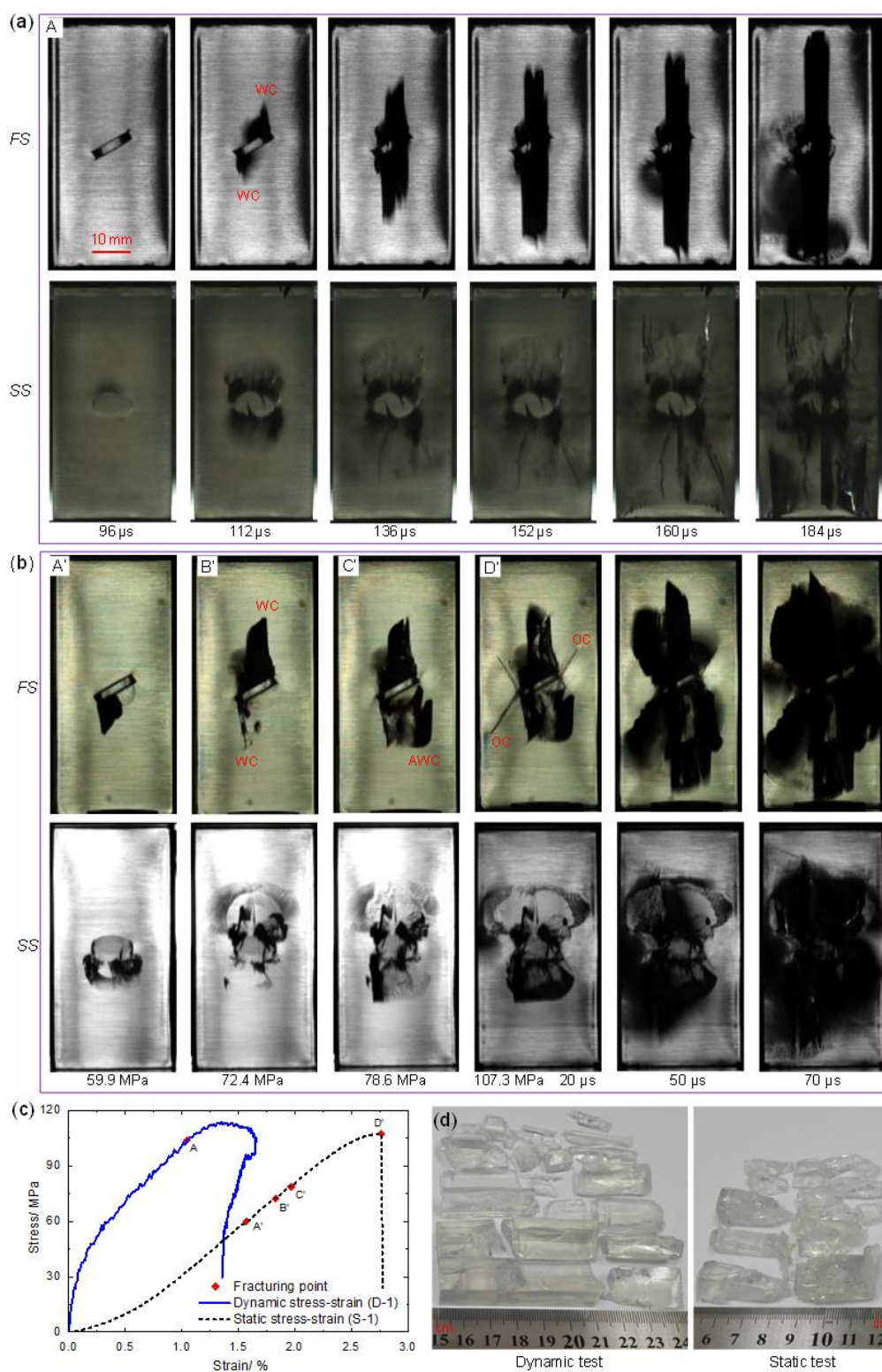


Figure 4.13 Fracturing of sample with single 3D flaw under dynamic and static compression. (a) and (b) Progressive fracturing in dynamic and static tests; (c) Axial

stress-strain curves; (d) Failure fragments after compression tests. The capital letters A and A'-D' in (a)-(c) indicate fracturing activities at different loading stages. Other abbreviations have the same meaning as those in Fig. 4.5.

grow and extend to the ends of the sample, finally resulting in a splitting failure of the sample, whereas under static compression, wing cracks are intermittently generated but cannot propagate a long distance, and the final burst-like failure is caused by secondary cracks. In addition, under dynamic loading, there are no anti-wing cracks generated at the tips of the pre-existing flaw, which is the other difference from that under static loading (Fu et al. 2016).

4.3.2.4 *Three-dimensional crack growth in specimens with double 3D internal flaws*

Figure 4.14 displays the comparative results of real-time crack coalescence and propagation in specimens with double pre-existing 3D internal flaws under dynamic compression with comparison with those under static compression. In dynamic test, wing cracks initiated at the inner tips of the flaws when the specimen was loaded to approximately 90% of the peak stress (Fig. 4.14a). The extension and interaction of wing cracks led to the coalescence of the pre-existing flaws (Fig. 4.14a). Subsequently, two wing cracks almost simultaneously initiated at the outer tips of the upper and lower pre-existing flaws when the loading time was increased to about 104 μs , as shown in Fig. 4.14a. Then, the outer-wing cracks propagated along the loading direction toward the ends of the sample with loading time increasing to approximately 200 μs . However, the development of the coalescent wing cracks was constrained by the dominant propagation of the outer-wing cracks and could not expand to a larger region (see Fig. 4.14a). The continuous propagation of the outer-wing cracks finally resulted in the tensile failure of the specimen (Fig. 4.14d). Similarly, there were no anti-wing cracks generated at the tips of the pre-existing flaws in specimens with double 3D internal flaws under dynamic loading.

In the static test, the coalescence (Fig. 4.14b-A') between two pre-existing flaws is attributed to the generation and propagation of wing cracks generated at the inner tips of the pre-existing flaws at approximately 56.7% of the peak stress (86.7 MPa). Wing and anti-wing cracks were intermittently initiated from the outer tip of the lower flaws with increasing load, but they could only propagate by roughly the length of the initial flaw

(Fig. 4.146b-A'~C'). The failure of the sample was also caused by the secondary cracks which were generated in the coalescent region after the peak stress (Fig. 4.14b-C').

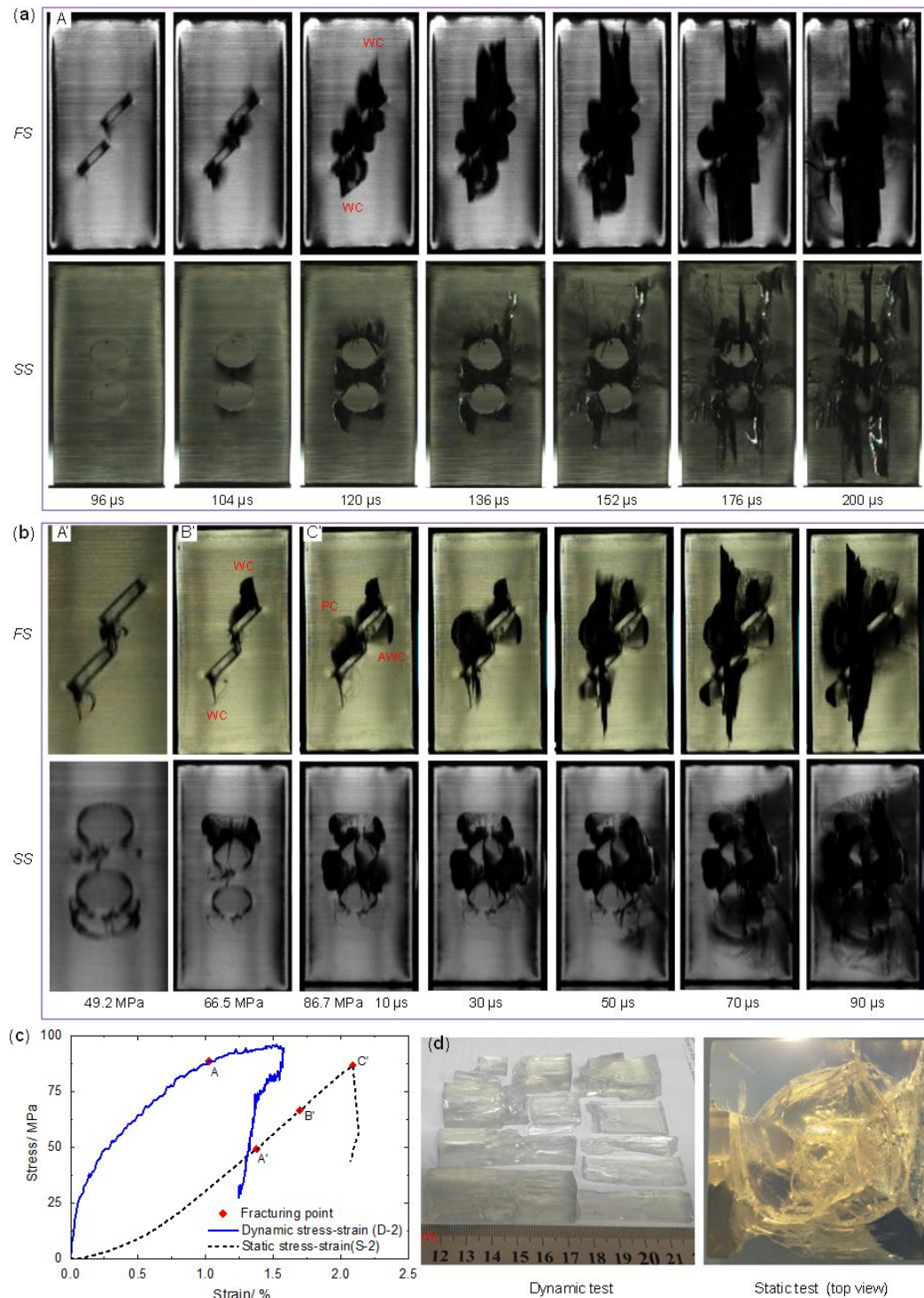


Figure 4.144 3D crack growth of specimen with double 3D flaws under dynamic and static compression. (a) and (b) Progressive fracturing in dynamic and static tests; (c) Axial stress strain curves; (d) Failure fragments after compression tests. The capital letters in (a)-(c) and other abbreviations as well as time marks have the same meaning

as those in Fig. 4.13.

The major difference between 3D crack growth behaviors in dynamic and static compressions is that crack growth under dynamic loading is less complex than that in static test. Only wing cracks are generated in the SHPB test, while anti-wing and petal cracks are found in the static test. Notably, petal crack is the one that initiates along the front of the pre-existing internal flaw(s) and propagates perpendicular to the flaw surface (Wong et al. 2004a; Yin et al. 2014). The splitting failure of the sample in dynamic loading is induced by the propagation of outer-wing cracks along the direction of axial stress, as shown in Fig. 4.14a, while the burst-like failure of the specimen under static compression is caused by the burst growth of secondary cracks. The failure pattern in the static test is complex and full of chaotic cracks compared with the SHPB test (Fig. 4.14d).

4.3.2.5 Crack propagation velocity

With the aid of the HSC, real-time crack propagation and coalescence during testing can be clearly monitored and recorded, and hence, the crack propagation velocity can be roughly determined. Notably, the crack propagation velocity is an average velocity value during a time interval (i.e., $8 \mu\text{s}$), which is defined as the ratio of the propagation length over the time interval between the adjacent two high-speed images. Figure 4.15 illustrates crack propagation velocities in specimens with single and double flaws subjected to dynamic and static compressions. Note that crack propagation velocities under static loading in Fig. 4.15 refer to those of secondary cracks but not wing cracks, since wing cracks cannot propagate any significant distance.

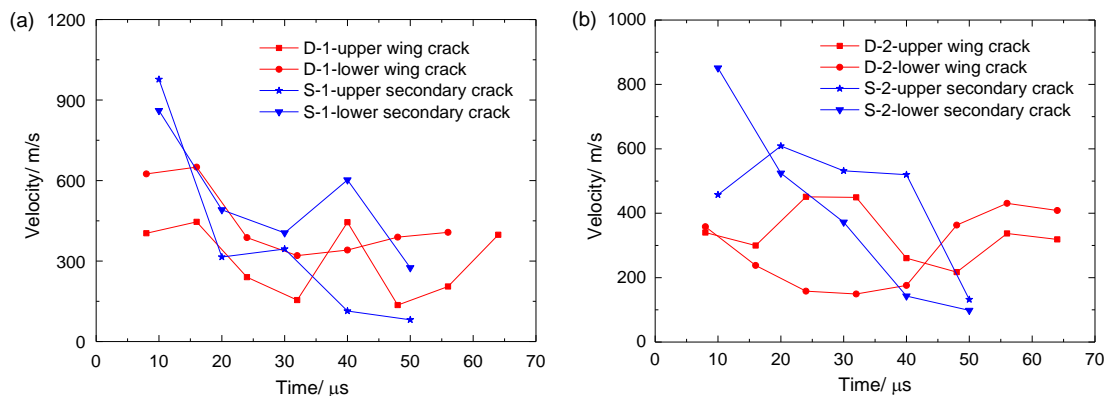


Figure 4.15 Comparison of crack propagation velocities in dynamic and static compression tests. (a) and (b) Specimens containing single and double pre-existing 3D

internal flows, respectively

Under dynamic loading, wing crack propagation velocity is relatively stable, i.e., the terminal speed is slightly lower than the beginning speed, as shown in Fig. 4.15. For example, the initial and terminal speeds of the upper wing crack in the double flawed specimen are approximately 350 and 319 m/s, respectively. However, in the static tests, the propagation velocities of secondary cracks quickly drop with increasing propagation time or distance (Fig. 4.15). The difference in velocity drop between dynamic and static tests is probably because σ_1 could be roughly maintained during the entire crack propagation process, which occurs during the loading and unloading stages of the SHPB tests, whereas under static loading conditions, σ_1 may soon drop to zero as the loading force sharply decreases after the peak force (Gao et al. 2015; Li et al. 2017a). However, the maximum crack propagation velocity (625 m/s) under dynamic loading is lower than that under static loading (977 m/s).

4.4 Discussion

In this chapter, it was found that the wing crack growth and failure pattern of the 3DP resin with a single flaw of 30° agreed well with the observations of previous studies performed on other materials, e.g., PMMA (Adams and Sines 1978; Germanovich et al. 1994), silica glass (Germanovich et al. 1994) and polyester resin "Polylite 61-209" (Dyskin et al. 2003), which had a similar internal flaw of 30° under static compression, as shown in Fig. 4.16. Wing cracks are generated at the upper and lower tips of the pre-existing flaw and wrapped around the flaw boundary, yet the length is approximately the same as that of the pre-existing flaw. In addition, during compression loading, the single flawed specimen with α of 30° deforms without lateral swelling and shows an almost linear stress-strain behavior up until the final burst-like failure occurs (see Figs. 4.4 and 4.5b). This indicates that the 3DP artificial rock sample has good brittleness, which is similar to that of brittle rock materials such as sandstone (Yang and Jing 2011) and marble (Li et al. 2017c). Moreover, the stripped fragments, as shown in Fig. 4c, after failure indicate that the sample with α of 30° was failed in a splitting dominant mode, which agrees with the failure mode of some brittle rock and rock-like materials, e.g., sandstone (Yang and Jing 2011), marble (Li et al. 2017c; Yang et al. 2009) and cement mortar (Dyskin et al. 2003). Consequently, the study of 3D crack growth using 3DP resin

specimens with pre-existing 3D internal flaws is concluded to be feasible.

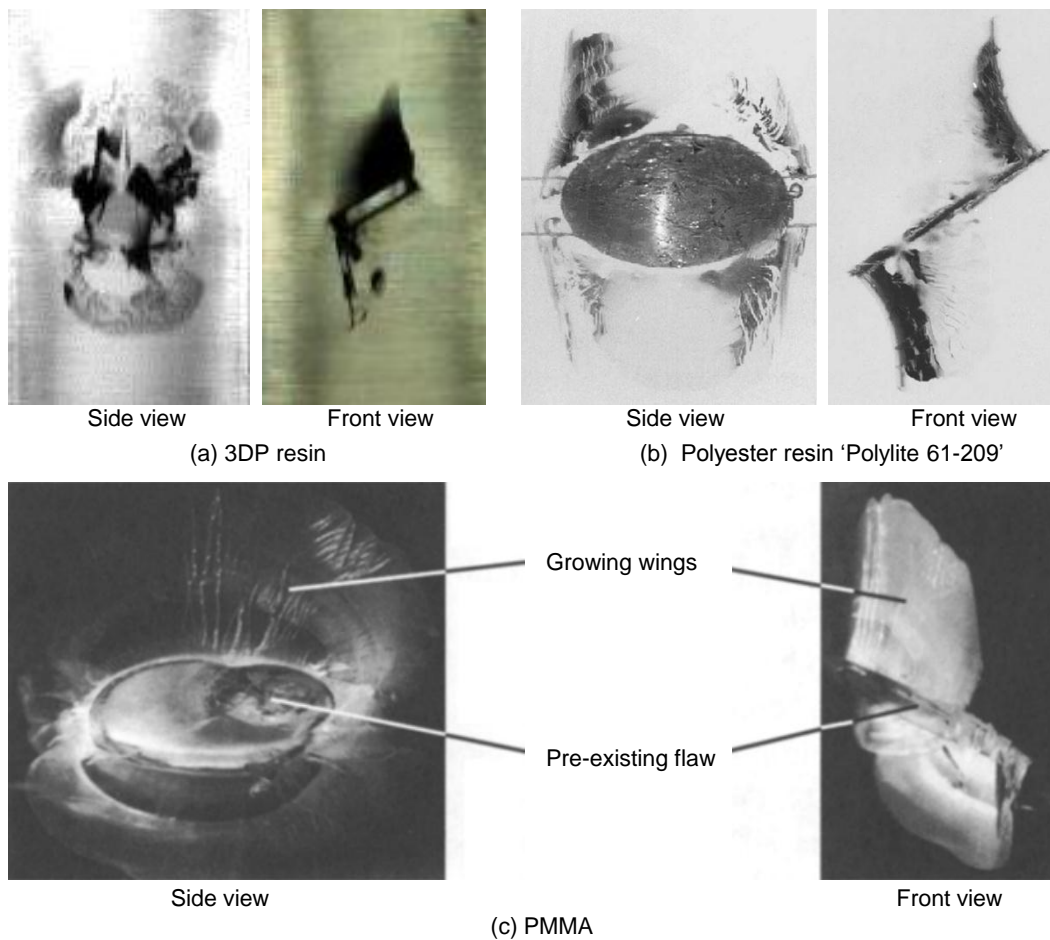


Figure 4.16 Patterns of wing cracks generated at the tips of the pre-existing flaw. (a) Present findings from 3DP resin; (b) Findings from regular resin (Dyskin et al. 2003); (c) Findings from PMMA (Germanovich et al. 1994). In (b) and (c) the flaws were produced by embedding aluminum foil disk and high energy laser pulse, respectively.

Wing crack growth in specimens with 3D internal flaws demonstrates a significant difference between dynamic and static loading conditions (Figs. 4.12 and 4.13). Under dynamic compression, wing cracks continuously grow to the sample ends, while they can only propagate a limited distance under static loading. This is because under dynamic loading, after crack initiation, the SIF remains equal to the dynamic fracture toughness of the resin, which drives wing cracks to grow continuously until sample failure (Li et al. 2000), whereas in the static compression test, the wrapping of wing cracks around the edge of the pre-existing 3D internal flaw restricts the wing cracks from propagating a long distance (Dyskin et al. 2003).

Under similar static loading conditions, the crack growth and failure behaviors of resin specimens containing 3D internal flaws significantly differ from those in specimens with pre-existing 2D throughout flaws. Under uniaxial compression, wing cracks initiate at the tips of the 2D flaw, grow with increasing compression stress, and finally split the rock and rock-like samples approximately along the loading direction, as shown in Figs. 4.17a, b (Horii and Nemat-Nasser 1985; Yang and Jing 2011). Nemat-Nasser and Horii (1982) believed that the initiation mechanism of wing cracks from 2D flaws is due to the relative sliding of the pre-existing flaw faces. In contrast to the 2D case, wing cracks formed at the 3D flaw tips can only propagate a limited distance (Figs. 4.17c, d). Dyskin et al. (2003) attributed this limited propagation distance to the wing cracks wrapping around the flaw edge.

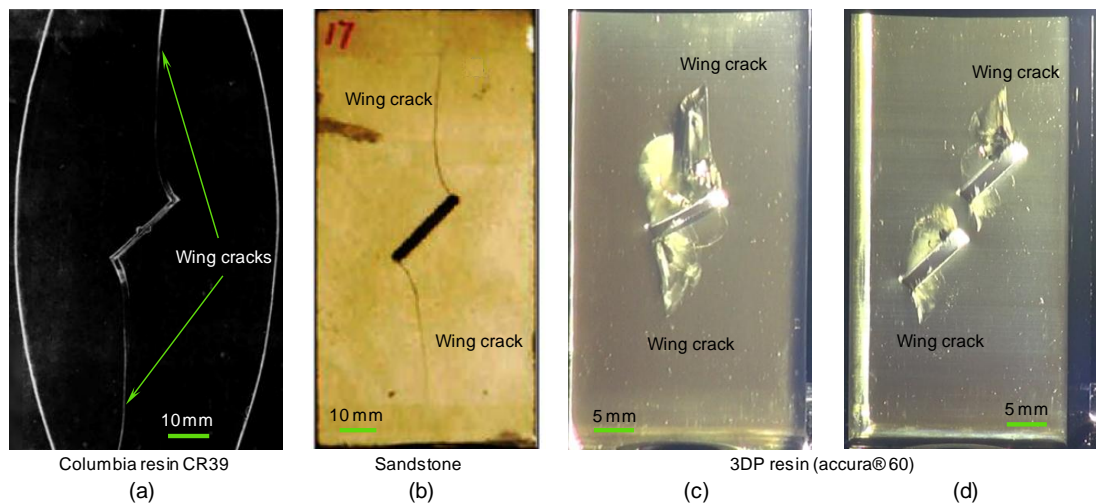


Figure 4.17 Wing cracks in samples with 2D and 3D flaws under static compression. (a) and (b) 2D wing cracks initiated in specimen produced by Columbia resin CR39 (Horii and Nemat-Nasser 1985) and sandstone (Yang and Jing 2011) with single pre-existing 2D flaw; (c) and (d) 3D wing cracks generated in 3DP resin sample with single and double pre-existing 3D internal flaws

Under dynamic compression, crack growth behaviors among specimens with single, pre-existing 2D and 3D internal flaws are distinct. For a specimen with a 2D flaw, the dominant shear crack results in failure with an X-shaped pattern, as shown in Fig. 4.18a (Li et al. 2017a; Zou and Wong 2014). Li and Wong (2012) reported that the high compressive stress around the 2D flaw tips lead to rapid generation and propagation of shear cracks. In contrast to the 2D case, wing cracks initiate at the 3D internal flaw tips

and continuously propagate toward the sample ends (Fig. 4.18b). This failure mode may be due to pre-existing flaw sliding, which is similar to that observed in 2D crack propagation under static compression (Nemat-Nasser and Horii 1982). However, further studies are required to reveal the mechanism of differing crack growth behaviors between 2D and 3D flaws under dynamic loading.

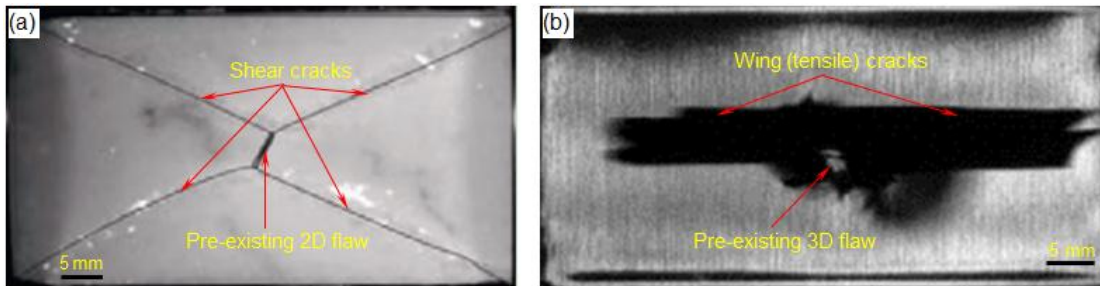


Figure 4.18 Crack patterns in samples with 2D and 3D flaws under dynamic loading. (a) Marble specimen with a single pre-existing 2D flaw (Zou and Wong 2014); (b) 3DP resin sample with a single pre-existing 3D internal flaw

In addition, different from the static compression tests (Fu et al. 2016; Zhou et al. 2018a), under dynamic loading, anti-wing cracks did not initiate in both single flawed and doubled-flawed specimens. This phenomenon may be attributed to stress wave propagation that could alter the stress field around the 3D flaw tips, where anti-wing cracks could be generated in static compression tests. This mechanism is similar to the explanation for why shear cracks rather than tensile cracks always form first around the 2D flaw tips under dynamic loading (Li et al. 2017a; Li and Wong 2012). This is because under dynamic loading, the arrival of the stress wave generates compressive stress at points where tensile cracks often initiate under static loading, which constrained the tensile crack evolution at that moment (Li and Wong 2012). Nevertheless, further studies, such as numerical simulation, are needed to verify this mechanism.

Apart from flaw shape, the flaw number also exerts a remarkable influence on σ_1 and σ_c . Under static compression, the minimum strengths for specimens with single flaws and double pre-existing flaws are 99.9 MPa and 79.3 MPa, respectively, and the minimum σ_1 decreases by 28.5% when the number of flaws changes from one to two. In SHPB tests, when the number of 3D flaws increased from single to double, the dynamic strength and σ_1 changed from 113.7 MPa to 95.9 MPa and 103.8 MPa to 84.9 MPa, respectively. This indicates that increasing pre-existing flaws could not only weaken the rock strength but

also reduce the initial cracking stress. Therefore, more attention should be given to the initial cracking stress when considering the stability and safety of rock structures containing multiple pre-existing flaws. Although increasing flaws reduce σ_1 and σ_c , the ratio of σ_1/σ_c almost keeps constant for specimens with single flaw and double pre-existing flaws. It is possibly because the crack initiation stress in uniaxial compression is a stable and robust material property and characteristic of intact rock, which is independent of the boundary conditions and specimen shapes (Bieniawski 1967; Diederichs et al. 2004; Xu et al. 2018). In addition, the ratio of σ_1/σ_c increases from approximately 56% to approximately 90% when the loading type changes from static compression to dynamic compression. This is because the fracture toughness of resin is rate-dependent, which often presents a higher value under dynamic loading conditions (Jajam et al. 2013). Moreover, the failure mode of the flawed specimens appears to be unaffected by the flaw number, because the final failure pattern of the specimen with single pre-existing flaw is similar to that of the specimen with double pre-existing flaws under static compression, except the sample with α of 0° and 90° , as shown in Fig. 4.19.

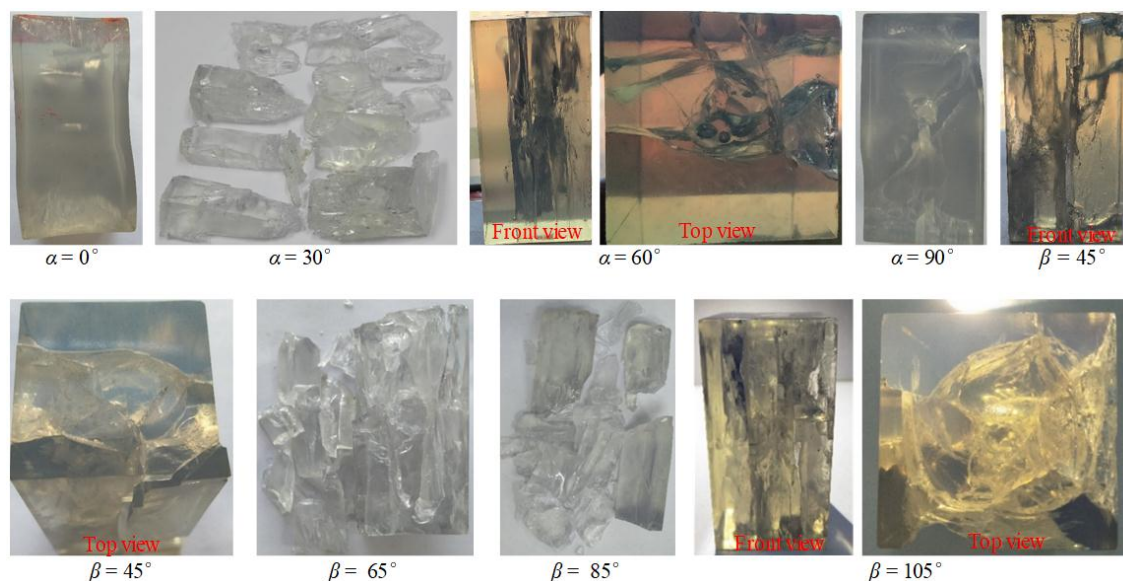


Figure 4.19 Fragments of the specimens after static compression tests

In this chapter, the 3DP resin mechanical behaviors are dependent on the loading conditions, e.g., the dynamic compressive strength and tangential modulus increase with increasing strain rate. The effects of the strain rate on the 3DP resin mechanical properties are believed to be correlated to secondary molecular processes, which means that an increasing strain rate decreases the molecular mobility of the polymer chains stiffening

the chains (Richeton et al. 2006). This mechanism is similar to the temperature effect on the compressive strength of polymers, where the very low environmental temperature strongly constrains the movement of polymer chains and yielding a higher compressive strength of polymers with temperatures below the glass transition temperature (Zhou and Zhu 2018).

In addition to the fast-propagated wing and secondary cracks, a type of slowly generated crack was also found in this work. During the late loading stage, oblique cracks were generated at the tips of pre-existing 3D flaws with α of 30° , and the cracks extended slowly toward the specimen boundary at a speed of approximately 0.7 mm/s (Fig. 4.20a). These cracks are similar to the en echelon cracks formed at the shear zones developed from 2D flaw tips in PMMA specimens, as shown in Fig. 4.20b (Petit and Barquins 1988). The formation of oblique cracks may be more or less associated with plastic deformation at the flaw tips, as shown in Fig. 4.20c (Petit and Barquins 1988), because the present test was performed at room temperature, which may induce plastic deformation at the compressed points, i.e., flaw tips, under high stress/strain levels.

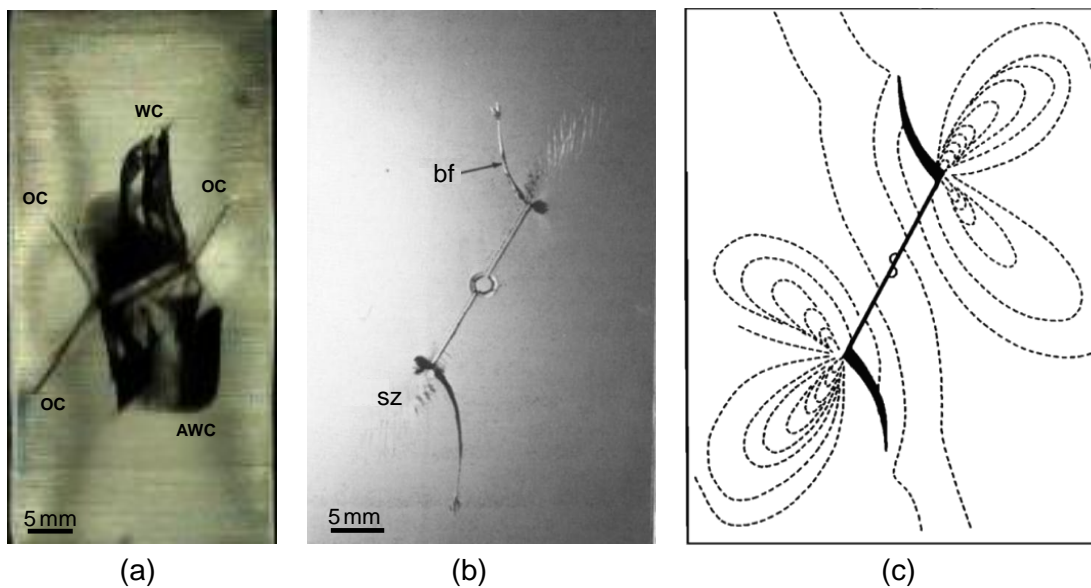


Figure 4.20 Comparison of oblique cracks generated at the tips of 3D and 2D flaws. (a) Oblique cracks generated in 3DP resin specimen with a 3D internal flaw; (b) Shear cracks generated at the tips of the PMMA plate with a 2D throughout flaw (Petit and Barquins 1988); (c) Stress concentration shown by distribution of isochromes (lines of equal value of maximum shearing stress) from photograph taken after branch fracture generation in (b). bf and sz refer to branch fracture and shear zone, respectively.

Although the 3DP resin specimens have been proven to be suitable for investigating 3D crack growth behaviors, an unexpected result was found in the present study. For samples with α equal to 0° and 90° , there were no macrocracks (e.g., wing and secondary cracks) generated at the pre-existing flaw tips during the entire loading process. Instead, oblique cracks were formed at the flaw tips during the late loading stages. Moreover, these two samples developed large plastic deformation and tilted toward one side in the postpeak region (Fig. 4.21). Nemat-Nasser and Horii (1982) theoretically and numerically proved that the mode I SIF at the flaw tip nearly vanished when the normal direction of the 2D pre-existing flaw was nearly parallel or perpendicular to the maximum compression. In addition, to further analyze the stress distributions around the flaw tips under uniaxial compression, 3D numerical modeling was conducted using the FEM based commercial software ANSYS. The dimension of the numerical model is identical to the 3DP sample in laboratory. The mechanical properties of the numerical model are the same as those of the intact 3DP sample whose uniaxial compressive strength, density, Young's modulus and Poisson's ratio are 113.8 MPa, 1200 kg/m³, 3.5 GPa and 0.4, respectively. A four-node linear tetrahedral element was utilized for the numerical model and only the minimal principal stress (maximum tensile stress) was analyzed. The compression was applied at the top of the model while the bottom of the sample was set as a fix boundary. 3D FEM numerical modeling shows that the minimum principal stresses (maximum tensile stress) at the flaw tips with α equal to 0° and 90° are much lower than those at the flaw tips with α equal to 30° and 60° , as shown in Figs. 4.22b and c. Therefore, it is believed that the low SIFs or tensile stresses at the pre-existing flaw tips with α equal to 0° and 90° impede the growth of the wing cracks under compression.

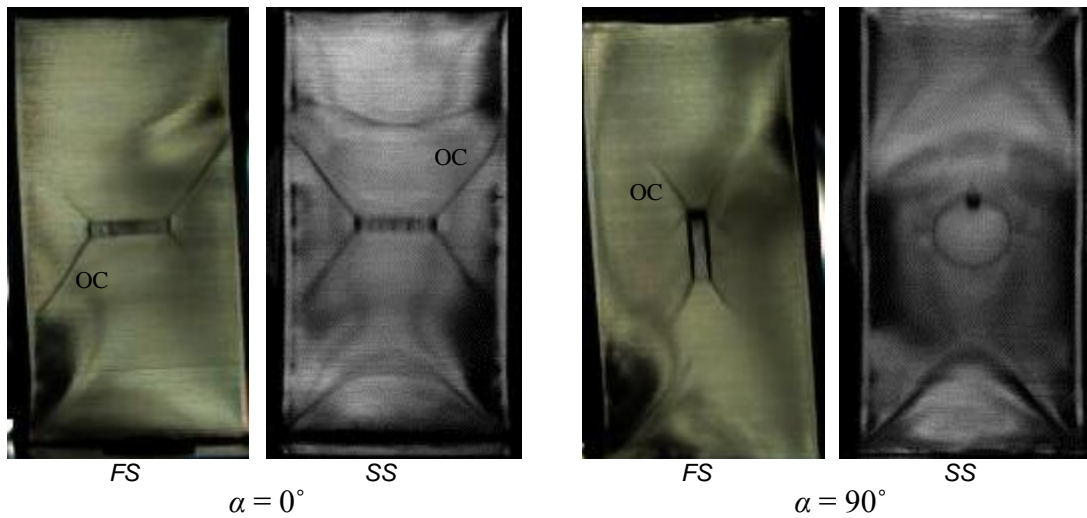


Figure 4.21 Failure patterns of single-flawed specimens with $\alpha =$ (a) 0° and (b) 90°

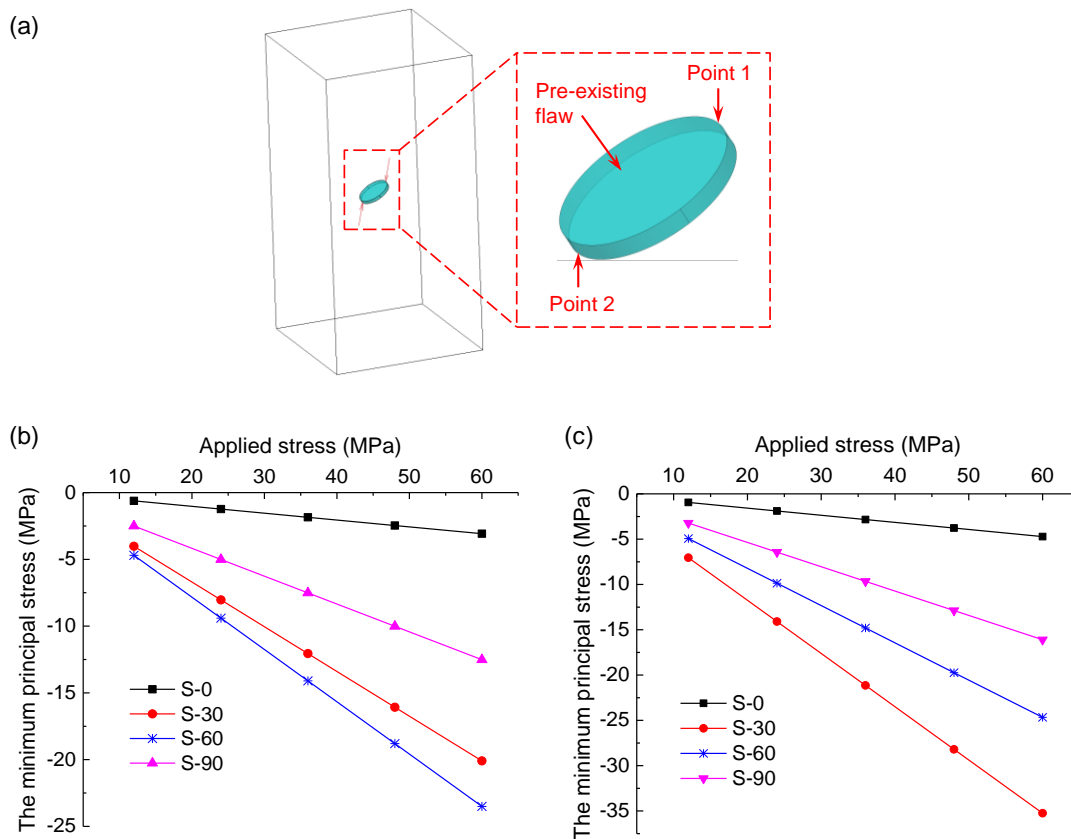


Figure 4.22 The minimum principal stresses at flaw tips in 3D FEM modeling. (a) Sketch of a FEM model with single internal flaw and two key points at the flaw tips where wing cracks initiate in physical test; (b) and (c) The minimum principal stress at point 1 (upper right corner of the flaw) and point 2 (lower left corner of the flaw) of the flawed-samples with α equal to 0° , 30° , 60° and 90° under different applied stresses. Note that in FEM modeling compressive stress is positive and tensile stress is negative.

4.5 Conclusions

In this chapter, static and dynamic compression tests were performed on 3D printed artificial rock samples containing single and double internal 3D flaws, with the aim to study the effects of flaw geometry and loading types on mechanical and 3D crack growth behaviors. The main conclusions of this chapter are summarized as follows.

- (1) The SLA 3DP technique can be used to rapidly, repeatedly and precisely produce resin-based artificial rock samples with 3D internal flaws. These flawed 3DP resin samples are suitable for studying 3D crack growth problems.
- (2) The flaw geometry affects the mechanical properties of the resin samples. The single flawed sample whose $\alpha = 60^\circ$ has the lowest σ_c and ε_a . σ_c and ε_a of the double flawed samples generally increase with β . σ_1 , σ_c and ε_a of the sample decrease when the number of flaws changes from one to two.
- (3) β affects the crack coalescence between the inner tips of the double pre-existing flaws. Wing cracks generated at the inner tips of the pre-existing flaws cannot coalesce with each other, except for β of 105° . Flaw angle, ligament angle and flaw number have nearly no influence on crack propagation and the final failure mode of the flawed samples.
- (4) The loading type affects the mechanical properties of specimens with 3D internal flaws. From static loading to dynamic loading, σ_c increases by approximately 8%, and the maximum axial strain corresponding to the peak stress decreases by 51.2% and 27.2% for 3DP resin specimens with single and double pre-existing 3D internal flaws, respectively. The Young's modulus, σ_1 and σ_1/σ_c increase when the loading type changes from static compression to dynamic compression.
- (5) The major differences between 3D crack growth under dynamic and static compressions are the propagation features of the wing cracks and the sample failure mode. Under dynamic compression, wing cracks can continuously extend toward the sample ends, resulting in a splitting failure of the sample, while under static compression, wing cracks and anti-wing cracks can only intermittently propagate approximately 1-1.5 times the initial flaw length, and the final, burst-like failure results from the secondary cracks. In addition, anti-wing cracks are not observed under dynamic compression.

- (6) Under static loading, the maximum secondary crack propagation velocity in single flawed specimens is higher than that in the double flawed specimens. The crack propagation velocity is more stable under dynamic loading, and the maximum crack propagation velocity in SHPB tests is lower than the propagation velocity in static compression tests.

In this chapter, preparation of rock-like sample with regular 3D internal flaws and study of 3D crack growth behaviors are conducted. However, existence of irregular internal flaws in rocks is more general but more significant due to the real situation. Therefore, replication of internal defects and investigation of the mechanical and fracture behavior of rocks using 3DP are needed and will be conducted in Chapter 5.

CHAPTER 5 REPLICATION OF INTERNAL DEFECTS AND INVESTIGATION OF MECHANICAL AND FRACTURE BEHAVIOR OF ROCK USING 3DP AND MICRO-CT

This Chapter focuses on using 3DP, in combination with X-ray micro-CT, to replicate internal defects and study the mechanical and fracture behaviors of rock. Natural volcanic rock specimens are replicated using SLA 3DP (identified in Chapter 3) and X-ray micro-CT. Comparative compressive and Brazilian disc experiments are conducted on both 3DP artificial rocks and prototype volcanic rock samples to validate the applicability and efficiency of the proposed method. The pros and cons of the proposed method are discussed. Finally, the potential means to facilitate the application of 3DP in studying rock failure are suggested.

5.1 Introduction

Apart from the regular flaws stated in Chapter 4, there are also numerous irregular defects ranging from grain boundaries to microcracks inside the rock masses. Previous studies reveal that rock failure under external loading is greatly affected by these pre-existing defects and is usually preceded by the development of new microcracks and the formation, growth, and coalescence of pre-existing cracks (Peng and Johnson 1972; Sayers and Kachanov 1995; Zhu et al. 2018). Therefore, understanding the mechanical and fracture behaviors of rocks affected by pre-existing defects, especially microcracks, is important for the design and stability assessment of structures built on or in rock.

Laboratory experiment, as a fundamental and effective method, has been widely used to investigate the failure mechanism of rocks under various conditions (Liu et al. 2004). Till now, many advanced techniques such as scanning electron microscopy (SEM) (Baud et al. 2004; Brooks et al. 2013), AE detection (Lockner et al. 1991; Townend et al. 2008) and X-ray micro-CT (Kawakata et al. 1999; Yang et al. 2015) have been adopted to study the progressive failure process of rock. These advanced techniques do offer means to observe and study rock fracture behavior. However, the failure mechanism of rock, particularly the spatial evolution of micro-cracks in real time, is still difficult to clearly reveal with those advanced techniques. It is because they could not accurately and real-timely monitor and capture micro-cracks development inside rocks attributed to

their inherent drawbacks, e.g., the destruction of rock samples for the SEM, the relatively low accuracy of AE source location for the AE, and the difficulty in detecting micro-cracks under dynamic loading for the X-ray CT (Liu et al. 2004; Zhao et al. 2014). Thereby, developing and exploring more effective techniques or methods that can be utilized to conveniently fabricate rock or rock-like specimens with its internal defects identical to that of the natural rocks and to investigate damage evolution inside rock samples in real-time are appealing.

In this chapter, 3DP, in combination with X-ray micro-CT, is proposed to replicate the internal defects of natural rocks. First, natural volcanic rock specimens are replicated using the SLA 3DP and X-ray micro-CT techniques. Then, comparative experimental tests, i.e., uniaxial compression and indirect Brazilian disc tests under static and dynamic loading conditions, are conducted on both 3DP rock samples and prototype rock specimens to validate the applicability and efficiency of the proposed 3DP methods. Subsequently, the pros and cons of this method is compared and discussed. Finally, the potential means to facilitate the application of 3DP in studying rock failure are suggested.

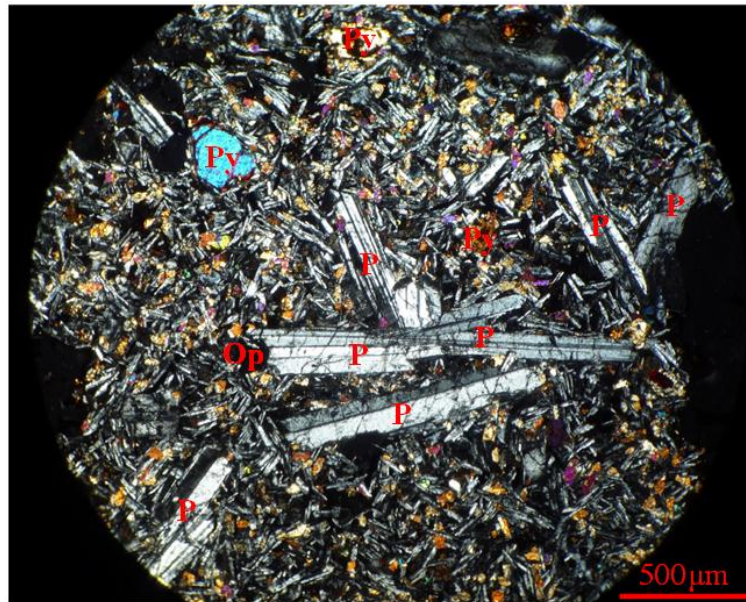
5.2 Experimental setup

5.2.1 Rock sample preparation

In this Chapter, Hainan volcanic rock (Basalt), collected from the Crater Park in Haikou, China, is chosen as the prototype natural rock. It is an igneous rock with a porosity of 7.2%, which was measured by the water saturation method in according with the ISRM suggested method (Franklin 1979). Optical microscopy analysis (Fig. 5.1) shows that the main mineralogical constituents are plagioclase, pyroxene and opaque mineral, with volume percentages of 58.5%, 35.4% and 6.2%, respectively. Their grain sizes are between 0.1-1.3, 0.1-0.9 and 0.1-0.2 mm, respectively.

During fabrication, rock cores with a diameter of approximately 49 mm were firstly drilled from a large volcanic rock block, which were then cut into standard rock samples. According to the International Society for Rock Mechanics Suggested Methods (Fairhurst and Hudson 1999; Zhou et al. 2012), the ratio of length to diameter of specimen for the indirect Brazilian disc tests is 0.5:1, and the ratios for static and dynamic compression tests are 2:1 and 1:1, respectively. All the specimens were ground and

polished to have a surface roughness smaller than 0.02 mm.



P: Plagioclase, P: Pyroxene, Op: Opaque mineral

Figure 5.1 Micrograph of the volcanic rock using optical microscope

5.2.2 X-ray micro-CT scanning of rock samples

In nature, rock contains numerous pre-existing micro-defects such as fissures, voids and inclusions. The existence of these micro-defects significantly affects the mechanical and fracture properties of rocks (Peng and Johnson 1972). Thereby, to effectively study the deformation and failure behaviors of rocks, the pre-existing defects shall be duplicated in the replicated rock samples and the 3D numerical models. To fulfill this requirement, an X-ray Micro-CT XRM 500 scanner was used to precisely image and map the surface and internal defects of the volcanic rock specimens. The scanner has a 160 kV X-ray light source with an exposure time of 18 s. The maximum scanning range is 100×100 mm, and the corresponding pixel of its charge coupled device is 2000×2000 .

Figure 5.2a presents the general principle of X-ray micro-CT scanning, in which an X-ray source generates a cone-shaped X-ray beam. After penetrating rock sample, the X-ray signal is attenuated and absorbed due to the density and composition variation through the section. By rotating the specimen incrementally to 360° , the X-ray projection data in different orientations can be obtained by the detector. They are then used to back-calculate the attenuation coefficients of the materials, which can be utilized to

represent the spatial locations of different components of the material (Ketcham et al. 2001; Wang et al. 2003; Yang et al. 2015). Figure 5.2b shows a 2D micro-CT image of a volcanic rock sample, in which the black color represents cracks and voids while the white and grey colors represent mineral grains.

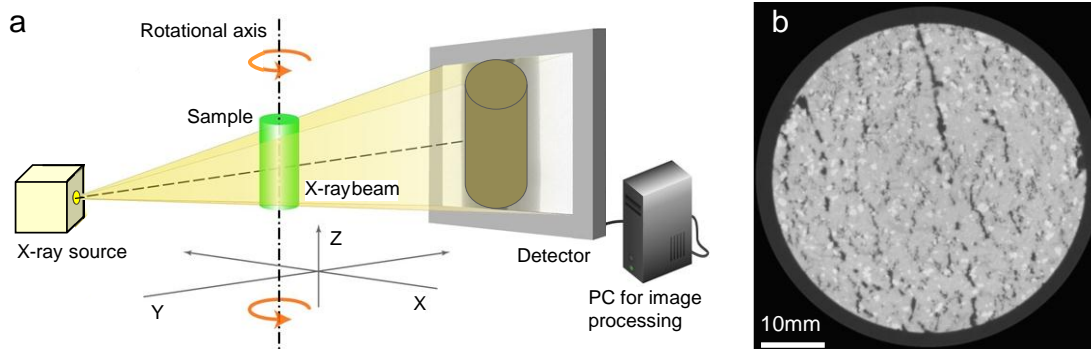


Figure 5.2 (a) Principle of X-ray micro-CT scanning; (b) 2D micro-CT image of a volcanic rock sample with a spatial resolution of 50 μm , where the black color within the circle represents cracks and voids, while the white and grey colors represent mineral grains.

5.2.3 Reproduction of natural rocks using 3DP

For replication of natural rocks using 3DP, a key process is to prepare 3D digital rock core via 3D reconstruction technique. In this chapter, the Materialise Mimics software program (MM 16.0) is applied to create 3D digital rock core from the 2D X-ray micro-CT images. During 3D reconstruction, the 2D micro-CT images are first consecutively stacked to reconstruct the 3D micro-CT data of the rock sample. Then thresholding segmentation is implemented within the MM 16.0 to automatically distinguish and extract the defects from the rock matrix. Note that an optimum threshold grey value should be selected when performing thresholding segmentation, because it guarantees the quality of the 3D digital rock core. In this Chapter, by trial and error, the threshold grey value is set as 28,500. Notably, the range of the grey values of the micro-CT image is between 8600 and 57788.

The 3DP material *accura*® 60 identified in Chapter 3 is utilized to replicate natural volcanic rock samples. It is a photosensitive material that can be solidified by ultraviolet irradiation. The density of the cured 3DP resin is 1.2 g/cm^3 . The specific component of

the accura® 60 is unavailable from the manufacturer.

The SLA-based Viper si² is adopted to fabricate manmade resin-based 3DP rocks through reproducing the natural rock specimens. The printer has a maximum build envelope of 250 × 250 × 250 mm (XYZ-directions), and its theoretical resolution in vertical can be up to 2.5 μm. Nevertheless, to balance the printing time with the printing resolution, the vertical resolution (layer thickness) is set at 50 μm, which means that the resolution of the 3D printing in vertical direction is exactly the same as that of the micro-CT layer spacing. The wavelength of the laser is 354.7 nm. During printing, a computer-controlled ultraviolet laser beam illuminates and solidifies the liquid photopolymer resin layer by layer according to the printing settings until the object is ready (Zhou and Zhu 2016). The advantages of the SLA-based Viper si² include smooth surface finishing, excellent optical clarity, high accuracy and excellent fine feature detail that require minimal finishing.

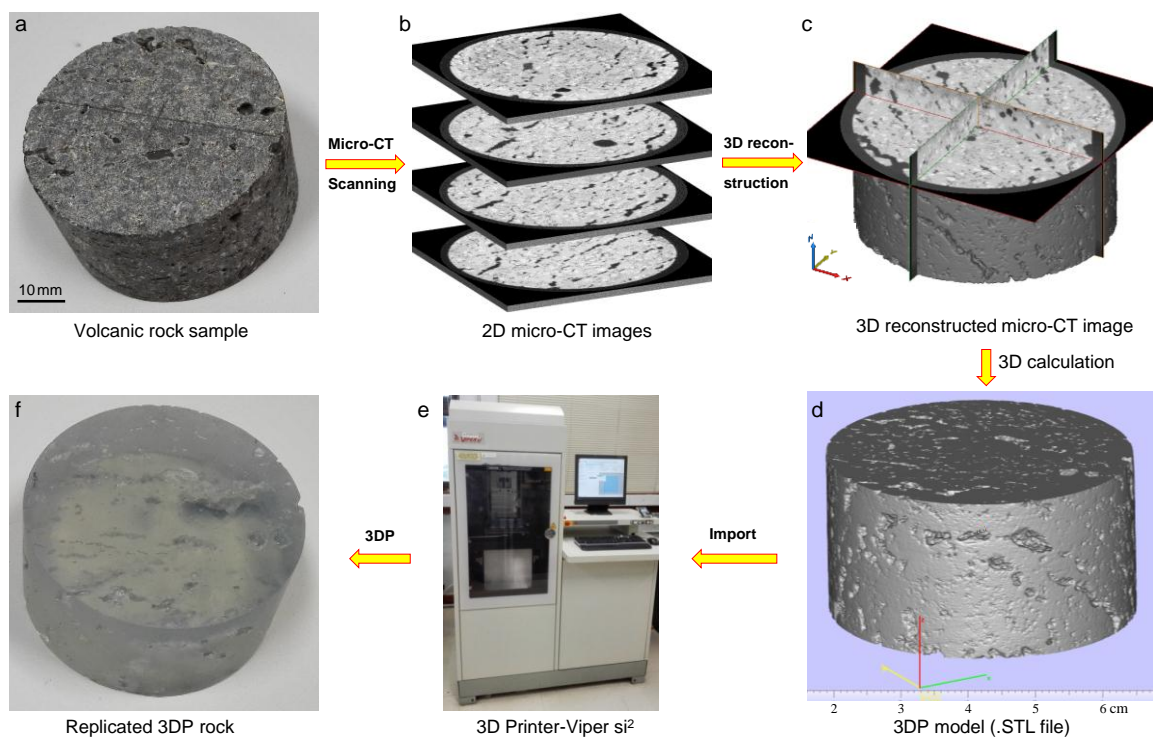


Figure 5.3 Workflow of replicating natural volcanic rock sample. (a) Natural volcanic rock sample. (b) 2D micro-CT images with resolution of 50 μm. (c) 3D reconstructed micro-CT image. (d) STL formatted 3DP model generated using MM 16.0 software program. (e) Reproducing volcanic rocks using the Viper si² system. (f) Post-processing of the replicated rocks

Figure 5.3 demonstrates the workflow of preparing resin-based 3DP rock, which mainly consists of five procedures. First, to obtain a consecutive 2D micro-CT images through scanning the volcanic rock sample horizontally plane by plane using the X-ray Micro-CT XRM 500 scanner. Second, to reconstruct 3D CT data of the volcanic rock sample from the 2D micro-CT images using the MM 16.0 software program. Third, to implement 3D calculation using the MM 16.0 software program to obtain a STL formatted file that can be read and executed by the 3D system Viper si². Fourth, to reproduce the volcanic rock samples using the Viper si² system. Lastly, to post-process the reproduced samples such as transparentizing the specimens through grinding and polishing procedures. Note that the reproduced specimen is solidified by ultraviolet irradiation except the micro- and macro-defects, in which the liquid resin is not drained.

5.2.4 Testing apparatus

Uniaxial compression tests and the indirect Brazilian disc tests under static loading conditions are conducted on both the natural volcanic rock samples and resin-based 3DP rock specimens. The TAW-2000 electro-hydraulic servo controlled testing system described in Chapter 4 is utilized to perform the unconfined uniaxial compression and the indirect Brazilian disc tests at a loading rate of 2 mm/min. The extensometers are used to record the axial and lateral deformation during compression tests, while the strain gauges attached on specimens are utilized to electronically measure tensile strain during Brazilian disc tests.

Dynamic compression and Brazilian disc tests are performed using the same SHPB system that has been described in Chapter 4 in detail. Once the dynamic stress equilibrium in the sample is achieved, based on the one-dimensional stress wave theory, the dynamic compressive stress $\sigma(t)$ can be calculated using Eq. (2.1), and the dynamic tensile stress $\sigma_T(t)$ of the specimen can be derived as (Zhou et al. 2012):

$$\sigma_T(t) = \frac{2P}{\pi DT} \quad (5.1)$$

where P is the force (kN) of the transmitted wave; D and T are the diameter and thickness of the Brazilian disc specimen (mm), respectively.

A high-speed camera (HSC) Photron FASTCAM SA1.1 is applied to monitor and record

the failure evolution process of the specimens in static Brazilian disc tests and dynamic tests. The frame rate was 100,000 frames per second with resolution of 192×192 pixels. Under dynamic loading, the HSC is triggered by a TTL pulse generated from the oscilloscope synchronously with the incident signal. In static Brazilian disc tests, the HSC is manually triggered upon the generation of new cracks immediately after the peak force.

5.3 Results

5.3.1 Static uniaxial compression tests

Results of static uniaxial compression test on the resin-based 3DP rock and its prototype volcanic rock are shown in Table 5.1 and Fig. 5.4. It can be seen that the uniaxial compressive strength (UCS) (82.2 MPa) and the Poisson's ratio (0.33) of the resin-based 3DP rock agreed well with those of the prototype volcanic rock (81.3 MPa for UCS and 0.28 for the Poisson's ratio). The shape of the stress-strain curve, particularly the significant drop of stress after the peak stress, of the resin-based 3DP rock is comparable to that of the prototype volcanic rock. The failure pattern of the resin-based 3DP rock before the final burst-like failure is to some extent similar to that of the prototype volcanic rock (Figs. 5.4b, c). However, the strain at peak stress of the resin-based 3DP rock is approximately ten times higher than that of the natural one.

Table 5.1 Mechanical properties of the volcanic rock and resin-based 3DP rock in static compression tests

Sample	σ_c (MPa)	ε_A (%)	ε_L (%)	E (GPa)	ν	V_P (m/s)
Volcanic rock	81.32	0.23	-0.11	40.1	0.28	4857.8
Resin-based 3DP rock	82.21	2.63	-1.36	3.5	0.33	2368.5

Mechanical parameters σ_c , ε_A , ε_L , E and ν are static uniaxial compressive strength, axial strain, lateral strain, the Young's modulus and Poisson's ratio. V_P is P-wave velocity.

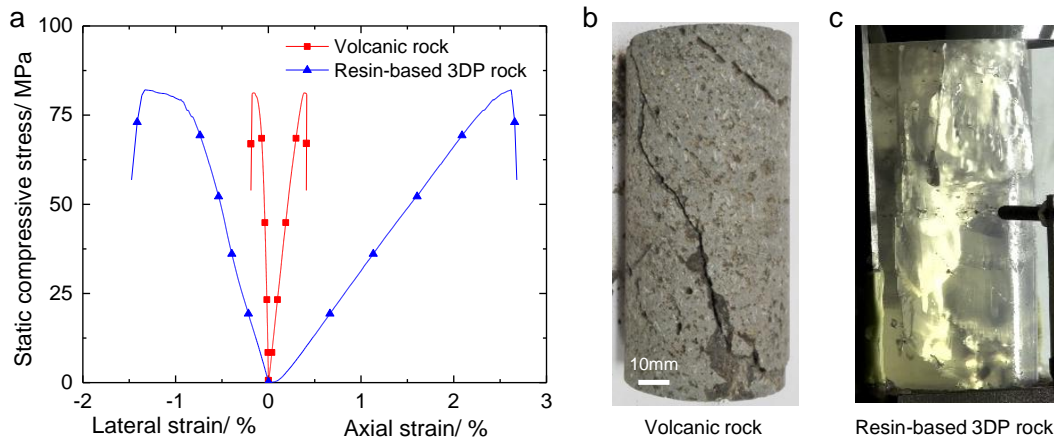


Figure 5.4 Stress-strain curves and failure patterns in static uniaxial compression tests. (a) Stress-strain curves of the natural volcanic rock and resin-based 3DP rock. (b-c) Failure patterns of volcanic rock and resin-based 3DP rock after compression tests

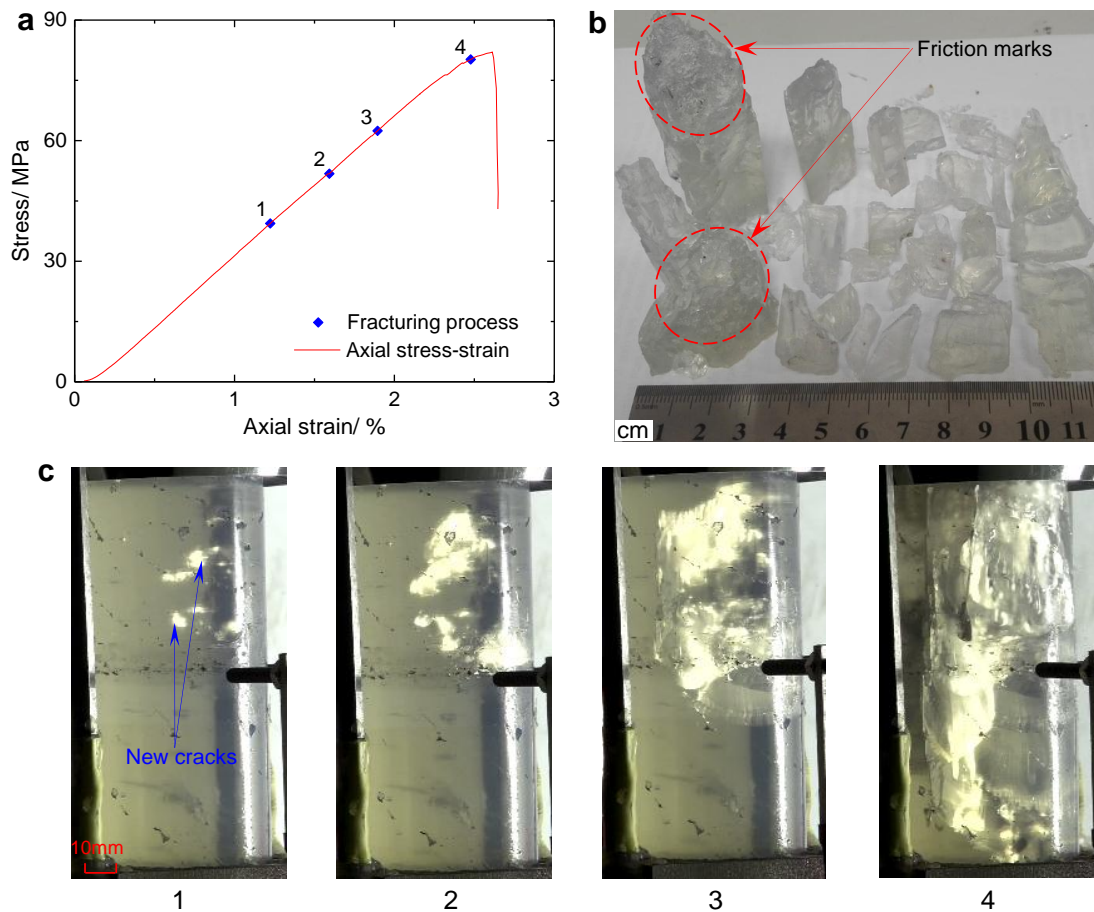


Figure 5.5 Progressive fracturing process of resin-based 3DP rock in static compression test. (a) Axial stress-strain curve. (b) Fragments after compression test. (c) Progressive fracturing images. The numbers on the stress-strain curve and below the sample images represent the observed fracturing sequences at different loading levels

In addition, we detected progressive fracturing within the resin-based 3DP rock during uniaxial compression test, attributed to the transparency of the 3DP resin (Fig. 5.5). It is found that new cracks initiated at the pre-existing defects when the resin-based 3DP sample was loaded to approximately 50% of UCS. With increase of the stress, new cracks propagated and coalesced into a failure plane approximately parallel to the axial direction, and finally led to the burst-like failure of the sample. Analysis of the fragments indicates that the failure mode of the resin-based 3DP sample is a tensile-shear mixed one, as some fragment surfaces presented friction marks (see Fig. 5.5c).

5.3.2 Static Brazilian disc tests

Tensile stress-strain behaviors of resin-based 3DP rock and its prototype volcanic rock derived from static Brazilian disc tests is shown in Fig. 5.6, in which the tensile strain was measured by the strain gauge attached on the back surface of the sample (see Fig. 5.7). As shown in Fig. 5.6, the tensile strength of the resin-based 3DP rock (9.6 MPa) is comparable to that of the prototype rock (7.1 MPa), while its tensile strain at peak stress (0.38%) is approximately triple of that of the prototype volcanic rock (0.13%). In Brazilian disc test, the strain discrepancy between the 3DP rock and its prototype natural one is significantly reduced compared with that in compression test. In addition, the tensile stress-strain behaviors of the 3DP sample and the prototype volcanic rock are almost identical. To be specific, both tensile stress-strain curves are concave downward and nonlinear in the early loading stage, while they exhibit almost linear behavior prior to the sharp drop of stress.

The high-speed photography images in Fig. 5.7 demonstrate the fracturing process of the resin-based 3DP rock and its prototype volcanic rock in static Brazilian disc tests. In general, the fracturing process and failure pattern of the resin-based 3DP sample agreed well with those of the prototype volcanic rock specimen. For instance, new cracks generated approximately 5 mm away from the top loading point, then propagated along the loading plane, and finally split the sample into two halves. However, it is found that the fracturing velocity of resin-based 3DP rock is slightly slower than that of the prototype volcanic rock specimen (see crack tips in Fig. 5.7).

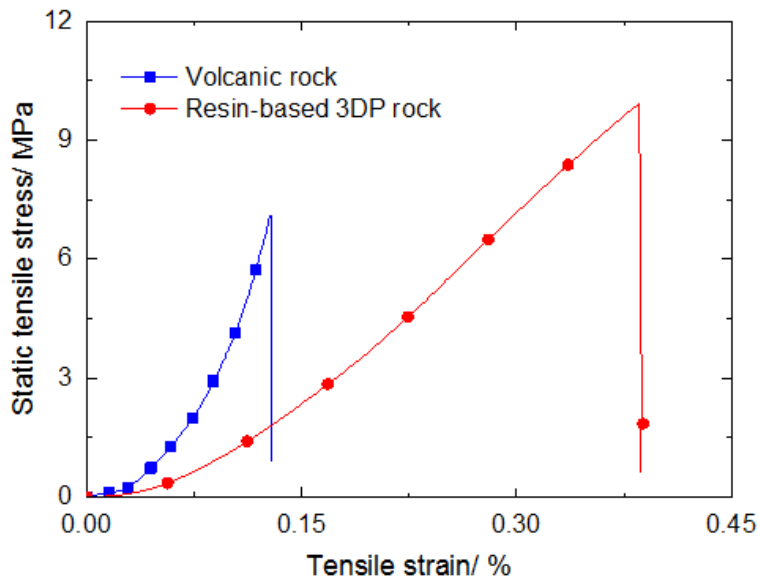


Figure 5.6 Tensile stress-strain curves of volcanic rock and resin-based 3DP rock from static Brazilian disc tests

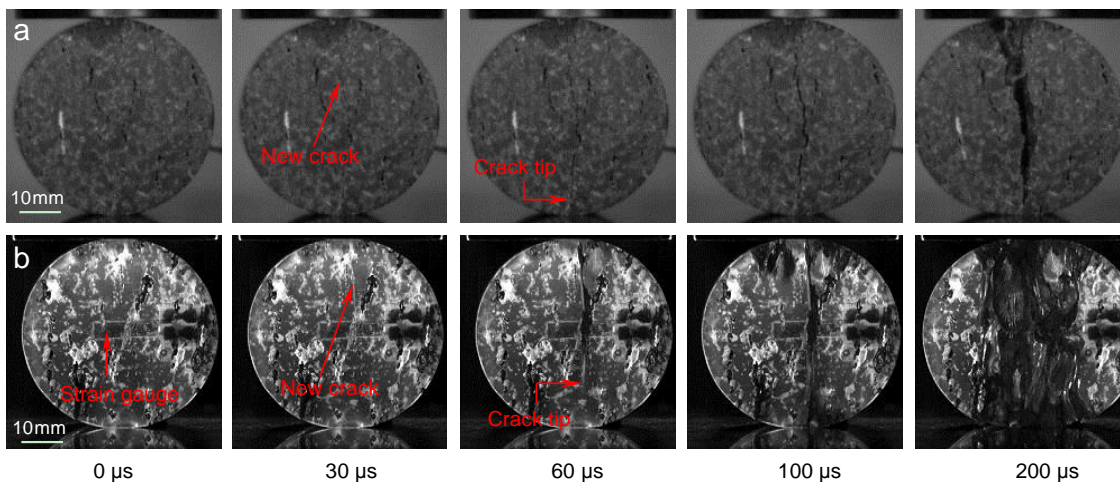


Figure 5.7 Fracturing process in static Brazilian disc tests. (a-b) Fracturing process of natural volcanic rock and resin-based 3DP rock sample, respectively. The time below the high-speed images indicates the relative time recorded since the onset of new cracks

5.3.3 Dynamic uniaxial compression tests

Achieving dynamic stress equilibrium at both ends of the sample guarantees the effectiveness of dynamics tests (Zhou et al. 2010). Therefore, examining stress equilibrium is essential when processing dynamic testing data. Figure 5.8 presents the dynamic stress equilibrium in the volcanic rock sample and resin-based 3DP rock sample

in SHPB tests. The results show that stresses applied on the incident and transmitted interfaces of both manmade 3DP and natural rock specimens are approximately equal in the vicinity of the peak stress. It indicates that the stress equilibrium in the present tests can be achieved and the validity of the SHPB tests is thus proved. Note that the natural rock and 3DP specimens took approximately 50 μs before achieving stress equilibrium. This is because hard samples such as brittle rock and ceramics usually require three to four round-trips for the stress wave inside the sample to reach dynamic stress equilibrium (Song and Chen 2004a).

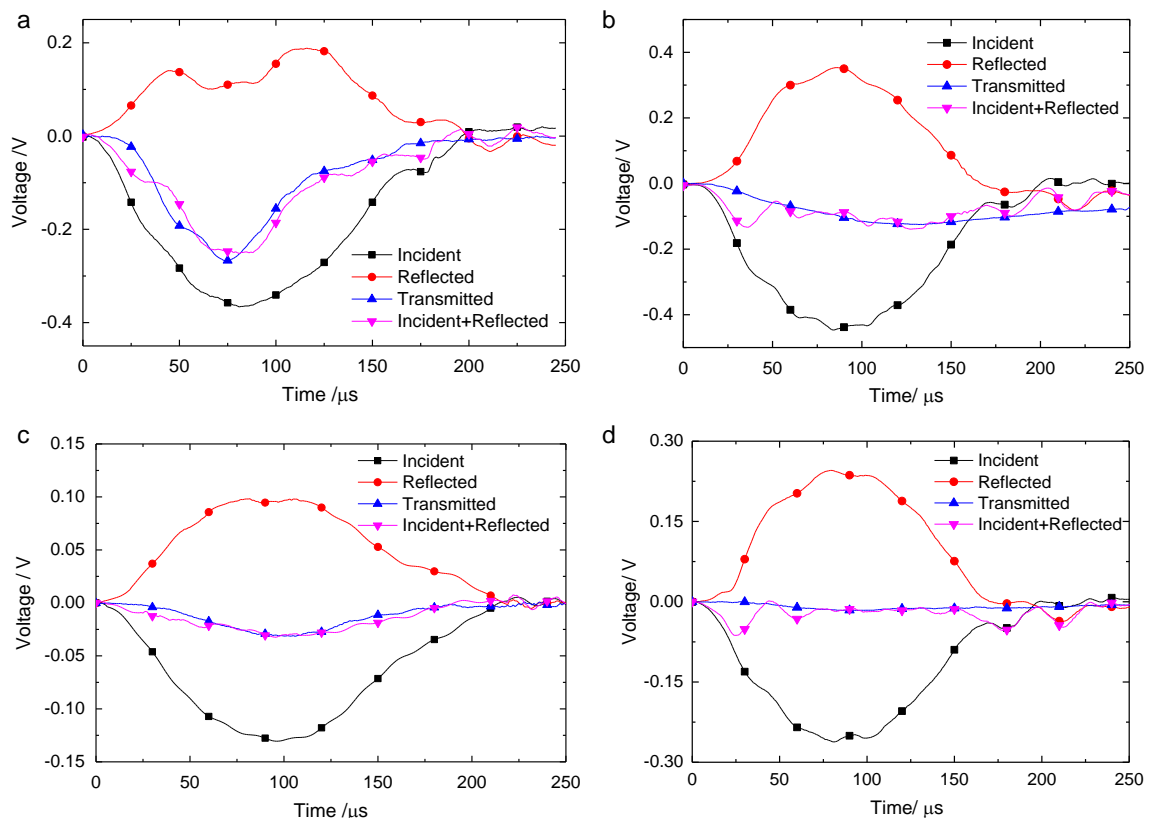


Figure 5.8 Stress equilibrium in dynamic compression and Brazilian disc tests. (a-b) Volcanic rock sample and 3DP rock sample in dynamic compression tests. (c-d) Volcanic rock sample and 3DP rock sample in dynamic Brazilian disc tests

Figure 5.9 shows the results of the volcanic rock and the corresponding resin-based 3DP rock in dynamic uniaxial compression tests. It can be seen that although the post-peak dynamic stress evolution in the resin-based 3DP rock is postponed, the dynamic UCS (165.6 MPa) and the pre-peak stress-time behaviour agreed well with those of the prototype volcanic rock sample (173.1 MPa for dynamic UCS). The high-speed photography images in Fig. 5.9b demonstrate that the dynamic fracturing process and

failure pattern of the resin-based 3DP rock are to some extent similar to those of the prototype volcanic rock, i.e., new cracks firstly generated at the dispersed pre-existing micro-defects, then interacted and coalesced as the load increased. Similarly, due to the transparency of the 3DP resin, progressive fracturing within the resin-based 3DP rock under dynamic loading was also detected. New cracks initiated and propagated within resin-based 3DP rock, eventually leading to catastrophic failure of the sample (Fig. 5.9b).

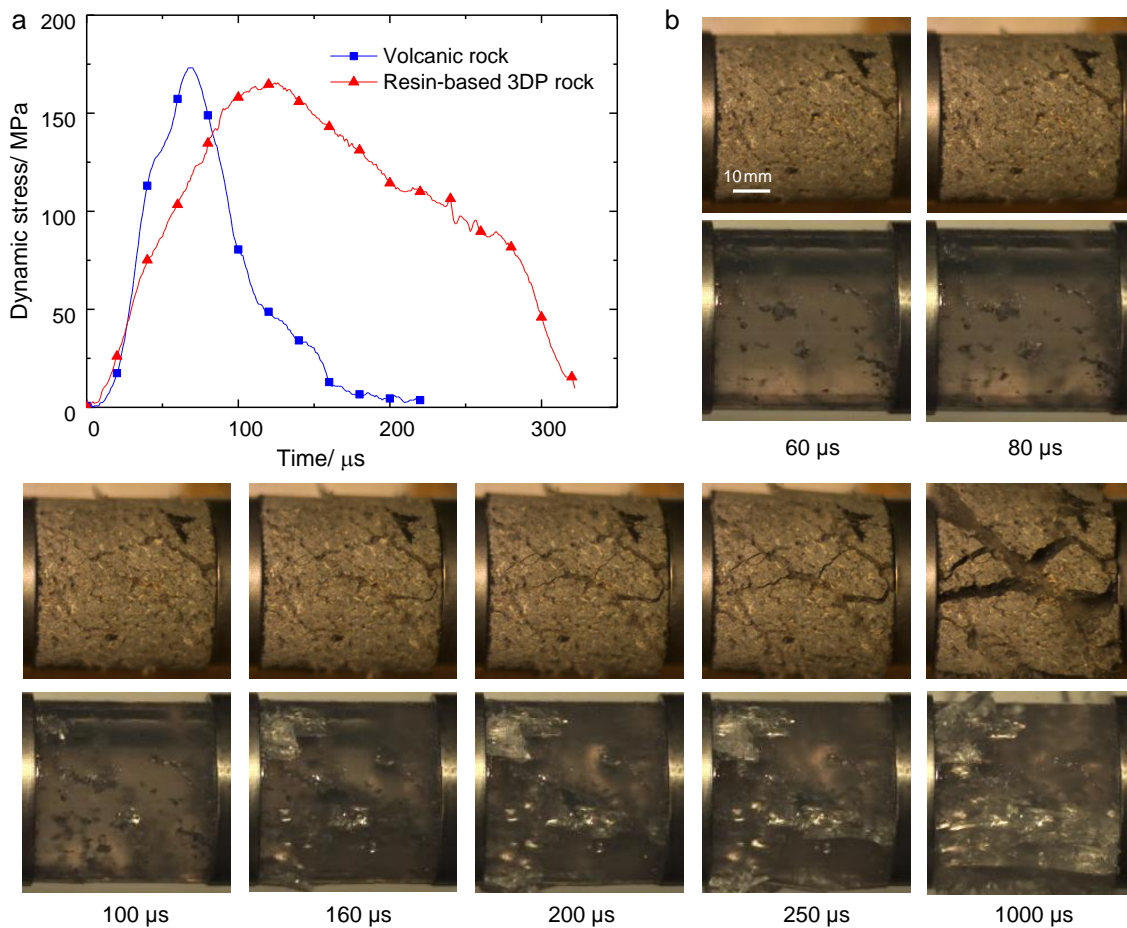


Figure 5.9 Dynamic compression tests on volcanic rock and resin-based 3DP rock samples. (a) Compressive stress-time curves. (b) Dynamic fracturing processes. The upper and lower rows of high-speed photography pictures show the fracturing process of volcanic rock and 3DP rock, respectively. The time below the high-speed images indicates the absolute time recorded since the beginning of the dynamic loading

5.3.3.1 Dynamic Brazilian disc tests

Figures 5.8c and d show the stress equilibrium in dynamic Brazilian disc tests. It can be seen that the tensile stress equilibrium can be well achieved on the two opposite loading

surfaces of the specimens prior to the peak stress and this state can be maintained for a certain period in the post-peak region (approximately 50 μs).

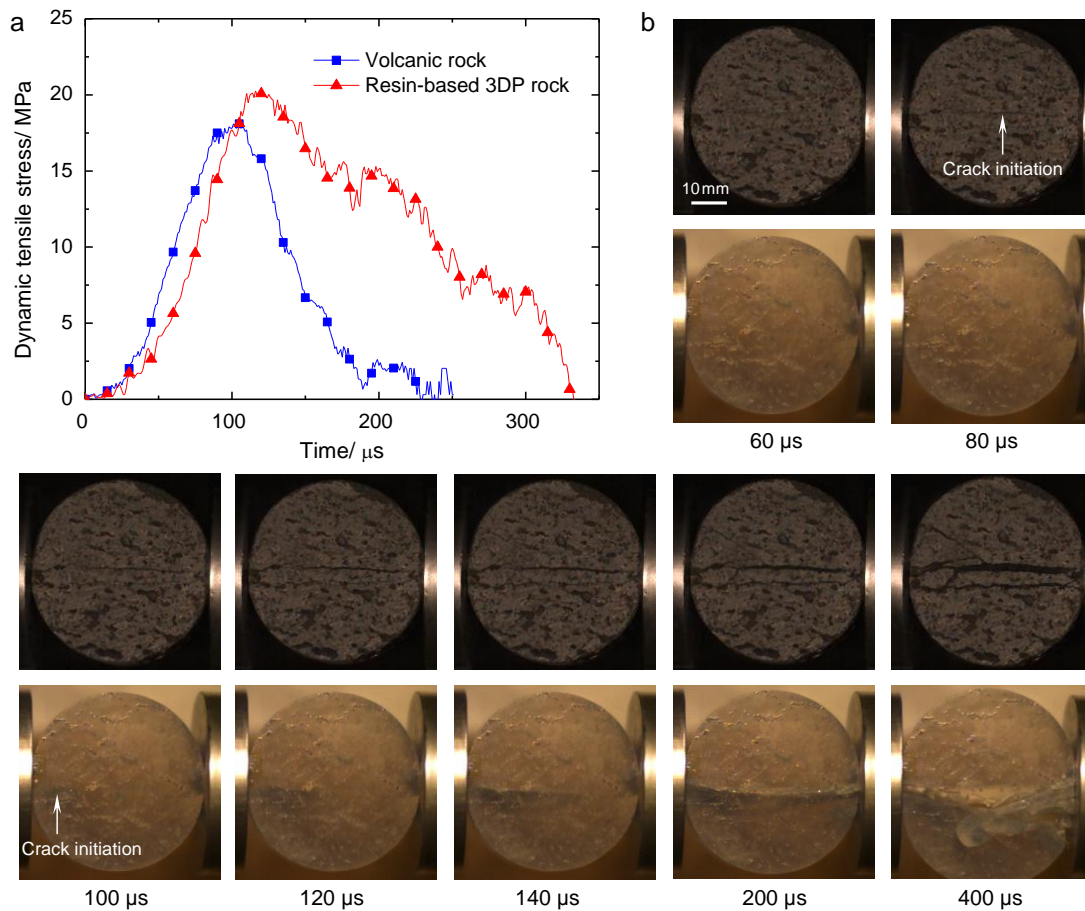


Figure 5.10 Dynamic Brazilian disc tests on volcanic rock and resin-based 3DP rock. (a) Tensile stress-time curves. (b) Dynamic fracturing processes. The upper and lower rows of high-speed photography pictures show the fracturing process of volcanic rock and 3DP rock, respectively. The time below the high-speed images indicates the absolute time recorded since the beginning of the dynamic loading

The results of the resin-based 3DP rock and its prototype volcanic rock in dynamic Brazilian disc tests are shown in Fig. 5.10. The dynamic tensile strength (20.3 MPa) and the pre-peak stress-time curve of the 3DP specimen are coincident with those of the prototype volcanic rock (18.5 MPa for dynamic tensile strength). In addition, although the post-peak tensile stress evolution of the 3DP sample is postponed, the magnitude of the delay is shortened, compared with in dynamic uniaxial compression test. Figure 5.10b presents the fracturing process of the volcanic rock and its corresponding resin-based 3DP sample in dynamic Brazilian disc tests. Despite the inconsistency of the crack initiation point (crack initiation point occurred around the center and loading point for the

prototype rock and 3DP rock, respectively), the fracturing process and failure mode of the two specimens in dynamic Brazilian disc tests are almost identical. Besides, under dynamic loading, it is found that the crack initiation time in resin-based 3DP rock is approximately 20 μs later than that in prototype volcanic rock (Fig. 5.10b).

5.4 Discussion

In this Chapter, studies on laboratory tests indicate that combined with X-ray micro-CT and 3D reconstruction techniques, SLA 3DP method can effectively replicate natural volcanic rock samples with defects. Meanwhile, some laboratory testing results of the resin-based 3DP rocks agreed well with those of the prototype rock samples. The strength difference between the resin-based 3DP rocks and the natural ones under static and dynamic loading (except for the static Brazilian disc test) is as small as approximately 10%. The fracturing behaviors of the 3DP rocks are similar to those of the prototype volcanic rocks, especially in the Brazilian disc tests (Figs. 5.7 and 5.10). In addition, the brittleness of the resin-based 3DP rock is good, i.e., the stress-strain curves exhibit nearly linear behavior prior to a sharp drop of stress (Figs. 5.4-6). The plastic deformation of the 3DP sample after the yield stress is almost negligible (Fig. 5.4).

Moreover, attributed to the transparency of the 3DP resin, progressive fracturing in resin-based 3DP rocks under static and dynamic loading was successfully detected (Figs. 5.5 and 5.9). Although the quality of the high-speed images of fracturing process is not good enough and only qualitative analysis of the internal crack propagation has been made in this chapter, it is believed that the transparent nature of the 3DP resin could compensate for the difficulty of traditional techniques, e.g., acoustic emission detection (Lockner et al. 1991) and X-ray CT scanning (Kawakata et al. 1999) in clear monitoring and analysis of the internal crack growth behaviors in real-time.

However, some unsatisfactory results from laboratory tests on resin-based 3DP rock samples were also found in this chapter. In static uniaxial compression test, the deformation of the resin-based 3DP rock is approximately ten times higher than that of the natural one. This is mainly due to the lower Young's modulus of the resin-based 3DP rock (3.5 GPa) compared with the prototype volcanic rock. It also explains why the onset of fracturing time of resin-based 3DP rock in SHPB tests is approximately 20 μs later than that in prototype volcanic rock (Fig. 5.10b). Compared with natural rock, the 3DP rock

experiences larger elastic deformation (approximately 2%) at the initial stage of loading, thereby delaying the fracturing process.

In static Brazilian disc test, the tensile strength of the 3DP rock (9.6 MPa) is found higher by about one-third than that of the prototype rock (7.1 MPa). This discrepancy may be attributed to three factors. First, the relatively low Young's modulus (3.5 GPa) of the 3DP resin results in a larger axial deformation which enlarges the contact areas between the sample and the platens of the compression machine. And a larger contact area causes an increase in the maximum loading force applied to the resin-based 3DP rock. This mechanism has been verified by both experimental study (Erarslan and Williams 2012; Wang et al. 2004) and numerical simulation (Wang et al. 2014). Second, the incomplete agreement of the diametrical planes in loading direction between the 3DP rock and the prototype volcanic rock samples may also cause difference in the test results. It is because a slight twist of the Brazilian disc sample may result in a remarkable change of the geometry, e.g., crack length, area and inclination angle, of the pre-existing defects within the diametrical plane in loading direction, which thereby could exert effects on the mechanical and fracture behaviors of the Brazilian disc samples. Third, the scale of micro-cracks that is less than 50 μm were not retained in the resin-based 3DP rock due to the limitation of printing resolution, which may also result in a relatively high strength of the printed specimen.

It should be noted that although the natural volcanic and resin-based 3DP samples contain many micro and macroscopic voids and fissures, to a large extent they did not undermine the elasticity assumption and validity of the physical Brazilian disc tests in the present study. First, the porosity of the volcanic rocks used in this chapter is 7.2% which is far lower than the threshold porosity of 15% proposed by Ju et al. (2013), where they reported that the geometrical and statistical characteristics of crack structures will significantly affect the split behaviors of the Brazilian disc samples with porosity higher than 15%. Second, most of the cracks and voids are 3D internal ones and none of the relatively large cracks are located in the diametrical plane, i.e., the loading direction, as shown in Fig. 5.16. According to Wang et al. (2014) and Van de Steen et al. (2005), when the pre-existing voids or pores are deviated a certain distance from the loading direction and their diameter over the disc is less than 8%, the effects of those pre-existing voids and pores on the mechanical and fracture behaviors of the Brazilian disc samples are

negligible. Third, the experimental results in the present study indicate that the natural volcanic rock and resin-based 3DP specimens exhibit good elastic-brittle properties, e.g., linear elastic behavior of tensile stress-strain curves prior to the peak stress and a steep drop of the stress after the peak point, as shown in Figs. 5.4 and 5.6. Fourth, the physical samples are split along the loading diametrical plane without intersecting the pre-existing relatively large voids.

Under dynamic loading, the relatively low longitudinal wave speed of the resin-based 3DP rock (2368.5 m/s) slows down propagation of the stress wave within the sample which results in later onset of fracturing in SHPB tests, compared with natural rocks (Fig. 5.10). The delay of the fracturing time can also interpret why the post-peak dynamic stress evolution in the resin-based 3DP rocks lasts longer than that in natural rocks in SHPB tests.

As mentioned above, the internal fracturing under compression is not well monitored and observed in the present laboratory tests on resin-based 3DP rock samples. This may be attributed to several factors, among which the curved and imperfect polishing surface as well as inappropriate lighting condition might be dominant. Therefore, prismatic 3DP samples with relatively small dimension are recommended in future tests, because the flat surface can not only improve the grinding and polishing accuracy but also improve the quality of the HSCs. In addition, other than one, two high-speed cameras are recommended to monitor the internal crack growth from the adjacent two surfaces, in order to observe and understand internal fracturing more clearly.

Although the advantages of the 3DP method in replication of internal defects and study of mechanical and fracture behaviors of natural rocks are evident as discussed in the aforementioned part, it has some limitations which needs to be solved and improved in future studies.

For instance, the Young's modulus of the 3DP resin is lower than that of the prototype natural rock. This results in different deformational behavior between resin-based 3DP rock samples and the natural ones. Defects in the 3DP artificial rock samples are not empty but filled with liquid resin material as described in Section 5.2.3, which may affect their mechanical and failure properties. Besides, the artificial rock was produced by only one 3DP material which is impossible to reflect the heterogeneity of the rock materials.

5.5 Conclusions

This Chapter reports replication of internal defects of natural rocks using the SLA 3DP method with the combination of X-ray micro-CT, and application of this method to investigate the mechanical and fracture properties of rocks under static and dynamic loading conditions. Main conclusions are as follows:

- (1) Combining with high resolution X-ray micro-CT and 3D reconstruction techniques, 3DP method can effectively replicate the pre-existing defects of natural rock specimens into resin-based 3DP rock samples, which can be further used to investigate the mechanical and fracture behaviors of natural rocks.
- (2) The compressive strength, dynamic tensile strength, the Poisson's ratio and the fracturing properties of the resin-based 3DP rocks agree well with those of the prototype natural rocks, which verifies the applicability of the resin-based 3DP rocks to study mechanical and fracture properties of brittle rocks such as volcanic rocks and porous rocks.
- (3) The transparent feature of the resin-based 3DP rocks enables us to compensate for the difficulty of conventional techniques such as acoustic emission and X-ray CT scanning in direct observation of the internal crack growth in real-time.

In Chapters 4 and 5, the crack growth behaviors of 3D internal micro- and macro-defects and its influences on the mechanical and fracture properties of resin-based artificial rocks are studied. However, in addition to the effects of pre-existing micro and macrocracks on the mechanical and fracture behavior of rocks, the presence of those defects will also significantly affect seismic behaviors of rocks (King et al. 1986). Therefore, it is worthwhile to study the effects of the pre-existing micro and macrodefects on wave propagation and attenuation in rocks. In Chapter 6, quantification of damage evolution and its effects on low-amplitude ultrasonic P-wave propagation in rock samples will be conducted. And study of the coupling effects of JMC, loading rate and water content of the infilling mixture on the mechanical and seismic properties of a single rough joint with stress wave propagation in rock bars will be presented in Chapter 7.

CHAPTER 6 DAMAGE EVOLUTION IN GRANITE UNDER UNIAXIAL COMPRESSION AND ITS EFFECT ON ULTRASONIC P-WAVE PROPAGATION

In this chapter, quantification of damage evolution in granite samples under static compression and investigation of its effect on ultrasonic P-wave propagation and attenuation in granite are presented. AE is used to quantitatively characterize damage evolution during uniaxial compression. Ultrasonic P-wave propagation in the granite sample along the loading direction is measured during the loading process and after each compression test. Micro-CT scanning was performed to quantitatively determine the degree of damage inside the granite sample after uniaxial compression. The damage effects on P-wave propagation in granite is quantitatively analyzed and discussed.

6.1 Introduction

Apart from the effects of pre-existing micro and macrocracks on the mechanical and fracture behavior of rocks, as shown in Chapters 4 and 5, the existence of those defects will also affect seismic wave and ultrasonic wave propagation and attenuation behaviors (King et al. 1986). Since investigating wave propagation and attenuation in heterogeneous rocks weakened by pre-existing defects and damages provides information for Earth crustal characterization, earthquake prognosis, mining, geological rock mass quality, and oil and gas exploration, it is therefore necessary to further study the relationship between ultrasonic wave propagation and rock damage to better understand the propagation and attenuation of stress waves in damaged rocks. Herein, the pre-existing defects are termed initial damage, which is specifically used to describe the physical and mechanical property deterioration of rocks.

Although numerous studies have been conducted to investigate ultrasonic wave propagation across intact rock and rock masses (Barnhoorn et al. 2018; Browning et al. 2017; Han 2016; He and Ahrens 1994; Kaneko et al. 1979; King 2002; Pyrak-Nolte et al. 1990a, b; Stanchits et al. 2006; Svitek et al. 2017; Toksöz et al. 1976; Wang et al. 2016), the effects of rock damage on wave propagation have not been quantitatively investigated in detail.

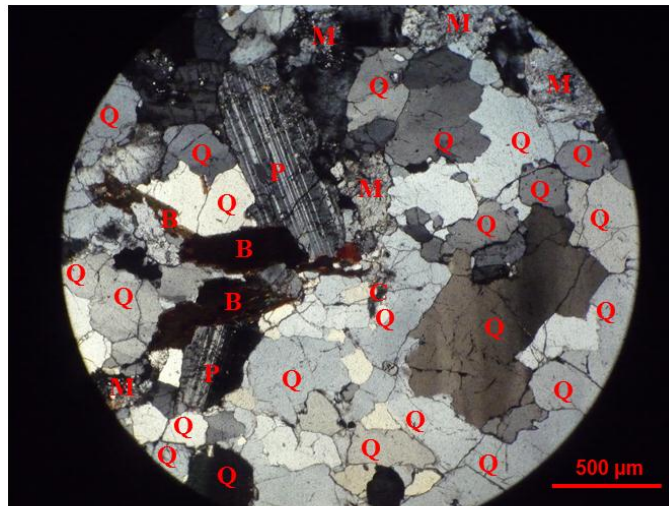
In this chapter, uniaxial compression tests, ultrasonic P-wave propagation and AE tests are simultaneously performed on granite samples, with the aim to quantitatively analyze damage evolution in granite samples under static compression and its effects on ultrasonic P-wave propagation and attenuation in granite. AE activities during uniaxial compression are monitored and recorded in real-time and then used to quantitatively characterize damage evolution in a granite sample and its effect on ultrasonic wave propagation velocity and amplitude. Micro-CT scanning is used to nondestructively obtain the stress-induced micro and macrocracks inside the granite samples, which is then applied to quantitatively characterize the damage coefficient of the granite after the loading and unloading processes.

6.2 Experimental setup

6.2.1 Sample preparation

Experiments were conducted on granite specimens taken from a quarry in Hunan, China. Microscopic investigation was conducted to identify the mineralogical composition and grain sizes using the optical microscope, as shown in Figure 6.1. The optical microscopy analysis shows that mineral composition of the granite contains 39.3% quartz, 21.4% microcline, 19% biotite, 17.9% plagioclase and 2.4% chlorite in volume. Statistical analysis of mineral particle size within thin sections under optical microscopy shows that the grain size of the minerals ranges from 0.1 mm to 2.0 mm with an average value of about 0.8 mm. The physical and mechanical properties of the granite are shown in Table 6.1, in which the compressive and tensile strengths are determined under static loading conditions.

According to the International Society for Rock Mechanics suggested method (Fairhurst and Hudson 1999), the nominal ratio of length to diameter of the specimens was set as 2:1 with a diameter of about 49 mm. All the specimens were ground and polished to have a surface roughness smaller than 0.02 mm. Figure 6.2 presents some of the well prepared granite samples.



Q: Quartz, P: Plagioclase, M: Microcline, B: Biotite, C: Chlorite

Figure 6.1 Thin section of the tested granite

Table 6.1 Physical and mechanical properties of the granite

Rock type	Density (Kg/m ³)	V_p (m/s)	E (GPa)	Porosity	ν	σ_c (MPa)	σ_t (MPa)
Granite	2642	4355	64	0.7%	0.25	168	8.2

V_p is the longitudinal wave velocity, E and ν are the Young's modulus and the Poisson's ratio, σ_c and σ_t are static compressive strength and tensile strength, respectively



Figure 6.2 Prepared granite samples

6.2.2 Testing system

The damage evolution tests were performed at the Advanced Research Center of Central South University, China. During testing, the real-time stress-strain, AE activities and ultrasonic P-wave propagation in the granite specimens along the loading direction were continuously monitored and recorded, as shown in Figure 6.3. Uniaxial compression tests were conducted on an MTS 647 hydraulic wedge grip machine with a displacement control mode of 0.075 mm/s. An AE detection sensor and a PCI-2 AE data-collecting system were used to detect and record the AE activities during the entire loading process. AE signals were amplified by 40 dB using Physical Acoustic Corporation preamplifiers. The AE signal acquisition rate was 1.0 MHz with a threshold trigger value of 40 dB. The ultrasonic P-wave propagation in the rock specimen was measured with an assembly device consisting of an Olympus 5077PR square wave pulser, a Tektronix digital phosphor oscilloscope 2012B and a pair of P-wave transducers with a central frequency of 1.0 MHz.

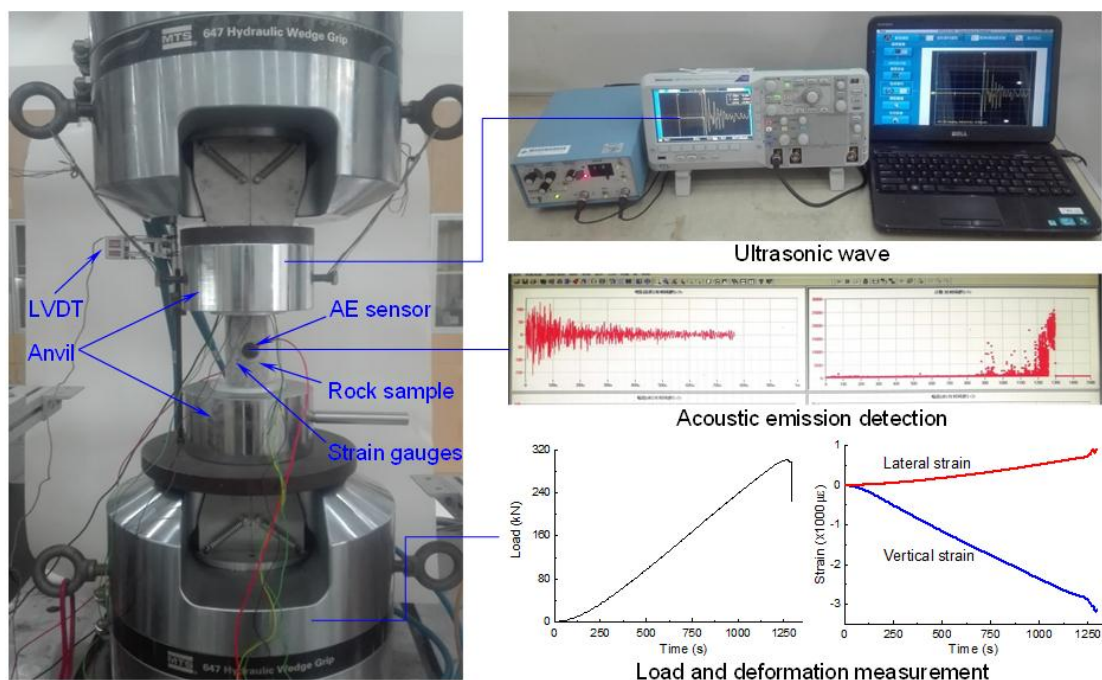


Figure 6.3 Experimental setup for P-wave propagation measurement and AE detection under uniaxial compression

To evaluate the influence of damage on P-wave propagation and attenuation, the granite specimens were first compacted to different loading levels with respect to the uniaxial compression strength (UCS) of the granite. The specimens were immediately unloaded

when they were compressed to the targeted loading values. During loading, the P-wave propagation in the specimen along the loading direction was measured under different loading levels. AE activities were monitored and recorded in real-time during the loading process. In addition, ultrasonic P-wave propagation in specimens before and after the loading processes was also measured to examine the effects of loading-induced damage on wave propagation and attenuation in granite specimens.

Regarding the P-wave velocity measurement, it contains two steps. First, the two anvils were directly contacted with each other (see Fig. 6.4a), and then the time (t_1) of P-wave propagation through the thickness of the two anvils was measured and recorded under different axial pressures. Then, the time (t_2) of P-wave propagation across the anvils and granite sample under different axial stresses were measured and recorded, as shown in Fig. 6.4b. Thus, P-wave velocity (V_P) of the granite sample can be determined as:

$$V_P = \frac{L}{t_2 - t_1} \quad (6.1)$$

where L is the length of the granite sample (unit: mm). Notably, t_1 and t_2 should correspond to the same axial stress.

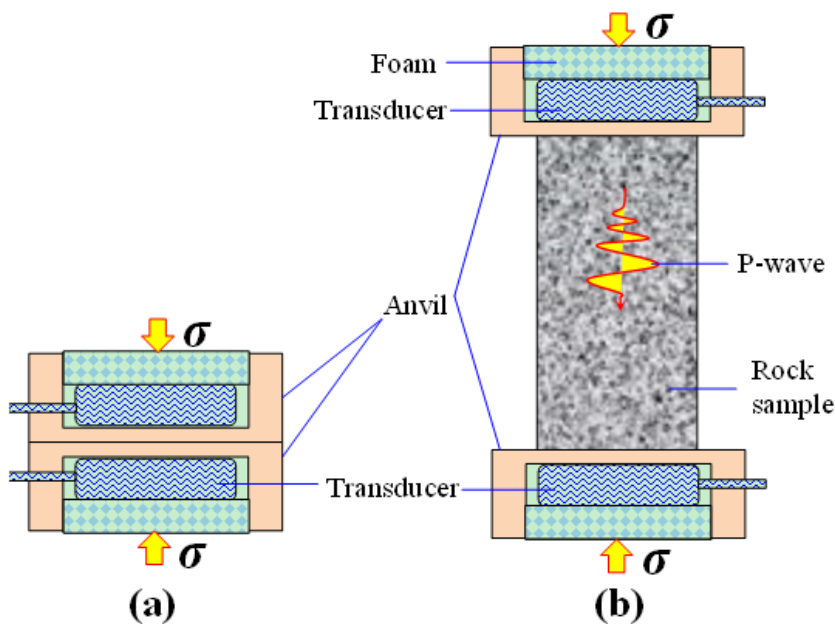


Figure 6.4 P-wave velocity measurement method. (a) P-wave propagation through the anvils; (b) P-wave propagation through the anvils and the granite sample.

6.3 Results

6.3.1 P-wave propagation during loading process

6.3.1.1 P-waveforms

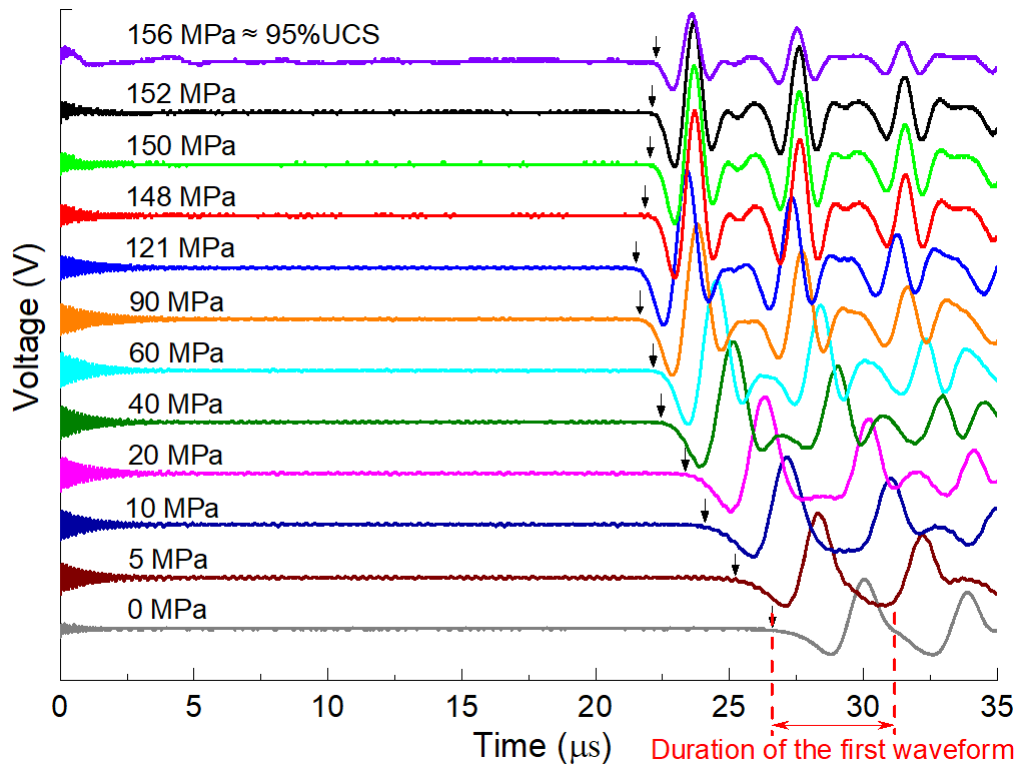


Figure 6.5 P-waveforms under different loading stresses. The arrows indicate the arriving time of the first transmitted waveform with respect to the starting point at 0 μs

Transmitted P-waveforms propagated across the granite specimens during the loading process were measured in real-time. The results showed that the variation laws of the P-wave propagation velocity, i.e., length of specimen divided by propagation time, and the amplitude of the first arriving waveform were similar for all tested samples, except for the inconsistency of changes in magnitude. Figure 6.5 shows the waveforms of P-wave propagation in a typical sample during the entire loading process. The arrows in the figure indicate the arrival time of the first transmitted waveform with respect to the starting point at 0 μs . The P-wave propagation time first decreased with increasing uniaxial compression stress from 0 MPa to approximately 120 MPa and then slightly increased as the stress further increased to the peak stress, i.e., approximately 161 MPa of the

specimen. In contrast, the amplitude of the first arriving waveform gradually increased as the axial stress was loaded from 0 to approximately 90 MPa and then decreased with further increasing axial stress. Moreover, the length/duration of the first transmitted waveform, as shown in Fig. 6.5, was continuously compacted with the increase in axial load.

6.3.1.2 *P-wave spectra*

To examine the frequency spectra variation during the loading process, the transmitted waveforms must be transformed from the time domain to the frequency domain. However, the transmitted waveforms consist of the first arriving waveform and subsequent reflected waveforms, which originate from various microcracks inside the rock sample and the interfaces between the rock sample and testing device. Since the first arriving waveform is more interesting for engineering applications, it is therefore necessary to isolate the first arriving pulse from the transmitted waveforms. Thus, a suitable window function shall be applied to taper the waveforms. The criterion of selecting an appropriate taper is that it should exert a negligible effect on the spectra of the initial pulse and preserve more low-frequency contents without excessive distortion in the high-frequency range (Pyrak-Nolte et al. 1990a). After trials, a half-cosine taper with unitary amplitude and a $4.075 \mu\text{s}$ window (see Fig. 6.6) was applied to the received P-waveforms. Figure 6.6 demonstrates two examples of the selected transmitted waveforms, the taper and the tapered waveforms received from a typical sample under axial stresses of 0 MPa and 60 MPa, respectively. The complete waveforms are presented in Fig. 6.5. After obtaining all the tapered first arriving waveforms, the Fast Fourier Transform was performed to gain the frequency spectra of the tapered waveforms.

Figure 6.7 presents the spectra of the first arriving waveforms at different compressive stresses. The results indicate that the amplitude of the spectra increased by approximately twice when the stress increased from 0 MPa to 148 MPa. Then, the amplitude sharply decreased to the initial value at an axial stress of 0 MPa, as the stress further increased to the peak stress vicinity. In contrast to the amplitude of the spectra, the central frequency increased from 244.1 kHz to 518.8 kHz when the stress changed from 0 MPa to 148 MPa and then remained constant, despite the stress increase.

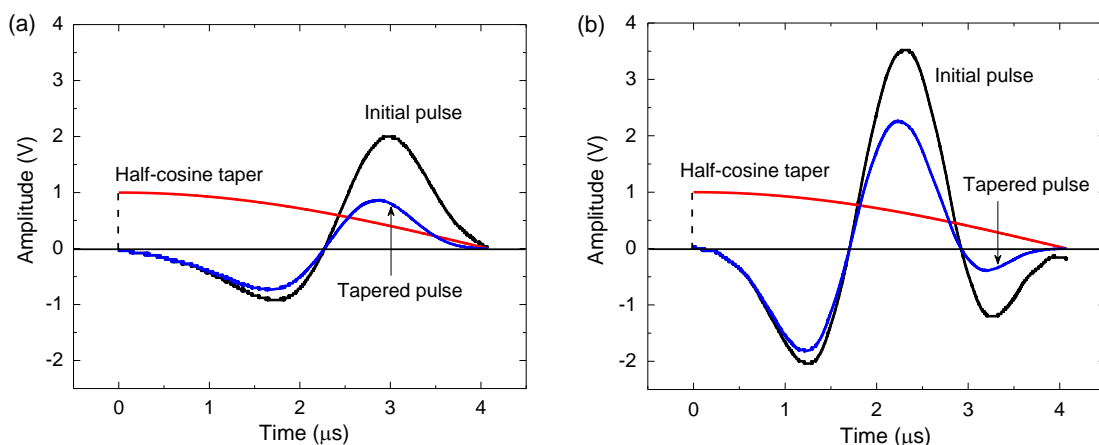


Figure 6.6 Examples of the initial pulse, a half-cosine taper and the tapered pulse. (a) and (b) Initial pulses obtained under the axial stresses of 0 MPa and 60 MPa, respectively.

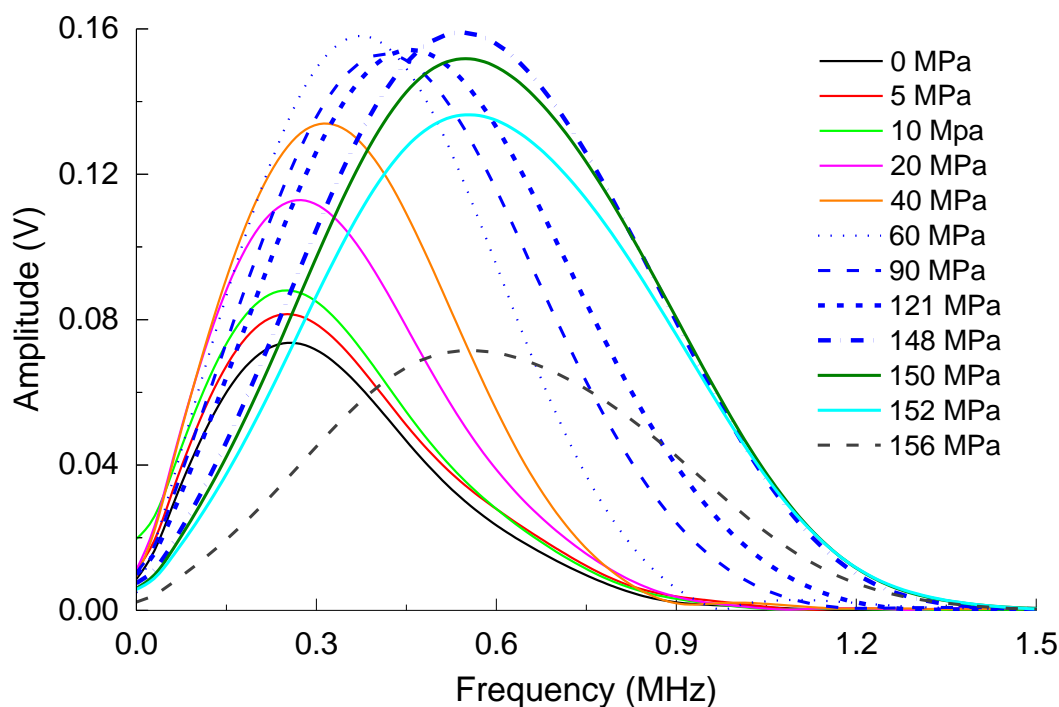


Figure 6.7 Spectra of the first-arriving waveform as shown in Fig. 6.5

6.3.1.3 P-wave velocity

Figure 6.8 summarizes the relationship between P-wave velocity (V_P) and axial stress during the loading process. The results show that the axial stress significantly affects the V_P in the granite sample, and the relationship between V_P and the loading percentage (ω) of the axial stress with respect to UCS can be appropriately characterized by a

polynomial function, as shown in Eq. (6.2). The V_P dramatically increased when the axial stress increased from 0 MPa to approximately 25% of UCS and continued to slightly increase until approximately 50% of UCS. Then, V_P remained nearly constant before gradually declining as the axial stress approached 100% of UCS. However, V_P prior to the peak stress was still much higher than that at the initial loading point. During loading, the average maximum V_P increased by approximately 20% compared to the initial V_P .

$$V_P = 4756.7 + 31.42 \cdot \omega - 0.248 \cdot \omega^2 \quad (6.2)$$

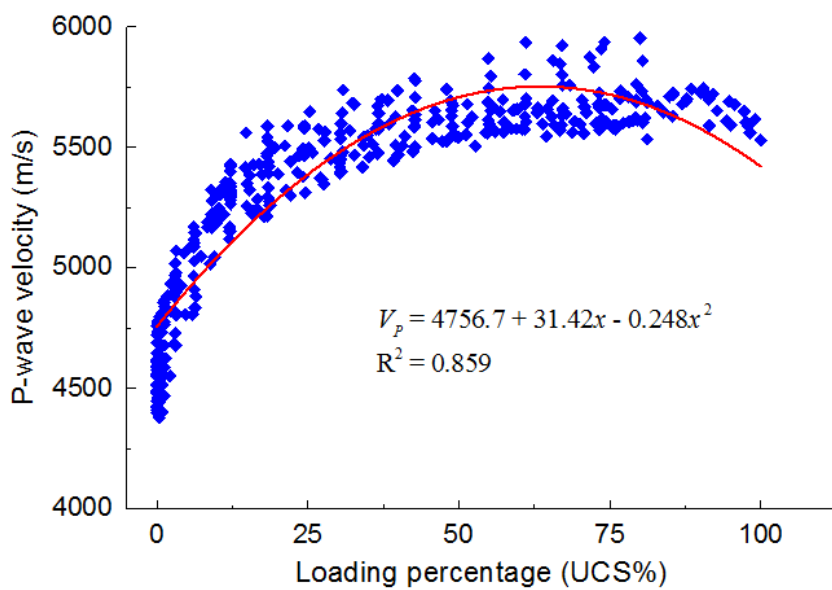


Figure 6.8 Variation of P-wave velocity with respect to axial loading percentages

6.3.1.4 P-wave amplitude

Figure 6.9 presents the variation in the normalized amplitude of the first arriving P-wave with respect to axial stress. Due to the inhomogeneous feature of the granite material, the increasing magnitude of the P-wave amplitude (A_P) for each granite sample was different even under the same loading pressure. Therefore, to examine the relationship between A_P and axial stress, the normalized amplitude was applied. The normalized amplitude is defined as the ratio of an individual A_P of a granite sample under a certain axial stress to the maximum A_P of the sample during the loading process. In general, the variation in the normalized A_P with respect to axial stress is similar to that of V_P and can also be fitted by a polynomial function, as shown in Eq. (6.3). The normalized A_P steeply increased, with the axial stress changing from 0 MPa to

approximately 40% of UCS and then remained nearly stable before sharply dropping with the axial stress surpassing approximately 70% of UCS. During the loading process, the maximum normalized A_P was nearly tripled compared to the initial value. This phenomenon indicated that the effects of axial stress on normalized A_P were more significant than the effects on the V_P .

$$A_P = 0.2962 + 0.02118 \cdot \omega - 1.787E-4 \cdot \omega^2 \quad (6.3)$$

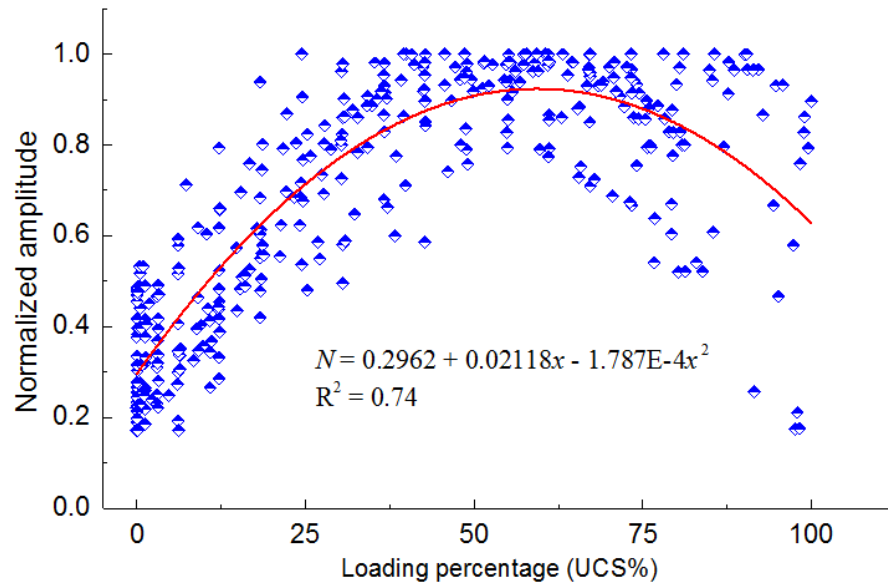


Figure 6.9 Variation of normalized P-wave amplitude with respect to axial loading percentages

6.3.2 AE

Figure 6.10 illustrates the axial stress-time curves and AE activities of typical granite samples under different loading levels, i.e., 20%, 40%, 60%, 78%, 87%, 92%, 97% and 100% of UCS. Generally, AE behaviors of all the granite samples were similar. AE behavior was quiet and inactive before loading to 20% of UCS. At this stage, few AE counts were generated due to closure/compaction of the pre-existing microcracks or voids inside the specimen at the initial loading stage (see Figs. 6.10a). The AE remained inactive during the linear elastic deformation stage with an axial stress of less than 60% of UCS (see Fig. 6.10b and c). This indicated that few microcracks were initiated and propagated inside the rock sample during the elastic deformation stage. However, when the axial stress was equal to or over 60% of UCS, AE became active, and increasingly more AE counts were generated and detected, as shown in Figs. 6.10c and d. This feature

indicated that 60% of UCS may correspond to the microcrack initiation stress threshold of the granite sample. Over this threshold stress, microcracks would randomly generate throughout the sample and for the most part, were isolated from one another (Eberhardt et al. 1999). When the axial stress exceeded 80% of UCS, AE counts were continuously generated, and a large number of AE counts abruptly occurred with the axial stress approaching the peak stress, as shown in Figs. 6.10e-h. This phenomenon suggested that the granite sample may enter the unstable cracking stage when the axial stress surpasses 80% of UCS, in which microcracks increased both in number and size, propagated and interacted with one another, eventually coalesced into macrocracks and finally led to the brittle failure of the sample.

6.4 Analysis

6.4.1 Damage evolution during loading process

As described previously, AE is a process of sudden release of stored elastic strain energy resulting from dislocations, microcrack growth, frictional slips, pore collapses, etc. (Eberhardt et al. 1999). Thus, AE signals detected during rock compression can be applied to characterize damage evolution inside rock samples. In this chapter, AE counts were utilized to quantitatively analyze damage evolution during the loading process, which is as follows (Liu et al. 2009; Ohtsu and Watanabe 2001):

$$D = \frac{N_A}{N_T} \quad (6.4)$$

where D is damage coefficient, N_A is accumulated AE counts in the process of loading, N_T is the total accumulated AE counts during the whole loading period.

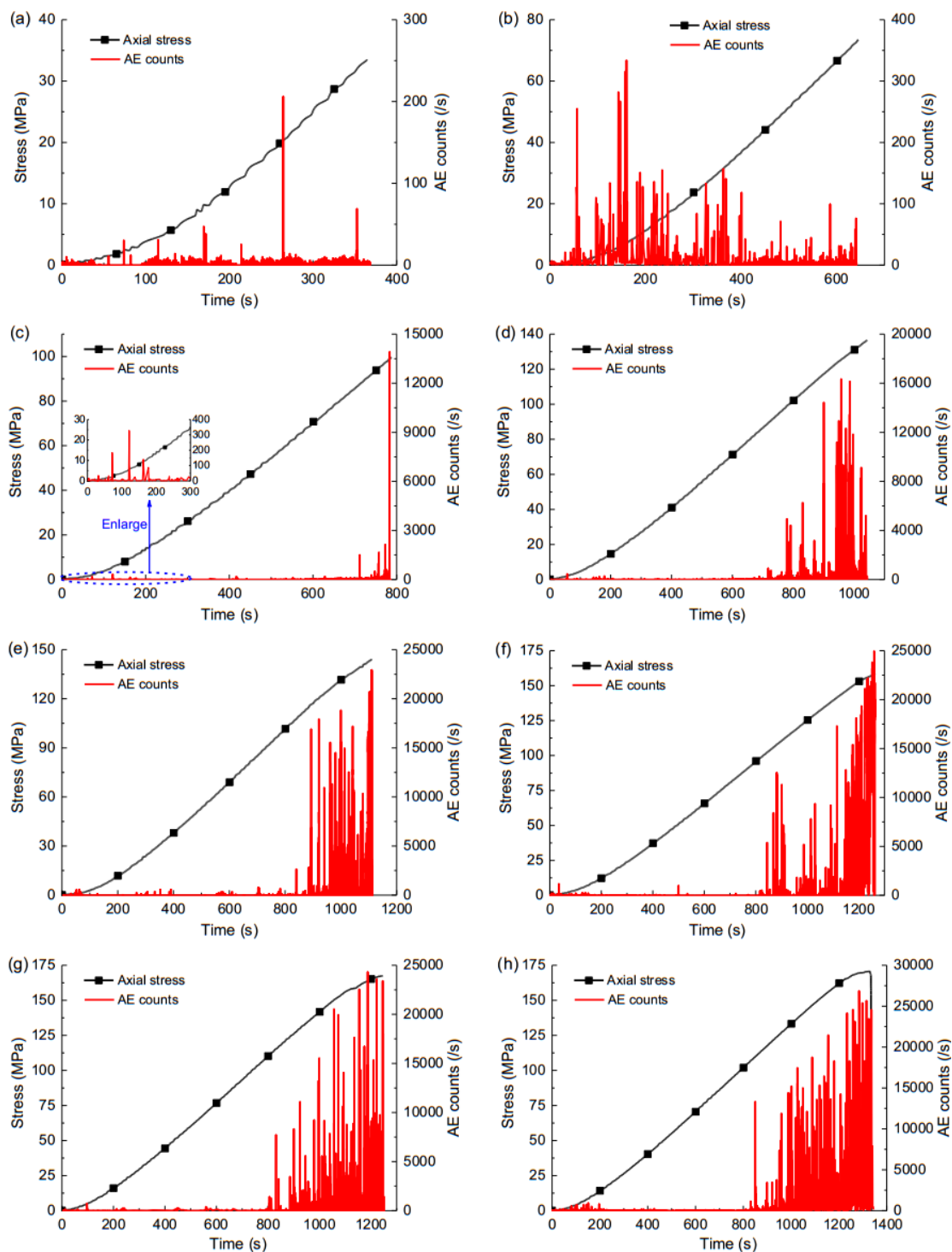


Figure 6.10 Axial stresses and AE activities of the granite samples subjected to different loading levels. (a)-(h) indicate the samples that were loaded to 20%, 40%, 60%, 78%, 87%, 92%, 97% and 100% of UCS, respectively.

Table 6.2 AE counts and damage coefficient of the granite samples compressed to different loading levels

Sample	σ (MPa)	UCS%	AE counts	D	Note
G-1	33.5	19.9	14673	0.0014	No failure
G-2	33.7	20.1	9124	0.0009	No failure
G-3	36.1	21.5	1143	0.0001	No failure
G-4	67.5	40.2	44128	0.0043	No failure
G-5	67.1	39.9	41304	0.0040	No failure
G-6	73.4	43.7	39193	0.0038	No failure
G-7	97.3	57.9	56003	0.0054	No failure
G-8	97.1	57.8	35589	0.0034	No failure
G-9	99.5	59.2	92487	0.0089	No failure
G-10	123.7	73.6	2093037	0.2023	Tiny failure
G-11	123.5	73.5	178567	0.0173	Tiny failure
G-12	126.8	75.5	549524	0.0531	Tiny failure
G-13	128.4	76.4	1058200	0.1023	Tiny failure
G-14	131.6	78.3	1232229	0.1191	Slight failure
G-15	137.8	82.0	332279	0.0321	Slight failure
G-16	136.5	81.3	1950804	0.1885	Slight failure
G-17	146.3	87.1	3552765	0.3434	Partially failed
G-18	153.8	91.5	3808225	0.36806	Partially failed
G-19	156.3	93.0	6293751	0.6083	Partially failed
G-20	163.2	97.1	5985595	0.5785	Partially failed
G-21	160.3	100	11158454	1	Failed
G-22	168.8	100	10279496	0.9935	Failed
G-23	174	100	9601502	0.9280	Failed

Figure 6.11 shows a plot of the axial stress-time curve, AE counts and the damage coefficient determined by AE counts during the loading process. Note that the sample is the same as that in Fig. 6.10h. The results indicated that AE was inactive before loading to 60% of UCS, and the damage coefficient was nearly zero. At over 60% of UCS, AE became active, and the damage coefficient increased. When axial stress surpassed 80% of UCS, particularly approaching UCS, a large number of AE counts occurred and the

damage coefficient sharply increased to 1, and then, the sample failed.

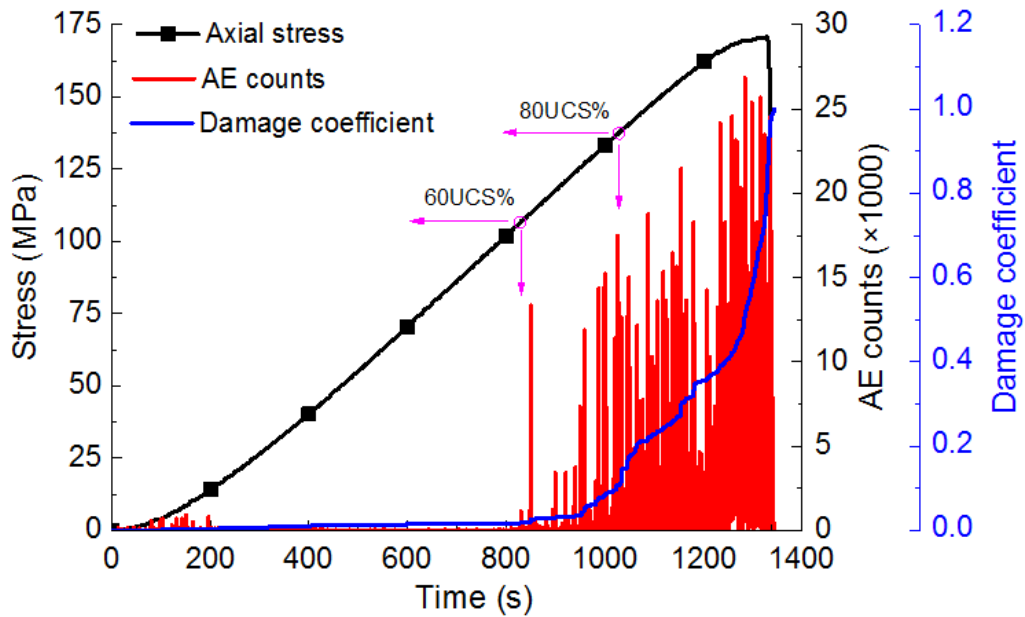


Figure 6.11 AE activity and damage evolution of a typical specimen (G-23) under uniaxial compression

To obtain the relationship between the damage evolution and loading percentage of the axial stress with respect to UCS for the granite, the statistical AE counts of the granite samples compacted to different loading levels were used to quantitatively characterize the damage coefficient. Thus, the damage coefficient of the granite sample is redefined as the ratio of the granite sample AE counts that was compressed to a certain load degree, e.g., 20% or 40% of UCS, to the average granite sample AE counts that were compressed to the final failure. Therefore, Eq. (6.4) can be modified into the following:

$$D = \frac{N_S}{\bar{N}} \quad (6.5)$$

where N_S is the statistical granite sample AE counts compressed to a certain loading degree, and \bar{N} is the average granite sample AE counts that were compressed to failure.

Substituting granite sample AE counts into Eq. (6.5), the damage degrees of the granite samples subjected to the corresponding axial stresses can be obtained (see Table 6.2). Figure 6.12 demonstrates the relationship between the damage degree and loading percentage under compression. The damage evolution of the granite is nonlinear under

compression and can be well fitted by an exponential function:

$$D = 2E-05 \cdot e^{0.1078 \cdot \omega} \quad (6.6)$$

where ω is the loading percentage of the axial stress with respect to the UCS, $0 \leq \omega \leq 100$.

The result shows that very little damage developed when the axial stress was below 60% of UCS. D drastically increased when the axial stress was greater than 80% of UCS.

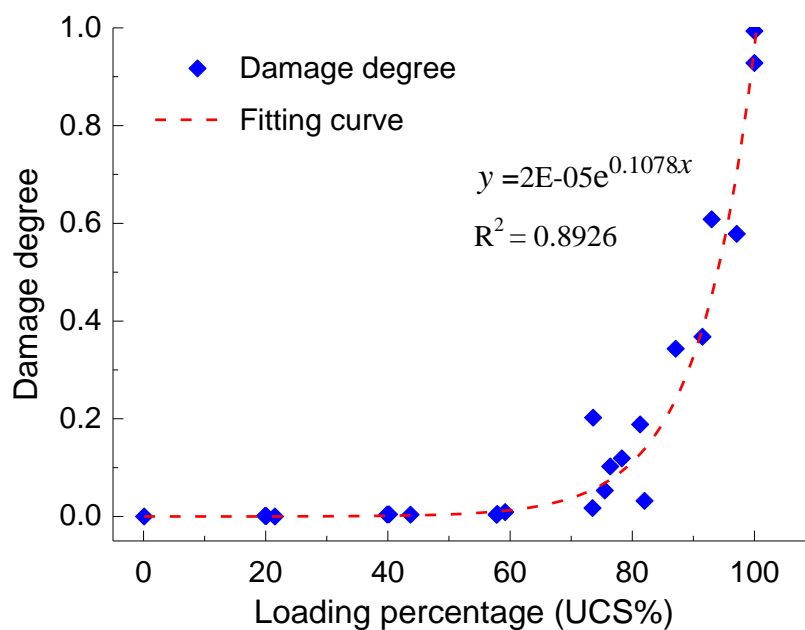


Figure 6.12 Relationship between damage degree and loading percentage

To examine the fitting function effectiveness for analyzing damage evolution during static uniaxial compression, the damage coefficient calculated by the fitting function is compared with the damage coefficient determined through an experiment on a typical granite sample, as shown in Fig. 6.11. From Fig. 6.13, the calculated results agree well with the experimental results, which indicate that the fitting function is suitable for analyzing damage evolution inside the granite sample under uniaxial compression.

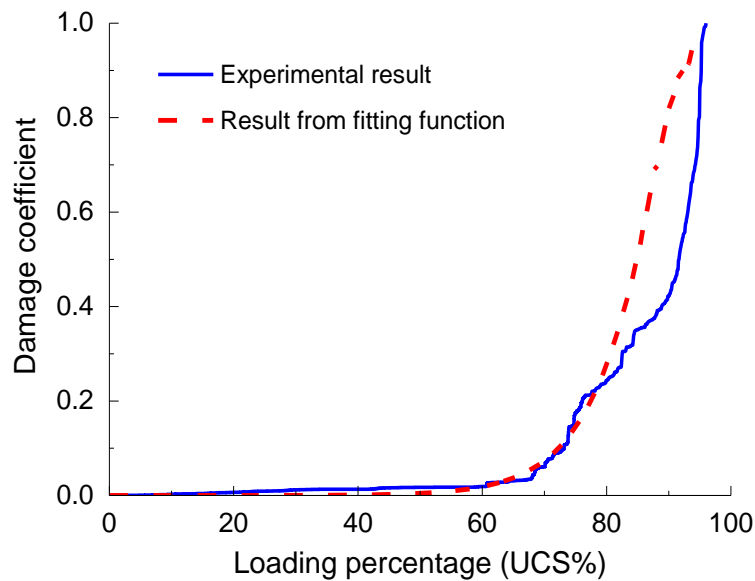


Figure 6.13 Comparison of damage coefficient determined by fitting function and AE counts in experiment of sample G-23

6.4.2 Effect of damage evolution on P-wave propagation

6.4.2.1 Relationship between D and V_P

The testing results showed that the V_P changed with axial stress and that axial stress could generate D inside the granite sample. Thus, it is believed that a change in V_P is caused by damage generation. Figure 6.14 demonstrates the principle of how V_P is correlated with D by the AE counts during the loading process. From Fig. 6.14a, the relationship between V_P and axial stress during loading can be first obtained, as shown in Fig. 6.8 and Eq. (6.2). Through Fig. 6.14b, D can be determined using AE counts at different stresses, as shown in Figs. 6.11 and 12 and Eqs. (6.4 and 6.6). Finally, the relationship between D and V_P during loading could be obtained, as shown in Fig. 6.14c.

Figure 6.15 shows the damage evolution effect on V_P under the compression process, where both the experimental results and the results calculated from by fitting functions are presented. Based on the experimental results, the relationship between D and V_P can be divided into three stages. In the first stage, when D was less than approximately 0.0025 (corresponding to approximately 50% of UCS), V_P sharply increased. In the second stage, V_P was nearly constant, with D increasing from 0.0025 to approximately

0.32 (corresponding to approximately 90% of UCS). In the third stage, V_P gradually decreased with D . As shown in the figure, the results calculated by the fitting functions agree well with the experimental results, particularly at the first stage where the results determined by the two methods nearly coincide with each other. Although there is no second stage in the calculated results, the discrepancy beyond the first stage between the two methods is within 5%. The results indicate that the fitting functions, i.e., Eqs. (6.2 and 6.6), obtained from the experimental results could be used to reveal the effect of damage evolution on P-wave propagation velocity in the granite samples.

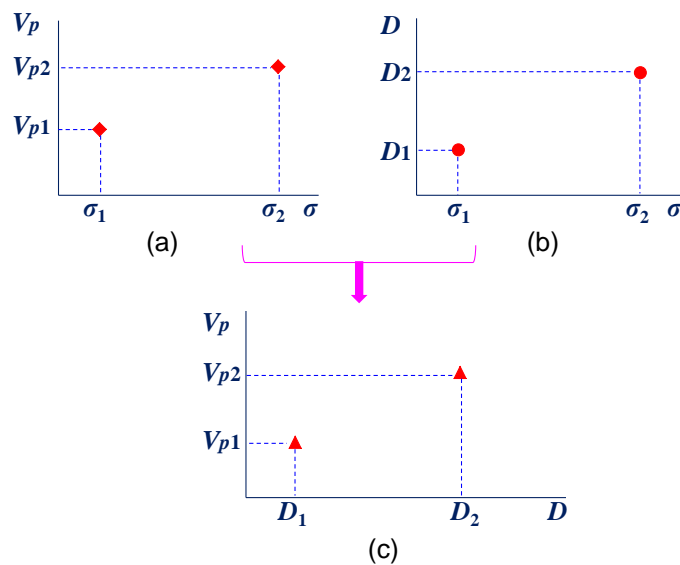


Figure 6.14 Principle of using D determined by AE to analyze V_P

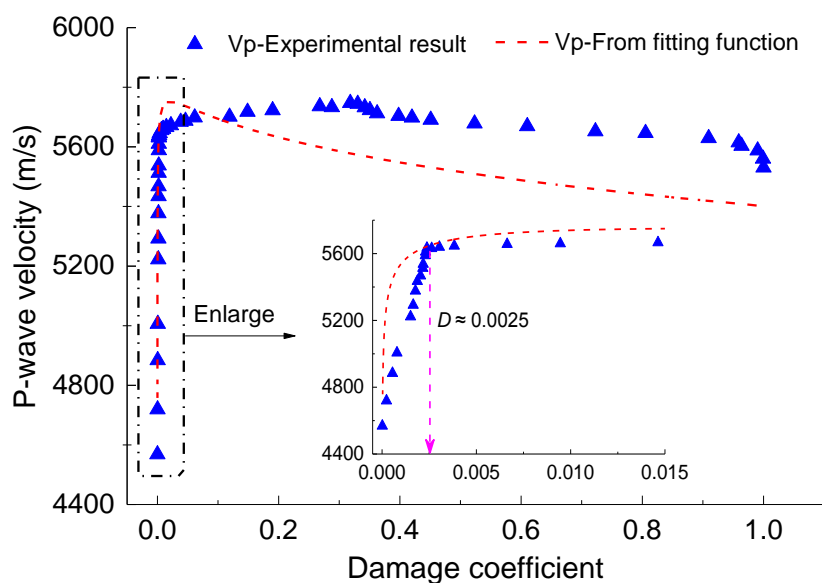


Figure 6.15 Relationship between V_P and D

6.4.2.2 Relationship between D and A_P

Figure 6.16 illustrates the principle of using D to analyze A_P during the loading process. Similarly, the relationship is first obtained between A_P and axial stress during loading, as shown in Fig. 6.16a. Then, D could be determined using AE counts at different stresses, as shown in Fig. 6.16b. Finally, the relationship between D and A_P could be obtained, as shown in Fig. 6.16c.

Figure 6.17 shows the effect of D on A_P during loading, which is determined by both experimental results and fitting functions. The calculated results are computed by the fitting functions, as shown in Eqs. (6.3 and 6.6). The results show that when D is less than 0.0066 (corresponding to approximately 65% of UCS), A_P sharply increased from approximately 0.3 to 1.0. Subsequently, A_P decreased from the peak value to approximately 0.4. The decreasing A_P rate accelerated when D was greater than 0.8 (corresponding to approximately 92% of UCS). Similar to the wave velocity, the results obtained from fitting functions agree well with the experimental results, except for the relatively large discrepancy near $D=1$. Thus, the fitting functions obtained from the experimental results, i.e., Eqs. (6.3 and 6.6), are concluded to be suitable for analyzing the effect of D on A_P in the granite samples.

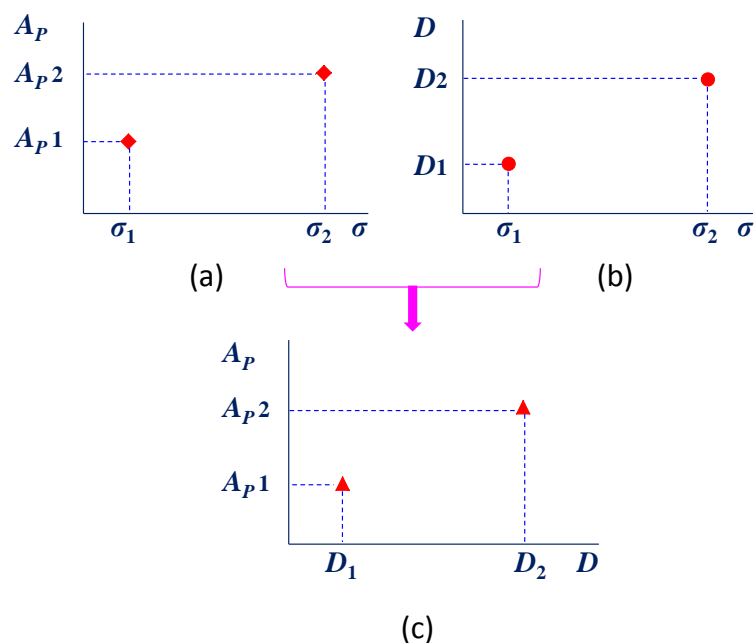
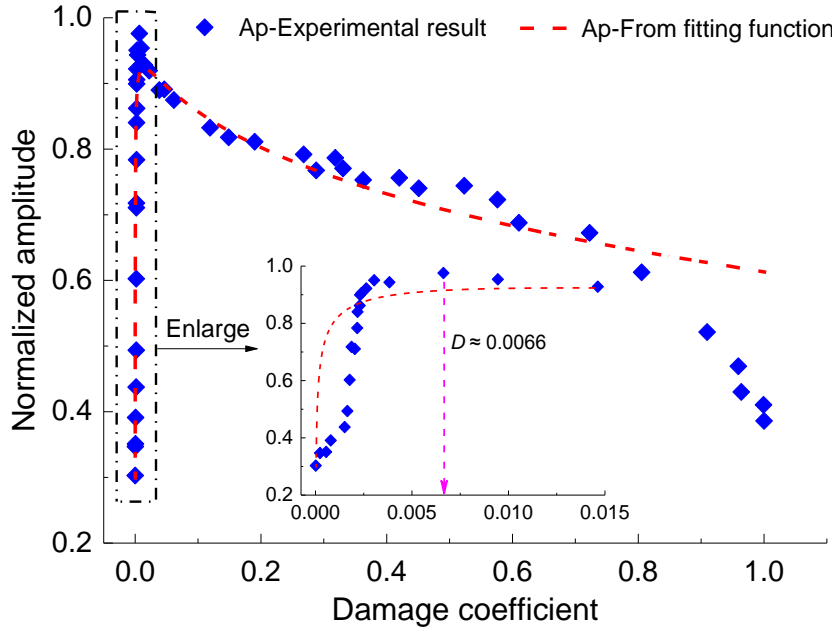


Figure 6.16 Principle of using D determined by AE to analyze A_P

Figure 6.17 Relationship between A_p and D

6.4.3 Damage induced after uniaxial compression

6.4.3.1 P-wave propagation in granite sample after loading and unloading process

When the granite specimens were compressed to the targeted loading values, the specimens were immediately unloaded. Then, P-wave propagation in the recovered specimen without axial loading was measured to assess the loading-induced damage (D') influence on the P-wave propagation and attenuation. Figure 6.18 illustrates the P-wave propagation measurement in the granite sample before and after the loading process. Thus, the P-wave velocity and amplitude before and after compression can be obtained. The variation in the P-wave velocity (ΔV_p) and amplitude (ΔA_p) can be determined as follows:

$$\Delta V_p = \frac{V_p' - V_{p0}}{V_{p0}} \times 100\% \quad (6.7)$$

$$\Delta A_p = \frac{A_p' - A_{p0}}{A_{p0}} \times 100\% \quad (6.8)$$

where V_{p0} and V_p' represent the P-wave velocity before and after loading process, A_{p0} and A_p' refer to the peak amplitude of the first-arriving waveform before and after compression.

Table 6.3 Variation of V_P and A_P after uniaxial compression process

Sample	UCS%	V_P (m/s)			A_P (V)		
		V_{P0}	$V_{P'}$	ΔV_P (%)	A_{P0}	$A_{P'}$	ΔA_P (%)
G-1	19.9	4603	4812	4.54	3.24	3.4	4.94
G-2	20.1	4697	4922	4.79	3.08	3.18	3.25
G-3	21.5	4487	4621	2.98	3.26	3.44	5.52
G-4	40.2	4414	4553	3.14	2.68	2.92	8.96
G-5	39.9	4342	4504	3.73	3.24	3.64	12.35
G-6	43.7	4406	4689	6.43	3.01	3.26	8.30
G-7	57.9	4394	4686	6.64	2.88	3.29	14.24
G-8	57.8	4460	4698	5.33	2.92	3.25	11.30
G-9	59.2	4496	4767	6.02	3.18	3.70	16.35
G-10	73.6	4220	4562	8.12	3.06	3.53	15.36
G-11	73.5	4295	4640	8.02	2.68	3.15	17.54
G-12	75.5	4439	4740	6.80	1.48	1.69	14.21
G-13	76.4	4376	4749	8.52	2.28	2.71	18.86
G-14	78.3	4515	4916	8.87	3.16	3.80	20.25
G-15	82.0	4338	4766	9.86	3.08	3.68	19.48
G-16	81.3	4373	4727	8.10	1.96	2.44	24.49
G-17	87.1	4242	4705	10.91	2.88	3.12	8.33
G-18	91.5	4376	4661	6.52	2.56	2.62	2.34
G-19	93.0	4373	4732	8.22	2.66	2.74	3.01
G-20	97.1	4385	4497	2.57	3.48	1.8	-48.28
G-21	100	4423	3990	-9.79	2.76	0.0126	-99.54
G-22	100	4416	4055	-8.18	2.92	0.0004	-99.99
G-23	100	4410	4011	-9.05	3.28	0.028	-99.15

Table 6.3 demonstrates the variation in V_P and A_P in the granite specimens after the loading and unloading processes, where a positive variation means an increasing V_P or A_P compared with those in the samples without loading. Compared with V_{P0} , $V_{P'}$ of the unloaded specimens gradually increased with increasing pressure level and approached the maximum value of approximately 11% at 87% of UCS. The increased magnitude of V_P sharply declined to approximately 2.6% when the specimens were compressed to 97% of UCS. In contrast, the $V_{P'}$ of the failed specimen, as shown in Fig. 6.19b, decreased by approximately 9%. In terms of A_P , with an increasing axial stress to 80% of UCS, $A_{P'}$

increased by approximately 21% with respect to A_{P0} . Similar to the P-wave velocity, the increment of A_P also declined with a further increase in the loading levels. However, when the specimens were compacted to 97% of UCS, the $A_{P'}$ of the unloaded specimens decreased by approximately 50% compared to the initial value before loading. Moreover, the $A_{P'}$ of the recovered failed specimens was close to zero, which is significantly different from the P-wave velocity.

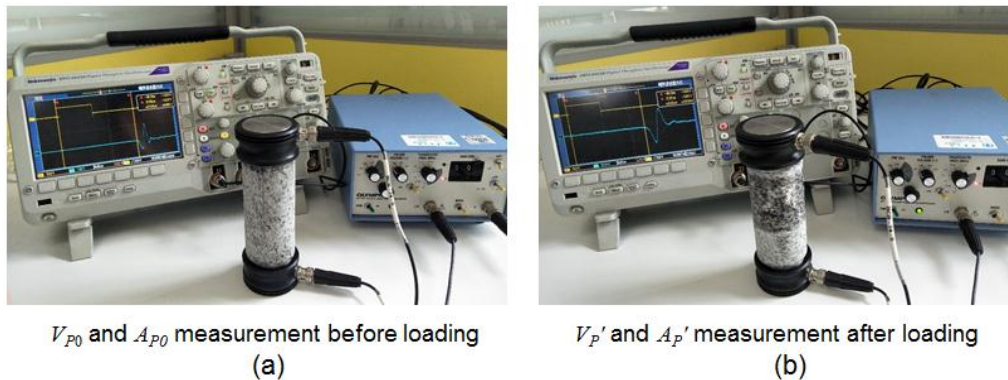


Figure 6.18 Measurement of P-wave propagation in granite sample before and after loading process

6.4.3.2 Characterization of stress-induced damage using micro-CT

As stated previously, the variation in V_P and A_P after uniaxial compression is also believed to be caused by stress-induced damage inside the rock samples. Therefore, to quantitatively determine the loading-induced damage, a NanoVoxel 2000 micro-CT scanner was used to scan the damaged samples at a resolution of $61 \times 61 \times 61 \mu\text{m}^3$, as shown in Fig. 6.19a. Notably, as micro-CT scanning is time consuming and costly, only some of the damaged samples were scanned in this chapter. After scanning the damaged samples, a series of 2D micro-CT images were obtained. Figure 6.19b demonstrates one of the 2D micro-CT images of the failed granite sample G-23. Then, by setting a proper threshold value in the Mimics software, e.g., -912 in Fig. 6.20a, the micro and macrocracks can be appropriately extracted from the solid matrix of the granite sample in each 2D micro-CT image, as shown in Figs. 6.20. Finally, the crack area in each 2D micro-CT image could be automatically calculated by the Avizo software. Based on the classical continuous damage theory (Kachanov 2013), the sample damage could be determined by Eq. (6.9):

$$D' = \frac{1}{n} \sum_{i=1}^n \frac{A_i'}{A_i} \times 100\% \quad (6.9)$$

where A_i is the area of the i -th micro-CT image of a damaged sample, A_i' is the total crack area in the i -th micro-CT image of a damaged sample subjected to certain loading stresses, and n is the total number of micro-CT images of a sample.

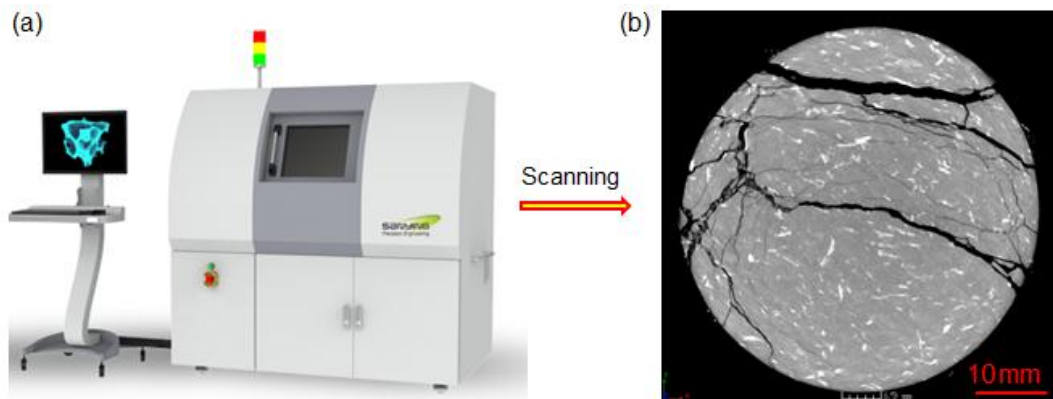


Figure 6.19 (a) NanoVoxel 2000 micro-CT scanner; (b) 2D micro-CT image of a failed granite sample (G-23)

To appropriately compute D' , the crack areas of the damaged samples must be precisely counted, especially the failed ones, as shown in Fig. 6.20a. Regarding the failed sample, as shown in Fig. 6.20a, the sample is separated by the fault. The fault is formed by large, open cracks and voids rather than dense micro and macrocracks, and the openness of the largest macrocrack is nearly 2 mm. Thus, the crack areas will undoubtedly be much greater than the real area if we directly count the crack area of the entire failed sample. To avoid this problem, it is proposed to statistically count the crack areas in some representative regions, which are termed the characterized rock elements. This concept/method is similar to the method of quantitatively analyzing the crack density of the damaged rock sample using SEM or optical microscopy on a small thin section of the cracked sample (Wu et al. 2000). The selection criteria of the characterized rock element are as follows: (1) the element should be near but excluding the fault in the failed sample; (2) the element should contain not only sufficient microcracks but also include at least one or two coalesced crack(s) that have extended to the element boundary. The first criterion could help to avoid fault interference, while the second criterion guarantees that the characterized rock element could fail by the cracks inside its volume.

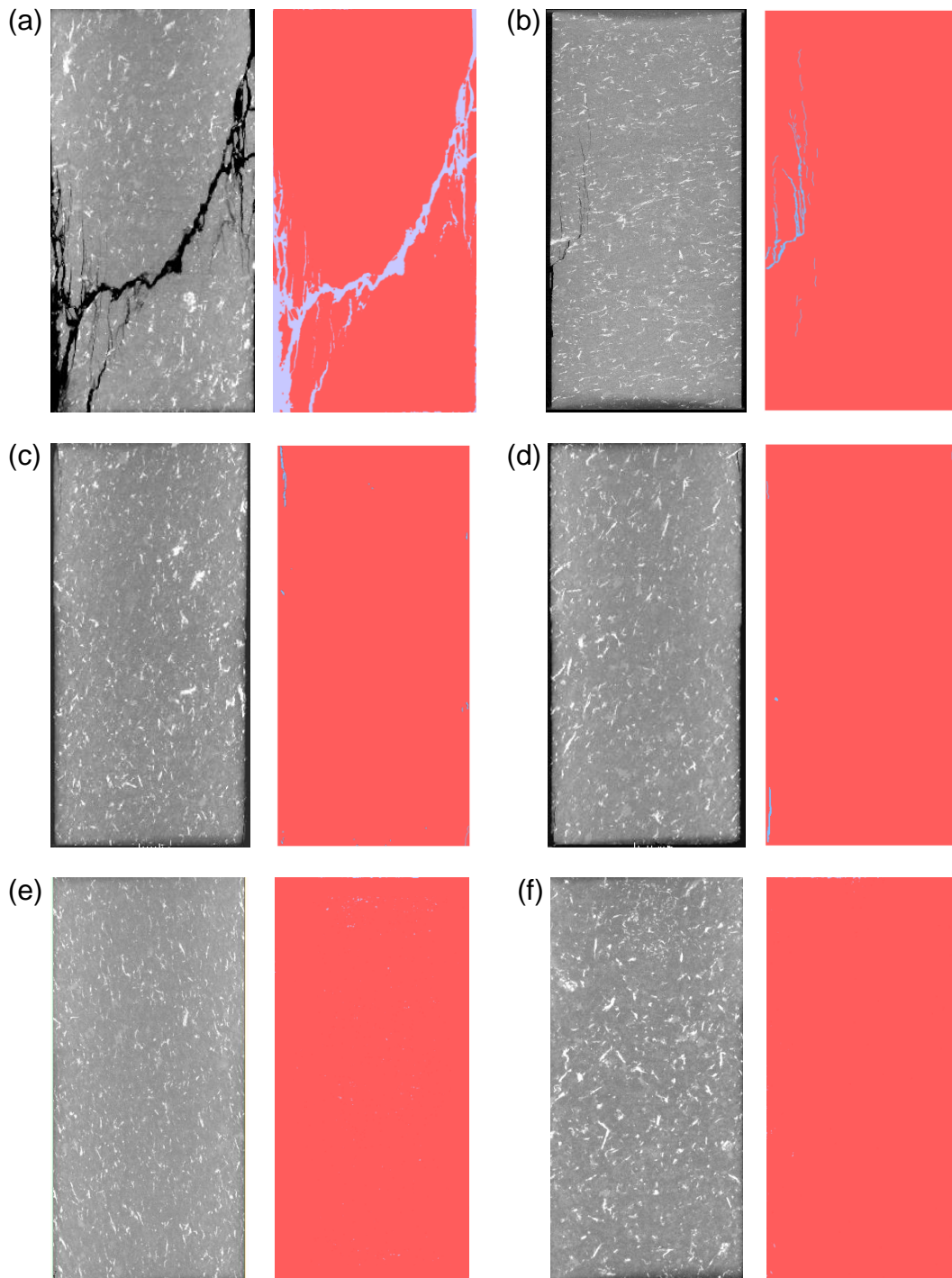


Figure 6.20 2D micro-CT images and the corresponding cracks of the granite samples subjected to different axial stresses. The loading percentage of the samples from (a) to (f) are 100%, 97%, 87%, 80%, 60% and 40% of UCS, respectively. The red and blue colors in the images beside the micro-CT images indicate solid materials and cracks, respectively.

Figure 6.21 illustrates the elements that have been extracted to properly analyze the

crack area of failed sample G-23. Two characterized rock elements were selected in two orthogonal directions parallel and perpendicular to the loading direction. The dimensions of the two elements are $24.4 \times 12.2 \times 12.2 \text{ mm}^3$ and $12.2 \times 12.2 \times 24.4 \text{ mm}^3$, respectively. Based on the method described above, the crack areas of these two elements can be obtained, which can then be used to determine D' by Eq. (6.9). D' of the elements along the horizontal and vertical directions are 2.05% and 1.83%, respectively. Therefore, the average damage, i.e., 1.94%, of these two elements is used to represent D' of failed sample G-23.

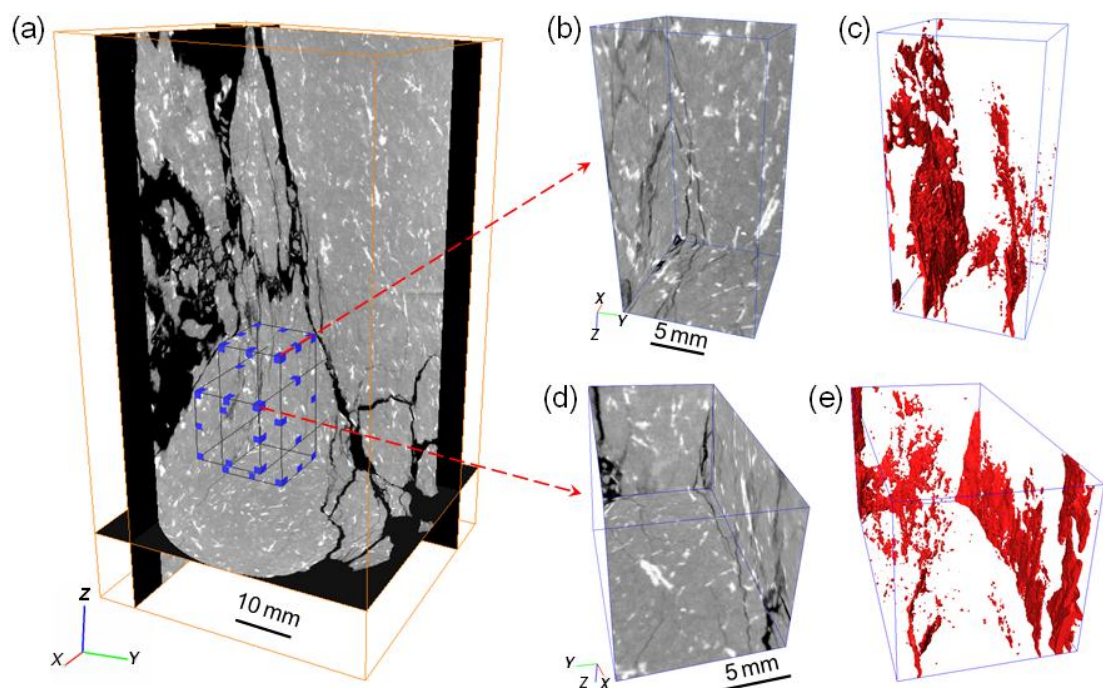


Figure 6.21 Determination of cracks from two characterized rock elements extracted from the failed granite sample G-23. (a) Exhibition of the locations of the two characterized rock elements; (b) and (d) The characterized rock elements that are parallel and perpendicular to the loading directions, respectively. (c) and (e) Cracks (marked by red colour) within the characterized rock elements shown in (b) and (d), respectively.

Table 6.4 summarizes the damaged rock crack areas and their D' determined by Eq. (6.9). In general, the crack areas are very small compared to the scanning areas of the entire damaged sample. When the addition of the axial stress to the sample was below 60% of UCS, the crack areas generated in the samples were extremely small, resulting

in a very low D' . Similar to the damage evolution during the loading process (see Fig. 6.12), D' increased with axial stress above approximately 80% of UCS and sharply grew to the peak, i.e., 1.94%, with the stress reaching the UCS.

Table 6.4 Crack areas and damage coefficient of the damaged rocks

Sample	UCS%	Crack area (mm ²)	Scanning area (mm ²)	D'	D_N
G-4	40	59.17	1557009.0	0.0038%	0.002
G-9	60	91.47	1524556.7	0.006%	0.0032
G-16	80	730.34	1587702.3	0.046%	0.024
G-17	87	2218.13	1584381.4	0.14%	0.072
G-20	97	8069.17	1551763.5	0.52%	0.268
G-23	100	1155*	59536**	1.94%	1.0

* the average crack areas in the characterized rock elements; ** the scanning areas of the characterized rock element.

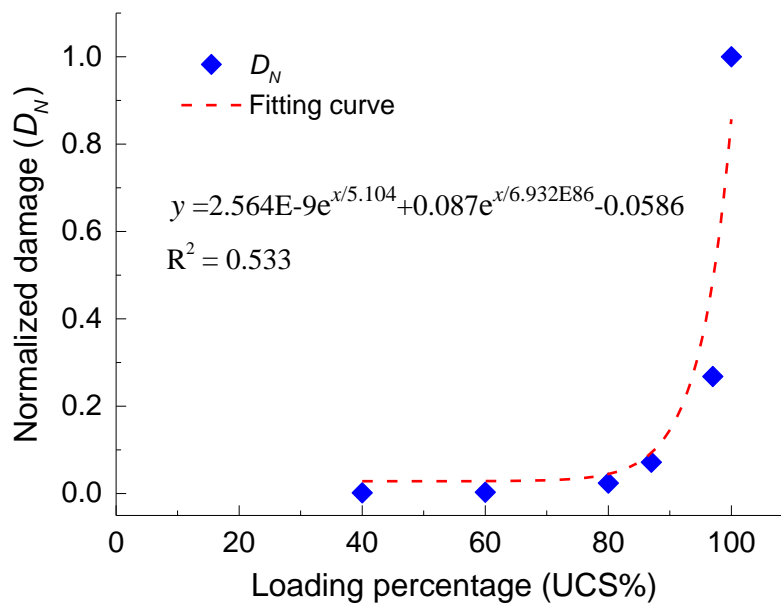


Figure 6.22 Variation of normalized damage of the granite samples after loading to different UCS%

Regarding failed sample G-23, the D' value equals 1.94%, which is far less than the theoretical result that the damage should be 100% when the material completely fails

(Kachanov 2013). To make D' comparable to D during the loading process, the normalized damage coefficient D_N is adopted to characterize the stress-induced damage of the granite sample after loading and unloading. D_N is defined as the ratio of D' of the sample that experienced the loading and unloading processes under a certain load degree of UCS to the peak D' of the completely damaged granite sample. The variation in D_N with respect to the loading percentages after the loading and unloading processes is shown in Fig. 6.22. The result indicates that the evolution of D_N is highly nonlinear and can be fitted by an exponential function, as shown in Eq. (6.10):

$$y = 2.564E-9 \cdot e^{x/5.104} + 0.087 \cdot e^{x/6.932E86} - 0.0586 \quad (6.10)$$

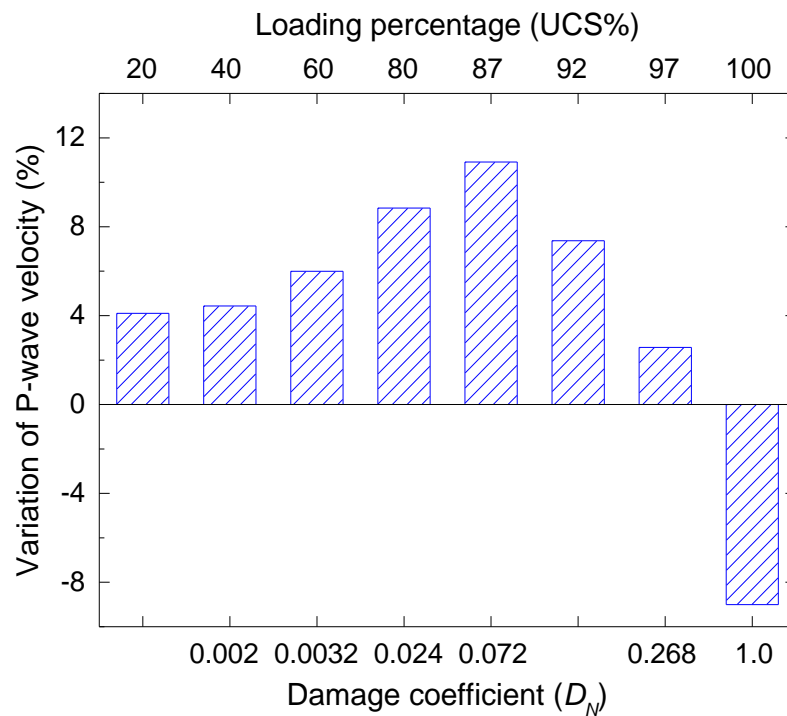


Figure 6.23 Relationship between V_P and D_N

6.4.3.3 Relationship between D_N and V_P and A_P

Figure 6.23 demonstrates the effect of D_N on the average variation in V_P obtained in the granite specimens with micro-CT after loading and unloading, where a positive variation means an increase in wave velocity compared with the value without loading, and vice versa. Compared with V_P before loading, V_P of the unloaded specimens increased with increasing D_N when the damage coefficient was less than 0.268. The failed sample V_P is approximately 9% lower than the value before loading. Based on this

figure, the effect of stress on the compaction of the pre-existing cracks and pores inside the rock samples would not completely disappear after axial pressure unloading. Despite the newly induced damage, the wave velocity remains higher than in samples before loading if the sample does not fail.

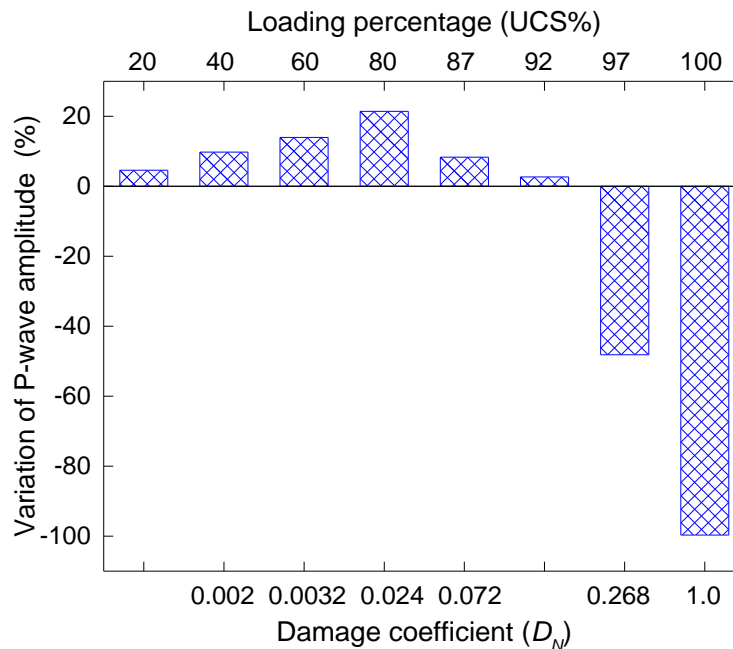


Figure 6.24 Relationship between A_P and D_N

Figure 6.24 illustrates the effect of D_N on the average A_P variation obtained with micro-CT after the loading and unloading processes. Similar to wave velocity, the stress effect on the compaction of pre-existing cracks and pores inside the rock samples would not completely disappear after axial pressure unloading. That is, when D_N is smaller than approximately 0.1, the A_P of the unloaded granite samples gradually increased with increasing D_N . The maximum increment of A_P is approximately 21%, with D_N equal to 0.024. However, when D_N is large, the A_P of the unloaded specimen is lower than the value without loading. In particular, when the sample failed, or when D_N is 1.0, the wave amplitude variation is nearly -100%, meaning that the transmitted wave amplitude is nearly zero. In addition, Figs. 6.23 and 6.24 show that the D_N effect on the wave amplitude is more significant than the effect on wave velocity.

6.5 Discussion

The experimental results show that the P-wave propagation velocity, the peak amplitude

of the first arriving-waveform and the spectra amplitude during the loading process first increased and then decreased with increasing pressure from 0 to peak stress, as shown in Figs. 6.7-9. This variation is probably due to the compaction and closure of pre-existing defects during the initial loading stage, which leads to contact conditions consolidation between individual minerals and a change in the friction conditions and thus results in an increase in V_P and A_P (Kaneko et al. 1979; Meredith et al. 1991; Svitek et al. 2017). In contrast, when the stress exceeded a critical value, e.g., approximately 80% of UCS, dilatancy or volumetric strain is generated due to reopening, generation, propagation and coalescence of the closed and new microcracks, which thereby leads to a significant damage increase inside the granite samples, as shown in Figs. 6.12 (Brace et al. 1966; Kaneko et al. 1979; Meredith et al. 1991). Consequently, the damage increase results in V_P and A_P attenuation. The V_P and A_P change results, as shown in Figs. 6.8 and 6.9, are comparable to the previous results presented by Barnhoorn et al. (2018), Gupta (1973), Martínez-Martínez et al. (2016) and Stanchits et al. (2006). In addition, the V_P and A_P of the transmitted waveform prior to the UCS are still greater than those values under the initial conditions, as shown in Figs. 6.8 and 6.9. This behavior is probably the result of the crack closure effect on wave propagation dominating the competition between stress-induced horizontal crack closure and vertical cracking prior to failure stress (Lockner et al. 1977).

From the results shown in Figs. 6.8 and 6.9 and Table 3, the variation in A_P with the microcracking/damage progress in granite samples is approximately 3~10 times more sensitive than that of V_P . This phenomenon could be explained by two reasons. On the one hand, the V_P change is mainly due to the formation of stress-induced microcracks (Kaneko et al. 1979). The stress-driven crack orientation as observed under the SEM and micro-CT scanning are more or less parallel to the maximum compressive stress axis (Barnhoorn et al. 2018; Tapponier and Brace 1976; Zhou et al. 2018). Therefore, the propagation-parallel cracks contribute less to the P-wave slowness along the loading direction (Barnhoorn et al. 2018). On the other hand, the A_P change is due to a combination of multiple factors, such as the ultrasonic wave frequency, wave propagation velocity and the internal friction coefficient (Kaneko et al. 1979). Similar to V_P , the internal friction coefficient of the rock material is affected by stress-driven crack formation (Walsh 1966). Consequently, A_P would be more affected by the microcracking/damage progress than V_P .

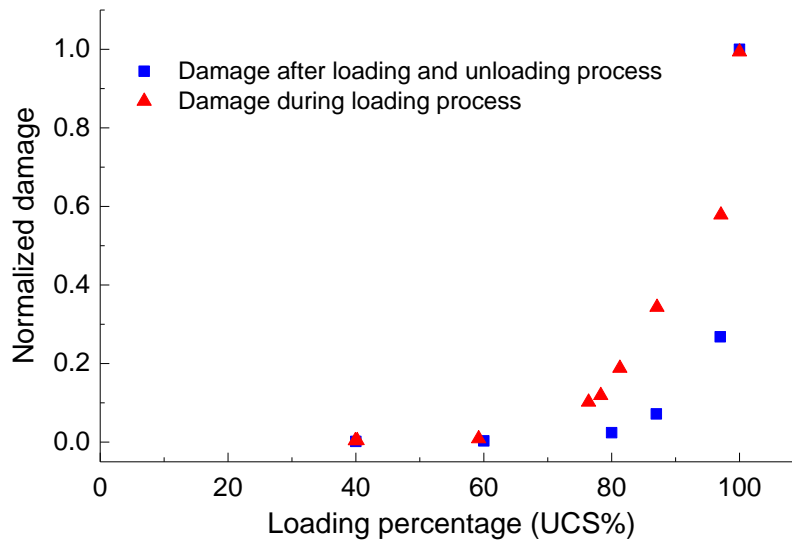


Figure 6.25 Comparison of normalized damages between after loading and unloading process and during loading process

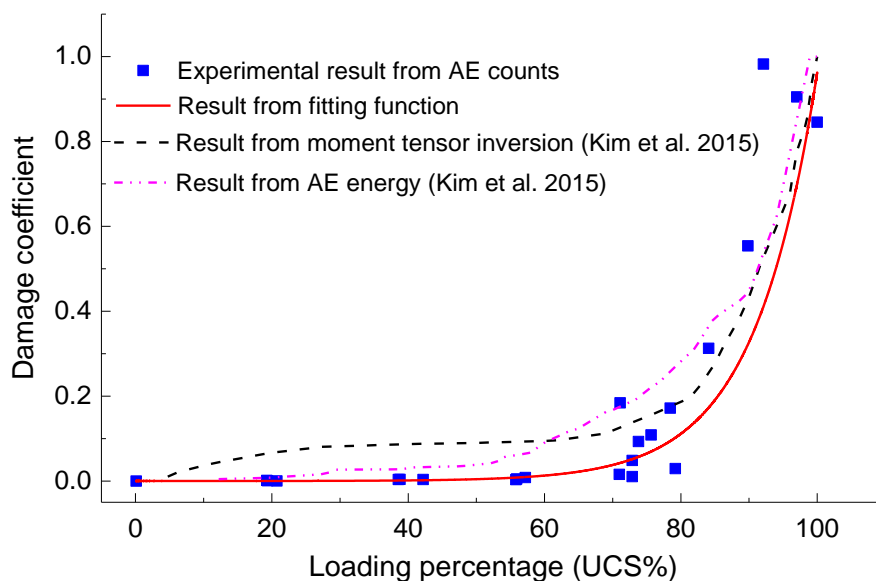


Figure 6.26 Comparison of normalized damages characterized in this chapter with the previous studies (Kim et al. 2015)

As seen from Fig. 6.25, when the stress applied to the granite sample is over 60% of UCS, the damage coefficient of the unloaded granite sample is smaller than that for the corresponding sample subjected to the same axial stress during the loading process. One possible reason could be the use of different methods in calculating the damage coefficient during the loading and post-loading processes, which caused the discrepancy. Another possible reason could be the closure of the stress-driven cracks after unloading,

which leads to a damage coefficient decrease. This is because the elastic opening and closure of microcracks is reversible if the stress is relieved, while the inelastic processes cannot be reversed (Browning et al. 2017; Han 2016; Rao and Ramana 1992). In addition, the micro-CT resolution applied for scanning the damaged samples is 61 μm , which cannot distinguish and detect the microcracks with scales smaller than 61 μm . Therefore, the unloaded sample may have in a relatively lower damage coefficient.

In this chapter, the AE counts are used to quantitatively characterize the damage evolution of a granite sample during the loading process, as shown in Eq. (6.5). The experimental result indicates that damage evolution during loading can be well fitted by an exponential function (see Eq. 6.6). To examine the validity and effectiveness of Eq. (6.6) and the damage evolution determined by AE counts in this chapter, our results are compared with previous results reported by Kim et al. (2015), as shown in Fig. 6.26. As seen in the figure, the damage coefficients determined by AE counts and fitting function during the loading process coincide with those obtained from the moment tensor inversion and AE energy (Kim et al. 2015). In particular, the transition normalized stress for damage evolution during the loading process, which is revealed by the present study and the previous study, is nearly identical, i.e., between 70%-80% of UCS. Therefore, the application of AE counts to quantitatively determine damage evolution during the loading process is concluded to be feasible, and Eq. (6.6) is suitable for analyzing damage evolution of the present granite sample during the loading process.

6.6 Conclusions

This chapter reports the study of granite damage evolution under static uniaxial compression using AE and micro-CT and the effects of damage evolution on ultrasonic P-wave propagation during the loading and post-unloading processes. The main conclusions are as follows:

- (1) P-wave propagation in granite samples is stress dependent. With increasing stress, the P-wave velocity and amplitude of the transmitted waveform first increased and then decreased when the axial stress exceeded a critical percentage of the UCS. The critical values are approximately 90 UCS% and 70 UCS% for P-wave velocity and amplitude, respectively.

-
- (2) AE is inactive when the axial stress is less than 60 UCS%, AE activities are continuously generated and numerous AE counts occur with the axial stress reaching the peak stress.
 - (3) AE counts could be used to quantitatively characterize damage evolution during the loading process. Crack areas determined by X-ray micro-CT scanning could be adopted to quantitatively characterize stress-induced damage inside rock samples after the loading and unloading processes.
 - (4) Damage evolution during the loading and post-unloading process are both highly nonlinear and can be well fitted with exponential functions. The fitting function is suitable for analyzing damage evolution during axial compression.
 - (5) The degree of damage is negligible when the axial stress applied to the rock sample is below approximately 60 UCS%. Eighty UCS% appears to be a transition point, above which damage evolution during loading and post-unloading are both significantly increased. The damage coefficient during the loading process is greater than the damage coefficient after unloading.
 - (6) Damage evolution in rock samples influences P-wave velocity, spectra and amplitude. However, compared with P-wave velocity, wave amplitude attenuation is more sensitive to damage/stress.

In this chapter, microcrack evolution and its effect on ultrasonic P-wave propagation in granite rock sample are studied. However, the existence of pre-existing defects in rocks on the macroscale is more general but more significant to the seismic behaviors of rocks due to more remarkable wave attenuation at these defects. Therefore, studies of seismic behaviors of rocks with macrodefects are needed and will be conducted in Chapter 7.

CHAPTER 7 INFLUENCE OF JMC, WATER CONTENT AND LOADING RATE ON THE MECHANICAL AND SEISMIC PROPERTIES OF A SINGLE ROUGH JOINT IN SHRB TESTS

In this chapter, stress wave propagation across a single rough joint is conducted in a modified SHRB system, with the aim to explore the influences of JMC and the infilling mixture water content and loading rate on the rough joint mechanical and seismic behaviors. Establishment and verification of the modified SHRB are first introduced. Stress wave propagation across the joint with and without infilling materials is performed under three elevated loading rates. The influences of JMC, loading rate and sand-clay mixture water content on deformation, specific stiffness, wave transmission and reflection coefficients and dissipation energy rate of the rough joint are analyzed in detail. The results show that JMC plays a dominant role in affecting the mechanical and seismic properties of the joint compared with the infilling mixture and loading rate.

7.1 Introduction

Apart from the pre-existing defect in grain scale, as studied in Chapter 6, there are numerous pre-existing defects on the macroscale, such as the flaws presented in Chapters 4 and 5, joints and joint sets. On the one hand, the presence of joints in rock masses may undermine the rock matrix strength and stiffness, thereby easily destabilizing the rock mass (Sagong and Bobet 2002; Sinha and Singh 2000), and on the other hand, the wave propagation across the joints may be attenuated (Pyrak-Nolt et al. 1990a; Zhu and Zhao 2013). Therefore, understanding the mechanical and seismic behaviors of joints is of great concern for rock engineers and seismologists to evaluate the safety and stability of underground structures subjected to static and dynamic loads.

To date, many theoretical and experimental studies have been conducted to investigate wave propagation across rock joints and joint sets. For instance, the DDM (Mindlin 1960; Pyrak-Nolte et al. 1990a, b; Schoenberg 1980) and the DSDM (Zhu et al. 2011b) have been applied to accurately predict transmission and reflection coefficients for a given incident wave propagation through linear or nonlinear joints and viscous joints, respectively (Cai and Zhao 2000; Fan and Wong 2013; Li et al. 2010; Pyrak-Nolte et al. 1990a, b; Wu et al. 2012, 2014; Zhao et al. 2006; Zhu et al. 2011a, b). Based on the

ultrasonic testing system and the SHPB device, a number of experiments have been performed with closed and filled joints. Those previous studies revealed that the normal stiffness of natural joints subjected to dynamic loading was higher than the normal stiffness of natural joints under static loading (Pyrak-Nolte et al. 1990a; Pyrak-Nolte and Nolte 1992). In addition, the dynamic normal stiffness of joints increased with JMC but decreased with joint thickness (Chen et al. 2015; Li et al. 2017), and the water content and filling thickness decreased the deformation of the quartz sand filled joint (Li and Ma 2009; Li et al. 2010). Moreover, Pyrak-Nolte et al. (1990a) revealed that adding normal stress and wetting the joint with liquid could both increase the transmission coefficient and reduce frequency attenuation.

However, natural joints are neither always open nor solely filled with sand and clay mixtures. Instead, the joint surfaces are often partially contacted or even bonded via the joints' asperities, while the remaining part is filled or partially filled with mixtures of sand, clay, water and air (Barton 1974; Sinha and Singh 2000; Zhao 1997a). Nevertheless, studies considering joint geometry coupling effects, e.g., JMC and notch thickness, and filling materials such as infilling types and water content, on stress wave propagation have never been reported thus far. Therefore, investigations focusing on the abovementioned issue are needed.

This chapter presents an experimental study on stress wave propagation through a single rough joint in SHRB tests, aiming to explore the influences of JMC and the infilling mixture water content and loading rate on the rough joint mechanical and seismic behaviors. The SHRB system preparation and composition is first described in detail. Then, single rock bar impact tests in combination with ultrasonic wave propagation tests are conducted to determine the critical incident stress wave amplitude. Subsequently, verification tests are conducted to confirm the SHRB system feasibility and validity. Finally, the mechanical properties, i.e., stress-strain curves, deformation and specific stiffness, and the seismic behaviors such as transmission and reflection coefficients and energy dissipation rate of the rough joints are investigated and analyzed in detail.

7.2 Experiment setup

7.2.1 Rock bar preparation

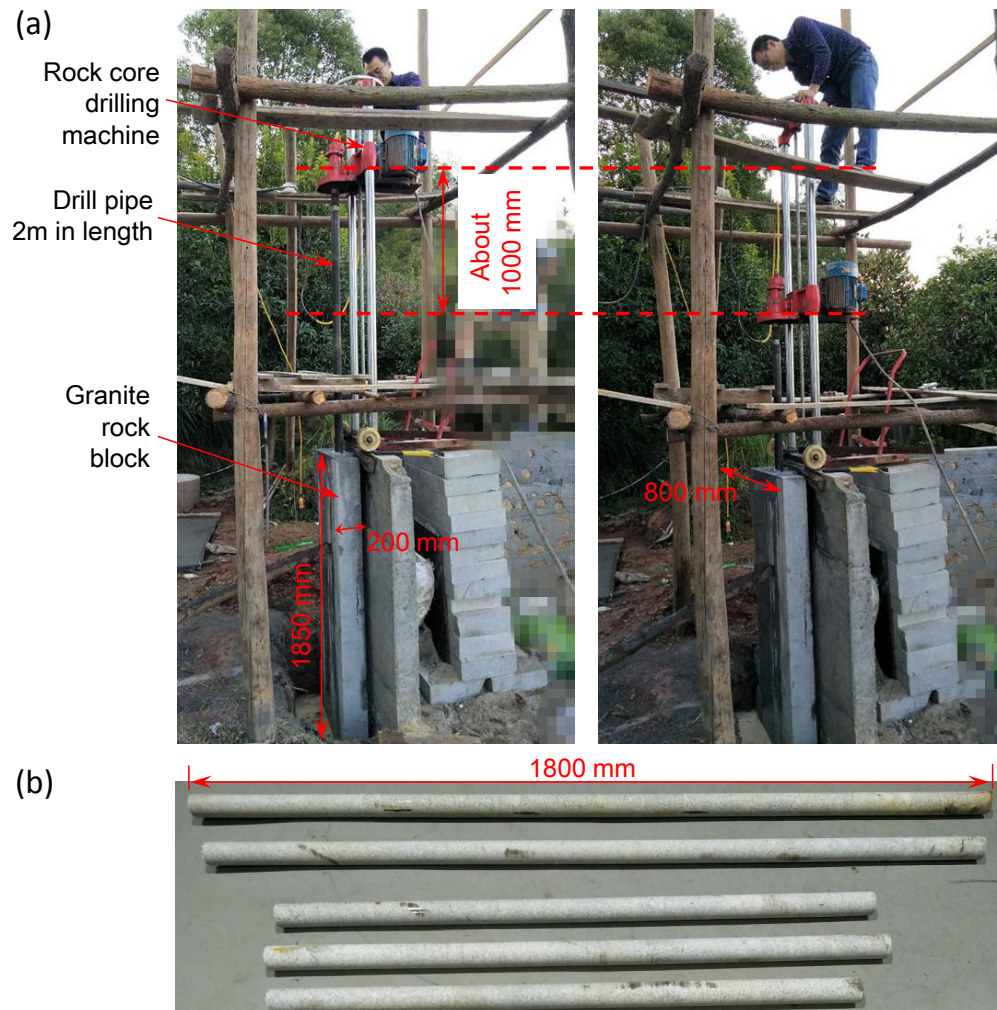


Figure 7.1 Rock bar drilling site

To establish the SHRB system, the key task is to successfully prepare high-quality long rock bars. To achieve this goal, we directly drilled long rock bars in a large granite block instead of collecting rock bars from the engineering geological drilling site. Figure 7.1a shows the rock bar drilling site where the granite block was verified to be without obvious surface macrocracks. The granite block dimensions were approximately 1.85 m in length, 0.8 m in width and 0.2 m in thickness. An electric hand drill with a drill pipe 2 m in length was used to core the long rock bars. To successfully drill long rock bars and guarantee their quality, the drilling speed was controlled at approximately 6 mm/min, and tap water was used to cool the drill and the head of the rock bar during the rock coring process. Figure 7.1b exhibits granite rock bars with lengths between 1.1 m and 1.8 m and

diameters of approximately 48 mm. The long granite bars were examined and determined to be without visible surface cracks and damages during the drilling process.

7.2.2 Split Hopkinson rock bar

Figure 7.2 shows the SHRB system with a spring clamping device and a schematic view of the rock bar sections at Geotechnical Institution of Tianjin University. The SHRB system mainly consists of an incident, a transmission and an absorption rock bar with a diameter of approximately 48 mm, a striker launching device, an incident steel bar with a diameter of 50 mm, and a data acquisition unit. The incident and transmission rock bar lengths are 1.77 m and 1.64 m (with length/diameter > 30). The physical and mechanical properties of the granite bars are the same as those displayed in Table 6.1 in Chapter 6. The surface of the granite bars was polished by sand paper, and the bar ends were ground flat and polished to less than 0.05 mm.

A gas gun device was adopted to launch the striker in this chapter, which generated stress waves in rock bars under relatively higher loading rates (up to approximately 900 GPa/s) compared to those launched by the compressed spring device (Wu et al. 2012) and pendulum hammer (Li and Ma 2009). A steel incident bar with a diameter of 50 mm and length of 2.5 m was placed in front of the rock bars, which could aid the incident rock bar in avoiding direct impacts from the steel striker. A short cylindrical striker made of hardened 60 Si₂Mn with a diameter of 50 mm and length of 25 mm was applied to generate incident wave pulses with short durations when impacting the end of the steel bar. To eliminate wave dispersion and oscillation in the rock bars, a C1100 copper disc with a diameter of 10 mm and thickness of 1 mm was adopted as the pulse shaper. This disc was placed at the center of the steel bar impact end and assisted in generating a smooth and nondispersive incident wave pulse when impacted by the striker.

The data acquisition unit contains an 8-channel dynamic strain amplifier and an 8-channel Hioki 8860-50 recorder with a sampling rate of 10 MHz per second. The strain signals in bars were detected and recorded by the strain gauges placed on the surface of the bars. To guarantee the strain signal measurement accuracy and assess the initial damage effect within the rock bars on the wave propagation, two sets of strain gauges were placed on each rock bar. Since the incident wave duration was approximately 120 μs, which is determined by the steel striker length (20 mm), the strain gauge stations were

350 mm away from the rock bar ends, as shown in Fig. 7.2b. The strain gauge groups were arranged to approximately seven times the diameter length from the bar end to eliminate the lateral inertia effect (Meng and Li 2003; Wu et al. 2012) and adjacent to the rock bar ends to minimize the material damping influence. Furthermore, this arrangement provides enough distance to separate the incident waveform from the reflected waveform generated at the incident rock bar and transmitted rock bar contact interface.

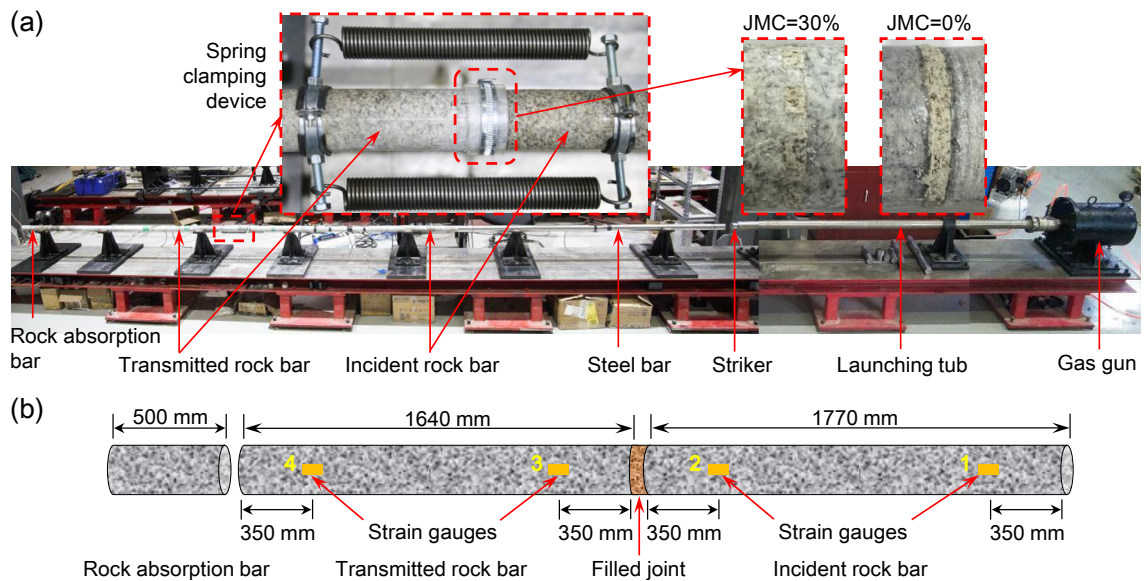


Figure 7.2 (a) Split Hopkinson rock bar system with spring clamping device; (b) Schematic view of the rock bars section

7.2.3 Rock joint

To study the JMC effect on wave propagation and attenuation in a rock mass, symmetrically arranged rough joint asperities and saw cut notches (Fig. 7.3a) were directly fabricated at the transmission rock bar front end. The width of the joint aperture was set to 6 mm, and the joint thickness was 4 mm. Figure 7.3a shows the original rough joint arrangements with a JMC of 30%. During testing, the rough joint asperities were gradually ground off and polished to generate new joint surface arrangements with a lower JMC, i.e., 19%, 8% and 0%, as shown in Figs. 7.3b-d. The purpose of grinding off the joint asperities rather than cutting the rough joint asperities on other rock bars was mainly to avoid the influences of heterogeneity and initial damages inside the rock bars on the wave propagation results.

Naturally, joints and faults are often filled with rock debris, soil and water, which affect

the seismic properties of rock discontinuities. In this chapter, the filling material and water content effects on wave propagation across rock joints is investigated. The filling material is a mixture of quartz sand and kaolin clay. According to Wu et al. (2014), the quartz sand was sieved to control its particle size between 1 mm and 2 mm, and the kaolin clay powder was screened through a 0.25 mm sieve. The weight ratio of quartz sand to kaolin clay is set as 7:3 because the sand-clay mixture with a 30% clay weight fraction of kaolin clay can completely fill the void space among the quartz sand particles (Wu et al. 2014). To investigate the sand-clay mixture water content effects on wave propagation, four water contents are applied, i.e., 0%, 15%, 20% and 25% in weight percentage. The sand-clay mixture bulk densities with water contents of 0%, 15%, 20% and 25% are 1.31 g/cm³, 1.91 g/cm³, 1.88 g/cm³ and 1.86 g/cm³, respectively. Figure 7.4 shows the sand-clay mixtures with four different water contents. The mixture without water is loose and cannot be fully compacted, while the mixture with 15% water content is very dense and has low viscosity. With increasing water content, the viscosity of the mixtures increases. For the mixture with a water content of 25% in particular, the water seeped out without any compaction.

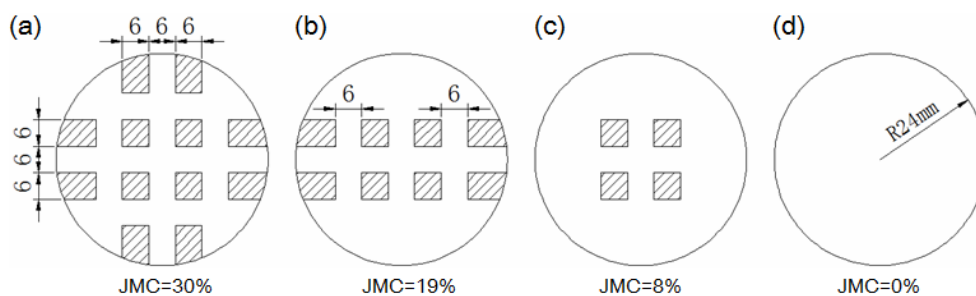


Figure 7.3 Schematic view of distribution of the joint with different JMC. The shaded part indicates the asperities on joint surface.



Figure 7.4 Illustration of sand-clay mixture with different water content

When filling the joint, the rough joint asperities were lubricated with a thin layer of Vaseline before coming into contact with the incident rock bar. Then, the stirred sand-clay mixtures were gradually placed in the joint layer by layer. To fully fill the joint notches,

the mixtures were compacted by the same operator with an iron rod with a diameter of 2 mm. Figure 7.2a demonstrates two joints (JMC=30% and 0%) filled with a sand-clay mixture with a water content of 15%. A transparent PVC tub was used to prevent sand-clay mixture outflow, as shown in Fig. 7.2a. A 1-mm-thermoplastic-film layer was placed between the rock bar surface and the PVC tub to fill the small gap. To ensure the result repeatability, three parallel tests were performed for each joint filling condition.

7.2.4 Spring clamping device

In this chapter, a spring clamping device was installed between the incident and transmitted rock bars (see Fig. 7.2a) to combine the two bars tightly together. The stiffness coefficient of the spring is 20.3 N/mm. During all tests, the two springs were stretched by the same distance (5 mm) to provide identical axial pressure of approximately 56 KPa.

7.2.5 Data processing

Based on one-dimensional wave propagation theory, the dynamic stress $\sigma(t)$, strain $\varepsilon(t)$ and closure $D(t)$ of the joint can be determined by (Zhou et al. 2012):

$$\sigma(t) = \frac{E}{2} [\varepsilon_1(t) + \varepsilon_R(t) - \varepsilon_T(t)] \quad (7.1)$$

$$\varepsilon(t) = \frac{C}{L_s} \int_0^t [\varepsilon_1(t) - \varepsilon_R(t) - \varepsilon_T(t)] dt \quad (7.2)$$

$$D(t) = L_s \cdot \varepsilon(t) = C \int_0^t [\varepsilon_1(t) - \varepsilon_R(t) - \varepsilon_T(t)] dt \quad (7.3)$$

where E and C are the Young's modulus and P -wave velocity of the granite rock bars; L_s is the thickness of the joint; $\varepsilon_1(t)$, $\varepsilon_R(t)$ and $\varepsilon_T(t)$ are incident strain, reflected strain and transmitted strain measured by the strain gauges mounted on the incident and transmitted rock bars as shown in Fig. 7.2b; t is the duration of the waveform.

Transmission coefficient T_c and reflection coefficient R_c are commonly utilized to analyze the influence of JMC, loading rate and sand-clay mixture water content on wave propagation across rock joints. T_c and R_c are defined as the ratio between the peak values of the transmitted/reflected wave and the incident wave, which are derived as (Li et al.

2017b):

$$T_c = \frac{\max \varepsilon_T(t)}{\max \varepsilon_I(t)} \quad (7.4)$$

$$R_c = \frac{\max |\varepsilon_R(t)|}{\max \varepsilon_I(t)} \quad (7.5)$$

In addition to T_c and R_c , wave energy is also widely analyzed to determine the rock joint effects on the wave propagation through the joint. According to the one-dimensional wave propagation theory in the SHPB test, the energy of the incident E_I , reflected E_R , and transmitted E_T waves can be determined by the following (Zhang and Zhao 2014b):

$$E_I = \frac{AE^2}{\rho C} \int_0^t \varepsilon_I^2(t) dt \quad (7.6)$$

$$E_R = \frac{AE^2}{\rho C} \int_0^t \varepsilon_R^2(t) dt \quad (7.7)$$

$$E_T = \frac{AE^2}{\rho C} \int_0^t \varepsilon_T^2(t) dt \quad (7.8)$$

where A and ρ are the cross-sectional area and density of the rock bars, respectively.

After the surfaces of the joint asperities were lubricated, the friction between the joint asperities and incident rock bar was negligible. Meanwhile, as no visible micro and macrocracks were found at the rock bar surfaces, the energy attenuation caused by the initial damage inside the rock bars could be neglected. Hence, the energy dissipated by the joint (filled or nonfilled one) can be derived as follows:

$$E_D = E_I - E_R - E_T \quad (7.9)$$

7.3 Results

7.3.1 Determination of the critical incident stress

Before conducting the SHPB tests on rock bars with a single joint, we first performed wave propagation in a single rock bar with a relatively short length, i.e., 850 mm. This is because we need to determine a critical incident stress value that will not damage rock bars with low dynamic tensile strength, i.e., 18.4 MPa. To determine the maximum

allowable incident stress, a single, short rock bar was sequentially impacted with elevated incident stress. Notably, an absorption rock bar was used to transmit the incident wave in the short rock bar, which could protect the short rock bar from being spalled by the reflected tensile stress wave generated at the bar end. After each impact, ultrasonic P-wave propagation tests were conducted with the short rock bar. By analyzing the evolution law of the P-wave velocity, amplitude and waveform of the transmitted wave, the critical incident stress, which causes damage in the rock bar, could be found. The reason for using ultrasonic tests to determine the critical incident stress is that ultrasonic wave propagation is sensitive to defects such as microcracks and voids, and these tests have been widely applied to assess the microstructural state of concrete and rock (Prassianakis and Prassianakis 2004; Zhou et al. 2018b).

Figure 7.5 illustrates the effects of elevated impacts on ultrasonic P-wave propagation in the short rock bar. As seen in Fig. 7.5a, the P-wave velocity of the short rock bar was kept nearly constant even though the rock bar was impacted 17 times with an increasing dynamic loading stress up to approximately 100 MPa. However, the peak-to-peak amplitudes of the first arriving transmitted waveform showed the opposite trend, as shown in Fig. 7.5b. The average value sum of the maximum amplitude and the absolute average value of the minimum amplitude (see Fig. 7.5c) fluctuated slightly during the first eight impacts with incident stresses of less than 30.1 MPa. Then, from the ninth impact, the average value sum decreased with incident stresses over 34.7 MPa. Regarding waveform, although the first halves of the waveform lengths of the transmitted waves were nearly identical to each other, the length of the whole waveform was remarkably extended with an impact stress surpassing 34.7 MPa. Moreover, the peak waveform amplitude gradually decreased and shifted to the right from the ninth impact with an incident stress equal to 34.7 MPa (see Fig. 7.5c). Based on the above results, the incident stress applied to the rock bars should be less than 30.1 MPa in the case of inducing damage in the rock bar, which may attenuate the wave propagation in rock bars. Therefore, three incident stress levels of 10 MPa, 15 MPa and 25 MPa were selected to study the loading rate effects on wave propagation and attenuation in rock bars with a single joint.

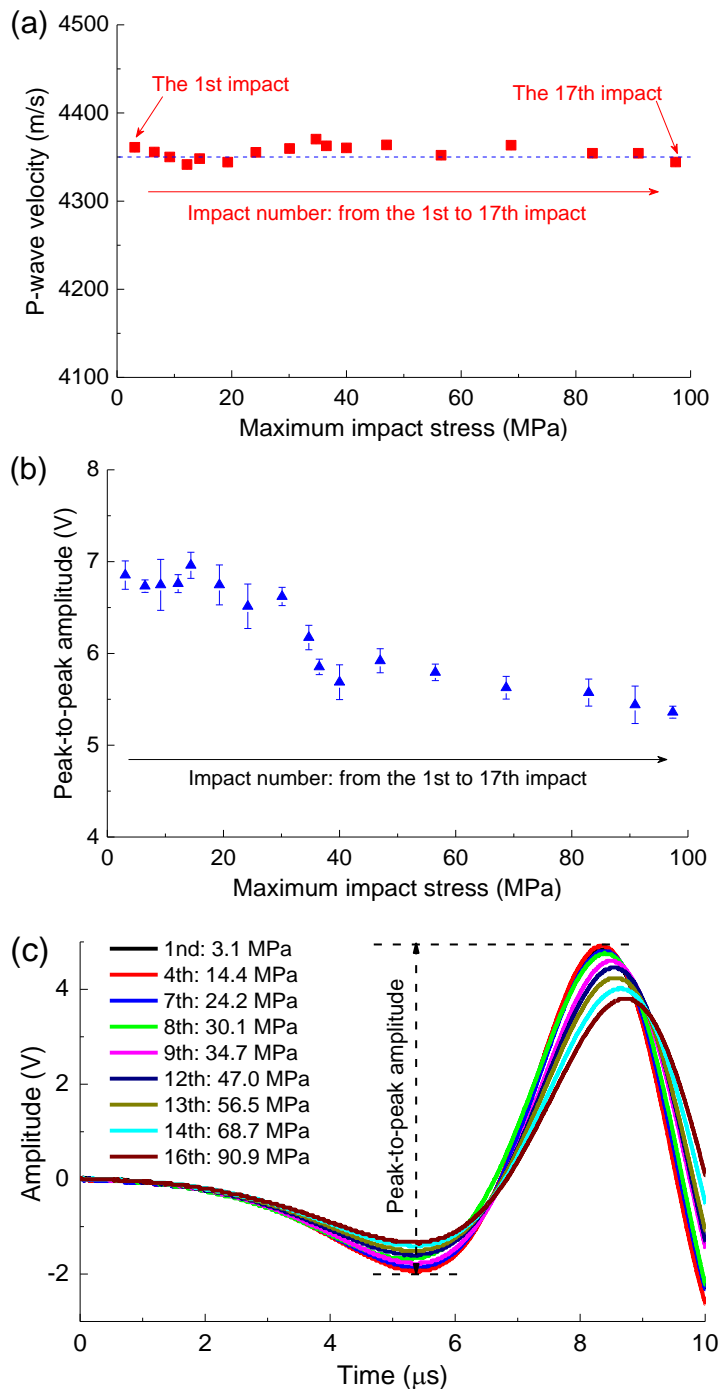


Figure 7.5 (a) P-wave velocity of the rock bar after each impact; (b) The peak-to-peak amplitude of the first arriving ultrasonic waveform after each impact; (c) Nine typical waveforms of the first arriving ultrasonic wave after the corresponding impact

7.3.2 Verification of the SHRB test

A verification test was first conducted by directly contacting the rear end of the incident rock bar to the rear end of the transmitted bar (without joint notches) to confirm the

SHRB system feasibility and validity. Figure 7.6a shows waveforms recorded by the four strain gauge sets placed on the rock bars (see Fig. 7.2b) during this test. Although the strain signals along the two bars exhibit some discrepancies, such as the peak amplitude gradually decreasing along the bars, the discrepancy between the two signals in the same rock bar was less than 5%. This discrepancy could be attributed to the attenuation caused by the initial damage inside the rock bars and the reflection at the interface between the incident and transmitted bars due to the small mismatch of the two rock bars. In addition, the strain signals recorded by the two adjacent strain gauges (gauges 2 and 4) mounted on the incident bar and transmitted bar were similar. Figure 7.6b shows the stress equilibrium calculated using the strain signals measured by strain gauges 2 and 4. The transmitted stress was nearly coincident with the sum of the incident stress and reflected stress, which indicated that the stress equilibrium was well achieved and maintained during the loading duration. Therefore, the wave propagation in the SHRB tests is concluded to be feasible and valid, and the accuracy of computing the wave propagation and attenuation using the strain signals recorded by the two strain gauges adjacent to the joint can be guaranteed.

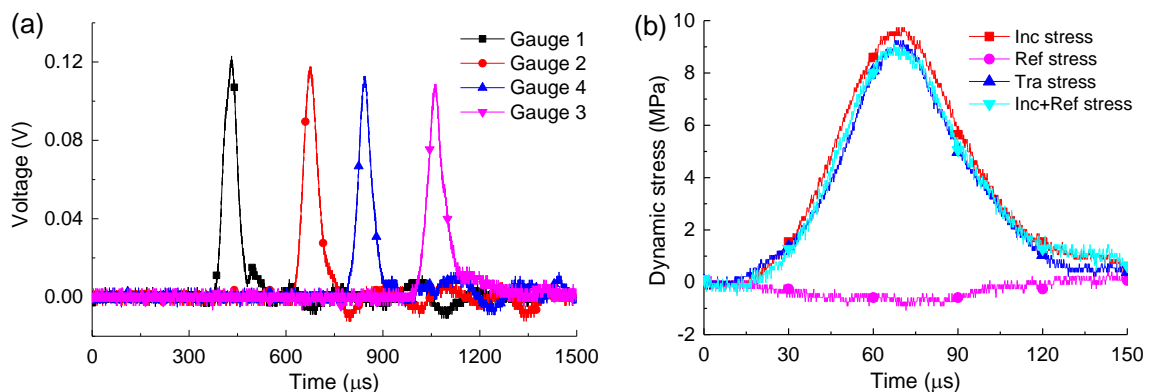


Figure 7.6 (a) Strain signals recorded on the incident and transmitted rock bars; (b) Stress equilibrium between incident and transmitted rock bars

7.3.3 SHRB wave propagation with single rough joint

A total of sixty experimental cases were studied, including five water contents (i.e., nonfill condition, 0%, 15%, 20% and 25%), four JMCs (i.e., 30%, 19%, 8% and 0%) and three loading rates (i.e., approximately 300 GPa/s, 520 GPa/s and 860 GPa/s). Three parallel tests were performed for each case to guarantee the repeatability of the results. The loading rate was defined as the slope at half the peak stress of the incident stress-time

curve, as shown in Fig. 7.7. Table 7.1 summarizes some of the major results in average values, in which ω , k_n and d represent water content, joint specific stiffness and closure of the joint, respectively.

Table 7.1 Summary of some major results in average values

JMC (%)	ω (%)	Loading rate (GPa/s)	k_n (MPa/mm)	T_c (%)	R_c (%)	R_e (%)	d (mm)
30	-	311	489	64.8	26.0	13.9	0.015
		537	858	68.6	21.9	14.3	0.019
		860	1303	71.9	18.7	11.8	0.024
	0	273	602	70.5	22.3	9.0	0.014
		550	939	73.7	19.6	8.6	0.018
		905	1646	75.0	16.0	9.6	0.023
	15	345	614	71.8	20.6	8.2	0.012
		533	1121	74.3	18.4	10.4	0.015
		863	1610	76.5	15.0	11.2	0.021
	20	324	636	70.9	22.3	9.4	0.013
		504	1020	72.7	20.0	9.7	0.016
		879	1453	75.9	16.0	9.4	0.021
25	311	311	69	22.3	11.3	0.014	
	512	850	70.4	20.3	14.4	0.019	
	883	1337	73.8	16.5	12.7	0.024	
19	-	302	339	46.6	35.9	15.6	0.021
		529	542	52.1	30.7	16.4	0.029
		860	879	53.4	25.7	16.0	0.036
	0	294	403	53.9	33.7	12.7	0.018
		505	762	57.0	28.3	16.6	0.025
		876	1037	59.0	24.3	13.9	0.033
	15	268	455	57.1	31.8	13.2	0.018
		550	811	60.1	25.3	12.6	0.023
		837	1148	60.8	22.9	11.9	0.030
	20	300	437	56.3	34.1	13.1	0.022

		564	763	58.7	29.2	11.7	0.026
		834	1028	59.6	23.6	13.6	0.034
		335	429	53.5	34.8	16.5	0.023
	25	494	707	57.2	30.8	13.6	0.027
		865	1051	58.2	24.5	15.6	0.035
		308	246	33.9	46.3	22.1	0.034
	-	520	412	36.0	41.6	23.1	0.046
		867	696	37.8	34.3	21.6	0.060
		296	309	38.2	44.5	20.0	0.034
	0	539	524	40.0	37.3	21.2	0.041
		881	862	41.9	30.3	19.0	0.054
		307	383	39.6	42.6	20.0	0.032
8	15	495	591	41.2	34.5	19.6	0.042
		886	930	42.2	27.7	20.8	0.049
		304	334	38.3	40.6	20.5	0.031
	20	499	562	39.3	34.7	22.8	0.043
		847	915	41.0	26.7	21.0	0.050
		328	303	37.0	44.7	21.5	0.036
	25	575	567	39.0	39.4	21.2	0.045
		896	915	40.7	31.0	23.4	0.054
		298	41	6.7	63.9	43.3	0.065
	0	526	86	6.5	56.0	45.5	0.108
		908	241	7.6	52.3	50.0	0.187
		349	143	12.9	59.4	38.3	0.051
	15	549	290	14.6	52.9	42.0	0.083
		879	550	17.7	50.2	45.3	0.113
0		274	128	10.7	60.4	39.9	0.057
	20	512	265	12.0	54.7	44.7	0.085
		832	532	13.7	50.6	46.6	0.125
		338	120	9.7	61.4	42.5	0.063
	25	496	264	11.3	55.1	43.7	0.087
		821	506	12.1	54.1	46.8	0.137

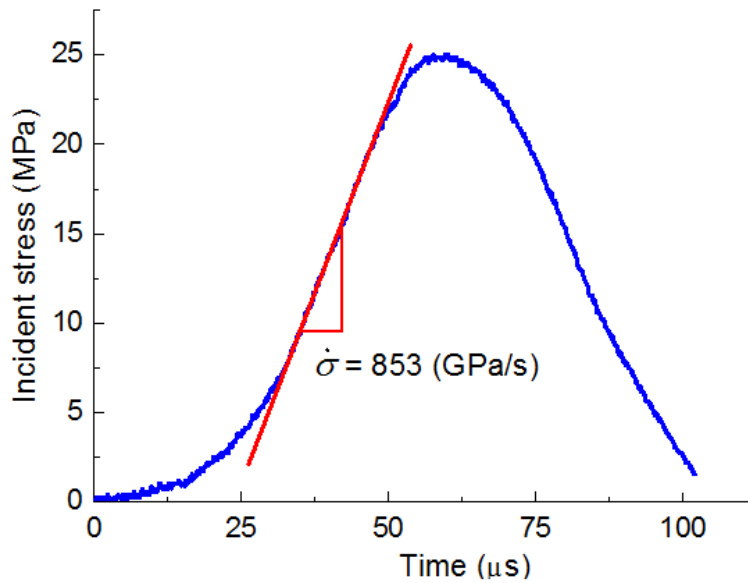


Figure 7.7 Loading rate calculation from incident stress-time curve

7.3.3.1 Stress-strain behaviors

As the effects of JMC, loading rate and sand-clay mixture water content on stress-strain behaviors exhibit a similar trend, only some of the typical stress-strain curves are presented and analyzed. Figure 7.8a shows some typical stress-strain curves of the unfilled joints subject to different loading rate impacts. Both the peak stress and maximum strain of the nonfilled joints increase with the loading rate for the same JMC. For a specific loading rate, the peak stress of the joint increases with increasing JMC, whereas the maximum strain of the joint shows the opposite trend. In addition, the elastic modulus of the joint, defined as the prepeak linear portion slope in the stress-strain curve, increases with an increasing loading rate and JMC.

Figure 7.8b shows the effects of the sand-clay mixture water content on the dynamic stress-strain behaviors of the joint (JMC=19%) subject to a given loading rate of approximately 860 GPa/s. The peak stress and the elastic modulus of the joint filled with the sand-clay mixture are larger than those of the nonfilled joint, despite the difference induced by the water contents. In contrast, the maximum strains of the filled joints with different water contents are all lower than the nonfilled joint. The peak stress of the filled joint reaches a peak when the water content increases from 0% to 15% and then slightly decreases with further increases in water content.

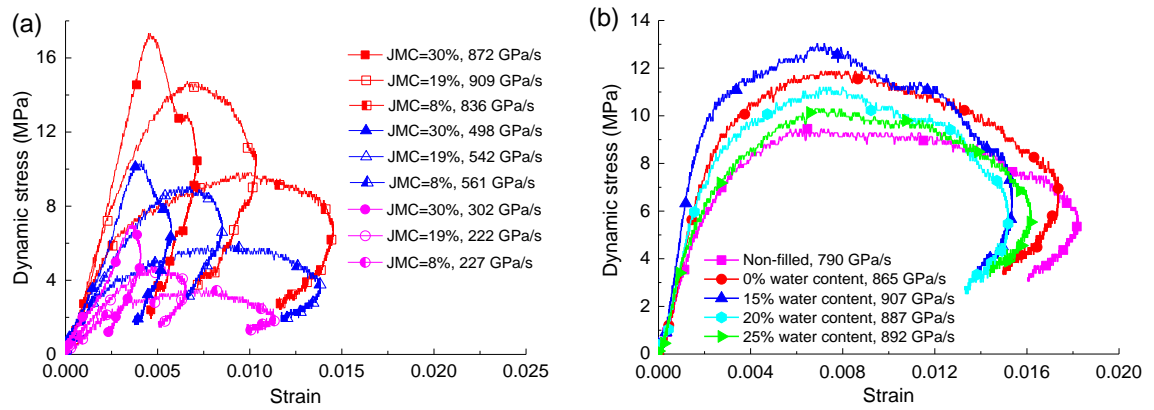


Figure 7.8(a) Typical stress-strain curves of the unfilled joints under different loading rate impacts; (b) Typical stress-strain curves of the joint (JMC=19%) filled with sand-clay mixture with different water contents

7.3.3.2 Deformation behaviors

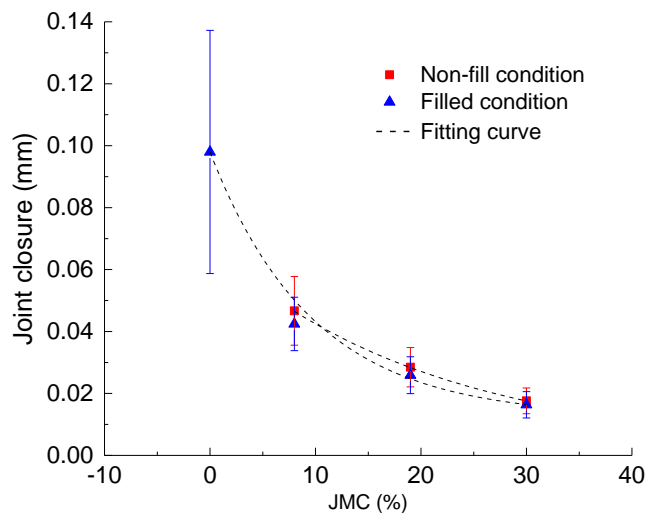


Figure 7.9 Joint closure vs JMC of the non-filled and filled joints

The average joint closure d as a function of JMC is shown in Fig. 7.9. As shown in the plot, the average closures of the filled and nonfilled joints both decrease in an exponential manner with increasing JMC regardless of the loading rate effect. When JMC is between 8% and 30%, which is attributed to the sand-clay mixture, d is approximately 9% lower than that of the nonfilled joint. For the nonfilled joint, d reduces by 62% when the JMC rises from 8% (0.047 mm) to approximately 30% (0.018 mm). Regarding the filled joints, d decreases in a steeper manner with increasing JMC compared to the nonfilled cases. This value drastically decreases from approximately 0.1 mm to 0.042 mm when the JMC changes from 0% to 8% and then continuously decreases to the lowest point of 0.016 mm

when the JMC further increases to 30%. Figure 7.9 also illustrates that the error bar scale gradually increases with a decreasing JMC. This is because the loading rate effect is more apparent for the joint with a smaller JMC, resulting in a more scattered result, as shown in Fig. 7.10.

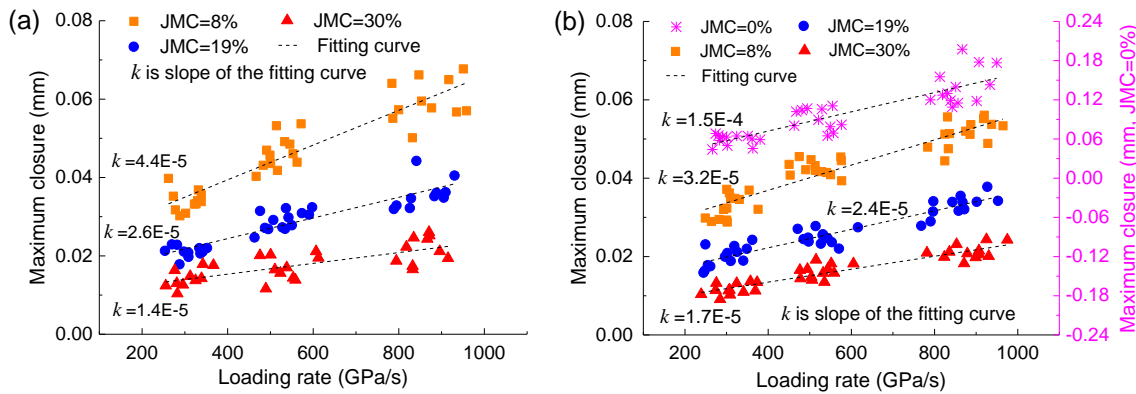


Figure 7.10 (a) Joint closure vs loading rate of the non-filled joint; (b) Joint closure vs loading rate of the joint filled with sand-clay mixture

Figure 7.10 shows a plot of the loading rate effect on the joint closure evolution with and without the sand-clay mixture. This figure shows that the joint closure exhibits a distinct loading-rate-dependent characteristic, which increases almost linearly with an increasing loading rate. The fitting curve slope for the joint with smaller JMC is steeper than the slope of the curve for the joint with a larger JMC, which indicates that the loading rate effect is more remarkable for the joint with a smaller JMC. For a given loading rate, the maximum closure of the joint sharply decreases with increasing JMC, and the rate of decrease is larger for the high loading rate, as shown in Fig. 7.10.

Figure 7.11 summarizes the water content effects on the average closure of the joints filled with the sand-clay mixture, which is subject to the impact of three elevated loading rates. Similar to the variation in R_c affected by water content, the joint closure evolution also appears as a concave shape, and the lowest point occurs at a water content of approximately 15%. Likewise, the loading rate plays a significant role in joint closure, but the general variation tendency of d with water content change remains unmodified. In general, for a given loading rate, d slightly declines when the joint changes from a nonfilled condition to a dry-filled condition and continues to decline with further increasing water content. Then, the filled joint closure reaches the bottom at a 15% water

content and then gradually increases when the water content further increases. Although d increases with a water content over 15%, the maximum joint closure with a 25% water content is basically still less than the maximum joint closure of the nonfilled joint. For the joint with JMC=0%, as the joint gap is filled with a only the sand-clay mixture, the maximum closure of the joint exhibits the strongest loading rate effect (see Figs. 7.10b and 7.11d), and d is several times larger than that of the joint with a JMC between 8% and 30%.

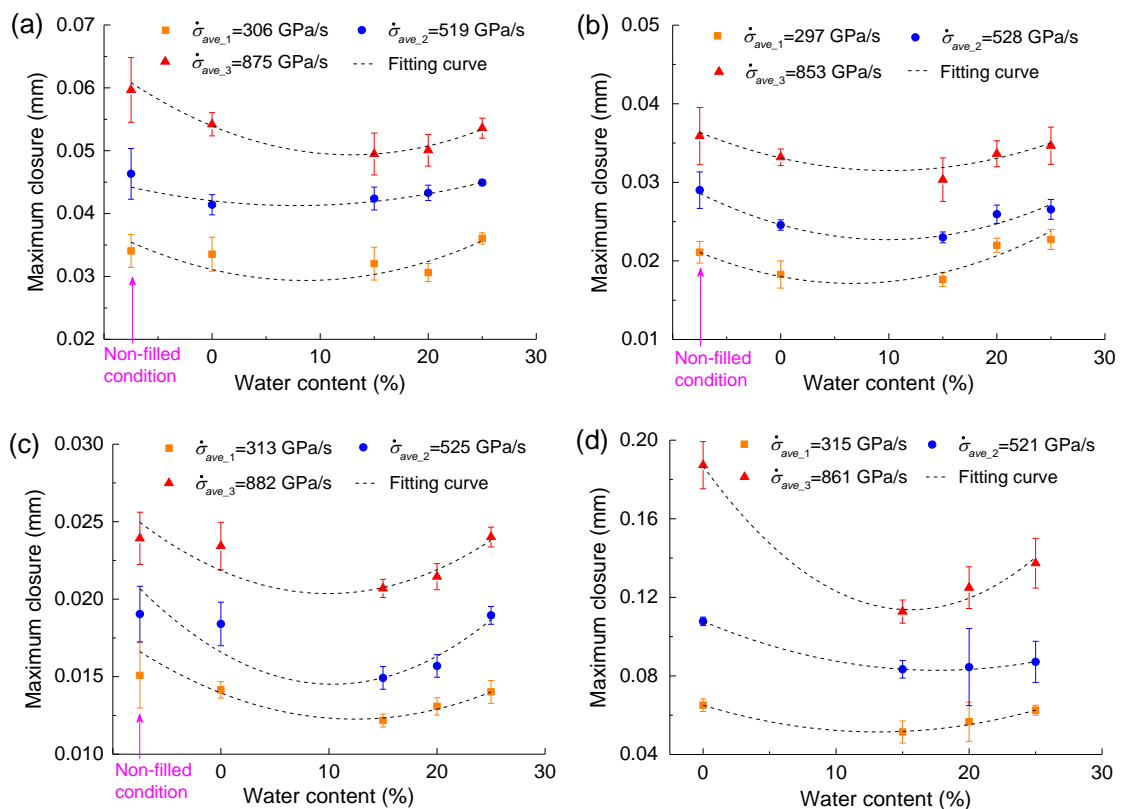


Figure 7.11 Joint closure vs water content and loading rate of the joint with infilling material. (a)-(d): Joints with JMC equal to 8%, 19%, 30% and 0%, respectively

The water content has a comparable effect on the maximum closure of the filled joints with a JMC between 8% and 30%, but the water content affects the filled joint more with a JMC=0, especially at high loading rates. Specifically, when the JMC is between 8% and 30%, the maximum closure is reduced by an average of approximately 7% when the water content rises from 0% to 15% and increases by an average of approximately 6.5% when the water content changes from 15% to 25%. However, under the impact of 860 GPa/s, the maximum filled joint closure with a JMC=0% decreases by approximately 40% when the water content increases from 0% to 15%.

7.3.3.3 Joint specific stiffness

During the compressive loading process, a stress increment generates elastic deformation of the joint asperities, which leads to a displacement increment across the joint. The ratio of these two quantities is generally termed the joint specific stiffness k_n (Pyrak-Nolte et al. 1990a). A large number of experimental studies have shown that k_n is not a constant value for a joint with a specific geometry, which behaves in a nonlinear fashion with increasing stress during compression. In this chapter, since we mainly focus on the overall variation of k_n as a function of JMC, loading rate and filling conditions, the nonlinear evolution of k_n during the compression process is not considered. To simplify the analysis, the joint specific stiffness is therefore defined as the tangent gradient of the prepeak linear portion of the transmitted stress-closure curve (Wu et al. 2014). Figure 7.12 outlines the joint specific stiffness calculation from a typical transmitted stress-closure curve.

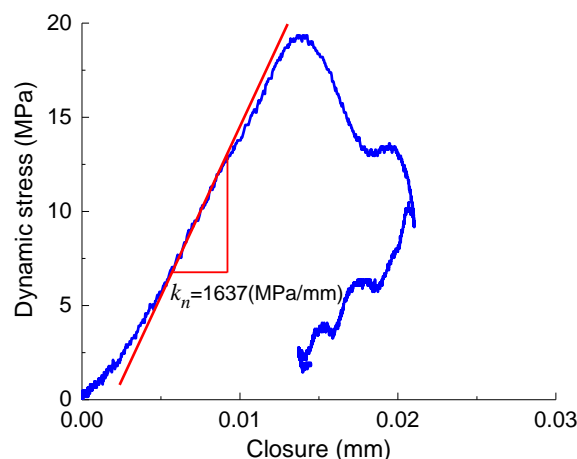


Figure 7.12 Joint specific stiffness calculation from transmitted stress-closure curve

Figure 7.13 shows the variation in k_n with the filled and nonfilled joint JMCs subject to three elevated loading rate impacts. The results reveal that k_n increases almost linearly with increasing JMC, and for a given JMC, k_n increases with an increasing loading rate. For a given nonfilled or filled joint, the k_n increases by an average of approximately one and three-fifths when the loading rate changes from the lowest (~ 310 GPa/s) to the highest (~ 860 GPa/s). Meanwhile, the loading rate effect on k_n is enhanced with increasing loading rate, which is found based on the slope variation for the fitting curves. In addition, the k_n of the filled joint is stiffer than the corresponding nonfilled joint when subjected to a comparable loading rate impact. Furthermore, the sand-clay mixture is more helpful for improving the k_n of the joint with a smaller JMC. For instance, by

comparison with the nonfilled joint k_n , the filled joint k_n with a JMC equal to 8% increased by an average of 35.2%, while this value was only enhanced by approximately 19% for the joint with a JMC of 30%.

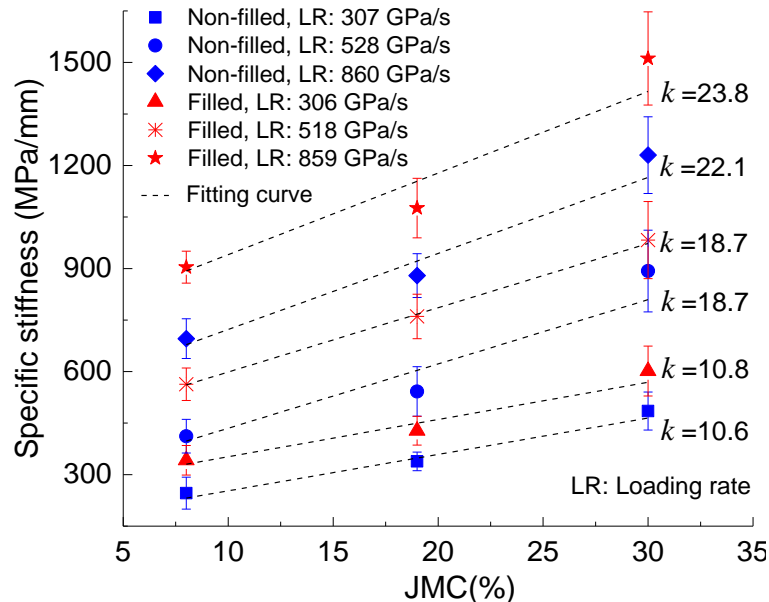


Figure 7.13 Variation of joint specific stiffness with JMC of the filled and non-filled joints under different loading rate impacts. k is the slope of the fitting curve.

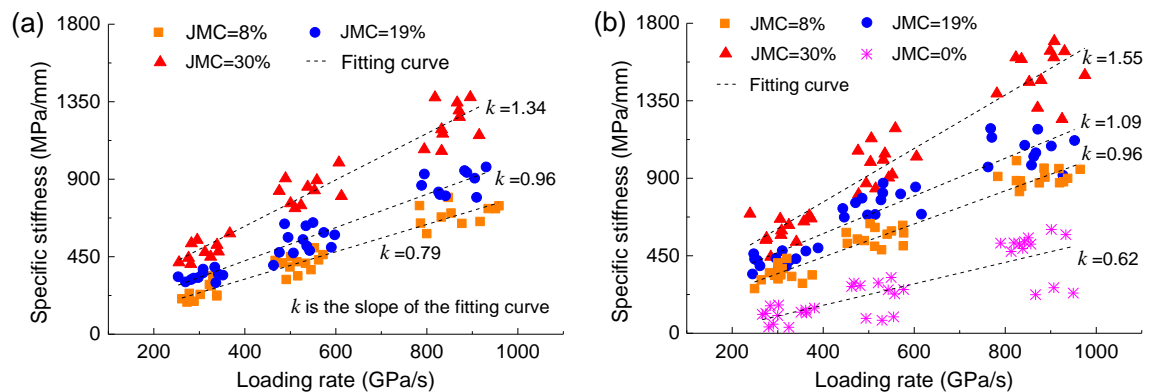


Figure 7.14 Joint specific stiffness vs loading rate of the non-filled and filled joints. (a) Non-filled joint; (b) Joint filled with sand-clay mixture. k is the slope of the fitting curve.

The loading rate influence of the nonfilled and filled joints on k_n is demonstrated in Fig. 7.14. As joint specific stiffness is inversely proportional to joint closure, the variation in k_n with loading rate therefore shows the opposite trend (see Fig. 7.10). That is, the larger the joint JMC, the stronger the loading rate effect on k_n , and vice versa. Moreover, the joint filled with the sand-clay mixture displays a more pronounced loading rate effect

than the corresponding nonfilled joint. These two phenomena are confirmed by the slope variation of the fitting curve, as shown in Fig. 7.14.

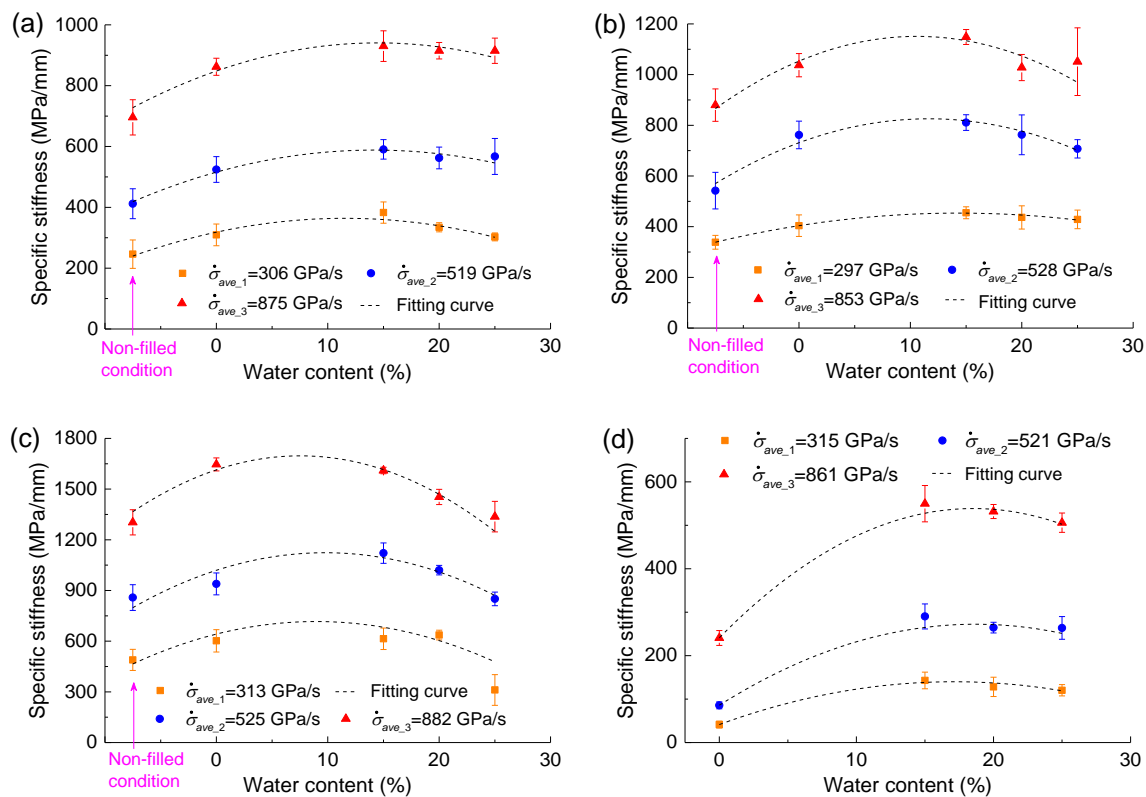


Figure 7.15 Joint specific stiffness vs water content and loading rate of the joint filled with sand-clay mixture. (a)-(d): Joints with JMC equal to 8%, 19%, 30% and 0%

Figure 7.15 reveals the water content effect on the average k_n of the joints filled with the sand-clay mixture. The results clearly indicate that the loading rate has a strong effect on the evolution of k_n , specifically, the higher the loading rate, the greater the joint specific stiffness. However, the loading rate effect does not disturb the water content influence on the evolution of k_n . Similar to the variation of T_c affected by the water content, the variation of k_n also shows a convex shape. The k_n value peaks at a water content of approximately 15% and increases by an average of approximately 10% when the water content changes from 0% to 15%. Nevertheless, for the filled joint with a JMC of 30%, when the water content is increased to 25%, the average k_n is nearly 10% lower than the corresponding nonfilled joint. With regard to the filled joint with a JMC=0%, the k_n shows not only a strong loading rate-dependent behavior but also exhibits noticeable water content-dependent characteristics, as shown in Fig. 7.15d. When the water content is

increased to 15%, k_n increases by more than twice the number of dry-filled joints.

7.3.3.4 Transmission and reflection coefficients

Figure 7.16 shows the experimental results of the wave transmission T_c and reflection R_c coefficients as a function of JMC for the joints with and without filling materials. Despite the influences generated by the loading rate and water content, the T_c of the nonfilled and filled joints exponentially increases with JMC. For the nonfilled joint, when the JMC changes from 8% to 30%, T_c steeply increases from 36% to 67%, with a growth rate as high as 31%. Subsequently, the T_c increase rate gradually declines, and only increases by approximately 30% when the JMC increases from 30% to 100%. This result is consistent with the findings reported by Chen et al. (2015). Notably, the JMC equal to 100% refers to the case in which the incident rock bar rear end directly connects with the transmitted rock bar front end with a JMC=0%. The T_c of the filled joint shows a similar behavior, sharply increasing from 12% to 72% with a JMC increasing from 0% to 30%. For the joint with JMC=0%, the filling thickness is the same as the joint notches, i.e., 4 mm. Notably, the T_c of the filled joint with JMC=8% ($T_c=40\%$) is more than three times that of the fully filled joint with JMC=0% ($T_c=12\%$).

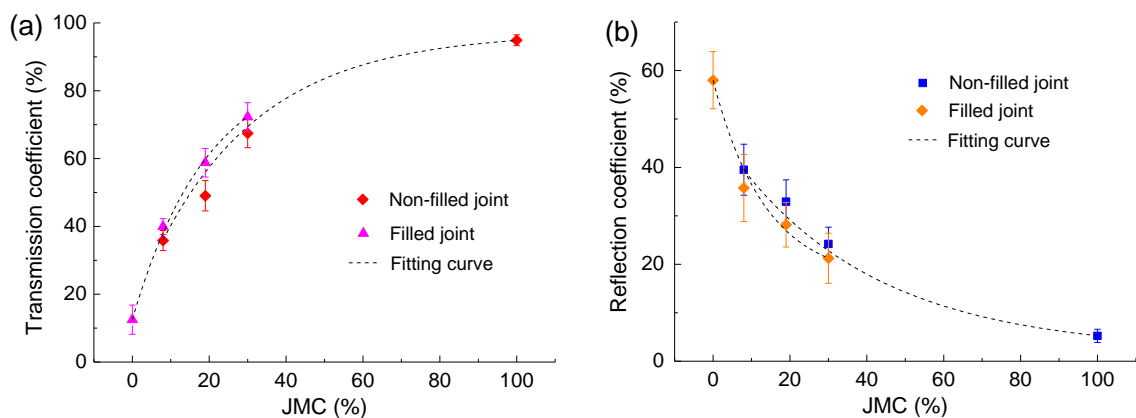


Figure 7.16 (a) Transmission and reflection coefficients vs JMC of the joint with and without infilling with error bars. (a) Transmission coefficient; (b) Reflection coefficient.

Note that the effects of water content and loading rate are not considered.

In contrast to T_c , R_c exponentially decreases with the JMC increase for the joint with or without the sand-clay mixture. Regarding the nonfilled joint, R_c declines by 16% with the JMC increasing from 8% to 30%. R_c continuously declines with the JMC further

increasing and nearly vanishes when the JMC is equal to 100%. For the joint filled with the sand-clay mixture, the R_c of the filled joint is lower by approximately 4% than that of the nonfilled joint with the same JMC. This value sharply decreases from 58% to 21% when the JMC increases from 0% to 30%. Notably, the R_c is comparable to T_c when the JMC equals 8%. This means that with a JMC of over 8%, most of the incident wave will be transmitted through the joint, below which most of the incident wave will be reflected by the joint.

From the above analysis, the JMC can be concluded to greatly affect the wave propagation in a rock mass with a single joint, and the infilling (sand-clay mixture) plays an insignificant role during this process. This is because the T_c increases by an average of approximately 6% when the joint is filled with a sand-clay mixture, while R_c decreases by approximately 4% compared with the nonfilled rock joint.

Figure 7.17 demonstrates that T_c for the nonfilled and filled joints gradually increases with increasing loading rate, while the loading rate effect is not significant for the joints filled with the sand-clay mixture. In contrast, R_c clearly decreases with an increasing loading rate for the joints with or without filling mixtures. The fitting curve gradient for R_c is steeper than that for T_c , which indicates that the loading rate effect of R_c is more remarkable. In addition, for the filled joint with a JMC equal to 0%, the T_c is much lower than that of the joint with a JMC between 8% and 30%, but R_c has the highest value.

Figure 7.18 demonstrates the water content influence on the T_c and R_c of the joint filled with the sand-clay mixture subject to three elevated loading rates. In general, a high loading rate leads to a higher T_c and lower R_c for a given JMC. Nevertheless, the loading rate does not alter the overall evolution laws of T_c and R_c as functions of water content for a given JMC. Additionally, variations in T_c and R_c of the joint with different JMCs are basically the same as functions of water content, despite the fact that the variation magnitudes of T_c and R_c are inconsistent under different JMCs.

In general, variation of T_c appears as a convex shape, while that of R_c appears as a concave shape. T_c peaks at a water content of approximately 15%, while R_c reaches the minimum value at nearly the same water content. Considering the filled joint with a JMC equal to 8% as an example, when the average loading rate is 519 GPa/s, the T_c increases from 36.0% to 40.0% with the joint changing from the nonfilled condition to the fully

filled state with a water content of 0%, and the value reaches the peak of 41.2% when the water content increases to 15%. Subsequently, T_c gradually declines with further increasing water content and decreases to 39.0% at a water content of 25%. However, R_c shows the opposite trend. This value decreases to the lowest value of 34.5% at a water content of 15% and then gradually increases to 39.4% with a water content equal to 25%.

As mentioned above, the T_c of all the joints filled with the sand-clay mixture is higher than that of the nonfilled joint. Specifically, the average increase magnitude of T_c peaks at 6.9% when the JMC equals 19%, and for a water content of 15%, the average increase magnitude maximizes at 8.7%.

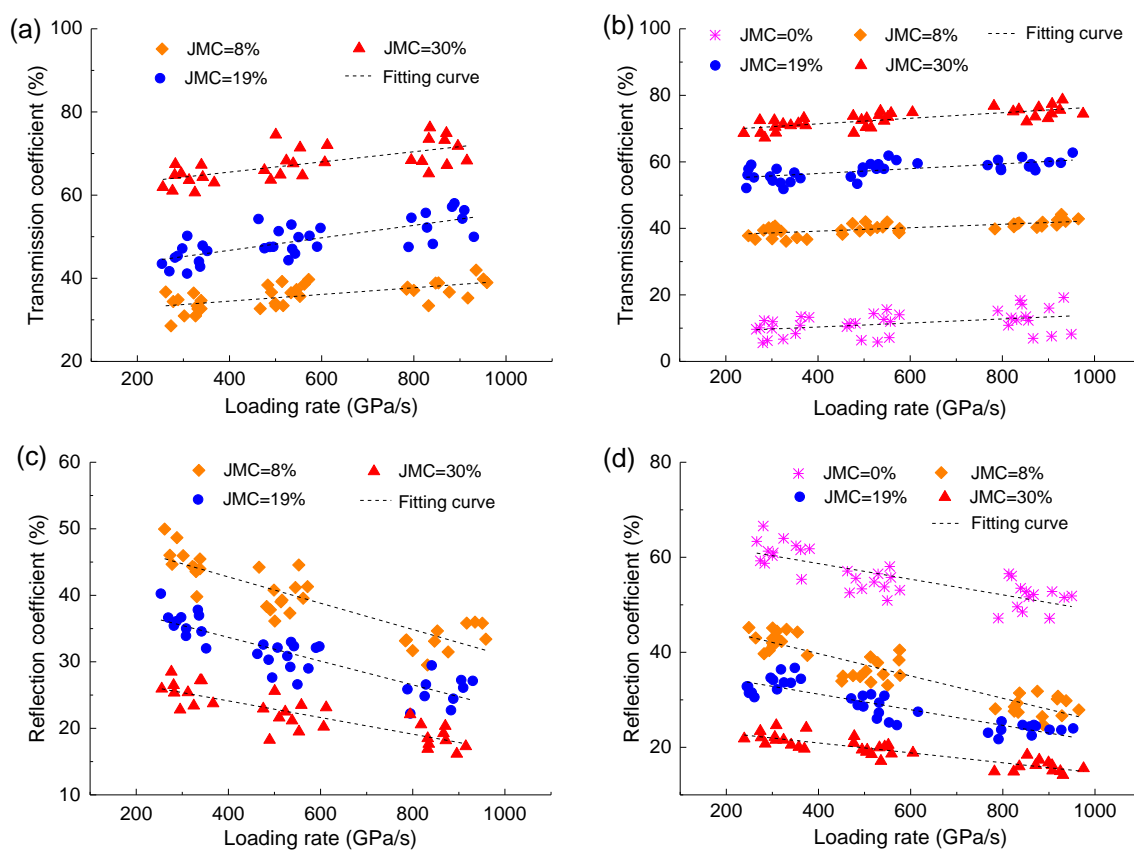


Figure 7.17 Transmission and reflection coefficients vs loading rate of the joint with and without filling materials. (a) and (c) Joint without sand-clay mixture; (b) and (d) Joint filled with sand-clay mixture

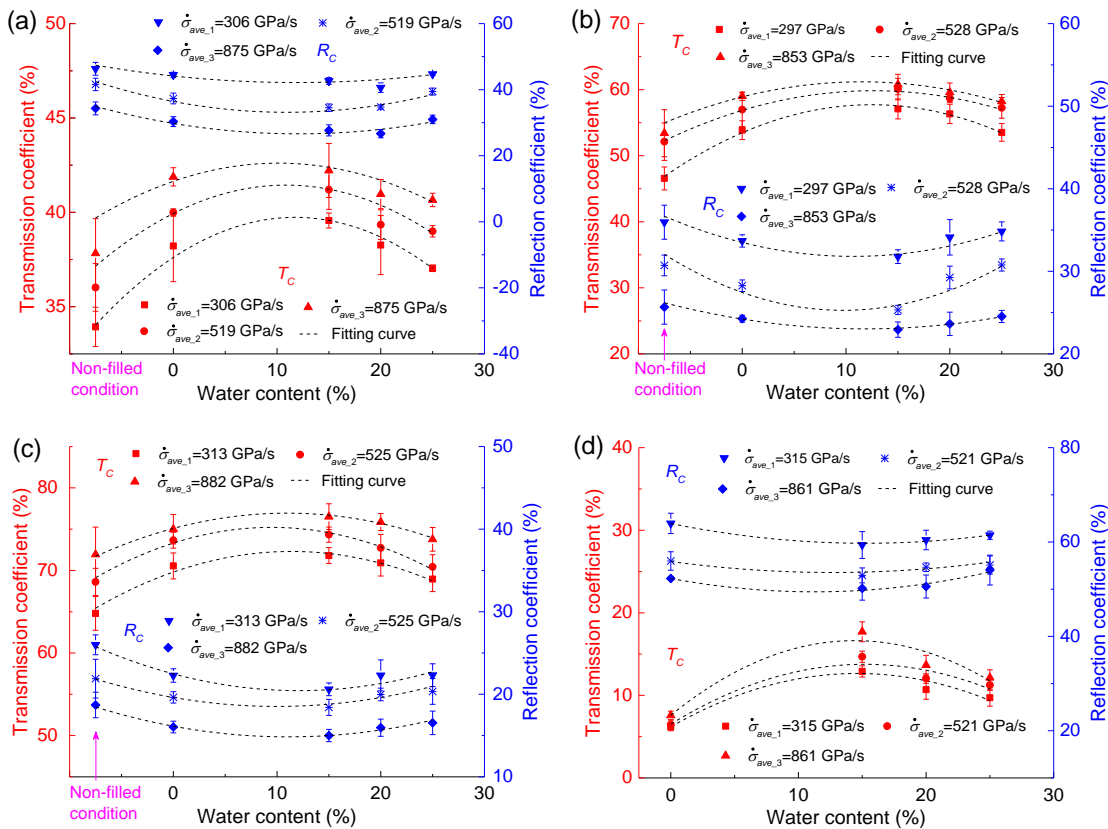


Figure 7.18 Transmission and reflection coefficients vs water content and loading rate of the joint filled with sand-clay mixture. (a)-(d): Joints with JMC equal to 8%, 19%, 30% and 0%, respectively

7.3.3.5 Energy dissipation

In general, when a wave propagates through a jointed rock mass, wave attenuation will be induced due to wave reflection and transmission at discontinuous joints, dynamic damage of the rock matrix, and dynamic damage of joints. In this chapter, since the impact loading was very low (e.g., less than 30 MPa), the plasticity or dynamic damage of the rock bars as well as the joint induced by the impact could be neglected. This is because there is a critical fatigue impact stress, i.e., approximately 50% of the dynamic strength, below which most no damage would be generated under repetitive impacts (Zhou et al. 2018b). This means that no irreversible energy could be attenuated except for the wave reflection and transmission at the joint surfaces and energy dissipation (E_D) by the joint. Herein, E_D originates from the joint displacement and sand-clay mixture compaction in the filled joint during the wave propagation and can be determined by Eq. (9). To minimize the incident wave variation, the normalized dimensionless variable R_e (energy dissipation

rate), which is defined as the ratio between the peak values of E_D and E_I , is employed to quantify the joint condition effects on energy consumption during stress wave propagation across the joint. R_e is determined by the following:

$$R_e = \frac{\max E_D}{\max E_I} \quad (7.10)$$

Figure 7.19a describes the variation in the average R_e as a function of the JMC and loading rate for the joints with JMCs between 8% and 30%, and the water content effect is not considered. The results show that R_e decreases almost linearly with increasing JMC, regardless of the joint filling condition. The filled joint R_e is smaller than that of the nonfilled joint, and the average decreasing magnitude of R_e rises from approximately 7.4% to 20.8% when the JMC changes from 8% to 30%. The R_e decrease with increasing JMC is mainly because the joint with a larger JMC deforms less (see Fig. 7.10) under the same dynamic load, which then consumes less energy. In addition, for a specific JMC (between 8% and 30%), the R_e s of the joint impacted by different loading rates nearly overlapped with each other, which indicates that the R_e might be unaffected by the loading rate.

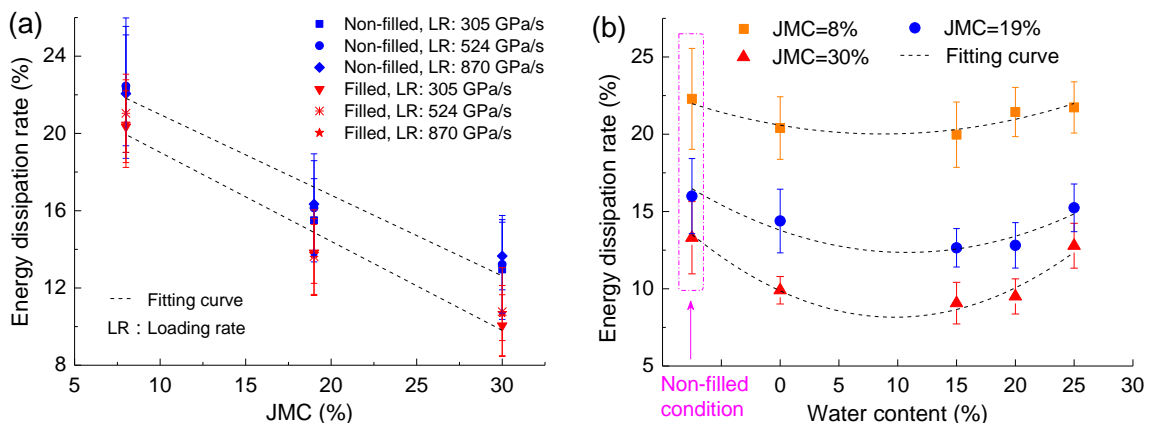


Figure 7.19 Energy dissipation rate vs JMC and loading rate of the non-filled and filled joints; (b) Energy dissipation rate vs water content of the joints filled with sand-clay mixture with error bars

The water content effects on the joint R_e with different JMCs is plotted in Fig. 7.19b. The results reveal that water content plays an important role in energy dissipation for stress wave propagation across a filled joint. For a filled joint, the R_e slightly declines with increasing water content and bottoms out at a water content of approximately 15%; subsequently, R_e gradually rises with a further increase in water content. R_e decreased by

an average of 19% with a water content change from 0% to 15%, and the filled joint R_e with a water content of 25% was greater by an average of approximately 14% than the corresponding dry-filled joint. In addition, similar to the JMC effect illustrated in Fig. 7.19a, the higher the JMC, the lower the energy dissipation rate of a filled joint with a given water content.

In contrast to the joints with JMCs between 8% and 30%, the R_e of the filled joint with a JMC=0% increases slightly with a loading rate increase, as shown in Fig. 7.20a, and ascends by an average of 15% when the loading rate changes from approximately 315 GPa/s to 860 GPa/s. This is because the sample joint closure with a JMC=0% drastically increases with increasing loading rate/amplitude (see Fig. 7.10b), thereby leading to the R_e increase with loading rate. Similar to the loading rate effect, the water content also affects the filled joint R_e with a JMC=0%, as shown in Fig. 7.20b. The 15% water content seems to be a critical value, below which R_e decreases with increasing water content; however, above this value, the R_e gradually increases with increasing water content. R_e falls by an average of 9.5% with the water content changing from 0% to 15%. Nonetheless, the filled joint R_e with a water content of 25% is still slightly lower than that with a water content equal to 0%.

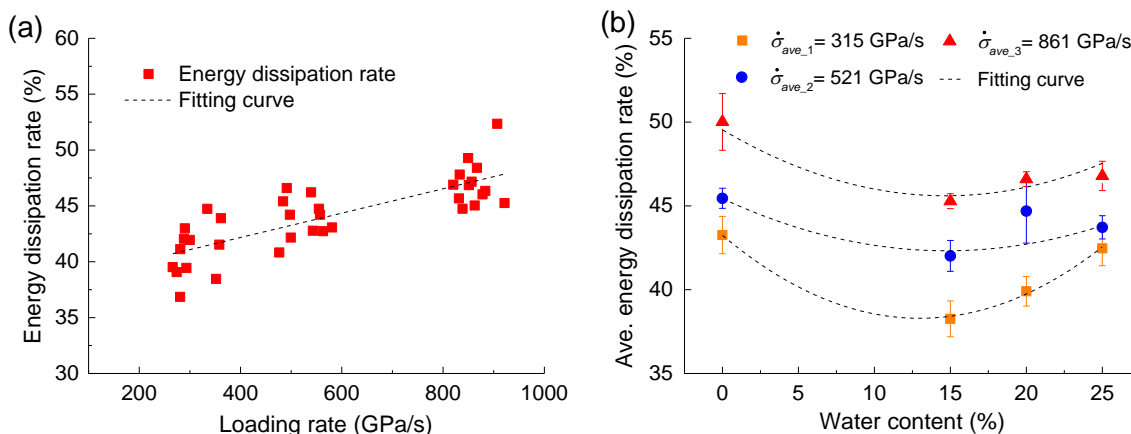


Figure 7.20 (a) Energy dissipation rate vs loading rate of the joint with JMC=0%; (b) Energy dissipation rate vs water content of the joint (JMC=0%) filled with sand-clay mixture with error bars

7.4 Discussions

In this chapter, an increasing JMC and joints filled with the sand-clay mixture show

increased T_c but decreased R_c and D as well as R_e (see Figs. 7.9, 7.16 and 7.19). This is mainly because the addition of JMC and filling of the joint notches with the sand-clay mixture could increase the equivalent wave impedance of the joint, thus improving the joint equivalent stiffness (see Fig. 7.13), thereby increasing T_c and reducing R_c (Li et al. 2015; Pyrak-Nolt et al. 1990a; Zhu et al. 2011b). Meanwhile, k_n is inversely proportional to joint deformation, and therefore, for a given loading stress, increasing k_n will undoubtedly lead to a reduction in D . Furthermore, when a joint only undergoes linear elastic deformation, its energy dissipation is mainly caused by joint closure/deformation, e.g., the smaller the deformation, the lower the energy dissipation (Ju et al. 2007). Hence, increasing the JMC and filling the joint notches with the sand-clay mixture also resulted in a reduction in R_e .

In addition, T_c , k_n and D are also found to slightly increase with increasing loading rate during wave propagation, as shown in Figs. 7.10, 7.14 and 7.17. This is because a high loading rate means a high dynamic loading amplitude during wave propagation, which could lead to the contact of the joint interfaces becoming increasingly closer and a better contact and seismic coupling (Wu et al. 2012), thereby yielding a higher k_n and T_c . Although the addition of k_n by increasing the loading rate could somewhat enhance the ability of the joint to resist deformation, the joint closure still shows an increase with increasing loading rate. This indicates that the reduction of D caused by the joint stiffness increase is insufficient to counteract the increase in D resulting from the increase in loading stress/amplitude.

In comparison to the joint filled with the dry sand-clay mixture, the T_c of the joint filled with the unsaturated sand-clay mixture (e.g., 15% in water content) is further increased by an average of approximately 10%, while the R_c , D and R_e are reduced by a few percentage points. This is because adding a small amount of water to the sand-clay mixture results in the formation of small capillary bridges between adjacent grains, which exert an attractive force between grains due to surface tension (Herminghaus 2005). In addition, the network of capillary forces drastically improves the stiffness and stability of the granular pile (Fiscina et al. 2010; Fournier et al. 2005), as opposed to the dry pile, which further enhances the k_n of the wet-filled joint, thereby reducing the joint attenuation and deformation as well as the energy dissipation rate.

Nevertheless, the attenuation and deformation characteristics of the wet-filled joint shift when the water content surpasses 15% (see Figs. 7.11, 7.18 and 7.19). For instance, with a water content of 25%, the filled joint T_c , R_c and D values are comparable to those of the corresponding dry-filled joint, while the R_e is even higher by an average of approximately 14%. This may be because the relatively high water content makes the sand-clay mixture like a gouge, which not only dramatically increases the viscosity of the mixture but also weakens the friction between the contact grains (Fukuyama and Mizoguchi 2010), thus undermining the filling mixture stiffness and stability. In addition, when the water content was 25%, the local joint asperities were wetted by a small amount of water seepage, which might weaken the elastic modulus of the joint asperities. Therefore, the equivalent joint specific stiffness might be weakened by those two factors. In addition, for the fully saturated sand-clay mixture, due to the formation of water flow passages, a small amount of free water was found to be squeezed out the transparent PVC tub, which increased the energy dissipation. Consequently, the combination of the above reasons results in an increase in joint attenuation and energy dissipation rate.

From the above analysis, we find that both the JMC and sand-clay mixture play important roles in stress wave propagation and attenuation across jointed rock masses. Nevertheless, the JMC plays a dominant role in controlling the seismicity of the joint compared to the filled mixture. Considering T_c and R_e as an example, the average T_c of the dry-filled joint with a JMC= 8% ($T_c \approx 40\%$) is approximately 5.7 times that of the dry-filled joint with a JMC=0% ($T_c \approx 7\%$), while the average R_e of the former ($R_e \approx 20\%$) is less than half of the latter ($R_e \approx 46\%$). This characteristic indicates that in engineering practice, the mechanical and seismic properties of the joint or jointed rock mass could be better manipulated by rationally adjusting the JMC.

7.5 Conclusions

In this chapter, an experimental investigation of the effects of JMC, water content and loading rate on the mechanical and seismic characteristics of a single rough joint in SHRB tests is reported. The main conclusions are summarized as follows:

- (1) The incident stress applied to the rock bars should be below 30.1 MPa to avoid the generation of damage in the granite rock bars and joint asperities that may attenuate wave propagation in the rock bars. Verification tests indicated that the attenuation

caused by the initial damage inside the rock bars was negligible and the stress equilibrium between the incident and transmitted rock bars could be well achieved and maintained. This finding confirms the feasibility and validity of performing wave propagation tests in the present SHRB system.

- (2) Transmission coefficient (T_c) of the filled or nonfilled joint exponentially increased with increasing JMC, and yet, the reflection coefficient (R_c) showed an inverse trend. The maximum joint closure (D) decreased exponentially with an increase in the JMC. The joint specific stiffness (k_n) increased linearly with increasing JMC but the dissipation energy rate (R_e) of the joint exhibited the opposite tendency.
- (3) Filling the joint with a sand-clay mixture could enhance its stiffness and wave propagation properties. By comparison with the nonfilled joint with a JMC between 8% and 30%, the T_c and k_n of the filled joint increased by an average of approximately 10% and 25%, respectively, and yet, the R_c , D and R_e of the filled joint declined slightly, by approximately 10%.
- (4) The k_n and R_c display clear loading-rate-dependent behavior. When the loading rate changed from approximately 310 GPa/s to 860GPa/s, the k_n and R_c increased by an average of 160% and 29%, respectively. Although the R_e of the filled joint with a JMC of 0% gradually increased with an increasing loading rate, the R_e of the joint with a JMC between 8% and 30% appeared to be unaffected by the loading rate.
- (5) The T_c and k_n increased with a water content increase from 0% to 15% yet declined with further increasing water content to 20% and 25%, whereas R_c , D and R_e exhibited the inverse trend.
- (6) The JMC plays a dominant role in affecting the mechanical and seismic properties of the joint, compared with the infilling mixture and loading rate.

CHAPTER 8 CONCLUSIONS AND SUGGESTIONS FOR FUTURE RESEARCH

8.1 Conclusions

In this thesis, an experimental investigation was performed to study crack growth and its influences on the mechanical and seismic properties of rocks. To study 3D crack growth behaviors, three-dimensional printing (3DP) is introduced to prepare brittle rock-like samples with 3D internal flaws using the most suitable 3DP material from the currently available 3DP materials. The influences of flaw geometry, i.e., flaw angle (α), flaw number and bridge angle (β), and loading type, i.e., static and dynamic loading, on the mechanical and fracture behaviors of 3DP artificial samples are studied. Combined with the micro-CT technique, the 3DP method is applied to replicate internal defects and investigate the mechanical and fracture behavior of rocks. In addition to 3D crack growth in artificial rock samples, an investigation on the damage evolution characterization and its effect on low-amplitude ultrasonic P-wave propagation in granite samples under uniaxial compression is also performed using AE and micro-CT. In addition, the coupling effects of the joint matching coefficient (JMC), loading rate and water content of the infilling mixture on the mechanical and seismic properties of a single rough joint are systematically studied with a modified SHRB system. The main conclusions of this thesis are summarized as follows:

(1) The 3DP samples produced with ceramics, gypsum and PMMA using powder-based 3DP failed at very low compressive stress and exhibited highly ductile behavior, causing these samples to be unsuitable for simulating common brittle and hard rocks. The FDM-fabricated SR20 sample exhibited apparent elastoplastic behavior, also making this sample unsuitable for modeling natural rocks. Despite the relatively large deformation, the strength and stress-strain behavior of the 3DP resin sample produced by the SLA method are comparable to those of natural rocks such as marble and sandstone. Meanwhile, the 3DP resin transparent feature makes it possible to directly observe and analyze internal crack evolution during rock fracturing, which may aid in better understanding the failure mechanisms of rocks. Consequently, the 3DP resin is identified as the most suitable 3DP material for replicating brittle and hard rocks, considering the presently available 3DP materials. To enhance the brittleness of the 3DP resin, three

methods including freezing, incorporation of a macrocrack and addition of microdefects were employed. After being treated by those three methods, the resin-based 3DP samples exhibited nearly linear stress-strain behavior prior to reaching peak stress and failed in a splitting manner, indicative of sufficient brittleness.

(2) The SLA 3DP can conveniently, repeatedly and precisely produce resin-based artificial rock samples with 3D internal flaws, which is much better than the traditional manufacturing methods. By combining micro-CT and 3D reconstruction techniques, the SLA 3DP can be used to replicate the internal defects of natural rocks. These flawed, resin-based samples are suitable for studying the mechanical and fracture behaviors of rocks under static or dynamic loading conditions.

(3) Both the flaw geometry and loading type have significant effects on the mechanical properties of the resin-based 3DP samples. The single flawed sample with a $\alpha = 60^\circ$ has the lowest compressive strength (σ_c) and axial strain at the peak stress (ε_a). The σ_c and ε_a of the double flawed samples generally increase with β increasing from 45° to 105° . The initiation stress of the first wing crack (σ_1), σ_c and ε_a of the sample all decrease when the flaw number changes from one to two. From static loading to dynamic loading, σ_c increases by approximately 8%, and ε_a decreases by approximately 51% and 27% for the resin-based 3DP specimens containing single and double 3D internal flaws, respectively.

(4) Loading type affects 3D crack growth behaviors more than flaw geometry. Wing cracks generated at the inner tips of the pre-existing flaws cannot coalesce with each other, except for $\beta=105^\circ$. α , β and flaw number seem do not influence the 3D crack shape, propagation manner or the final failure mode of the flawed samples. However, when changing the loading type from static compression to dynamic impact, the 3D crack growth behavior and the final failure mode of the flawed samples are completely changed. Under dynamic compression, wing cracks can continuously extend toward the sample ends, resulting in a splitting failure of the sample, while under static compression, the wing cracks and anti-wing cracks can only intermittently propagate approximately 1-1.5 times the length of the initial flaw. The final, burst-like failure is caused by secondary cracks. Furthermore, anti-wing cracks are not observed under dynamic compression. The crack propagation velocity is more stable under dynamic loading, but the maximum crack propagation velocity in the dynamic tests is lower than that in the static compression tests.

-
- (5) The compressive strength, dynamic tensile strength, Poisson's ratio and fracturing properties of the resin-based volcanic rocks agree with those of the prototype volcanic rock samples, which verify the applicability of using the 3DP-replicated artificial rocks to study the mechanical and fracture properties of brittle rocks, such as volcanic rocks and porous rocks.
- (6) The results of ultrasonic P-wave propagation in the granite sample during axial compression indicate that P-wave propagation in granite samples is stress dependent. The P-wave velocity and amplitude of the transmitted waveform first increase with axial stress and then decrease when the axial stress exceeds a critical percentage of the UCS. The transition stresses for P-wave velocity and amplitude are approximately 90 UCS% and 70 UCS%, respectively.
- (7) The cumulative AE counts can be used to quantify damage evolution during the loading process, while the crack areas determined by X-ray micro-CT can be adopted to quantify stress-induced damage inside the rock sample after loading and unloading processes. Damage evolution during the loading process and after unloading are both highly nonlinear and can be well fitted with exponential functions. The fitting function is verified for analyzing damage evolution during axial compression.
- (8) The degree of damage is negligible when the axial stress applied to the rock sample is below approximately 60 UCS%. An axial stress of 80UCS% appears to be a transition point, above which damage evolution during loading and after unloading are both significantly increased. The damage coefficient during the loading process is greater than that after unloading. Damage evolution in rock samples influences P-wave velocity, spectra and amplitude. However, compared with P-wave velocity, wave amplitude attenuation is more sensitive to damage/stress.
- (9) Stress wave propagation in SHRB shows that the transmission coefficient (T_c) of the filled and nonfilled joint exponentially increases with the JMC yet the reflection coefficient (R_c), and the maximum joint closure (D) exhibits the inverse trend. The joint specific stiffness (k_n) linearly increases with increasing JMC, but the dissipation energy rate (R_e) of the joint shows the opposite tendency.
- (10) The sand-clay mixture infilling the joint has a certain effect on the k_n and P-wave propagation properties. In comparison with the nonfilled joint, the T_c and k_n of the filled

joint increase by an average of approximately 10% and 25%, respectively, yet the R_c , D and R_e of the filled joint decline slightly, which is approximately 10%. The water content of the infilling material affects both the mechanical and seismic properties of the filled joint. T_c and k_n increase with increasing water content from 0% to 15% yet decline with further increasing water content to 20% and 25%, whereas R_c , D and R_e exhibit the inverse trend.

(11) k_n and R_c display a clear loading rate-dependent behavior. When the loading rate changed from approximately 310 GPa/s to 860 GPa/s, k_n and R_c increased by an average of 160% and 29%, respectively. However, the R_e of the joint with JMC between 8% and 30% appears to be unaffected by the loading rate.

(12) JMC plays a dominant role in affecting the mechanical and seismic properties of the artificial rough joint compared with the infilling mixture and loading rate.

8.2 Recommendations for future works

(1) In Chapter 3, to facilitate the application of 3DP to rock mechanics and rock engineering, further improvements and developments, e.g., developing more brittle and transparent 3DP resin materials, enhancing the strength and brittleness of the powder-based 3DP materials, improving the printing resolutions of the 3D printers, promoting the printing speed and efficiency and developing new supporting 3DP materials, are needed. The 3D crack growth experiments are recommended to be conducted in the laboratory or at low temperature, where the brittleness of the 3D-printed artificial rock samples could be enhanced via freezing treatment and the direct monitoring of fracture behaviors could be achieved in real-time utilizing high-speed cameras.

(2) In Chapter 4, despite the preliminary findings in this chapter that could facilitate a better understanding of rock failure behavior, notably, the limitation, e.g., low Young's modulus and almost no porosity, of the 3DP resin material means that the resin-based artificial rock samples cannot completely reflect the mechanical and fracture behaviors of natural rocks. Therefore, further improvements and developments, e.g., enhancing the Young's modulus and brittleness of the 3DP resin material, incorporating X-ray micro-CT and 3DP techniques to implant the real internal structure (e.g., porosity and micro and macrocracks) of the natural rock into the 3DP resin-based artificial rocks, are needed so that the 3DP resin's properties approach those of actual rocks. In addition, further efforts

are needed to more precisely and quantitatively characterize and analyze the 3D stress field around pre-existing flaws and the progressive fracture process subject to different loading conditions by means of the frozen stress technique, 3D photoelastic technique, etc.

(3) In Chapter 5, to facilitate the application of 3DP for studying rock behavior and to improve the similarity in mechanical properties between 3DP resin and natural rock in particular, some potential improvements could be adopted, e.g., development of additives to improve the stiffness and brittleness of the 3DP resin material and development of new printing technology that could be utilized to prepare 3DP samples with mixed 3DP materials to reflect the heterogeneity of natural rocks.

(4) In Chapter 6, to further confirm the present findings, additional experimental tests shall be conducted to repeat, supplement and even improve the present results. More micro-CT scanning of unloading samples should be conducted to enhance the accuracy of determining the damage coefficient of the damaged samples. In addition, triaxial compression tests shall be conducted to investigate anisotropic damage evolution and its influences on both P-wave and S-wave propagation in three orthogonal directions.

(5) In Chapter 7, to protect the rock asperities and rock bars from being damaged by the dynamic compressive load, only low-amplitude incident stress waves are applied to investigate wave propagation across a rock mass with a single rough joint. However, in engineering practices, rock joints and jointed rock masses are often subjected to high-amplitude stress waves, such as blast waves (Deng et al. 2015). When a high-amplitude wave propagates through a jointed rock mass, rock matrix and joints/joint asperities will damage or even fail, which in turn will affect wave propagation and attenuation across joint rock masses. Therefore, the interactive process of wave propagation and dynamic damage and the response in jointed rock masses subjected to high-amplitude stress waves should be investigated in the future.

REFERENCES

- Abdelrahman M, ElBatanouny MK, Ziehl P, Fasl J, Larosche CJ, Fraczek J (2015) Classification of alkali–silica reaction damage using acoustic emission: A proof-of-concept study. *Constr Build Mater* 95: 406-413
- Abouhussien AA, Hassan AA (2016) Detection of bond failure in the anchorage zone of reinforced concrete beams via acoustic emission monitoring. *Smart Mater Struct* 25(7): 075034
- Adams M, Sines G (1978) Crack extension from flaws in a brittle material subjected to compression. *Tectonophysics* 49: 97-118
- Ahrens TJ, Rubin AM (1993) Impact-induced tensional failure in rock. *J Geophys Res* 98(E1): 1185-1203
- Ai HA, Ahrens TJ (2007) Effects of shock-induced cracks on the ultrasonic velocity and attenuation in granite. *J Geophys Res* 112(B1): B01201
- Alber M, Fritschen R, Bischoff M, Meier T (2009) Rock mechanical investigations of seismic events in a deep longwall coal mine. *Int J Rock Mech Min Sci* 46(2), 408-420
- Anthony, S. (2014) SpaceX rocket carries the first ever zero-g 3D printer to the Space Station. <http://www.extremetech.com/extreme/190629-spacex-rocket-launches-to-the-space-station-carrying-the-first-ever-zero-g-3d-printer>. Accessed 26 April 2015
- ASTM D638 (2010) Standard test method for tensile properties of plastics, ASTM International, West Conshohocken, PA, 2010
- Atkinson BK, Meredith PG (1987a) The theory of subcritical crack growth with applications to minerals and rocks. In *fracture mechanics of rock*, ed. Atkinson BK, Academic Press, London. 2: 111-66
- Atkinson BK, Meredith PG (1987b) Experimental fracture mechanics data for rocks and minerals. In *fracture mechanics of rock*, ed. Atkinson BK, Academic Press, London. 28: 477-525
- Bandis SC, Lumsden AC, Barton NR (1983) Fundamentals of rock joint deformation. *Int J Rock Mech Min Sci Geomech Abstr* 20(6): 249-268
- Barnhoorn A, Verheij J, Frehner M, Zhubayev A, Houben M (2018) Experimental identification of the transition from elasticity to inelasticity from ultrasonic attenuation analyses. *Geophysics* 83(4): MR221-MR229

- Barton NR (1974) A review of the shear strength of filled discontinuities in rock. Norwegian Geotechnical Institute Publication no. 105, Oslo, Norway
- Barton N, Choubey V (1977) The shear strength of rock joints in theory and practice. *Rock Mech* 10(1-2): 1-54
- Baud P, Klein E, Wong TF (2004) Compaction localization in porous sandstones: spatial evolution of damage and acoustic emission activity. *J Struct Geol* 26: 603-624
- Belter JT, Dollar AM (2015) Strengthening of 3D printed fused deposition manufactured parts using the fill compositing technique. *PloS One* 10(4): e0122915
- Benson PM, Thompson BD, Meredith PG, Vinciguerra S, Young RP (2007) Imaging slow failure in triaxially deformed Etna basalt using 3D acoustic-emission location and X-ray computed tomography. *Geophys Res Lett* 34(3): L03303
- Bieniawski ZT (1967) Mechanism of brittle fracture of rock: part II-experimental studies. *Int J Rock Mech Min Sci* 4(4): 407-423
- Bobet A (2000) The initiation of secondary cracks in compression. *Eng Fract Mech* 66(2): 187-219
- Bobet A, Einstein HH (1998a) Fracture coalescence in rock-type materials under uniaxial and biaxial compression. I *Int J Rock Mech Min Sci* 35(7): 863-889
- Bobet A, Einstein HH (1998b) Numerical modeling of fracture coalescence in rock materials. *Int J Fract* 92: 221-252
- Bombolakis EG (1963) Photoelastic stress analysis of crack propagation within a compressive stress field. Ph.D thesis, Massachusetts Institute of Technology
- Brace WF (1964) Brittle fracture of rocks. *State of Stress in the Earth's Crust*. American Elsevier Publishing Co., New York, pp: 111-180
- Brace WF, Bombolakis EG (1963) A note on brittle crack growth in compression. *J Geophys Res* 68(12): 3709-3713
- Brace WF, Paulding Jr BW, Scholz CH (1966) Dilatancy in the fracture of crystalline rocks. *J Geophys Res* 71(16): 3939-3953
- Brooks Z, Ulm FJ, Einstein HH (2013) Environmental scanning electron microscopy (ESEM) and nanoindentation investigation of the crack tip process zone in marble. *Acta Geotech* 8(3): 223-245

- Browning J, Meredith PG, Stuart CE, Healy D, Harland S, Mitchell TM (2017) Acoustic characterization of crack damage evolution in sandstone deformed under conventional and true triaxial loading. *J Geophys Res* 122(6): 4395-4412
- Buswell RA, Soar R, Gibb AG, Thorpe A (2007) Freeform construction: mega-scale rapid manufacturing for construction. *Autom Constr* 16: 224-231
- Cai M, Morioka H, Kaiser PK, Tasaka Y, Kurose H, Minami M, Maejima T (2007) Back-analysis of rock mass strength parameters using AE monitoring data. *Int J Rock Mech Min Sci* 44(4): 538-549
- Cannon NP, Schulson EM, Smith TR, Frost HJ (1990) Wing cracks and brittle compressive fracture. *Acta Metall Mater* 38(10): 1955-1962
- Capel AJ, Edmondson S, Christie SD, Goodridge RD, Bibb RJ, Thurstans M (2013) Design and additive manufacture for flow chemistry. *Lab Chip* 13(23): 4583-4590
- Cai JG, Zhao J (2000) Effects of multiple parallel fractures on apparent wave attenuation in rock masses. *Int J Rock Mech Min Sci* 37:661-682
- Chen Q, Xu R, He Z, Zhao K, Pan L (2017) Printing 3d gel polymer electrolyte in lithium-ion microbattery using stereolithography. *J Electrochem Soc* 164(9): A1852-A1857
- Chen R, Xia K, Dai F, Lu F, Luo SN (2009) Determination of dynamic fracture parameters using a semi-circular bend technique in split hopkinson pressure bar testing. *Eng Fract Mech* 76(9): 1268-1276
- Chen S, Yue ZQ, Tham LG (2007) Digital image based approach for three-dimensional mechanical analysis of heterogeneous rocks. *Rock Mech Rock Eng* 40:145-168
- Chen X, Li JC, Cai MF, Zou Y, Zhao J (2015) Experimental study on wave propagation across a rock joint with rough surface. *Rock Mech Rock Eng* 48(6): 2225-2234
- Chia, H. N., Wu, B. M. (2015). Recent advances in 3D printing of biomaterials. *J Biol Eng* 9(1): 4
- Chong KP, Hoyt, PM., Smith JW, Paulsen BY (1980). Effects of strain rate on oil shale fracturing. *Int J Rock Mech Min Sci* 17(1): 35-43
- Chow TM, Meglis IL, Young RP (1995) Progressive microcrack development in tests on Lac du Bonnet granite-II. Ultrasonic tomographic imaging. *Int J Rock Mech Min Sci* 32(8): 751-761
- Curran DR, Seaman L, Shockey DA (1987) Dynamic failure of solids. *Phys Rep* 147(5):

253-388

- Dai F, Huang S, Xia K, Tan Z (2010a) Some fundamental issues in dynamic compression and tension tests of rocks using split hopkinson pressure bar. *Rock Mech Rock Eng* 43: 657-666
- Dai F, Chen R, Xia K (2010b) A semi-circular bend technique for determining dynamic fracture toughness. *Exp Mech* 50(6): 783-791
- Dal Ferro, N., Morari, F. (2015). From real soils to 3D-printed soils: reproduction of complex pore network at the real size in a silty-loam soil. *Soil Sci Soc Am J* 79(4), 1008-1017
- de Figueiredo J, Schleicher J, Stewart RR, Dayur N, Omoboya B, Wiley R, William A (2013) Shear wave anisotropy from aligned inclusions: ultrasonic frequency dependence of velocity and attenuation. *Geophys J Int* 193(1): 475-488
- Deng XF, Chen SG, Zhu JB, Zhou YX, Zhao ZY, Zhao J (2015) UDEC–AUTODYN hybrid modeling of a large-scale underground explosion test. *Rock Mech Rock Eng* 48(2): 737-747
- Diederichs MS, Kaiser PK, Eberhardt E (2004) Damage initiation and propagation in hard rock during tunnelling and the influence of near-face stress rotation. *Int J Rock Mech Min Sci* 41(5): 785-812
- Doan ML Gary G (2009) Rock pulverization at high strain rate near the San Andreas fault. *Nat Geosci* 2: 709-712
- Dyskin AV, Germanovich LN, Ustinov KB (1999) A 3-D model of wing crack growth and interaction. *Eng Fract Mech* 63: 81-110
- Dyskin AV, Jewell RJ, Joer H, Sahouryeh E, Ustinov KB (1994) Experiments on 3-D crack growth in uniaxial compression. *Int J Fract* 65(4): R77-R83
- Dyskin AV, Sahouryeh E, Jewell RJ, Joer H, Ustinov KB (2003) Influence of shape and locations of initial 3-D cracks on their growth in uniaxial compression. *Eng Fract Mech* 70: 2115-2136
- Eberhardt E, Stead D, Stimpson B (1999) Quantifying progressive pre-peak brittle fracture damage in rock during uniaxial compression. *Int J Rock Mech Min Sci* 36(3): 361-380
- Erarslan N, Williams DJ (2012) Experimental, numerical and analytical studies on tensile strength of rocks. *Int J Rock Mech Min Sci* 49: 21-30
- Evans AG (1978) A general approach for the statistical analysis of multiaxial fracture. *J Am Ceram Soc* 61: 302-308

- Fairhurst CE, Hudson JA (1999) Draft ISRM suggested method for the complete stress-strain curve for intact rock in uniaxial compression. *Int J Rock Mech Min Sci* 36: 279-289
- Fan LF, Wong LNY (2013) Stress wave transmission across a filled joint with different loading/unloading behavior. *Int J Rock Mech Min Sci* 60: 227-234
- Fang Z, Harrison JP (2002) Development of a local degradation approach to the modelling of brittle fracture in heterogeneous rocks. *Int J Rock Mech Min Sci* 39: 443-457
- Feng P, Meng X, Chen JF, Ye L (2015) Mechanical properties of structures 3D printed with cementitious powders. *Constr Build Mater* 93: 486-497
- Feng XT, Chen S, Zhou H (2004) Real-time computerized tomography (ct) experiments on sandstone damage evolution during triaxial compression with chemical corrosion. *Int J Rock Mech Min Sci* 41(2): 181-192
- Fereshtenejad S, Song JJ (2016) Fundamental study on applicability of powder-based 3D printer for physical modeling in rock mechanics. *Rock Mech Rock Eng* 49(6): 2065-2074
- Fiscina JE, Lumay G, Ludewig F, Vandewalle N (2010) Compaction dynamics of wet granular assemblies. *Phys Rev Lett* 105(4): 048001
- Flisch A, Wirth J, Zanini R, Breitenstein M, Rudin A, Wendt F, Mnich F, Golz R (1999) Industrial computed tomography in reverse engineering applications. DGZfP-Proceedings BB 67-CD, Paper 8, International Symposium on Computerized Tomography for Industrial Applications and Image Processing in Radiology, Berlin, Germany, March 15-17, 1999
- Fournier Z, Geromichalos D, Herminghaus S et al. (2005) Mechanical properties of wet granular materials. *J Phys Condens Matter* 17(9): S477
- Franklin JA (1979) Suggest methods for determining water content, porosity, density, absorption and related properties and swelling and slake-durability index properties. *Int J Rock Mech Min Sci* 16, 141-156.
- Frantz CE, Follansbee PS, Wright WJ (1984) New experimental techniques with the split hopkinson pressure bar. In: I. Berman and J.W. Schroeder (Editors), 8th International Conference on High Energy Rate Fabrication. ASME, San Antonio, pp: 17-21
- Fredrich JT, Evans B, Wong TF (1990) Effect of grain size on brittle and semibrittle strength: Implications for micromechanical modelling of failure in compression. *J Geophys Res* 95(B7): 10907-10920
- Frew DJ, Forrestal MJ, Chen W (2001) A split Hopkinson pressure bar technique to determine

- compressive stress-strain data for rock materials. *Exp Mech* 41(1): 40-46
- Frew D, Forrestal MJ, Chen W (2002) Pulse shaping techniques for testing brittle materials with a split Hopkinson pressure bar. *Exp Mech* 42: 93-106
- Fu JW, Chen K, Zhu WS, Zhang XZ, Li XJ (2016) Progressive failure of new modelling material with a single internal crack under biaxial compression and the 3-D numerical simulation. *Eng Fract Mech* 165: 140-152
- Fu JW, Zhang XZ, Zhu WS, Chen K, Guan JF (2017) Simulating progressive failure in brittle jointed rock masses using a modified elastic-brittle model and the application. *Eng Fract Mech* 178: 212-230
- Fukuyama E, Mizoguchi K (2010) Constitutive parameters for earthquake rupture dynamics based on high-velocity friction tests with variable sliprate. *Int J Fract* 163(1-2): 15-26
- Ganter M, Storti D, Utela B (2009) The printed pot. *Ceram Mon* 56: 36-39
- Gao G, Yao W, Xia K, Li Z (2015) Investigation of the rate dependence of fracture propagation in rocks using digital image correlation (DIC) method. *Eng Fract Mech* 138: 146-155
- Ge XR, Ren JX, Pu YB, Ma W, Zhu YL (1999) A real-in-time CT triaxial testing study of meso-damage evolution law of coal. *Chin J Rock Mech Eng* 18(5): 497-502 (in Chinese)
- Germanovich LN, Salganik RL, Dyskin AV, Lee KK (1994) Mechanisms of brittle fracture of rock with pre-existing cracks in compression. *Pure Appl Geophys* 143: 117-149
- Goebel THW, Schorlemmer D, Becker TW, Dresen G, Sammis CG (2013) Acoustic emissions document stress changes over many seismic cycles in stick-slip experiments. *Geophys Res Lett* 40(10): 2049-2054
- Golaski L, Gebiski P, Ono K (2002) Diagnostics of reinforced concrete bridges by acoustic emission. *J Acoust Emission* 20, 83-89
- Goldsmith W, Sackman JL, Ewerts C (1976) Static and dynamic fracture strength of barre granite. *Int J Rock Mech Min Sci* 13(11): 303-309
- Goodfellow SD, Tisato N, Ghofranitabari M, Nasser MHB, Young RP (2015) Attenuation properties of fontainebleau sandstone during true-triaxial deformation using active and passive ultrasonics. *Rock Mech Rock Eng* 48(6): 2551-2566
- Griffith WA, Rosakis A, Pollard DD, Ko CW (2009) Dynamic rupture experiments elucidate tensile crack development during propagating earthquake ruptures. *Geology* 37: 795-798

- Guo S, Hirosaki N, Yamamoto Y, Nishimura T, Mitomo M (2001) Dependence of fracture stress on applied stress rate in a Yb₂O₃-SiO₂-doped hot-pressed silicon nitride ceramic. *J Mater Res* 16: 3254-3261
- Gupta IN (1973) Seismic velocities in rock subjected to axial loading up to shear fracture. *J Geophys Res* 78(29): 6936-6942
- Han T (2016) A simple way to model the pressure dependency of rock velocity. *Tectonophysics* 675: 1-6
- Hart KR, Wetzel ED (2017) Fracture behaviors of additively manufactured acrylonitrile butadiene styrene (ABS) materials. *Eng Fract Mech* 177: 1-13
- He H, Ahrens TJ (1994) Mechanical properties of shock-damaged rocks. *Int J Rock Mech Min Sci* 31(5): 525-533
- He MC, Miao JL, Feng JL (2010) Rock burst process of limestone and its acoustic emission characteristics under true-triaxial unloading conditions. *Int J Rock Mech Min Sci* 47(2): 286-298
- Herminghaus S (2005) Dynamics of wet granular matter. *Adv Phys* 54(3): 221-261
- Hirth G, Tullis J (1994) The brittle-plastic transition in experimentally deformed quartz aggregates. *J Geophys Res* 99(B6): 11731-11747
- Hiller J, Lipson H (2009) Design and analysis of digital materials for physical 3D voxel printing. *Rapid Prototyp J* 15(2): 137-149
- Ho ST, Hutmacher DW (2006) A comparison of micro CT with other techniques used in the characterization of scaffolds. *Biomaterials* 27: 1362-1376
- Hoek E, Bieniawski ZT (1965) Brittle fracture propagation in rock under compression. *Int J Fract Mech* 1(3): 137-155
- Horii H, Nemat-Nasser S (1985) Compression-induced microcrack growth in brittle solids: axial splitting and shear failure. *J Geophys Res* 90(B4): 3105-3125
- Huang L, Stewart RR, Dyaur N, Baez-Franceschi J (2016) 3D-printed rock models: Elastic properties and the effects of penny-shaped inclusions with fluid substitution. *Geophysics* 81(6): 669-677
- Huang S, Feng XT, Xia K (2011) A dynamic punch method to quantify the dynamic shear strength of brittle solids. *Rev Sci Instrum* 82(5): 165

- Huang SH, Liu P, Mokasdar A, Hou L (2013a) Additive manufacturing and its societal impact: a literature review. *Int J Adv Manuf Technol* 67(5): 1191-1203
- Huang X, Qi S, Xia K, Shi X (2018) Particle crushing of a filled fracture during compression and its effect on stress wave propagation. *J Geophys Res: Solid Earth* 123:5559-5587
- Huang S, Xia K (2015) Effect of heat-treatment on the dynamic compressive strength of Longyou sandstone. *Eng Geol* 191:1-7
- Huang S, Xia K, Zheng H (2013b) Observation of microscopic damage accumulation in brittle solids subjected to dynamic compressive loading. *Rev Sci Instrum* 84(9): 093903
- Ishutov S, Hasiuk FJ, Harding C, Gray JN (2015) 3d printing sandstone porosity models. *Interpretation* 3(3): SX49-SX61
- Iturrioz I, Lacidogna G, Carpinteri A (2013) Acoustic emission detection in concrete specimens: Experimental analysis and lattice model simulations. *Int J Damage Mech* 23(3): 327-358
- Jiang C, Zhao GF (2015) A preliminary study of 3D printing on rock mechanics. *Rock Mech Rock Eng* 48(3): 1041-1050
- Jiang Q, Feng X T, Gong Y H, Song LB, Ran SG, Cui J (2016) Reverse modelling of natural rock joints using 3D scanning and 3D printing. *Comput Geotech* 73: 210-220
- Ju Y, Sudak L, Xie H (2007) Study on stress wave propagation in fractured rocks with fractal joint surfaces. *Int J Solids Struct* 44(13): 4256-4271
- Ju Y, Wang L, Xie H, Ma G, Zheng Z, Mao L (2017) Visualization and transparentization of the structure and stress field of aggregated geomaterials through 3D printing and photoelastic techniques. *Rock Mech Rock Eng* 50(6): 1383-1407
- Ju Y, Xie H, Zheng Z, Lu J, Mao L, Gao F, Peng RD (2014) Visualization of the complex structure and stress field inside rock by means of 3D printing technology. *Chin Sci Bull* 59(36): 5354-5365
- Ju Y, Yang Y, Peng R, Mao L (2013) Effects of pore structures on static mechanical properties of sandstone. *J Geotech Geoenviron Eng* 139: 1745-1755
- Kachanov LM (1958) Time of the rupture process under creep conditions. *Isv Akad Nauk SSR Otd Tekh Nauk*, 8: 26-31
- Kachanov L (2013) Introduction to continuum damage mechanics. Vol. 10. Springer Science & Business Media

- Kaneko K, Inoue I, Sassa K, Ito I (1979) Monitoring the stability of rock structures by means of acoustic wave attenuation. Proceedings 4th Congress of ISRM, pp: 287-292
- Karaca M, Egger P (1993) Failure phenomena around shallow tunnels in jointed rock. In: Proceedings of the International Symposium on Assessment and Prevention of Failure Phenomena in Rock Engineering, Istanbul, Turkey, pp 381-388
- Kawakata H, Cho A, Kiyama T, Yanagidani T, Kusunose K, Shimada M (1999) Three-dimensional observations of faulting process in Westerly granite under uniaxial and triaxial conditions by X-ray CT scan. *Tectonophysics* 313(3): 293-305
- Kawakata H, Cho A, Yanagidani T, Shimada M (1997) The observations of faulting in westerly granite under triaxial compression by x-ray ct scan. *Int J Rock Mech Min Sci* 34(3-4), 151.e1-151.e12
- Ketcham RA, Carlson WD (2001) Acquisition, optimization and interpretation of X-ray computed tomographic imagery: applications to the geosciences. *Comput Geosci* 27: 381-400
- Kim JS, Lee KS, Cho WJ, Choi HJ, Cho GC (2015) A comparative evaluation of stress–strain and acoustic emission methods for quantitative damage assessments of brittle rock. *Rock Mech Rock Eng* 48(2): 495-508
- King MS (2002) Elastic wave propagation in and permeability for rocks with multiple parallel fractures, *Int J Rock Mech Min Sci* 39(8): 1033-1043
- Kokkinis D, Schaffner M, Studart AR (2015) Multimaterial magnetically assisted 3D printing of composite materials. *Nat Commun* 6: 8643
- Kolsky H (1949) An investigation of the mechanical properties of materials at very high rates of loading. *Proc Phys Soc London Sect B* 62: 676
- Kolsky H (1953) *Stress waves in solids*. Oxford University Press, London
- Kumano A, Goldsmith W (1982) Behavior of diorite under impact by variously-shaped projectiles. *Rock Mech* 15(1): 25-40
- Kumar A (2012) The effect of stress rate and temperature on the strength of basalt and granite. *Geophysics* 33(3): 501
- Lemaitre J, Chaboche JL (1994) *Mechanics of solid materials*. Cambridge university press
- Li DY, Zhu QQ, Zhou ZL, Li XB, Ranjith PG (2017c) Fracture analysis of marble specimens with a hole under uniaxial compression by digital image correlation. *Eng Fract Mech* 183:

109-124

- Li H, Wong LNY (2012) Influence of flaw inclination angle and loading condition on crack initiation and propagation. *Int J Solids Struct* 49(18): 2482-2499
- Li HB, Zhao J, Li TJ (2000) Micromechanical modelling of the mechanical properties of a granite under dynamic uniaxial compressive loads. *Int J Rock Mech Min Sci* 37(6): 923-935
- Li JC, Li NN, Li HB, Zhao J (2017b) An SHPB test study on wave propagation across rock masses with different contact area ratios of joint. *Int J Impact Eng* 105: 109-116
- Li JC, Li HB, Zhao J (2015) An improved equivalent viscoelastic medium method for wave propagation across layered rock masses. *Int J Rock Mech Min Sci* 73: 62-69
- Li JC, Ma GW (2009) Experimental study of stress wave propagation across a filled rock joint. *Int J Rock Mech Min Sci* 46(3): 471-478
- Li JC, Ma GW, Huang X (2010) Analysis of wave propagation through a filled rock joint. *Rock Mech Rock Eng* 43(6): 789-798
- Li XB, Lok TS, Zhao J, Zhao PJ (2000) Oscillation elimination in the hopkinson bar apparatus and resultant complete dynamic stress-strain curves for rocks. *Int J Rock Mech Min Sci* 37(7): 1055-1060
- Li XB, Lok TS, Zhao J (2005b) Dynamic characteristics of granite subjected to intermediate loading rate. *Rock Mech Rock Eng* 38: 21-39
- Li X, Zhou T, Li D (2017a) Dynamic strength and fracturing behavior of single-flawed prismatic marble specimens under impact loading with a split-hopkinson pressure bar. *Rock Mech Rock Eng* 50(1): 1-16
- Liang ZZ, Tang CA, Li HX, Xu T, Zhang YB (2004) Numerical simulation of 3-d failure process in heterogeneous rocks. *Int J Rock Mech Min Sci* 41: 323-328
- Liang ZZ, Xing H, Wang SY, Williams DJ, Tang CA (2012) A three-dimensional numerical investigation of the fracture of rock specimens containing a pre-existing surface flaw. *Comput Geotech* 45: 19-33
- Lindholm US, Yeakley LM, Nagy A (1974) The dynamic strength and fracture properties of dresser basalt. *Int J Rock Mech Min Sci* 11(5): 181-191
- Lisjak A, Liu Q, Zhao Q, Mahabadi OK, Grasselli G (2013) Numerical simulation of acoustic emission in brittle rocks by two-dimensional finite-discrete element analysis. *Geophys J Int*

195: 423-443

- Liu BX, Huang JL, Wang ZY, Liu L (2009) Study on damage evolution and acoustic emission character of coal-rock under uniaxial compression. *Chin J Rock Mech Eng* 28(1): 3234-3238 (in Chinese)
- Liu HY, Kou SQ, Lindqvist PA, Tang CA (2004) Numerical studies on the failure process and associated microseismicity in rock under triaxial compression. *Tectonophysics* 384:149-174
- Liu J, Liu FH, Kong XJ, Yu L (2014) Large-scale shaking table model tests of aseismic measures for concrete faced rock-fill dams. *Soil Dyn Earthq Eng* 61-62 (3): 152-163
- Lockner D, Byerlee J, Kuksenko V, Ponomarev A, Sidorin A (1991) Quasi-static fault growth and shear fracture energy in granite. *Nature* 350(6313): 39-42
- Lockner DA, Walsh JB, Byerlee JD (1977) Changes in seismic velocity and attenuation during deformation of granite. *J Geophys Res* 82(33): 5374-5378
- Lok TS, Li XB, Liu D, Zhao PJ (2002) Testing and response of large diameter brittle materials subjected to high strain rate. *J Mater Civ Eng* 14(3): 262-269
- Lukić B, Forquin P (2016) Experimental characterization of the punch through shear strength of an ultra-high performance concrete. *Int J Impact Eng* 91: 34-45
- Ma T, Yang C, Chen P, Wang X, Guo Y (2016) On the damage constitutive model for hydrated shale using CT scanning technology. *J Nat Gas Sci Eng* 28: 204-214
- Mahabadi OK, Randall NX, Zong Z, Grasselli G (2012) A novel approach for micro-scale characterization and modeling of geomaterials incorporating actual material heterogeneity. *Geophys Res Lett* 39: L01303
- Main IG, Meredith PG, Jones C (1989) A reinterpretation of the precursory seismic b-value anomaly from fracture mechanics. *Geophys J Int* 96(1): 131-8
- Mangual J, ElBatanouny MK, Ziehl P, Matta F (2013) Acoustic-emission-based characterization of corrosion damage in cracked concrete with prestressing strand. *ACI Mater J* 110(1): 89-98
- Marks P (2011) 3D printing takes off with the world's first printed plane. *New Scientist* 211(2823): 17-18
- Martin CD, Chandler NA (1994) The progressive fracture of Lac du Bonnet granite. *Int J Rock Mech Min Sci* 31(6): 643-659

- Martínez-Martínez J, Fusi N, Galiana-Merino JJ, Benavente D, Crosta GB (2016) Ultrasonic and X-ray computed tomography characterization of progressive fracture damage in low-porous carbonate rocks. *Eng Geol* 200: 47-57
- Melosh HJ, Ryan EV, Asphaug E (1992) Dynamic fragmentation in impacts: hydrocode simulation of laboratory impacts. *J Geophys Res Planets* 97(E9): 14735-14759
- Meng H, Li QM (2003) An SHPB set-up with reduced time-shift and pressure bar length. *Int J Impact Eng* 28(6): 677-696
- Meredith PG, Ayling MR, Murrell SAF, Sammonds PR (1991) Cracking, damage and fracture in stressed rock: a holistic approach. Shah SP (ed.), *Toughening Mechanisms in Quasi-Brittle Materials*, Kluwer Academic Publishers, Dordrecht, The Netherlands, pp: 67-89
- Michna S, Wu W, Lewis JA (2005) Concentrated hydroxyapatite inks for direct-write assembly of 3-D periodic scaffolds. *Biomaterials* 26(28): 5632-5639
- Mindlin RD (1960) Waves and vibrations in isotropic, elastic plates. In: Goodier JN, Hoff JJ (eds) *Structural mechanics*. Pergamon, New York, pp 199-232
- Mitchell MG (2016) *Cell Biology: Translational impact in cancer biology and bioinformatics*. Elsevier, Cambridge, p 122
- Munz D, Fett T (1999) *Ceramics: mechanical properties, failure behaviour, materials selection*. Springer Verlag, New York, p 1
- NASA (2014) Space station 3-D printer builds ratchet wrench to complete first phase of operations. http://www.nasa.gov/mission_pages/station/research/news/3Dratchet_wrench. Accessed 26 April 2015
- Nasser MHB, Rezanezhad F, Young RP (2011) Analysis of fracture damage zone in anisotropic granitic rock using 3d x-ray ct scanning techniques. *Int J Fract* 168(1): 1-13
- Nemat-Nasser S, Horii H (1982) Compression-induced nonplanar crack extension with application to splitting, exfoliation, and rockburst. *J Geophys Res* 87: 6805-6821
- Ohtsu M, Watanabe H (2001) Quantitative damage estimation of concrete by acoustic emission. *Constr Build Mater* 15(5-6): 217-224
- Ortiz M (1985) A constitutive theory for the inelastic behavior of concrete. *Mech Mater* 4(1): 67-93
- Otani J, Obara Y (2004) X-ray CT for Geomaterials: soils, concrete, rocks. *Proceedings of the*

-
- International Workshop on X-Ray CT for Geomaterials: GEOX2003, Kimamoto, Japan, Royal Swets and Zeitlinger: Lisse
- Otten W, Pajor R, Schmidt S, Baveye PC, Hague R, Falconer RE (2012) Combining X-ray CT and 3D printing technology to produce microcosms with replicable, complex pore geometries. *Soil Biol Biochem* 51: 53-55
- Park CH, Bobet A (2009) Crack coalescence in specimens with open and closed flaws: a comparison. *Int J Rock Mech Min Sci* 46(5): 819-29
- Peng RD, Yang YC, Wang P, Zhang YJ (2012) Developments in detection of rock damage. *Appl Mech Mater* 152: 1018-1023
- Peng S, Johnson AM (1972) Crack growth and faulting in cylindrical specimens of Chelmsford granite. *Int J Rock Mech Min Sci* 9: 37-86
- Perkins RD, Green SJ, Friedman M (1970) Uniaxial stress behavior of porphyritic tonalite at strain rates to 10^3 /second. *Int J Rock Mech Min Sci* 7(5): 527-535
- Petit JP, Barquins M (1988) Can natural faults propagate under mode II conditions? *Tectonics* 7: 1243-1256
- Potyondy DO, Cundall PA (2004) A bonded-particle model for rock. *Int J Rock Mech Min Sci* 41: 1329-64
- Prassianakis IN, Prassianakis NI (2004) Ultrasonic testing of nonmetallic materials: concrete and marble. *Theor Appl Fract Mech* 42(2): 191-198
- Pyrak-Nolte LJ, Myer LR, Cook NGW (1990a) Transmission of seismic waves across single natural fractures. *J Geophys Res: Solid Earth* 95(B6): 8617-8638
- Pyrak-Nolte LJ, Myer LR, Cook NGW (1990b) Anisotropy in seismic velocities and amplitudes from multiple parallel fractures. *J Geophys Res: Solid Earth* 95(B7): 11345-11358
- Pyrak-Nolte LJ, Nolte DD (1992) Frequency dependence of fracture stiffness. *Geophys Res Lett* 19(3): 325-328
- Rabotnov YN (1963) On the equations of state for creep. *Progress in Applied Mechanics*, 12: 307-315
- Rao MVMS, Lakshmi KP (2005) Analysis of b-value and improved b-value of acoustic emissions accompanying rock. *Curr Sci* 89(9): 1577-1582
- Rao MVMS, Ramana YV (1992) A study of progressive failure of rock under cyclic loading by

- ultrasonic and AE monitoring techniques. *Rock Mech Rock Eng* 25(4): 237-251
- Raynaud S, Fabre D, Mazerolle F, Geraud Y, Latière HJ (1989) Analysis of the internal structure of rocks and characterization of mechanical deformation by a non-destructive method: x-ray tomodensitometry. *Tectonophysics* 159(1): 149-159
- Renard F, Bernard D, Desrues J, Ougier-Simonin A (2009) 3d imaging of fracture propagation using synchrotron x-ray microtomography. *Earth Planet Sci Lett* 286(1): 285-291
- Reyes O, Einstein HH (1991) Failure mechanisms of fractured rock—a fracture coalescence model. *Proc Seventh Int Congr Rock Mech* 1: 333-40
- Richeton J, Ahzi S, Vecchio KS, Jiang FC, Adharapurapu RR (2006) Influence of temperature and strain rate on the mechanical behavior of three amorphous polymers: characterization and modeling of the compressive yield stress. *Int J Solids Struct* 43(7), 2318-2335
- Roylance D (2001) Introduction to fracture mechanics. *Massachusetts Institute of Technology*, Cambridge, p 1
- Saba N, Jawaid M, Alothman OY, Paridah MT (2016) A review on dynamic mechanical properties of natural fibre reinforced polymer composites. *Constr Build Mater* 106, 149-159
- Sagong M, Bobet A (2002) Coalescence of multiple flaws in a rock-model material in uniaxial compression. *Int J Rock Mech Min Sci* 39(2): 229-241
- Sahouryeh E, Dyskin AV, Germanovich LN (2002) Crack growth under biaxial compression. *Eng Fract Mech* 69(18): 2187-2198
- Saksala T, Hokka M, Kuokkala V T, Mäkinen J (2013) Numerical modeling and experimentation of dynamic brazilian disc test on kuru granite. *Int J Rock Mech Min Sci* 59(8): 128-138
- Sammis CG, Rosakis AJ, Bhat HS (2009) Effects of off-fault damage on earthquake rupture propagation: Experimental studies. *Pure Appl Geophys* 166, 1629-1648
- Sayers CM, Kachanov M (1995) Microcrack-induced elastic wave anisotropy of brittle rocks. *J Geophys Res* 100(B3): 4149-4156
- Schmitt DR, Zoback MD (1993) Infiltration effects in the tensile rupture of thin walled cylinders of glass and granite: implications for the hydraulic fracturing breakdown equation. *Int J Rock Mech Min Sci* 30: 289-303
- Schoenberg M (1980) Elastic wave behavior across linear slip interfaces. *J Acoust Soc Am* 68(5):

1516-1521

- Scholz CH (1990) *The mechanics of earthquakes and faulting*. Cambridge University Press, Cambridge, New York, Sydney
- Seweryn, A., Poskrobko, S., Mróz, Z. (1997). Brittle fracture in plane elements with sharp notches under mixed-mode loading. *J Eng Mech* 123(6), 535-543
- Shatilo AP, Sondergeld C, Rai CS (1998) Ultrasonic attenuation in Glenn Pool rocks, northeastern Oklahoma. *Geophysics* 63(2): 465-478
- Shen B (1995) The mechanism of fracture coalescence in compression--experimental study and numerical simulation. *Eng Fract Mech* 51(1): 73-85
- Shen B, Stephansson O, Einstein HH, Ghahreman B (1995) Coalescence of fractures under shear stress experiments. *J Geophys Res* 100(B4): 5975-90
- Sinha UN, Singh B (2000) Testing of rock joints filled with gouge using a triaxial apparatus. *Int J Rock Mech Min Sci* 37(6): 963-981
- Song B Chen W (2004a) Dynamic stress equilibration in split hopkinson pressure bar tests on soft materials. *Exp Mech* 44(3): 300-312
- Song B Chen W (2004b) Loading and unloading split hopkinson pressure bar pulse-shaping techniques for dynamic hysteretic loops. *Exp Mech* 44(6): 622-627
- Stanchits S, Vinciguerra S, Dresen G (2006) Ultrasonic velocities, acoustic emission characteristics and crack damage of basalt and granite. *Pure Appl Geophys* 163(5-6): 975-994
- Stewart RR, Dyaar N, Omoboya B, De Figueiredo JJS, Willis M, Sil S (2012) Physical modeling of anisotropic domains: Ultrasonic imaging of laser-etched fractures in glass. *Geophysics* 78: D11-D19
- Svitek T, Vavryčuk V, Lokajíček T, Petružálek M, Kern H (2017) Effect of pressure on 3D distribution of P-wave velocity and attenuation in antigorite serpentinite. *Geophysics* 82(4): WA33-WA43
- Tang CA (1997) Numerical simulation of progressive rock failure and associated seismicity. *Int J Rock Mech Min Sci* 34:249-261
- Tang CA, Kaiser PK (1998) Numerical simulation of cumulative damage and seismic energy release during brittle rock failure-part I: fundamentals. *Int J Rock Mech Min Sci* 35(2):

113-121

- Tapponnier P, Brace WF (1976) Development of stress-induced microcracks in Westerly granite. *Int J Rock Mech Min Sci* 13(4): 103-112
- Teagle D, Ildefonse B (2011) Journey to the mantle of the Earth. *Nature* 471(7339): 437-439
- Teng CK, Yin XC, Li SY, Cai DE (1987) Experimental study of three dimensional fracture in plate sample with non-penetrating crack, *Acta Geophys Sinca* 30(4): 371-378 (in Chinese)
- Toksöz MN, Cheng CH, Timur A (1976) Velocities of seismic waves in porous rocks. *Geophysics* 41(4): 621-645
- Toksöz MN, Johnston DH, Timur A (1979) Attenuation of seismic waves in dry and saturated rocks: I. Laboratory measurements. *Geophysics* 44(4): 681-690
- Townend E, Thompson BD, Benson PM, Meredith PG, Baud P, Young RP (2008) Imaging compaction band propagation in Diemelstadt sandstone using acoustic emission locations. *Geophys Res Lett* 35(15): L15301
- Tuffen H, Smith R, Sammonds PR (2008) Evidence for seismogenic fracture of silicic magma. *Nature* 453(7194): 511-514
- Vaitkus A, Gražulyt J, Kleizien R (2014) Influence of static and impact load on pavement performance. The 9th International Conference on Environmental Engineering, Vilnius, Lithuania, pp 1-9
- Van de Steen B, Vervoort A, Napier JAL (2005) Observed and simulated fracture pattern in diametrically loaded discs of rock material. *Int J Fract* 131: 35-52
- Vásárhelyi B, Bobet A (2000) Modeling of crack initiation, propagation and coalescence in uniaxial compression. *Rock Mech Rock Eng* 33(2): 119-139
- Walsh JB (1966) Seismic wave attenuation in rock due to friction. *J Geophys Res* 71(10): 2591-2599
- Wang LB, Frost JD, Voyiadjis GZ, Harman TP (2003) Quantification of damage parameters using X-ray tomography images. *Mech Mater* 35: 777-790
- Wang QZ, Jia XM, Kou SQ, Zhang ZX, Lindqvist PA (2004) The flattened Brazilian disc specimen used for testing elastic modulus, tensile strength and fracture toughness of brittle rocks: analytical and numerical results. *Int J Rock Mech Min Sci* 41: 245-253
- Wang SY, Sloan SW, Tang CA (2014) Three-dimensional numerical investigations of the failure

- mechanism of a rock disc with a central or eccentric hole. *Rock Mech Rock Eng* 47: 2117-2137
- Wang X, Ge H, Wang J, Wang D, Chen H (2016) Evaluation of the micro-cracks in shale from the stress sensitivity of ultrasonic velocities. *Rock Mech Rock Eng* 49(12): 4929-4934
- Wawersik WR, Fairhurst C (1970) A study of brittle rock fracture in laboratory compression experiments. *Int J Rock Mech Min Sci* 7(5): 561-575
- Weibull W (1951) A statistical distribution function of wide applicability. *J Appl Mech* 18: 293-297
- Wong LNY (2008) Crack coalescence in molded gypsum and Carrara marble. Ph.D thesis, Massachusetts Institute of Technology, Cambridge
- Wong LNY, Einstein HH (2009a) Systematic evaluation of cracking behavior in specimens containing single flaws under uniaxial compression. *Int J Rock Mech Min Sci* 46: 239-249
- Wong LNY, Einstein HH (2009b) Crack coalescence in molded gypsum and carrara marble: part 1. macroscopic observations and interpretation. *Rock Mech Rock Eng* 42: 475-511
- Wong RHC, Chau KT (1997) The coalescence of frictional cracks and the the shear zone formation in brittle solids under compressive stresses. *Int J Rock Mech Min Sci* 34(3-4): 335.e1-335.e12
- Wong RH, Chau K (1998) Crack coalescence in a rock-like material containing two cracks. *Int J Rock Mech Min Sci* 35: 147-164
- Wong RHC, Chau KT, Tang CA, Lin P (2001) Analysis of crack coalescence in rock-like materials containing three flaws--part I: experimental approach. *Int J Rock Mech Min Sci* 38(7): 909-924
- Wong RHC, Huang ML, Jiao MR, Tang CA (2003) Crack propagation in brittle solid containing 3D surface fracture under uniaxial compression, *Chin J Rock Mech Eng* 22(1), 2145-2148 (in Chinese)
- Wong RHC, Huang ML, Jiao MR, Tang CA, Zhu WS (2004a) The mechanisms of crack propagation from surface 3-D fracture under uniaxial compression. *Key Eng Mater* 261: 219-224
- Wong RHC, Guo YS, Li LY, Chau KT, Zhu WS, Li SC (2006) Anti-wing crack growth from surface flaw in real rock, *Proc. of the 16th European Conference of Fracture*, 3-7 July, Alexandroupolis, Greece, 825-826

- Wong RHC, Law CM, Chau KT, Zhu WS (2004b) Crack propagation from 3-D surface fractures in PMMA and marble specimens under uniaxial compression. *Int J Rock Mech Min Sci* 41: 37-42
- Wong RHC, Li TC, Chau KT, Li SC, Zhu WS (2007) Crack growth study of a 3-D surface fracture under compressions using strain and acoustic emission measurements, Proc. of the 1st Canada-US Rock Mechanics Symposium, 27-31 May, Vancouver, Canada, 565-573
- Wong TF, David C, Zhu W (1997) The transition from brittle faulting to cataclastic flow in porous sandstones: Mechanical deformation. *J Geophys Res* 102(B2): 3009-3025
- Wu C, Fan W, Zhou Y, Luo Y, Gelinsky M, Chang J, Xiao Y (2012a) 3D-printing of highly uniform CaSiO₃ ceramic scaffolds: preparation, characterization and in vivo osteogenesis. *J Mater Chem* 22(24): 12288-12295
- Wu C, Luo Y, Cuniberti G, Xiao Y, Gelinsky M (2011) Three-dimensional printing of hierarchical and tough mesoporous bioactive glass scaffolds with a controllable pore architecture, excellent mechanical strength and mineralization ability. *Acta Biomater* 7(6): 2644-2650
- Wu W, Li JC, Zhao J (2012b) Loading rate dependency of dynamic responses of rock fractures at low loading rate. *Rock Mech Rock Eng* 45(3): 421-426
- Wu W, Li JC, Zhao J (2014) Role of filling materials in a P-wave interaction with a rock fracture. *Eng Geol* 172: 77-84
- Wu W, Zhu JB, Zhao J (2013) Dynamic response of a rock fracture filled with viscoelastic materials. *Eng Geol* 160: 1-7
- Wu XY, Baud P, Wong TF (2000) Micromechanics of compressive failure and spatial evolution of anisotropic damage in darley dale sandstone. *Int J Rock Mech Min Sci* 37(1-2): 143-160
- Wu Y, McGarry FJ, Zhu B, Keryk JR, Katsoulis DE (2005) Temperature effect on mechanical properties of toughened silicone resins. *Polym Eng Sci* 45(11): 1522-1531
- Xi DY, Qiu WL, Cheng JY, Yi LK, Zhang B, Xie D (1997) Relation between attenuation and porosity or saturation of rock. *Oil Geophys Prospect* 2: 005
- Xia K, Nasser MHB, Mohanty B, Lu F, Chen R, Luo SN (2008) Effects of microstructures on dynamic compression of Barre granite. *Int J Rock Mech Min Sci* 45(6): 879-887
- Xu S, Malik MA, Li Q, Wu Y (2016) Determination of double- k , fracture parameters using semi-circular bend test specimens. *Eng Fract Mech* 152: 58-71

- Xu X, Wu S, Jin A, Gao Y (2018) Review of the relationships between crack initiation stress, Mode I fracture toughness and tensile strength of geo-materials. *Int J Geomech* 18(10): 04018136
- Yan X, Gu P (1996) A review of rapid prototyping technologies and systems. *Comput Aided Design* 28(4): 307-318
- Yang GS, Liu H (2007) Study on the rock damage characteristics based on the technique of CT image processing. *J Chin Coal Soc* 32(5): 463-468 (in Chinese)
- Yang GS, Xie DY, Zhang CQ (1998) The quantitative analysis of distribution regulation of CT values of rock damage. *Chin J Rock Mech Eng* 17(3): 279-285 (in Chinese)
- Yang H, Duan HF, Zhu JB. An experimental study on ultrasonic P-wave propagation through a single fluid-filled rock joint. (submitted to *Rock Mech Rock Eng*)
- Yang SQ (2011) Crack coalescence behavior of brittle sandstone samples containing two coplanar fissures in the process of deformation failure. *Eng Fract Mech* 78: 3059-3081
- Yang SQ, Dai YH, Han LJ, Jin ZQ (2009) Experimental study on mechanical behavior of brittle marble samples containing different flaws under uniaxial compression. *Eng Fract Mech* 76(12): 1833-1845
- Yang SQ, Huang YH, Tian WL, Zhu JB (2017) An experimental investigation on strength, deformation and crack evolution behavior of sandstone containing two oval flaws under uniaxial compression. *Eng Geol* 217: 35-48
- Yang SQ, Jing HW (2011) Strength failure and crack coalescence behavior of brittle sandstone samples containing a single fissure under uniaxial compression. *Int J Fract* 168(2): 227-250
- Yang SQ, Ranjith PG, Huang YH, Yin PF, Jing HW, Gui YL, Yu QL (2015) Experimental investigation on mechanical damage characteristics of sandstone under triaxial cyclic loading. *Geophys J Int* 201: 662-682
- Yao W, Xu Y, Yu C, Xia K (2017) A dynamic punch-through shear method for determining dynamic mode II fracture toughness of rocks. *Eng Fract Mech* 176: 161-177
- Yin T, Bai L, Li X, Li X, Zhang S (2018) Effect of thermal treatment on the mode I fracture toughness of granite under dynamic and static coupling load. *Eng Fract Mech* 199: 143-158
- Yu Q, Tang CA, Tang S (2007) Digital image based characterization method of rock's heterogeneity and its primary application. *Chin J Rock Mech Eng* 26: 551-559. In Chinese

- Yu Q, Yang S, Ranjith PG, Zhu W, Yang T (2016) Numerical modeling of jointed rock under compressive loading using X-ray computerized tomography. *Rock Mech Rock Eng* 49: 877-891
- Yuan F, Prakash V, Tullis T (2011) Origin of pulverized rocks during earthquake fault rupture. *J Geophys Res* 116(B6): B06309
- Yue ZQ, Chen S, Tham LG (2003) Finite element modeling of geomaterials using digital image processing. *Comput Geotech* 30: 375-397
- Zhang QB, Zhao J (2013) Determination of mechanical properties and full-field strain measurements of rock material under dynamic loads. *Int J Rock Mech Min Sci* 60: 423-439
- Zhang QB, Zhao J (2014a) A review of dynamic experimental techniques and mechanical behaviour of rock materials. *Rock Mech Rock Eng* 47: 1411-1478
- Zhang QB, Zhao J (2014b) Quasi-static and dynamic fracture behaviour of rock materials: phenomena and mechanisms. *Int J Fract* 189(1): 1-32
- Zhang X-P, Wong LNY (2012) Cracking processes in rock-like material containing a single flaw under uniaxial compression- a numerical study based on parallel bonded-particle model approach. *Rock Mech Rock Eng* 45:711-737
- Zhang XP, Wong LNY (2013) Loading rate effects on cracking behavior of flaw-contained specimens under uniaxial compression. *Int J Fract* 180: 93-110
- Zhang Z, Zhang R, Xie H, Liu J, Were P (2015) Differences in the acoustic emission characteristics of rock salt compared with granite and marble during the damage evolution process. *Environ Earth Sci* 73(11): 6987-6999
- Zhao GF, Russell AR, Zhao X, Khalili N (2014) Strain rate dependency of uniaxial tensile strength in Gosford sandstone by the Distinct Lattice Spring Model with X-ray micro CT. *Int J Solids Struct* 51:1587-1600
- Zhao J (1997a) Joint surface matching and shear strength part A: joint matching coefficient (JMC). *Int J Rock Mech Min Sci* 34(2): 173-178
- Zhao J (1997b) Joint surface matching and shear strength part B: JRC-JMC shear strength criterion. *Int J Rock Mech Min Sci* 34(2): 179-185
- Zhao J, Zhao XB, Cai JG, Hefny AM (2006) A further study on P-wave attenuation across parallel fractures with linear deformational behavior. *Int J Rock Mech Min Sci* 43:776-788

- Zhao M, Xu R (2000) The rock damage and strength study based on ultrasonic velocity. *Chin J Geotech Eng* 22(6): 720-722 (in Chinese)
- Zhao XG, Cai M, Wang J, Ma LK (2013) Damage stress and acoustic emission characteristics of the Beishan granite. *Int J Rock Mech Min Sci* (64): 258-269
- Zhou T, Dong SL, Zhao GF, Zhang R, Wu SY, Zhu JB (2018b) An experimental study of fatigue behavior of granite under low-cycle repetitive compressive impacts. *Rock Mech Rock Eng* 51: 3157-3166
- Zhou T, Zhu JB (2016) Application of 3D printing and micro-CT scan to rock dynamics. In: *Proceedings of the 2nd international conference on rock dynamics and applications*. Suzhou; 18-20 May 2016. p. 247-252
- Zhou T, Zhu JB (2017) An experimental investigation of tensile fracturing behavior of natural and artificial rocks in static and dynamic Brazilian disc tests. *Procedia Eng* 191: 992-998. The 2017 ISRM European Rock Mechanics Symposium, Ostrava, Czech
- Zhou T, Zhu JB (2018) Identification of a suitable 3D printing material for mimicking brittle and hard rocks and its brittleness enhancements. *Rock Mech Rock Eng* 51: 765-777
- Zhou XP, Zhang JZ, Wong LNY (2018a) Experimental study on the growth, coalescence and wrapping behaviors of 3D cross-embedded flaws under uniaxial compression. *Rock Mech Rock Eng* 51(5): 1379-1400
- Zhou YX, Xia KW, Li XB, Li HB, Ma GW, Zhao J, Zhou ZL, Dai F (2012) Suggested methods for determining the dynamic strength parameters and mode-I fracture toughness of rock materials. *Int J Rock Mech Min Sci* 49: 105-112
- Zhou ZL, Li XB, Ye ZY, Liu KW (2010) Obtaining constitutive relationship for rate-dependent rock in SHPB tests. *Rock Mech. Rock Eng* 43:697-706
- Zhou ZL, Li XB, Zou Y, Jiang Y, Li GN (2014) Dynamic brazilian tests of granite under coupled static and dynamic loads. *Rock Mech Rock Eng* 47(2): 495-505
- Zhu JB, Perino A, Zhao GF, Barla G, Li JC, Ma GW, Zhao J (2011b) Seismic response of a single and a set of filled joints of viscoelastic deformational behaviour. *Geophys J Int* 186(3): 1315-1330
- Zhu JB, Zhao XB, Li JC, Zhao GF, Zhao J (2011a) Normally incident wave propagation across a joint set with the virtual wave source method. *J Appl Geophys* 73(3): 283-288
- Zhu JB, Zhao J (2013) Obliquely incident wave propagation across rock joints with virtual wave

source method. *J Appl Geophys* 88:23-30

Zhu JB, Zhao XB, Wu W, Zhao J (2012) Wave propagation across rock joints filled with viscoelastic medium using modified recursive method. *J Appl Geophys* 86, 82-87

Zhu JB, Zhou T, Liao ZY, Sun L, Li XB, Chen R. (2018) Replication of internal defects and investigation of mechanical and fracture behaviour of rock using 3D printing and 3D numerical methods in combination with X-ray computerized tomography. *Int J Rock Mech Min Sci* 106, 198-212

Zhu WC, Liu J, Yang TH, Sheng JC, Elsworth D (2006) Effects of local rock heterogeneities on the hydromechanics of fractured rocks using a digital-image-based technique. *Int J Rock Mech Min Sci* 43:1182-1199

Zhu WC, Niu LL, Li SH, Xu ZH (2015) Dynamic brazilian test of rock under intermediate strain rate: pendulum hammer-driven shpb test and numerical simulation. *Rock Mech Rock Eng* 48(5): 1867-1881

Zou CJ, Wong LNY (2014) Experimental studies on cracking processes and failure in marble under dynamic loading. *Eng Geol* 173: 19-31